Analysis of a Radial Flux Air-cored Permanent Magnet Machine with a Double-sided Rotor and Non-overlapping Windings

by

Peter Jan Randewijk

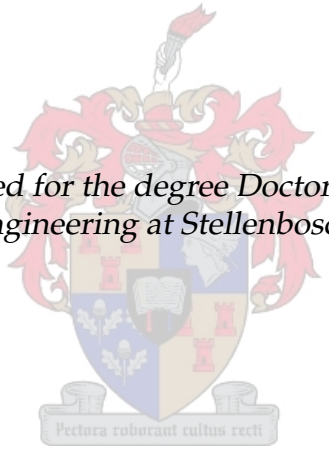

Dissertation presented for the degree Doctor of Philosophy in the Faculty of Engineering at Stellenbosch University

Promotor: Prof. Maarten Jan Kamper
Faculty of Engineering
Department of Electrical & Electronic Engineering

March 2012

Declaration

By submitting this dissertation electronically, I declare that the entirety of the work contained therein is my own, original work, that I am the sole author thereof (save to the extent explicitly otherwise stated), that reproduction and publication thereof by Stellenbosch University will not infringe any third party rights and that I have not previously in its entirety or in part submitted it for obtaining any qualification.

March 2012

Abstract

Analysis of a Radial Flux Air-cored Permanent Magnet Machine with a Double-sided Rotor and Non-overlapping Windings

P. J. Randewijk

Promotor: Prof. Maarten Jan Kamper
Faculty of Engineering
Department of Electrical & Electronic Engineering

Dissertation: PhD (Electrical Engineering)

March 2012

In this dissertation a new type of electrical machine, a Radial Flux Air-Cored Permanent Magnet machine with a Double-sided Rotor and utilising concentrated, non-overlapping windings, is proposed. The concept of the Double-sided Rotor Radial Flux Air-Cored Permanent Magnet machine, or RFAPM machine for short, was derived from the Double-sided Rotor Axial Flux Air-Cored Permanent Magnet (AFAPM) machine. One of the problems that AFAPM machines experience, is the deflection of the rotor discs due to the strong magnetic pull of the permanent magnets, especially with double-sided rotor machines. The main advantage of a RFAPM machine over a AFAPM machine is that the rotor back-iron is cylindrically shaped instead of disk shaped. Due to the structural integrity of a cylinder, the attraction force between the two rotors does not come into play any more.

The focus of this dissertation is on a thorough analytical analysis of the Double-Sided Rotor RFAPM machine. With the RFAPM being an air-cored machine, the feasibility to develop a linear, analytical model, to accurately predict the radial flux-density and hence the induced EMF in the stator windings, as well as the accurate calculation of the developed torque of the machine, needed to be investigated. The need for a thorough analytical examination of the Double-Sided Rotor RFAPM machine stemmed from the need to reduce the blind reliance on Finite Element Modelling (FEM) software to calculate the back-EMF and torque produced by these machines.

Another problem experienced with the FEM software was to obtain accurate torque results. Excessive ripple torque oscillations were sometimes experienced which took a considerable amount of time to minimise with constant refinement to the meshing of the machine parts. Reduction in the mesh element size unfortunately also added to the simulation time. The requirement for an accurate analytical model of the RFAPM machine was also necessary in order

to reduce the amount of time spent on successive FEM simulation to obtain the optimum pole arc width of the permanent magnet in order to minimise the harmonic content of the radial flux-density distribution in the the stator windings.

In this dissertation, the use of single-layer and double-layer, non-overlapping, concentrated winding for the RFAPM machine is also investigated. It was decided to include a comparison of these two non-overlapping winding configurations with a "hypothetical" concentrated, overlapping winding configuration. This would allow us to gauge the effectiveness of using non-overlapping winding with respect to the reduction in copper losses as well as in the reduction in copper volume. It would also allow us to investigate the extent of how much the developed torque is affected by using non-overlapping windings instead of overlapping windings.

Uittreksel

Analiese van 'n Radiale-vloed Lugkern Permanent Magneet Masjien met 'n Dubbelkantige Rotor en Nie- oorvleuelende Windings

P. J. Randewijk

Promotor: Prof. Maarten Jan Kamper
Fakulteit Ingenieurswese
Departement Elektries & Elektroniese Ingenieurswese

Proefskrif: PhD (Elektriese Ingenieurswese)

Maart 2012

In hierdie proefskrif word 'n nuwe tipe elektriese masjien, 'n Radiale-vloed Lugkern Permanent Magneet Masjien met 'n dubbelkantige rotor en nie-oorvleuelende Windings voorgestel. Die konsep vir die Radiale-vloed Lugkern Permanent Magneet Masjien, of RVLPM vir kort, is afgelei vanaf die Dubbelkantige Rotor, Aksiale-vloed Lugkern (AVLPM) masjien. Een van die probleme wat met AVLPM masjiene ondervind word, is die defleksie van die rotorjukke as gevolg van die sterk aantrekkingskragte van die permanente magnete, veral in dubbelkantige rotor masjiene. Die hoof voordeel wat die RVLPM masjien inhou bo die AVLPM masjien, is die feit dat die RVLPM se rotorjukke silindries is in plaas van ronde skywe. As gevolg van die strukturele integriteit van 'n silinders, speel die aantrekkingskrag van die permanente magnete nie meer 'n rol nie.

Die fokus van die proefskrif gaan oor die deeglike analitiese analise van die dubbelkantige RVLPM masjien. Weens die feit dat die RVLPM masjien 'n lugkern masjien is, is daar besluit om ondersoek in te stel na die moontlikheid om 'n lineêre, analitiese model vir die masjien op te stel waarmee die radiale-vloeddigtheid, teen-EMK asook die ontwikkelde draaimoment vir die masjien akkuraat bereken kan word. Die behoefde aan 'n akkurate analitiese model vir die dubbelkantige rotor RVLPM masjien is om die blinde vertroue te elimineer wat daar in Eindige-Element Modellering (EEM) sagteware gestel word om die teen-EMK en ontwikkelde draaimoment van die RVLPM masjien uit te werk.

'n Verdere probleem wat daar met EEM sagteware ondervind is, is die akkurate berekening van die ontwikkelde draaimoment. Oormatige rimpel draaimoment ossillasies is soms ondervind wat heelwat tyd geverg het om te minimeer, deur voortdurende verfyning van die EEM maas in die verskillende dele van die masjien. Soos die maas egter kleiner word, verleng dit die simulasie tyd van die EEM aansienlik. Nog 'n rede vir 'n akkurate analitiese model

van die RVLPM masjien, is om vinnige metode te verkry om die optimale permanente magneet pool hoekwydte te verkry, wat die minste Totale Harmoniese Vervorming (THV) in die radiale-vloeddigtheidsdistribusie in die statorgebied sal veroorsaak, sonder om herhaaldelike EEM simulasies te loop.

In die proefskrif word die gebruik van enkellaag en dubbellaag, nie- oorvleuelende, gekonsentreerde wikkelings vir die RVLPM masjien ook ondersoek. Daar is besluit om hierdie twee nie-oorvleuelende windingskonfigurasies met 'n "hipotetiese" gekonsentreerde, oorvleuelende windingskonfigurasie te vergelyk. Dit behoort ons in staat te stel om die doeltreffendheid van nie-oorvleuelende windings te bepaal, met betrekking tot die afname in koperverliese asook die afname in kopervolume. Verder sal dit ons in staat stel om ook mate waartoe die ontwikkelde draaimoment deur nie-oorvleuelende windings beïnvloed word, te ondersoek.

Dedications

Hierdie tesis word opgedra aan my wederhelfte,
Marilie Randewijk,
vir haar ondersteuning, geduld, moed inpraat en liefde
asook vir die hulp met die proeflees van die tesis.

Contents

List of Figures

List of Tables

Nomenclature

Abbreviations

2-D	Two Dimensional	
3-D	Three Dimensional	
AC	Alternating Current	
AFPM	Axial Flux Permanent Magnet	
AFAPM	Axial Flux Air-cored Permanent Magnet	
CLUI	Command Line User Interface	
CVW	Coulomb Virtual Work	
DC	Direct Current	
EMF	Electromotive Force	[V]
EV	Electric Vehicle	
FE	Finite Element	
FEA	Finite Element Analysis	
FEM	Finite Element Modelling	
GUI	Graphical User Interface	
LHS	Left Hand Side	
MST	Maxwell Stress Tensor	
NdBFe	Neodymium-Boron-Iron	
PCB	Printed Circuit Board	
PM	Permanent Magnet(s)	
RFAPM	Radial Flux Air-cored Permanent Magnet	
RHS	Right Hand Side	
THD	Total Harmonic Distortion	

Roman Symbols

a	number of parallel circuits per phase	
A	magnetic vector potential	[Wb/m]
A_m	cross sectional area of each magnet	[m^2]
A_g	cross sectional area of the airgap	[m^2]
A_{wire}	cross sectional area of each coil turn	[m^2]
B_c	flux density in the iron core	[T]

B_g	flux density in the airgap	[T]
B_m	flux density in the permanent magnet	[T]
B_{p_1}	peak flux density of the first harmonic	[T]
B_{rem}	remanent flux density of the permanent magnets	[T]
B_θ	azimuthal flux density component	[T]
C_M	machine constant	
d_r	magnetic or d-axis of the rotor	
d_s	magnetic or d-axis of the stator	
D	electrical flux density	[C/m^2]
E_p	peak sinusoidal phase voltage	[V]
h	height/thickness of the stator coils	[m]
h_m	magnet height/thickness	[m]
h_y	yoke height/thickness	[m]
H_c	magnetic field intensity in the iron core, or, coercivity of a permanent magnet	[At/m]
H_g	magnetic field intensity in the airgap	[At/m]
H_m	magnetic field intensity in the permanent magnet	[At/m]
I_p	peak sinusoidal phase current	[A]
k_Δ	coil side-width factor	
k_f	fill factor	
k_m	the magnet (or pole) width to pole pitch ratio	
k_E	voltage constant	[V/rad/s]
k_q	number of coils per pole (per phase)	
k_Q	number of coils per pole (for all three phase)	
k_T	torque constant	[Nm/A]
k_w	general winding factor	
$k_{w,pitch}$	winding pitch factor	
$k_{w,slot}$	winding slot width factor	
M	magnetisation	[A/m]
M_0	residual magnetisation	[A/m]
M_i	induced magnetisation	[A/m]
n	conductor density	
N	number of turns per coil	
p	number of pole pairs	
P_{cu}	total copper losses	[W]
P_e	electrical power	[W]
P_m	mechanical power	[W]
q	number of coils per phase	
Q	total number of coils $(Q = 3q)$	
R_{coil}	total copper resistance per coil	[Ω]
r_e	the average end-turn conductor radius	[m]
$r_{m\|_c}$	the radius as measured to the centre of the magnets	[m]
r_n	nominal stator radius	[m]

R_s	total copper resistance per phase	[Ω]
V_{Cu}	total copper volume of the stator	[m^3]
w	coil side-width of the stator coils	[m]
w_{ip}	inter-pole gap width	[m]
w_p	pole width	[m]

Other Symbols

ℓ	active copper length of the stator conductors	[m]
ℓ_c	mean magnetic flux path length in the iron core	[m]
ℓ_e	end-turn length of the stator conductors	[m]
ℓ_g	airgap length	[m]
ℓ_n	the average coil-turn length	[m]

Greek Symbols

χ_m	magnetic susceptibility	
δ	the angle measured from the centre of the coil side	[rad]
Δ	$\frac{1}{2}$ coil side-width angle of the stator coils	[rad]
γ	the angle between the magnetic axis of the rotor and that of the stator	[rad]
λ	flux-linkage of a single turn	[Wb-turns]
Λ	total flux-linkage per phase	[Wb-turns]
μ_{recoil}	recoil permeability $(\mu_0\mu_{r_{recoil}})$	
$\mu_{r_{recoil}}$	relative recoil permeability	
ϕ	azimuthal axis in cylindrical coordinates	
φ	average flux-linkage per coil	[Wb]
ρ_{cu}	copper resistivity	[Ωm]
τ_p	pole pitch angle	[rad]
$\tau_{p,res}$	resultant pole pitch angle	[rad]
τ_q	coil pitch angle	[rad]
$\tau_{q,res}$	resultant coil pitch angle	[rad]
θ_{ip}	inter-pole width angle	[rad]
ξ	stator length, ℓ, to the nominal stator radius, r_n, ratio	
θ_m	pole/magnet width angle	[rad]
θ_p	pole/magnet width angle	[rad]
θ_q	coil pitch (or coil span) angle	[rad]
θ_r	resultant coil pitch angle	[rad]
θ_s	slot width angle	[rad]

Constants

μ_0	permeability of free space $(4\pi \times 10^{-7})$

Accents or attributes

$\vec{\mathbf{a}}$	a unit vector
$\vec{\mathbf{A}}$	a vector field
$\hat{A}$	amplitude or peak value

Subscripts

AR	a quantity, e.g. A, B or H, due to the effect of the Armature Reaction alone
PM	a quantity, e.g. A, B or H, due to the effect of the Permanent Magnets alone
$1\|2\|\ldots$	specific harmonic component with "1" being the fundamental
$a \mid b \mid c$	phase a, b or c components
$\|O$	for the overlap winding configuration
$\|I$	for the non-overlap Type I winding configuration
$\|II$	for the non-overlap Type II winding configuration
n	the normal component
t	the tangential component
$x \mid y \mid z$	the Cartesian coordinates components
$r \mid \theta \mid z$	the cylindrical coordinates components

Superscripts

$I\|II\|\ldots$	the region or domain for which the quantity is valid for

CHAPTER 1

Introduction

It is not knowledge, but the act of learning, not possession but the act of getting there, which grants the greatest enjoyment.

KARL FRIEDRICH GAUSS

1.1 Introduction

In this dissertation a new type of electrical machine, a Radial Flux Air-Cored Permanent Magnet machine with a Double-sided Rotor and utilising concentrated, non-overlapping windings, is proposed. The RFAPM machine is a culmination of an electrical machine that

- makes use of the reduction in the cost of rare-earth permanent magnets[1],
- utilises the increase in strength of rare-earth permanent magnets in order to
- utilise the advantages arising from having air-cored stator windings,
- applies the concept of using concentrated, non-overlapping windings instead of overlapping windings and finally
- addresses the deflection problems experienced by the disc-shaped rotor yokes of Double-sided Rotor Axial Flux Air-Cored Permanent Magnet machines, due to the strong magnetic pull between the permanent magnets situated on the rotor yokes.

1.2 Background Information

The concept of the Double-sided Rotor Radial Flux Air-Cored Permanent Magnet machine, or RFAPM machine for short, was derived from the Double-sided Rotor Axial Flux Air-Cored Permanent Magnet (AFAPM) machine. The realisation of the RFAPM machine however, would

[1]This point was valid at the start of this research. Since 2011 however, there has been a sharp increase in the price of rare-earth permanent magnets due to new legislation passed in China, which is the main source of all rare-earth, permanent magnets in the world.

not have been possible without utilising concentrated, non-overlapping windings. The advantages of air-cored windings, specifically with regard to the superior efficiency of air-cored machines, would also not have been realised without the advancements made in the strength of rare-earth permanent magnets over the last decade. All of these contributed to the development of the RFAPM machine and will briefly be discussed in this section.

1.2.1 Rare-Earth Permanent Magnets

The discovery of samarium cobalt ($SmCo_5$), the first generation of the rare-earth permanent magnets, paved the way for the manufacturing of extremely compact motors and turbine generators, Gieras and Wing [1, sec. 2.3.3]. In comparison with the original Alnico permanent magnets, $SmCo_5$ has the advantage of,

- a high remanent flux density,
- an extremely high coercivity,
- a linear demagnetisation curve and
- a low temperature coefficient

Unfortunately $SmCo_5$ magnets are fairly expensive and thus their application was limited to "low volume" usage. The second generation of rare-earth permanent magnets, based on the fairly inexpensive Neodymium (Nd), reduced the cost of NdFeB permanent magnets significantly compared to $SmCo_5$ permanent magnets, whilst retaining all the benefits of $SmCo_5$ as mentioned above, Gieras and Wing [1, sec. 2.3.3]. The reduction in cost of NdFeB permanent magnets, combined with their high remanent flux-density and coercivity values, presented the opportunity for their usage in the manufacturing of medium to large sized motors and generators.

1.2.2 Slotless, Toothless and Core-less Windings

Due to the high flux-densities achievable in the air-gap using $SmCo_5$ permanent magnets, the idea of simply removing the stator teeth to render the machine toothless, or more commonly known as slotless, was first mentioned in the literature in 1982 by Hesmondhalgh and Tipping [2]. The main reasons for pursuing the design of slotless machines were, firstly to simplify the insertion of the stator winding especially for small, high-speed machines and secondly to eliminate tooth tip saturation and hence lower flux-densities in the stator backing iron.

Due to the high flux-density levels attainable with $SmCo_5$ permanent magnets, Hesmondhalgh and Tipping also investigated the torque generated when removing the stator backing iron and thus having a completely iron-less stator design. They found that, *"... the stator iron gives no inherent benefit as regards the absolute production of torque."* Hesmondhalgh and Tipping, however, did not recommend the usage of an iron-less stator for practical purposes as the iron provides a magnetic screen to reduce the eddy current losses in nearby conducting bodies.

In 1988, England [3] proposed a surface-wound, or slotless, permanent magnet motor in order to, *"... completely eliminate [the] cogging torque since there are no reluctance change in the magnetic circuit."* England presented a brushless servo motor utilising NdFeB permanent magnets with a ripple torque component of less than 1,5 %.

The idea of utilising slotless, permanent magnet machines for a direct-drive servo application, was proposed by Kaddouri and Le-Huy [4] in 1992, due to the low torque ripple of a these slotless machines. Their key conclusions, regarding the suitability of these type of machines for direct-drive applications, can be summarised as follows:

- Although the air-gap flux-density in the slotless motor is less, compared to the slotted motor, it is possible to increase the electrical loading of the machine because of the additional space available for more copper in order to achieve the same copper current density.
- The comparable efficiency for large diameter, "pancake-like", slotless motors are similar, but there is a marked decrease in efficiency for slotless motors as the diameter becomes smaller.
- Due to the higher electrical loading and the absence of any close thermal contact between the stator teeth and the stator windings in the slotless machine, particular attention has to be paid to the thermal design in slotless machines.

The effect of eddy current losses in the stator windings of a toothless (i.e. slotless) machine was first investigated by Arkadan *et al.* [5]. The reason for eddy current losses occurring in toothless machines are that instead of the flux flowing through the stator teeth, the flux now flows through the windings. Arkadan *et al.* however found that for a similar 75 kVA conventional designed permanent magnet motor, the core losses in the stator were more than the eddy current losses in the stator windings for a properly designed toothless machine.

The complete analytical analysis on the armature reaction field and the winding inductance for a slotless machine was first published by Atallah *et al.* [6] in 1998. The analytical analysis method proposed, used of a 2-D distributed current model for the armature reaction field and winding inductance calculation. This provided a more accurate representation than the 1-D current sheet method used for conductors situated in stator slots, Zhu and Howe [7].

The advantages and the disadvantages of slotless (or core-less) machines, can thus briefly be summarised as:

Advantages:

- no cogging torque
- no magnetic pull between the rotor and stator
- lower inductance and hence better voltage regulation for generator applications
- more accurate analytical analysis of the armature reaction field and winding inductance calculations, are possible

Disadvantages:

- lower flux density and hence a lower power density for the same amount of copper used
- low inductance for drive applications, resulting in a higher switching frequency required to minimise the ripple current drawn by the machine
- low inductance resulting in high fault currents in generator application
- eddy current losses in the copper windings

1.2.3 The Double-sided Rotor Axial Flux Permanent Magnet Machines

Axial Flux Permanent Magnet (AFPM) Machines are well documented in the literature and numerous patents exist for the various "flavours" of AFPM machines, Gieras *et al.* [8]. Of particular interest to us is the Axial Flux Air-cored Permanent Magnet (AFAPM) machine, Wang

[9]. Here the term "air-cored" is yet another term used to describe a slotless, core-less or iron-less stator machines, as discussed in section 1.2.2.

One of the problems that AFAPM machines experience, is the deflection of the rotor discs due to the strong magnetic pull of the permanent magnets, especially with double-sided rotor machines. This is discussed at length in Wang *et al.* [10] and Gieras *et al.* [8, sec. 8.10].

1.2.4 Non-overlapping, Concentrated Windings

The idea of using non-overlapping windings or coils for permanent magnet machines was first mentioned in the literature by Cros and Viarouge [11] in 2002 for sub-fractional machines. However these type of sub-fractional machines have been around for much longer, as can be seen from Figure 1.1, Wong [12], which shows a PCB mounted air-cored, non-overlapping, AFPM type floppy disk drive.

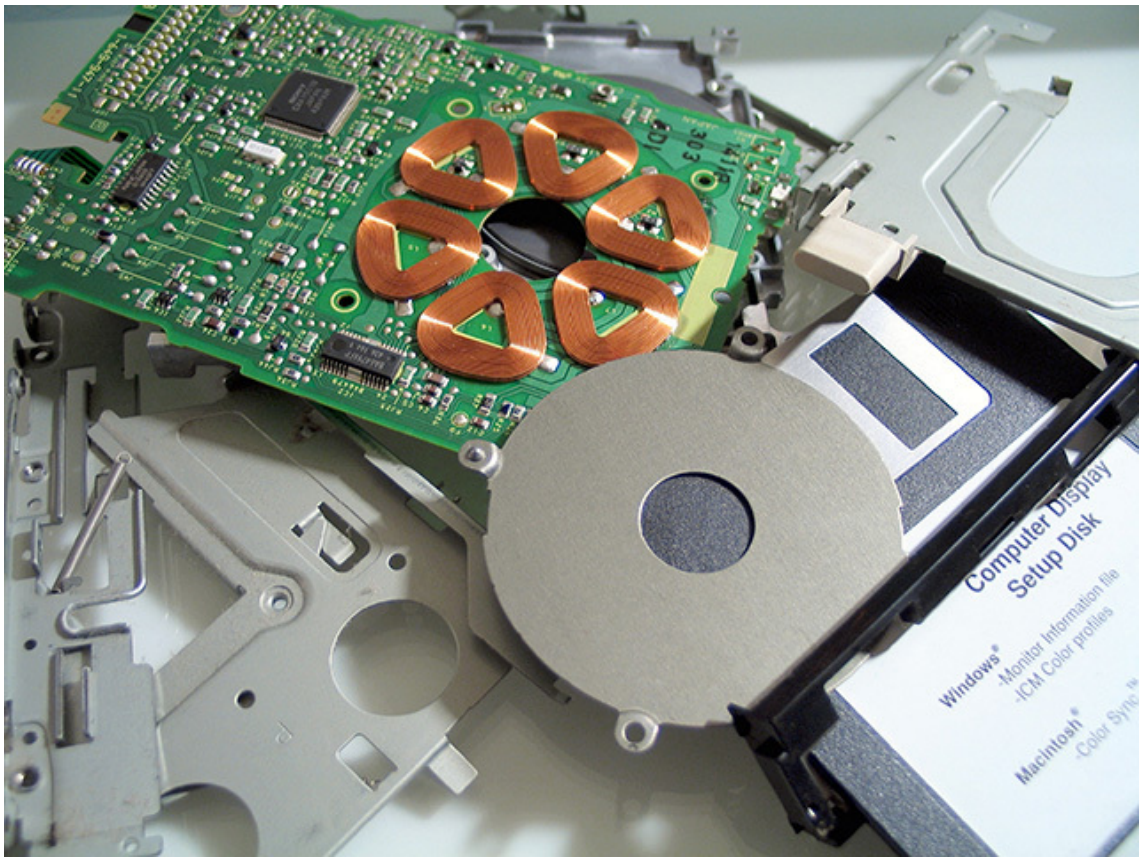

Figure 1.1: An old air-cored, non-overlapping, AFPM type floppy disk drive, Wong [12].

The main advantage of using non-overlapping windings is the fact that the end-winding length is reduced. This results in a reduction in the end-winding copper volume and thus of the total copper volume. Furthermore, non-overlapping coils are easier to manufacture and the manufacturing process is much simpler to automate. In 2008 Kamper *et al.* [13] demonstrated a 1 kW Double-Sided Rotor AFAPM machine making use of non-overlapping coils or as Kamper *et al.* preferred to call it, "non-overlapping concentrated' windings, to prevent any ambiguity in the description of the stator windings.

1.2.5 The Double-sided Rotor Radial Flux Air-Cored Permanent Magnet Machine

The Double-Sided Rotor RFAPM machine was first presented in 2007 by Randewijk *et al.* [14]. No other reference to this type of machine could be found in the literature prior to this date. The RFAPM machine is in essence a dual of the AFAPM machine of Kamper *et al.* [13] as can be seen in Figure 1.2, that shows a 16 pole RFAPM machine designed for a small wind generator application, Stegmann [15].

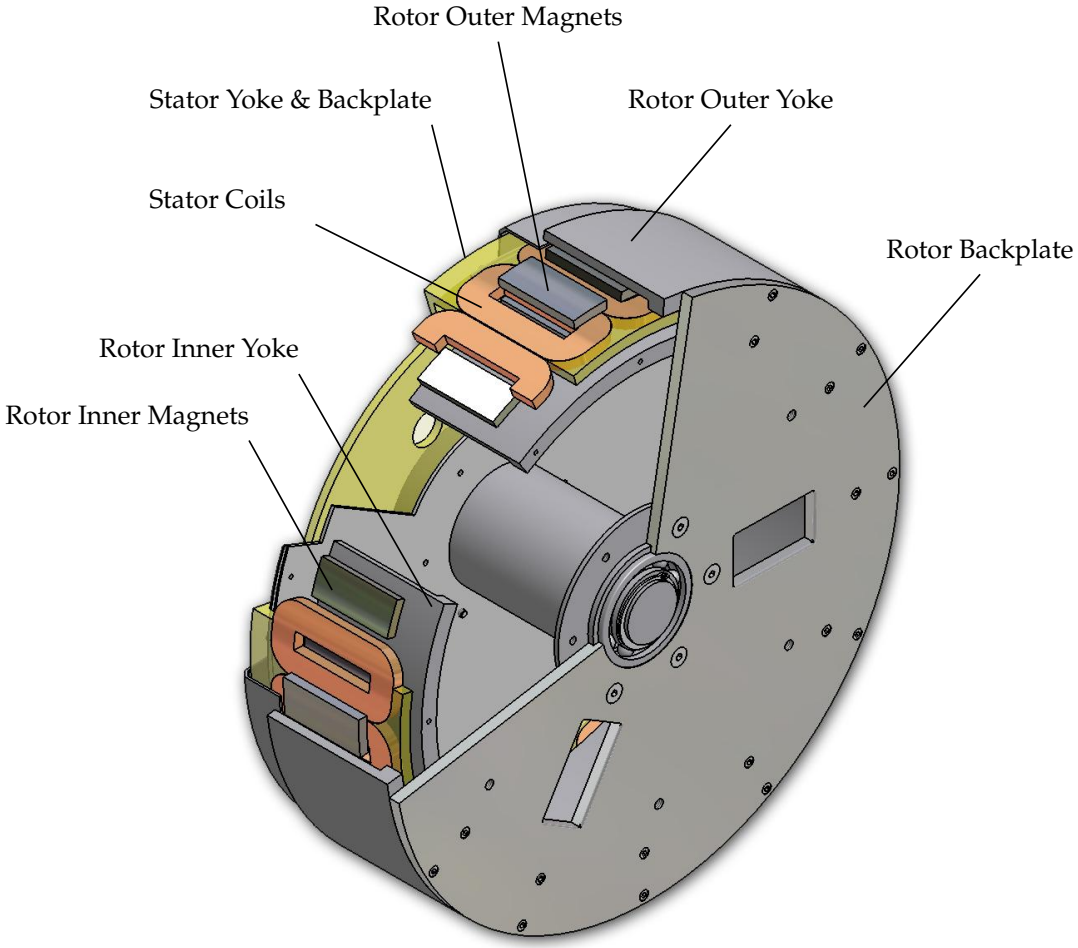

Figure 1.2: A 3-D view of a 16 pole RFAPM machine with non-overlapping windings, Stegmann [15].

The main advantage of a RFAPM machine over a AFAPM machine is that the rotor back-iron is cylindrically shaped instead of disk shaped. Due to the structural integrity of a cylinder, the attraction forces between the two rotors does not come into play any more. It was found instead, that the thickness of the rotor yoke is now determined by the amount of saturation allowed for in the rotor yoke in order to maintain the desired flux-density in the air-gap, Stegmann and Kamper [16]. Furthermore, Stegmann and Kamper also found that a Double-Sided Rotor RFAPM machine is approximately 30% lighter than a comparable AFAPM machine. This makes it ideally suited for low to medium power direct drive wind generators.

1.3 Dissertation Problem Statement

The focus of this dissertation is on a thorough analytical analysis of the Double-Sided Rotor RFAPM machine proposed by Randewijk *et al.* [14]. With the RFAPM being an air-cored machine, the feasibility to develop a linear, analytical model, to accurately predict the radial flux-density and hence the induced EMF in the stator windings, as well as the accurate calculation of the developed torque of the machine, needed to be investigated.

The need for a thorough analytical examination of the Double-Sided Rotor RFAPM machine stemmed from the need to reduce the blind reliance on FEM software to calculate the back-EMF and torque produced by these machines. This requirement especially came to the fore in two parallel MScEng research projects that were started to investigate the feasibility of using RFAPM machines for small wind turbines, Stegmann [15], as well as the feasibility of using the RFAPM machine for the primary drive chain in a small Electric Vehicle (EV), Groenewald [17]. The machine parameters for these two RFAPM machines are given in Appendix E, sections E.1 and E.2 respectively.

In these two MScEng research projects, problems were experienced to obtain accurate torque results using FEM. Excessive ripple torque oscillations were sometimes experienced which took a considerable amount of time to minimise with constant refinement to the meshing of the machine parts. Reduction in the mesh element size unfortunately also added to the simulation time, [18]. It was however uncertain as to the exact reason of the remaining ripple torque component specifically with regard to the uncertainty of whether any of the ripple torque could still be attributed to "computational noise" in the FEM result.

Also, it was disputable which portion of the ripple torque could be attributed to the harmonic content of the radial-flux density distribution and which portion to the slotting effect of the double-layer, non-overlapping, concentrated coil layout. The requirement for an accurate analytical model of the RFAPM machine was also necessary in order to reduce the amount of time spent on successive FEM simulation to obtain the optimum pole arc width of the permanent magnet in order to minimise the harmonic content of the radial flux-density distribution in the the stator windings.

Although both MScEng research projects used double-layer non-overlapping concentrated winding designs, it was decided to investigate the use of single-layer, non-overlapping, concentrated winding as well, as the end-windings of the single-layer winding configuration is even shorter than that of the double-layer winding configuration. Furthermore it was decided to include a comparison of these two non-overlapping winding configurations with a "hypothetical" concentrated, overlapping winding configuration. This would allow us to gauge the effectiveness of using non-overlapping winding with respect to the reduction in copper losses as well as in the reduction in copper volume. It would also allow us to investigate the extent of how much the developed torque is effected by using non-overlapping windings instead of overlapping windings.

1.4 Dissertation Work Layout

The layout of the dissertation can be summarised as follows:

Chapter 1: This chapter presents a brief introduction and some background information on the the Double-Sided Rotor RFAPM machine.

Chapter 2: This chapter will describe the construction of the Double-Sided Rotor RFAPM machine in more detail, especially with regard to the hypothetical overlapping as well as the single-layer and double-layer non-overlapping winding designs. The winding distribution factors, the winding factors as well as the current density distribution functions for the overlapping, single-layer non-overlapping and double-layer non-overlapping winding designs, will be deduced.

Chapter 3: In this chapter, the magnetic vector potential field produced by the permanent magnets of the RFAPM machine will calculated from first principles. For the analytical analysis the machine will be divided into a number of annuli-shaped subdomain regions. The governing Laplace and Poisson equation for each region will then be solved from the boundary condition values in order to obtain the complete magnetic vector potential solution for the machine. Maxwell® 2D, a commercial Finite Element Modelling (FEM) package from Ansys (formerly Ansoft) will be used to verify the analytical solution. The comparison between the analytical and the FEM solution will focus on the radial – and azimuthal flux-density distribution in the stator region. The flux-linkage and induced voltage (or back-EMF) for the different winding configurations, will also be compared.

Chapter 4: In this chapter, the armature reaction field produced by the different winding configurations will be analysed, using the same methodology as in Chapter 3, but with the permanent magnets "switched off". This will also allow us to calculate the three-phase inductances of the different winding configurations. Due to the fact that the analytical analysis will be done in 2-D, the effect of the end-windings on the synchronous inductance will not be taken into account. Again Maxwell® 2D simulations will be used to verify the analytical results obtained.

Chapter 5: This chapter will focus on the analytical calculation of the torque produced by the RFAPM machine, with specific emphasis on the ripple torque component of each winding configuration. In this chapter two FEM packages will be used to verify the analytical solution for the developed torque, Maxwell® 2D, as well as SEMFEM, which is a proprietary FEM package developed at Stellenbosch University and written in Fortran with some pre– and post processing done in Python™.

Chapter 6: In this chapter the end-winding effect will be investigated with regard to the difference in the winding resistance and hence copper losses for the different winding configurations. The effect of varying the current density in the different winding configurations to obtain equal copper losses will be investigated as well as the effect this has on the developed torque, copper volume, as well as the torque-per-copper-volume ratio as a function of the stator length and the coil-side width.

Chapter 7: The dissertation will conclude with the contributions made by this research, the conclusions drawn, as well as recommendations for future work to be done on this topic.

CHAPTER 2

Theoretical Winding Analysis of the Double-Sided Rotor Radial Flux Air-Cored Permanent Magnet Machine

My object has been, first to discover correct principles and then to suggest their practical development.

JAMES PRESCOTT JOULE

2.1 Introduction

In this chapter, three different winding configurations for the double-sided rotor RFAPM machine will be discussed. These are,

- the overlapping winding configuration, or Type O for short,
- the non-overlapping single-layer winding configuration, or Type I for short, and
- the non-overlapping double-layer winding configuration, or Type II for short.

Although the overlapping winding configuration is technically impossible for the rotor design shown in Figure 1.2, the discussion thereof will be done as a reference against which the Type I and Type II winding configurations can be bench-marked.

Our discussion will focus on the differences in the winding factors, the conductor density distributions and the current density distributions. The fundamental winding factor for each winding configuration will first be deduced, from first principles, from the flux-linkage calculation. The conductor density distribution will then be used to calculate the winding factors for all the winding space harmonics. It will be shown that, for the overlapping winding configuration, the working harmonic is the fundamental, or first harmonic of the conductor density

distribution, whereas for the non-overlapping winding configurations, the working harmonic is the second harmonic of the conductor density distribution.

The conductor density distribution will also be used in Chapters 3 and 4 to calculate the flux-linkage for the different winding configurations, from the magnetic vector potential caused by the permanent magnets and the armature windings respectively. This is necessary in order to calculate the induced voltage, or back-EMF, for the different winding configurations as well as the different three-phase synchronous inductances respectively.

Although it might not be apparent to the reader why the current density and specifically the three-phase current density distributions are deduced in this chapter, the reason for that is that it follows logically from the conductor density distribution calculations. The three-phase current density distribution will be used in Chapter 5 where the torque calculation, using the Lorentz method will be discussed, for the different winding configurations.

2.2 Terminology used for the Analysis

Before we begin our analysis of the double-sided rotor RFAPM machine, it is necessary to define a few quantities with which to describe the working and layout of the machine.

The speed by which the magnetic flux cuts the windings, is determined by the mechanical speed at which the rotor is turning, ω_{mech}. The frequency, ω in [rad/s], of the induced voltage and that of the subsequent phase current, is thus determined by the number of pole pairs of the machine, p, and the speed at which the rotor is turning and can be calculated as follows,

$$\omega = p\omega_{mech} \,. \tag{2.1}$$

The North (N) and South (S) poles of the RFAPM machine are equally spaced, which implies that the magnetic field produced by the poles are repeated every $\frac{360}{p}^{\circ}$ around the circumference of the rotor. With the magnetic field being periodic, it is easier to refer to the magnetic field as being repeated every 360° *electrical*. The relationship between the electrical degrees and the actual *mechanical* degrees is therfore determined by the number of pole pairs. Expressed in radians,

$$2\pi \quad [\text{elec.}] = \frac{2\pi}{p} \quad [\text{mech.}]. \tag{2.2}$$

With the N– and S–poles equally spaced, the pole pitch of a machine can thus be described in terms of either mechanical or electrical degrees as follows

$$\tau_p = \frac{\pi}{p} \quad [\text{mech.}] \quad \text{or} \tag{2.3}$$

$$= \pi \quad [\text{elec.}] \,, \tag{2.4}$$

with the resultant pole pitch, i.e. the angle between adjacent N– or S–poles,

$$\tau_{p,res} = 2\tau_p \tag{2.5}$$

$$= 2\pi \quad [\text{elec.}] \,. \tag{2.6}$$

The number of coils-per-phase per pole pair, is given by,

$$q = k_q p \, . \tag{2.7}$$

The total number of coils, for a three-phase system is, thus, simply,

$$Q = 3q \, . \tag{2.8}$$

The coil pitch of the machine is defined as

$$\tau_q = \frac{\pi}{q} \quad \text{[mech.]} \tag{2.9}$$

$$= \pi \quad \text{[elec.]} \tag{2.10}$$

and the resultant coil pitch as

$$\tau_{q,res} = \frac{2\pi}{q} \quad \text{[mech.]} \tag{2.11}$$

$$= 2\pi \quad \text{[elec.]} \, . \tag{2.12}$$

A coil that spans 180° *electrical*, or put differently, if the coil pitch is equal to half the resultant coil pitch, it is known as a *full-pitch* winding, Fitzgerald *et al.* [19, chap. 4].

2.3 Overlapping (Type O) Winding Configuration

For a RFAPM machine with overlapping (Type O) windings, the number of coils per phase and the number of permanent magnet pole pares will be the same so that from (2.7), we can say $k_q = 1$. This implies that a complete winding section will be equal to 360° *electrical*[1]. A RFAPM machine with overlapping windings' winding configuration is thus such that we have one phase coil per pole pair and thus for a three-phase machine, there will be three coils in total per pole pair.

In Figure 2.1 a linearised representation of two complete winding sections of a RFAPM machine with overlapping windings is shown relative to the permanent magnet poles at time, $t = t_0$. Furthermore, the magnetic or d-axis of the rotor, d_r, is shown relative to the magnetic axis, or d-axis of phase a of the stator, d_s, with γ the electrical angle between the two.

2.3.1 Flux-linkage of the Type O Winding Configuration

For air cored machines, the coil-side widths are usually much wider than for iron cored machines[2]. Thus, when the flux-linkage of an air cored coil is calculated, the distributed nature of the coil sides needs to be take into account, similar to the calculations for the flux-linkage in an AFAPM machine, see Kamper *et al.* [13].

[1] For the non-overlapping windings we will see that this is not the case.
[2] For non-overlapping winding configurations, this is even more so.

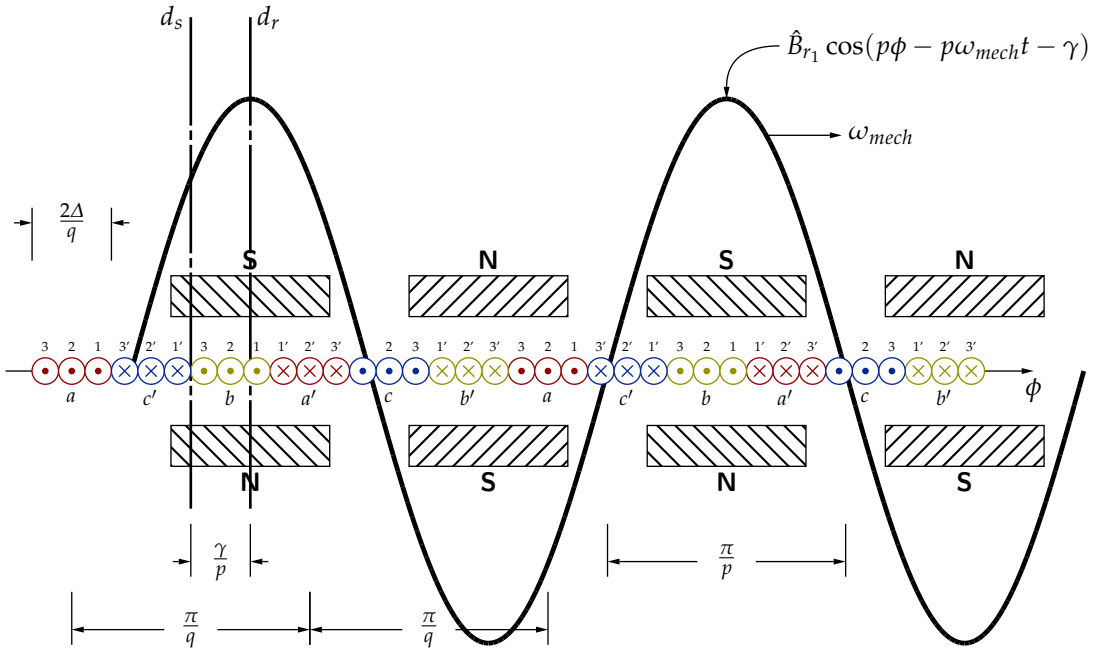

Figure 2.1: Winding layout for a three-phase RFAPM machine with a Type O winding configuration at time, $t = t_0$, with $k_q = 1$.

In Figure 2.1, the coils are depicted as if they consist of multiple layers with a single turn per layer, while is fact there are actually multiple turns per layer, as shown in Figure 2.2. In order to simplify our analysis, however, we assume that the radial flux density "seen" by each turn in a specific layer is the same and equal to the radial flux density in the centre of the coil in the radial direction (i.e. at $r = r_n$). We therefore assume that the coils are infinitely thin with all the layers of the coil located at r_n when we calculate the total flux-linkage for each coil.

Furthermore, if we assume that the machine is rotating at a constant speed, the flux-linkage can be considered to be sinusoidal. It is therefore only necessary to calculate the maximum, or peak value of the flux-linkage that would occur when the magnetic axis of the coil, i.e. d_s, is aligned with the magnetic axis of the permanent magnets, i.e. d_r. In order to calculate the total flux-linkage of each phase, we first need to calculate the flux-linkage of a single turn. With each side of the turn at an arbitrary angle, say δ, measured from the centre of each coil side in

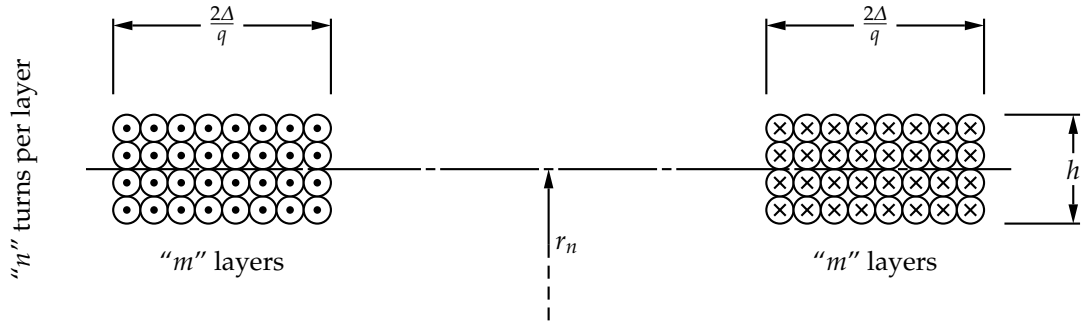

Figure 2.2: A linearised cross section representation of a coils with multiple layers and turns.

the azimuthal direction as shown in Figure 2.3 (a) and (b) for an "inner" and an "outer" turn respectively, the flux-linkage for a single turn can be calculated as follows,

$$\lambda_{|O}(\delta) = \int_0^{\ell} \int_{-\frac{\tau_q}{2}+\delta}^{\frac{\tau_q}{2}-\delta} \hat{B}_{r_1} \cos(p\phi) r_n d\phi dz \tag{2.13}$$

$$= \frac{r_n \hat{B}_{r_1}}{p} \int_0^{\ell} \left(\sin(\tfrac{p\pi}{2q} - p\delta) - \sin(-\tfrac{p\pi}{2q} + p\delta) \right) dz \tag{2.14}$$

$$= \frac{r_n \hat{B}_{r_1}}{p} \int_0^{\ell} \left(\sin(\tfrac{\pi}{2} - p\delta) - \sin(-\tfrac{\pi}{2} + p\delta) \right) dz \tag{2.15}$$

$$= \frac{2r_n \hat{B}_{r_1}}{p} \int_0^{\ell} \cos(p\delta) dz \tag{2.16}$$

$$= \frac{2r_n \ell \hat{B}_{r_1}}{p} \cos(p\delta) \tag{2.17}$$

with $\hat{B}_{r_1}$ the peak value of the fundamental component of the radial flux-density distribution[1] as shown in Figure 2.1.

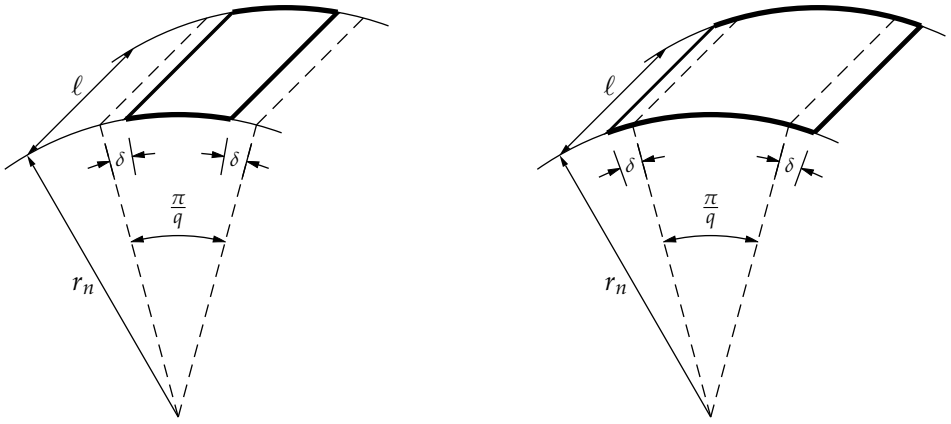

(a) Inner turn. (b) Outer turn.

Figure 2.3: The inner and outer turns of coil with a distributed coil side.

Next the average flux-linkage for each coil is calculated, which in effect is equal to the average flux-linkage of each turn over the distributed coil side starting from the minimum "inner" turn to the maximum "outer" turn as shown in Figure 2.3 (a) and (b) respectively. The average flux-linkage for each coil can therefore be calculated as follows,

$$\varphi_{|O} = \frac{q}{2\Delta} \int_{-\frac{\Delta}{q}}^{\frac{\Delta}{q}} \lambda_{|O}(\delta)\, d\delta \tag{2.18}$$

$$= \frac{q}{2\Delta} \int_{-\frac{\Delta}{q}}^{\frac{\Delta}{q}} \frac{2r_n \ell \hat{B}_{r_1}}{p} \cos(p\delta)\, d\delta \tag{2.19}$$

$$= \frac{2qr_n \ell \hat{B}_{r_1}}{\Delta p^2} \sin(\tfrac{p\Delta}{q})\,. \tag{2.20}$$

[1] It will be shown in Chapter 3 that the flux-density distribution in the centre of the windings can indeed be approximated to be sinusoidal with careful selection of the permanent magnet's pole arc width.

By multiplying the average flux linking for each coil with the total number of turns in each coil, N, we get the total flux-linkage per coil. The total flux-linkage per phase will however depend on the number of parallel connected coils, a, and the number of series connected coils, $\frac{q}{a}$, which is obtained by dividing the total number of coils by the total number of parallel circuits.

From Figure 2.1 we can see that due to the symmetrical spacing of the coils, each coil in the phase winding layout will have the same flux-linkage. Thus, if each coil also have the same current passing through it, it will have the same inductance. From Appendix A we can see that the total flux-linkage per phase only depend on the number of series connected coils, so that for the overlapping winding configuration the total flux-linkage per phase can be expressed as,

$$\Lambda_{a,b,c|O} = \frac{q}{a} \cdot N\varphi_{|O} \tag{2.21}$$

$$= \frac{2r_n \ell N k_q \hat{B}_{r_1}}{a} \cdot \frac{\sin(\frac{\Delta}{k_q})}{(\frac{\Delta}{k_q})} , \tag{2.22}$$

with k_q as defined in (2.7).

From (2.22), the coil side width – or "virtual" slot width factor for a RFAPM machine with overlapping winding, can be defined as

$$k_{w,slot|O} = \frac{\sin(\frac{\Delta}{k_q})}{(\frac{\Delta}{k_q})} , \tag{2.23}$$

so that (2.22) can be rewritten as

$$\Lambda_{a,b,c|O} = \frac{2r_n \ell N \hat{B}_{r_1} k_q k_{w,slot|O}}{a} . \tag{2.24}$$

2.3.2 Conductor Density Distribution of the Type O Winding Configuration

The winding distribution for phase a of an overlap RFAPM machine is shown in Figure 2.4. From the winding distribution and with the coil-side width equal to $\frac{2\Delta}{q}$, the conductor density in each "virtual" stator slot will be equal to

$$|n_a| = \frac{qN}{2\Delta} . \tag{2.25}$$

This allows us to define a conductor density distribution, see Slemon [20, section 5.1], for phase a of an overlap RFAPM machine as is graphically shown in Figure 2.5. Here a positive conductor density represents conductors coming out of the page and a negative conductor density, conductors going into the page.

The conductor density distribution provides an alternative way in which to calculate the flux-linkage directly from the magnetic vector potential, as will be shown in Chapter 3, section 3.12 due to the permanent magnets and in Chapter 4, section 4.8.2 due to the armature reaction. The former will be used to calculate the back-EMF of the machine, see section 3.13 and the latter to calculate the three-phase synchronous inductance of the machine, section 4.8.3.

The Fourier expansion for the conductor density distribution for phase a can be written as

$$n_{a|O}(\phi) = \sum_{m=1}^{\infty} b_{m_{n|O}} \sin(mq\phi) \tag{2.26}$$

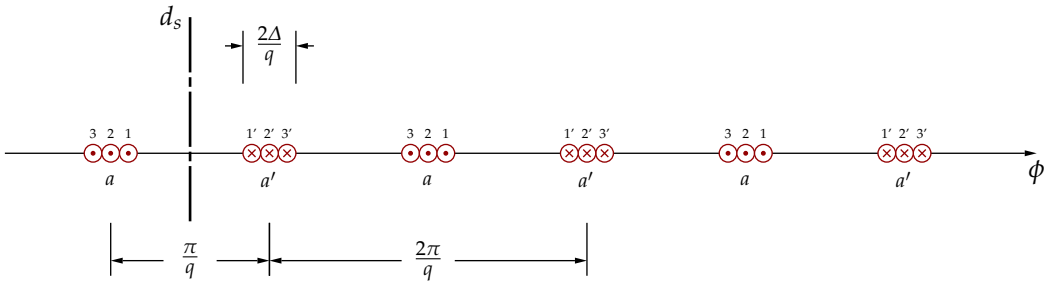

Figure 2.4: The winding distribution and relative coil position for phase a of an overlap machine with $k_q = 1$ and $k_\Delta = 1$.

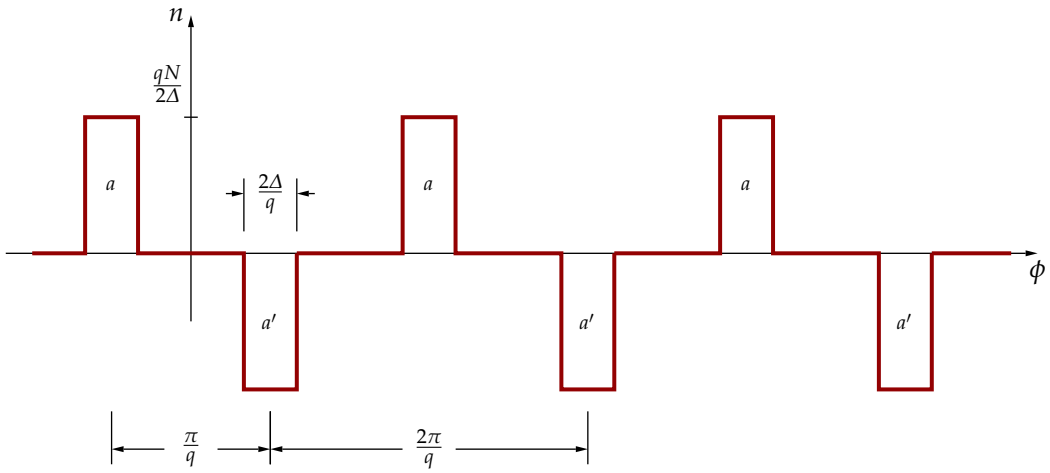

Figure 2.5: The conductor density distribution, n, for phase a of an overlap machine with $k_q = 1$ and $k_\Delta = 1$.

with

$$b_{m_{n|O}} = -\frac{2qN}{m\pi\Delta}\sin\left(m\tfrac{\pi}{2}\right)\sin(m\Delta)\ . \tag{2.27}$$

From (2.27) as well as for the subsequent conductor density distributions for the non-overlapping winding configurations that will be defined later, we are able to define a number of winding factors that takes cognisance of all the harmonics present in the winding distribution, similar to Holm *et al.* [21, Appendix A]. The first winding factor for the overlapping winding configuration is the pictch factor and is defined as,

$$k_{w,pitch,m|O} = \sin\left(m\tfrac{\pi}{2}\right)\ . \tag{2.28}$$

With $m = 1$, $k_{w,pitch,m|O} = 1$ which is consistent with (2.24) where only the fundamental component of the radial flux density was considered.

The second winding factor for the overlapping winding configuration, the coil side width – or "virtual" slot width factor, is defined as

$$k_{w,slot,m|O} = \frac{\sin(m\Delta)}{m\Delta}\ . \tag{2.29}$$

The slot width factor, $k_{w,slot,m|O}$ with $m = 1$ is the exactly the same as slot width factor in (2.23) where, once again, only the fundamental component of the radial flux density was considered.

In terms of the winding factors, (2.27) can now be written as,

$$b_{m_{n|O}} = -\frac{2qN}{\pi} \cdot k_{w,m|O} \tag{2.30}$$

with

$$k_{w,m|O} = k_{w,pitch,m|O} \cdot k_{w,slot,m|O} \,. \tag{2.31}$$

Another interesting thing to note, is that if we were able to represent the Fourier expansion up to infinity, we will note that,

$$\int_{-\frac{\pi}{2q}-\frac{\Delta}{q}}^{-\frac{\pi}{2q}+\frac{\Delta}{q}} n_{a|O}(\phi)d\phi \approx \int_{-\tau_q}^{0} n_{a|O}(\phi)d\phi = N \tag{2.32}$$

and

$$\int_{\frac{\pi}{2q}-\frac{\Delta}{q}}^{\frac{\pi}{2q}+\frac{\Delta}{q}} n_{a|O}(\phi)d\phi \approx \int_{0}^{\tau_q} n_{a|O}(\phi)d\phi = -N \,. \tag{2.33}$$

which is as expected.

2.3.3 Current Density Distribution of the Type O Winding Configuration

In this section the current density distribution and more specifically, the three-phase current density distribution for the Type O winding configuration will be deduced. This will be used in Chapter 4 to calculate the armature-reaction field, Zhu and Howe [7] and Zhu *et al.* [22], using subdomain analysis, Zhu *et al.* [23]. The three-phase current density distribution will also be used to calculate the developed torque for the Type O winding configuration in Chapter 5, by making use of the Lorentz' law method, similar to what was done by Holm [24].

The cross section of each "virtual" stator slot or coil-side, is shown in Figure 2.6 and can be calculated as follows,

$$A_{slot} = \int_{r_i}^{r_o} \int_{-\frac{\Delta}{q}}^{+\frac{\Delta}{q}} r\phi dr d\phi \tag{2.34}$$

$$= \frac{(r_o^2 - r_i^2)\Delta}{q} \,, \tag{2.35}$$

or in terms of the nominal radius and slot height, as

$$A_{slot} = \frac{2r_n h\Delta}{q} \,. \tag{2.36}$$

This implies that the magnitude of the current density in each "virtual stator slot", i.e. the "slot" current density,

$$|J_{z_a}| = \frac{Ni_a(t)}{aA_{slot}} \tag{2.37}$$

$$= \frac{qNi_a(t)}{2ar_n h\Delta} \tag{2.38}$$

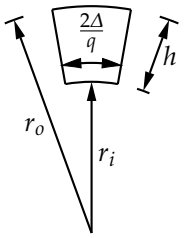

Figure 2.6: The "virtual stator slot" size.

or in terms of the conductor density,

$$|J_{z_a}| = \frac{|n_a|}{r_n h} \cdot \frac{i_a(t)}{a} \,. \tag{2.39}$$

The current density distribution for phase a of an overlap machine with $k_q = 1$ is shown in Figure 2.7.

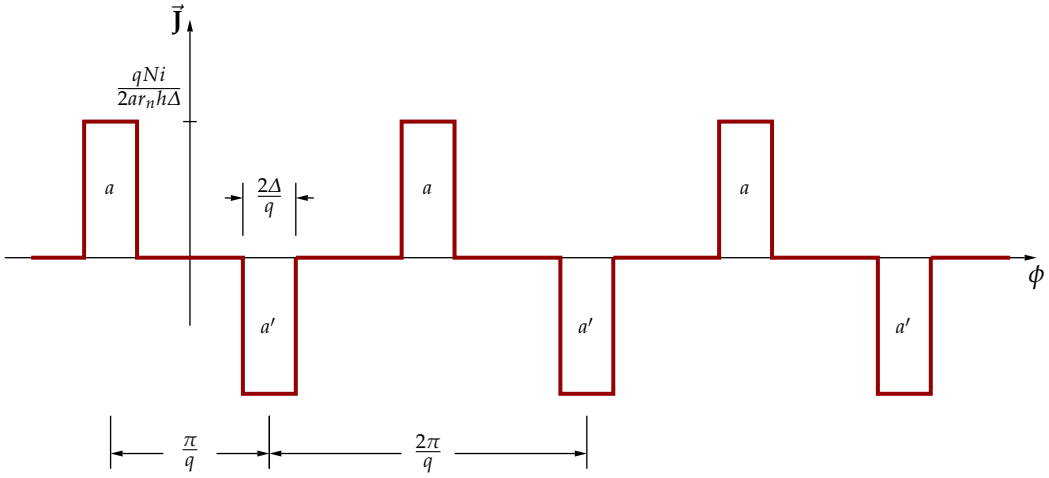

Figure 2.7: The current density distribution for phase a of an overlap machine with $k_q = 1$.

The Fourier expansion for the current density distribution for phase a can thus be written as

$$J_{z_{a|O}} = \frac{1}{ar_n h} \sum_{m=1}^{\infty} b_{m_{n|O}} i_a(t) \sin(mq\phi) \,. \tag{2.40}$$

This allows us to define the resultant current density distribution for all three phase, as

$$J_{z_{|O}} = J_{z_{a|O}} + J_{z_{b|O}} + J_{z_{c|O}} \tag{2.41}$$

$$= \frac{1}{ar_n h} \sum_{m=1}^{\infty} b_{m_{n|O}} \Big[\sin\big(mq\phi\big) i_a(t) + \sin\big(mq(\phi - \tfrac{2\pi}{3})\big) i_b(t) + \sin\big(mq(\phi - \tfrac{4\pi}{3})\big) i_c(t) \Big] \,. \tag{2.42}$$

In order to lower the acoustic noise associated with air cored PM machines, large external inductors are required, Rossouw and Kamper [25]. Only the fundamental component of the

current will therefore be considered. Thus, with (say)

$$i_a(t) = I_p \cos(\omega t) \tag{2.43}$$

and for a perfectly balanced three-phase load,

$$i_b(t) = I_p \cos(\omega t - \tfrac{2\pi}{3}) \text{ and} \tag{2.44}$$
$$i_c(t) = I_p \cos(\omega t - \tfrac{4\pi}{3}) \,, \tag{2.45}$$

the steady state solution of the current density at $\omega t = 0^\circ$ can be written as,

$$i_a(0) = I_p \text{ and} \tag{2.46}$$
$$i_b(0) = i_c(0) \tag{2.47}$$
$$= -\frac{I_p}{2} \,. \tag{2.48}$$

This will produce a three-phase current density distribution at $\omega t = 0^\circ$, as depicted in Figure 2.8. Unfortunately the three-phase current density distribution is time dependent so that the spacial current density distribution will vary with time. To illustrate this, the spacial distribution at $\omega t = 15^\circ$ and $\omega t = 30^\circ$ is shown in Figure 2.9 and 2.10 respectively.

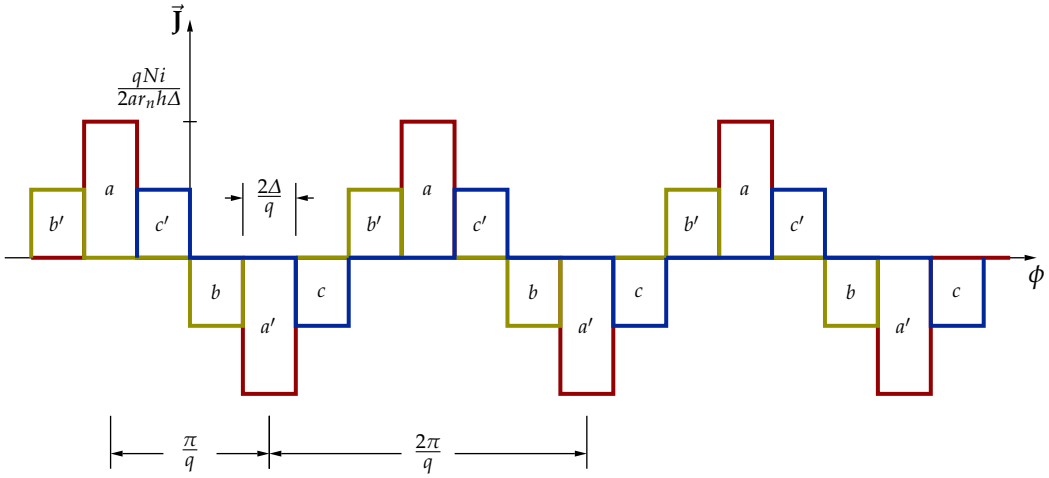

Figure 2.8: The combined current density distribution for all three phases of a Type O machine with $\omega t = 0^\circ$.

By substituting (2.43), (2.44) and (2.45) in (2.42) we get

$$J_{z_{|O}} = \frac{I_p}{ar_nh} \sum_{m=1}^{\infty} b_{m_{n|O}} \Big[\sin(mq\phi)\cos(\omega t) + \sin\big(mq(\phi - \tfrac{2\pi}{3})\big)\cos(\omega t - \tfrac{2\pi}{3}) + \,, \\ \sin\big(mq(\phi - \tfrac{4\pi}{3})\big)\cos(\omega t - \tfrac{4\pi}{3})\Big] \tag{2.49}$$

which, after some careful manipulation, will simplify to

$$J_{z_{|O}} = \begin{cases} \frac{3I_p}{2ar_nh} \sum_{m=1}^{\infty} b_{m_{n|O}} \sin\big(mq\phi + \omega t\big) & \text{for } m = 3k-2,\ k \in \mathbb{N}_1 \\ \frac{3I_p}{2ar_nh} \sum_{m=2}^{\infty} b_{m_{n|O}} \sin\big(mq\phi - \omega t\big) & \text{for } m = 3k-1,\ k \in \mathbb{N}_1 \end{cases} \tag{2.50}$$

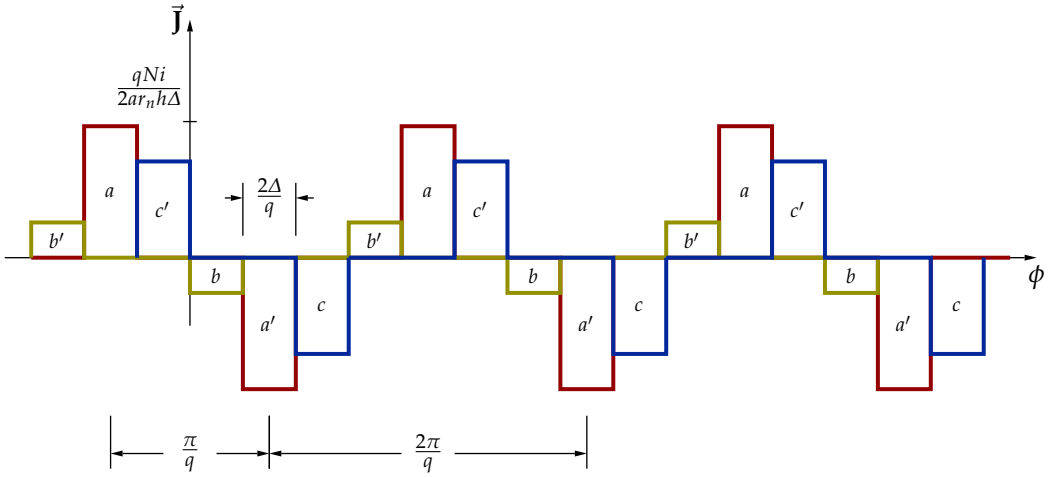

Figure 2.9: The combined current density distribution for all three phases of a Type O machine with $\omega t = 15°$.

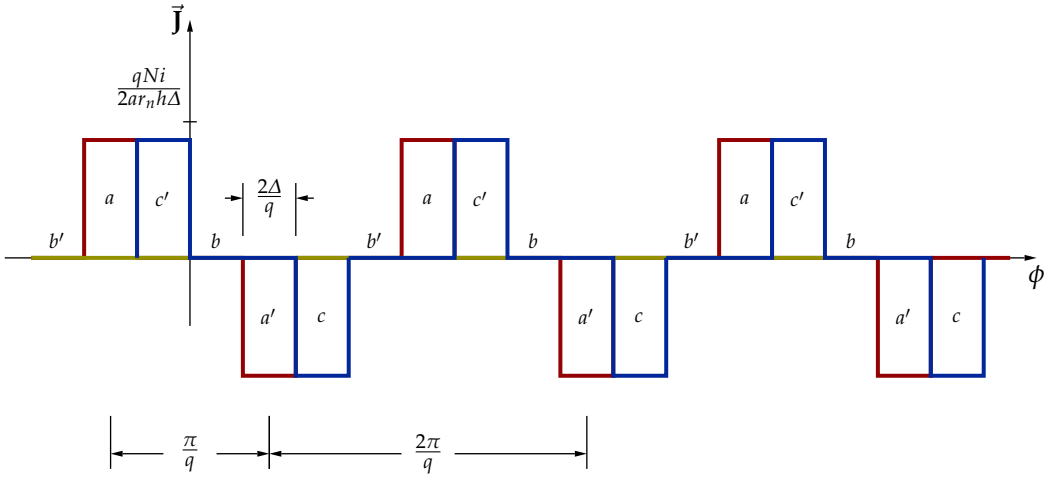

Figure 2.10: The combined current density distribution for all three phases of a Type O machine with $\omega t = 30°$.

or in terms of the winding factors, to

$$J_{z|O} = \begin{cases} -\frac{3qI_pN}{ar_nh\pi} \sum_{m=1}^{\infty} k_{w,m|O} \sin\left(mq\phi + \omega t\right) & \text{for } m = 3k-2,\ k \in \mathbb{N}_1 \\ -\frac{3qI_pN}{ar_nh\pi} \sum_{m=2}^{\infty} k_{w,m|O} \sin\left(mq\phi - \omega t\right) & \text{for } m = 3k-1,\ k \in \mathbb{N}_1 \end{cases} . \tag{2.51}$$

From (2.51) it can be seen that the $m = 3k-2,\ k \in \mathbb{N}_1$ time harmonics, which also includes the fundamental component, will rotate in the *abc* direction (appear to be moving to the "right" in Figures 2.8, 2.9 and 2.10) were as the $m = 3k-1,\ k \in \mathbb{N}_1$ time harmonics will rotate in the *acb* direction.

2.4 Non-Overlapping Single-layer (Type I) Winding Configuration

The three-phase coil configuration for a RFAPM machine with non-overlapping single-layer (Type I) windings is shown in Figure 2.11. The only difference between a RFAPM machine with overlapping, Type O, windings and that with non-overlapping single-layer, Type I, windings is with respect to the winding configuration, i.e. the stator layout. The pole pitch and the resultant pole pitch for a Type I machine is therefore similar to that of a Type O machine, see equations (2.4) and (2.6) respectively.

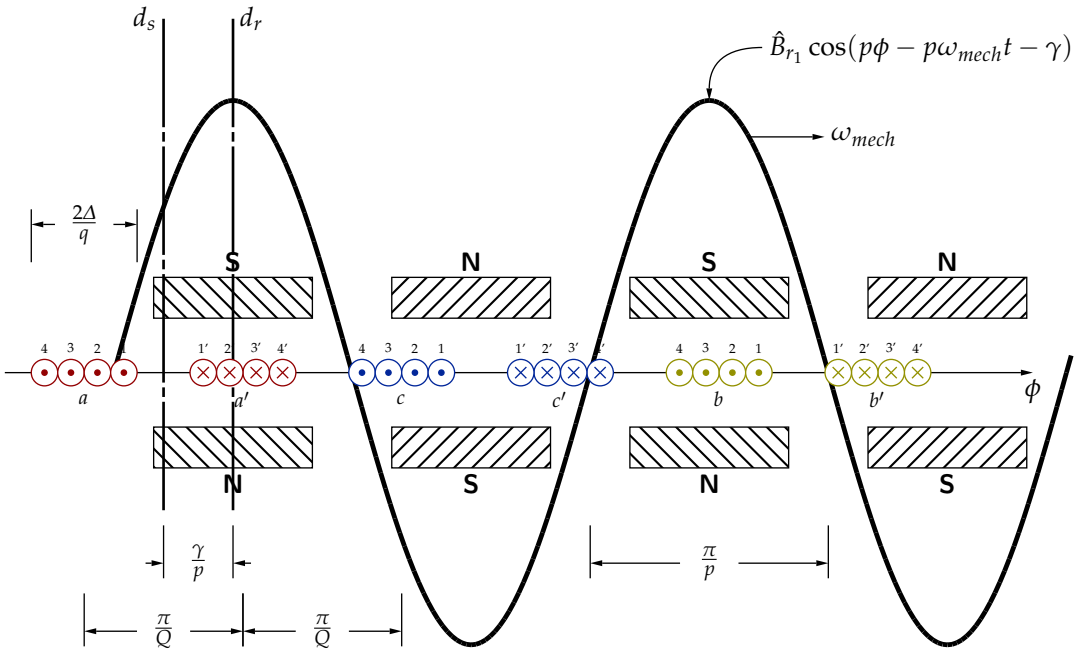

Figure 2.11: Coil configuration for a three-phase RFAPM machine with non-overlapping, single-layer (Type I) windings, with $k_q = \frac{1}{2}$.

However for the Type I windings configuration, we now have, from (2.7), that

$$k_q = \frac{q}{p} \tag{2.52}$$

$$= \frac{1}{2}\,. \tag{2.53}$$

This implies that we now not only have half the number of coils per phase as compared to the Type O winding configuration, but also that, for the Type I winding configuration, each winding section now spans 720° *electrical*. This can also be seen from the definition of the resultant coil pitch of the Type I winding configuration which, although defined similarly to the Type O winding's resultant coil pitch, yields twice the angle.

$$\tau_{q,res|I} = \frac{2\pi}{q} \quad \text{[mech.]} \tag{2.54}$$

$$= 4\pi \quad \text{[elec.]}\,. \tag{2.55}$$

In order to do a full comparative analysis of the winding configuration of the Type I windings, we define a new set of "degrees" namely the *winding section degrees*, or "wsec." for short. This allows us to redefine the resultant coil pitch angle as,

$$\tau_{q,res|I} = 2\pi \quad \text{[wsec.]} \,. \tag{2.56}$$

For the Type I winding configuration the definition for the coil pitch (or maybe less ambiguous, the average coil span) is defined slightly different from the Type O winding configuration, as

$$\tau_{q|I} = \frac{\pi}{Q} \quad \text{[mech.]} \,, \tag{2.57}$$

$$= \frac{2\pi}{3} \quad \text{[elec.]} \;\; \text{or} \tag{2.58}$$

$$= \frac{\pi}{3} \quad \text{[wsec.]} \,. \tag{2.59}$$

The Type I winding configuration can thus be regarded as having *fractional-pitch* coils, Fitzgerald *et al.* [19, Appendix. B], as $\tau_{q|I} < \frac{1}{2}\tau_{q,res|I}$.

An important difference between a RFAPM machine with overlapping windings shown in Figure 2.1 and that of a RFAPM machine with non-overlapping windings, e.g. the single-layer (Type I) and the double-layer (Type II) shown in Figure 2.11 and Figure 2.18[1] respectively, is that the whole surface area of the stator in the overlapping winding configuration is utilised by the stator windings compared to only $\approx \frac{2}{3}$ (for illustration purposes only) of the Type I and II winding configuration.

The maximum coil-side width in winding section degrees (i.e. terms of the resultant coil pitch), can thus be calculated as

$$\frac{2\Delta_{max}}{q} = \frac{2\pi}{q} \cdot \frac{1}{6} \tag{2.60}$$

so that

$$\Delta_{max} = \frac{\pi}{6} \quad \text{[wsec.]} \tag{2.61}$$

$$= \frac{\pi}{3} \quad \text{[elec.]} \tag{2.62}$$

$$= \frac{\pi}{6} \cdot \frac{1}{q} \quad \text{[mech.]} \tag{2.63}$$

The coil-side width factor, k_Δ, is now defined as,

$$k_\Delta = \frac{\Delta}{\Delta_{max}} \,, \tag{2.64}$$

and can be used not only to describe the coil-side width angle of the winding configuration, but also to describe the space utilisation of the stator's winding configuration.

Another important difference is the phase sequence of the different phase windings. If one were to compare the Type O winding configuration shown in Figure 2.1 with that of the Type I winding configuration shown in Figure 2.11, one would see that the sequence of the different

[1] See section 2.5.

phase windings' magnetic axes for the Type O windings is ABC compared to that of the Type I windings, which is ACB. However, on closer inspection we can see that although phase C's magnetic axis is located at 120 [wsec. °] from phase A, this corresponds to 240 [elec. °]. The same goes for phase B's magnetic axis which is located at 240 [wsec. °] which corresponds to 480 [elec. °] which is actually the same as 120 [elec. °].

2.4.1 Flux Linkage of the Type I Winding Configuration

The total flux-linkage per phase for the Type I winding is calculated in exactly the same manner as for the Type O winding. Once again we need to align the magnetic– or d-axis of the coil with the magnetic– or d-axis of the magnets in order to calculate the maximum or peak value of flux-linkage. This allows us to calculate the flux-linkage of a single turn with each turn side at an angle of δ from the centre of each coil side as follows,

$$\lambda_{|I}(\delta) = \int_0^{\ell} \int_{-\frac{\pi}{2Q}+\delta}^{\frac{\pi}{2Q}-\delta} \hat{B}_{r_1} \cos(p\phi) r_n d\phi dz \tag{2.65}$$

$$= \frac{r_n \hat{B}_{r_1}}{p} \int_0^{\ell} \left(\sin(\tfrac{p\pi}{6q} - p\delta) - \sin(-\tfrac{p\pi}{6q} + p\delta) \right) dz \tag{2.66}$$

$$= \frac{r_n \hat{B}_{r_1}}{p} \int_0^{\ell} \left(\sin(\tfrac{\pi}{3} - p\delta) - \sin(-\tfrac{\pi}{3} + p\delta) \right) dz \tag{2.67}$$

$$= \frac{2r_n \hat{B}_{r_1}}{p} \int_0^{\ell} \sin(\tfrac{\pi}{3}) \cos(p\delta) dz \tag{2.68}$$

$$= \frac{2r_n \ell \hat{B}_{r_1}}{p} \sin(\tfrac{\pi}{3}) \cos(p\delta) \tag{2.69}$$

again assuming a sinusoidal radial flux-density distribution.

Taking into account the number of turns per coil, as well as the total number of series and parallel connected coils, the total flux-linkage per phase can be calculated as follows,

$$\Lambda_{a,b,c|I} = \left(\frac{q}{a}\right) \left(\frac{qN}{2\Delta}\right) \int_{-\frac{\Delta}{q}}^{\frac{\Delta}{q}} \lambda_{|I}(\delta)\, d\delta \tag{2.70}$$

$$= \left(\frac{q}{a}\right) \left(\frac{qN}{2\Delta}\right) \int_{-\frac{\Delta}{q}}^{\frac{\Delta}{q}} \frac{2r_n \ell \hat{B}_{r_1}}{p} \sin(\tfrac{\pi}{3}) \cos(p\delta)\, d\delta \tag{2.71}$$

$$= \left(\frac{q}{a}\right) \left(\frac{qN}{2\Delta}\right) \frac{4r_n \ell \hat{B}_{r_1}}{p^2} \sin(\tfrac{\pi}{3}) \sin(\tfrac{p\Delta}{q}) \tag{2.72}$$

$$= \frac{2r_n \ell N k_q \hat{B}_{r_1} \sin\left(\frac{\pi}{3}\right)}{a} \cdot \frac{\sin(\frac{\Delta}{k_q})}{(\frac{\Delta}{k_q})} \,. \tag{2.73}$$

If we compare the total flux-linkage in (2.73) for the Type I winding configuration with that of the Type O winding configuration given by (2.22), we note the additional $\sin(\frac{\pi}{3})$ term. This is due to the fact that the Type I windings are a fractional pitch windings compared to the full pitch windings of the Type O winding configuration. We can therefore define the winding pitch factor for the Type I (non-overlapping) winding configuration, as

$$k_{w,pitch|I} = \sin\left(\frac{\pi}{3}\right) \,. \tag{2.74}$$

This implies that for the Type O (overlapping) winding configuration we can define the winding pitch factor, as

$$k_{w,pitch|O} = 1{,}0 \ , \tag{2.75}$$

as was also obtained in (2.28) with $m = 1$.

Furthermore, it is interesting to note that the "virtual" slot width factor for the non-overlapping Type I winding is exactly the same as for the overlapping winding configuration, so that in general the winding slot factor could be expressed as

$$k_{w,slot} = k_{w,slot|I} = k_{w,slot|O} = \frac{\sin\left(\frac{\Delta}{k_q}\right)}{\frac{\Delta}{k_q}} \ . \tag{2.76}$$

Taking into account the winding factors mentioned above for the various winding configurations, we can rewrite (2.24) and (2.73) into a general format, so that

$$\Lambda_{a,b,c|O} = \lambda_{a,b,c|I} = 2r_n \ell N \hat{B}_{r_1} k_q k_{w,pitch} k_{w,slot} \ . \tag{2.77}$$

2.4.2 Conductor Density Distribution of the Type I Winding Configuration

The winding distribution for phase a of a RFAPM machine with Type I windings is shown in Figure 2.12. From the winding distribution and the coil-side width, the conductor density distribution can be obtained as shown in Figure 2.13. Once again, a positive conductor density represents conductors coming out of the page and a negative conductor density, conductors going into the page.

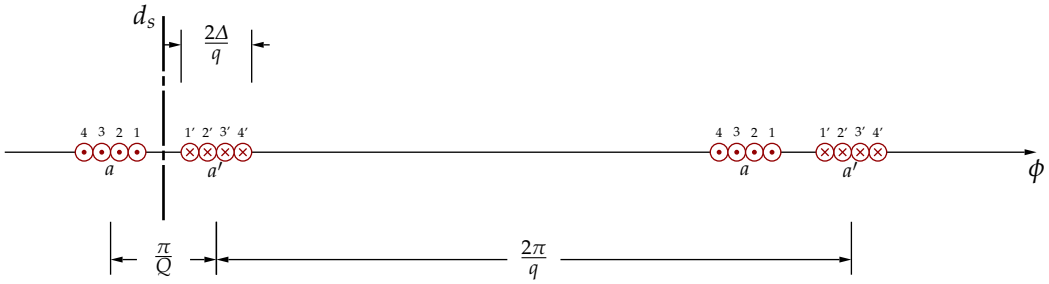

Figure 2.12: The winding distribution and relative coil position for phase a of a RFAPM machine with Type I non-overlapping windings with $k_q = \frac{1}{2}$ and $k_\Delta = \frac{2}{3}$.

As mentioned in section 2.3.2, the conductor density distribution allows us to calculate the flux-linkage due to the permanent magnets, as well as the flux-linkage created by the armature reaction. Again the former will be used to calculate the back-EMF of the machine and the latter to calculate the three-phase synchronous inductance of the machine when using a Type I winding configuration.

The Fourier expansion for the conductor density distribution for phase a can be written as

$$n_{a|I}(\phi) = \sum_{m=1}^{\infty} b_{m_{n|I}} \sin(mq\phi) \tag{2.78}$$

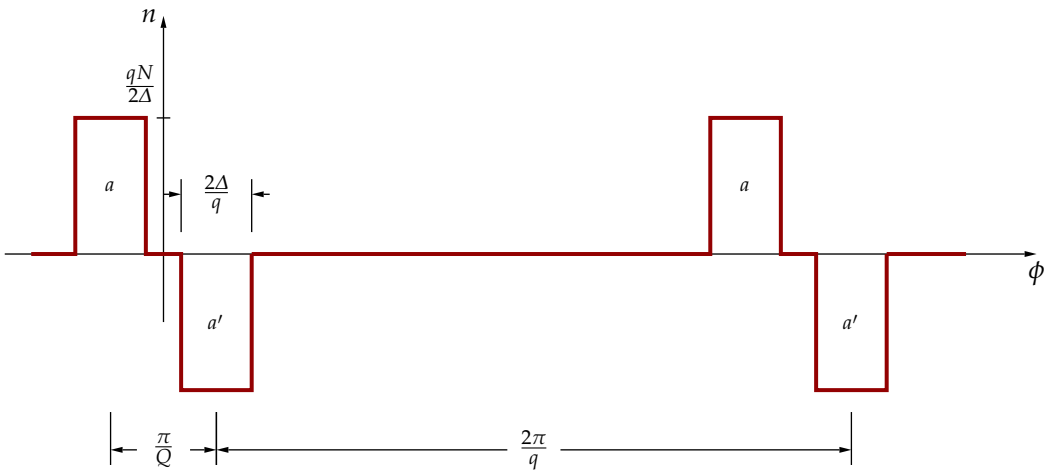

Figure 2.13: The conductor density distribution for phase a of a Type I concentrated coil machine with $k_q = \frac{1}{2}$ and $k_\Delta = \frac{2}{3}$.

with

$$b_{m_{n|I}} = -\frac{2qN}{m\pi\Delta}\sin(m\tfrac{\pi}{6})\sin(m\Delta) \tag{2.79}$$

$$= -\frac{2qN}{\pi}\cdot k_{w,m|I} \tag{2.80}$$

which is similar to (2.30) with

$$k_{w,m|I} = k_{w,pitch,m|I}\cdot k_{w,slot,m|I}\,, \tag{2.81}$$

where

$$k_{w,pitch,m|I} = \sin(m\tfrac{\pi}{6}) \tag{2.82}$$

and

$$k_{w,slot,m|I} = k_{w,slot,m|O} = \frac{\sin(m\Delta)}{m\Delta}\,. \tag{2.83}$$

If we now compare (2.82) with (2.74) we see that they are equal only when $m = 2$. The same is true for (2.83) compared to (2.76). This can be attributed to the fact that for a Type I RFAPM machine, the resultant coil pitch, see (2.55) is twice the resultant pole pitch (2.6). Thus when we only consider the fundamental radial flux density component, only the second harmonic of the conductor density distribution, i.e. $m = 2$, will contribute to the flux-linkage.

2.4.3 Current Density Distribution of the Type I Winding Configuration

In this section the three-phase current density distribution for the Type I winding configuration will be deduced. As was mentioned in section 2.3.3, this will be used in Chapter 4 to calculate the armature-reaction field as well as the developed torque for the Type I winding configuration, in Chapter 5.

With the "virtual stator slot" defined similarly to that shown in Figure 2.6[1] the current density distribution for phase a of a RFAPM machine with Type I windings, will have the form as shown in Figure 2.14 with $k_q = \frac{1}{2}$.

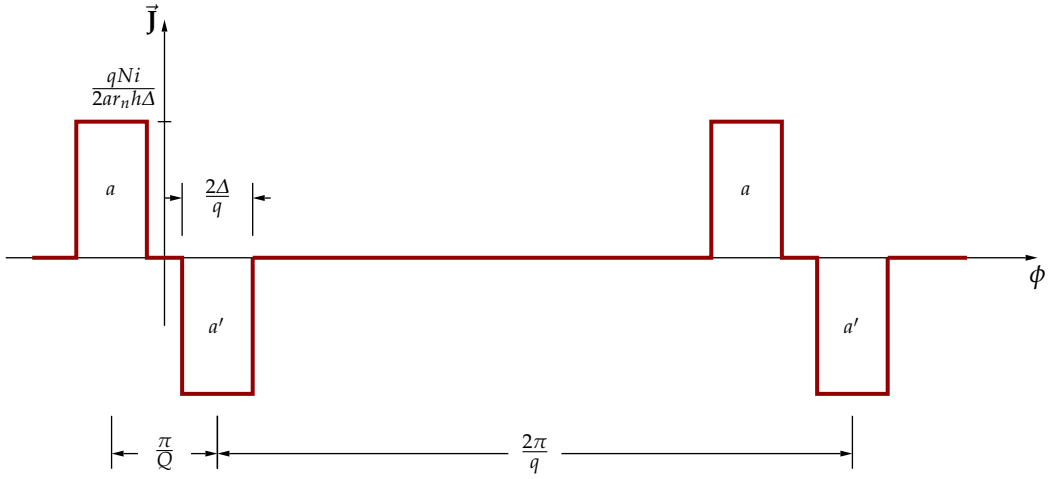

Figure 2.14: The current density distribution for phase a of a Type I non-overlapping winding configuration machine with $k_q = \frac{1}{2}$.

Take note that the only difference between the magnitude of the conductor density distribution in Figure 2.13 and the current density distribution in Figure 2.14, is the "factor" $\frac{i}{r_n h}$. This implies that the Fourier expansion for the current density distribution for phase a of a RFAPM machine with a Type I winding configuration can be written as:

$$J_{z_{a|I}} = \frac{1}{ar_nh} \sum_{m=1}^{\infty} b_{m_{n|I}} \sin(mq\phi) i_a(t) \tag{2.84}$$

Using the same approach as with the Type O machine and taking cognisance of the fact that the phase sequence is now ACB, the resultant steady-state three phase current density distribution from (2.51) will be equal to,

$$J_{z_{|I}} = \begin{cases} -\frac{3qI_pN}{ar_nh\pi} \sum_{m=1}^{\infty} k_{w,m|I} \sin\left(mq\phi + \omega t\right) & \text{for } m = 3k-1,\ k \in \mathbb{N}_1 \\ -\frac{3qI_pN}{ar_nh\pi} \sum_{m=2}^{\infty} k_{w,m|I} \sin\left(mq\phi - \omega t\right) & \text{for } m = 3k-2,\ k \in \mathbb{N}_1 \end{cases} \tag{2.85}$$

and is shown for $\omega t = 0^\circ$ in Figure 2.15.

The main difference between the three-phase current density distribution for the Type O winding configuration, equation (2.51) and and the three-phase current density distribution for the Type I winding configuration shown in (2.85), is that for the Type O winding configuration, the working harmonic is the fundamental component where as for the Type I winding configuration, the working harmonic is actually the second harmonic. This implies that for the Type O winding configuration, the $3k-2$ harmonics, which include the fundamental, is moving to the "right" as was shown in Figures 2.8, 2.9 and 2.10 (i.e. rotating counter clockwise). For

[1] See section 2.3.3.

the Type I winding configuration, however, the $3k-1$ harmonics, which include the working (or second) harmonic, will be moving to the "right" as shown in Figures 2.15, 2.16 and 2.17.

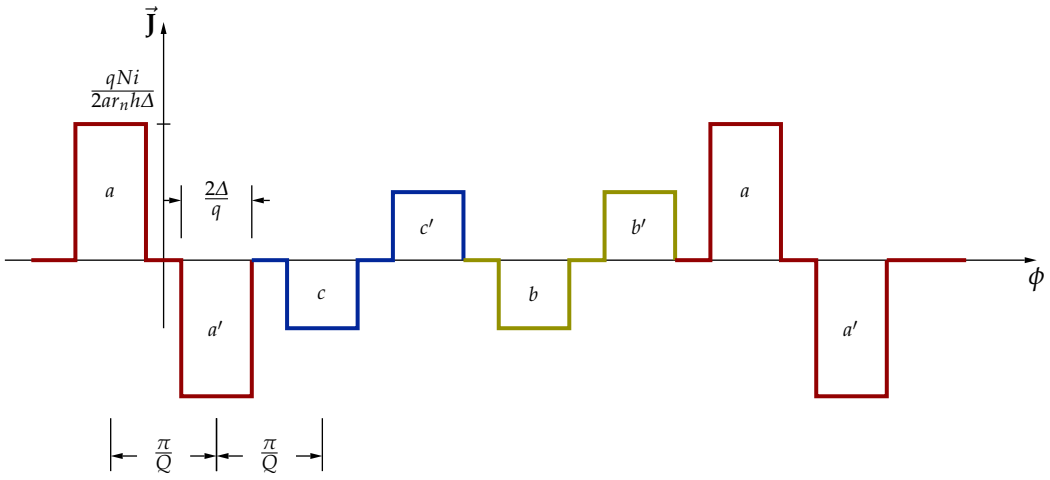

Figure 2.15: The combined current density distribution for phase all three phases of a Type I winding configuration at $\omega t = 0°$.

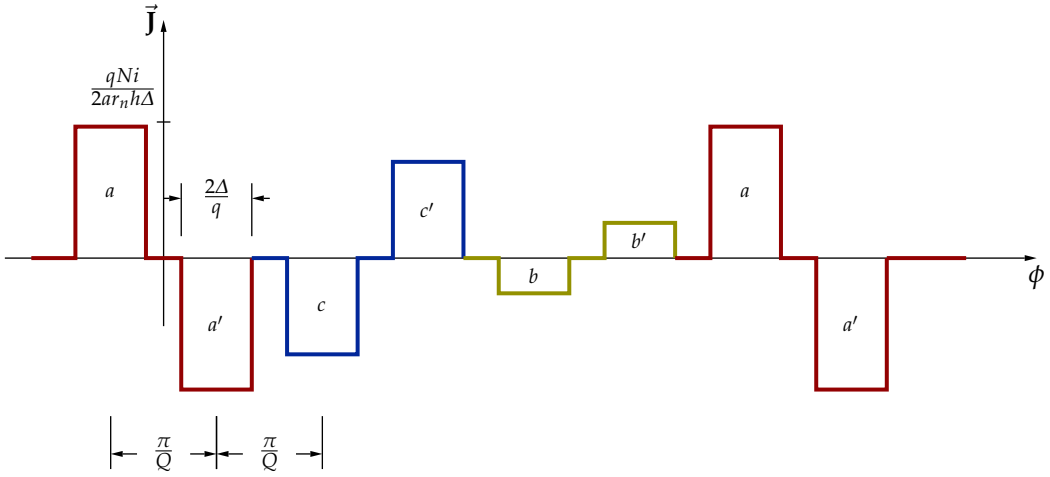

Figure 2.16: The combined current density distribution for phase all three phases of a Type I winding configuration at $\omega t = 15°$.

2.5 Non-Overlapping Double-layer (Type II) Winding Configuration

As shown in Figure 2.18, the pole pitch, τ_p and the resultant pole pitch, $\tau_{p,res}$, of a RFAPM machine with Type II winding configuration is similar to that of a RFAPM machine with a Type O winding configuration. Also for the Type II winding configuration the number of coils per phase is half the number of pole pair, so that $k_q = \frac{1}{2}$, which is the same as for the Type I

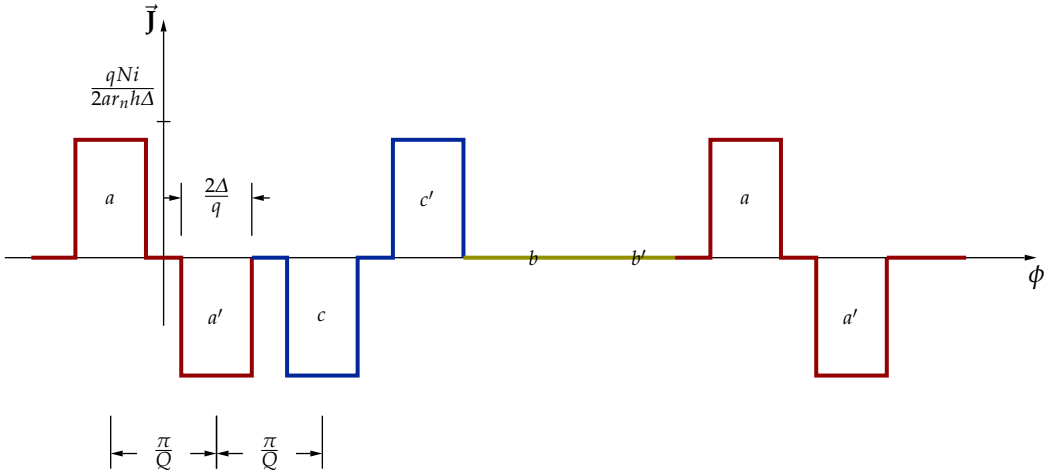

Figure 2.17: The combined current density distribution for phase all three phases of a Type I winding configuration at $\omega t = 30°$.

winding configuration. This is also true for the resultant coil pitch of the Type II winding configuration,

$$\tau_{q,res|II} = 4\pi \quad \text{[elec.]} \tag{2.86}$$

$$= 2\pi \quad \text{[wsec.]} \tag{2.87}$$

which is the same as for the Type I winding configuration.

The main difference between the Type I and the Type II winding configurations is that the Type I windings are non-overlap, single-layer windings which are symmetrically spaced, while the Type II windings are non-overlapping, double-layer windings, which are placed such

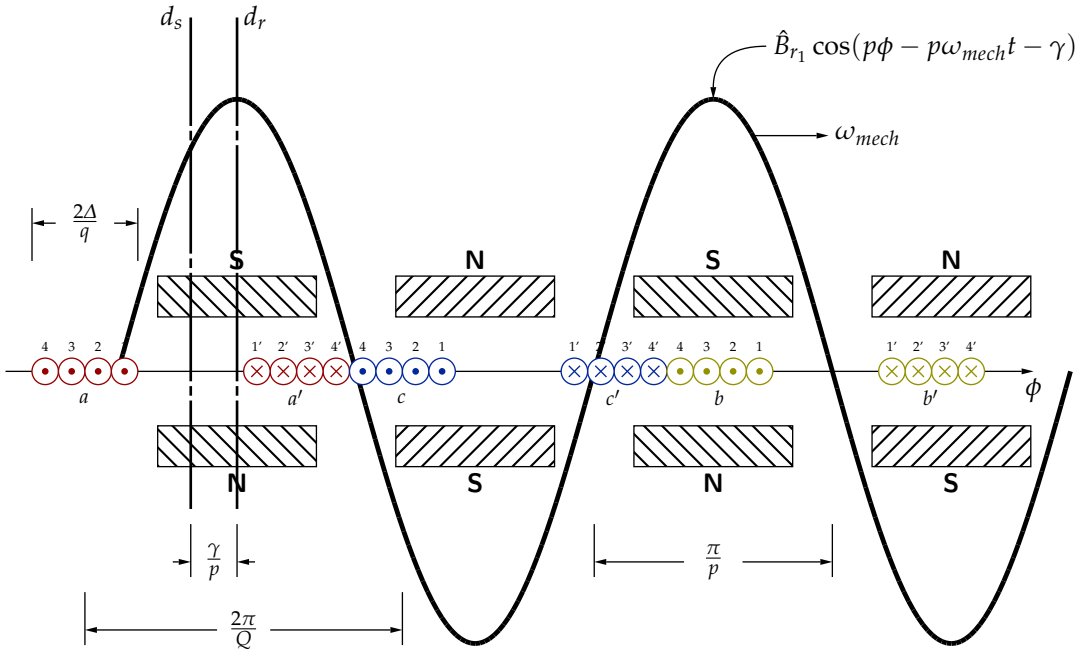

Figure 2.18: Coil configuration for a three-phase RFAPM machine with Type II windings with $k_q = \frac{1}{2}$.

so as to maximise the coil pitch or coil span of each coil. This implies that each coil of the Type II winding configuration will be touching their neighbouring coils on either side. By increasing the coil span, the flux-linkage can be increased at the expense of increasing the end-turn length. The coil span for the Type II concentrated coil RFAPM machine can be calculated from Figure 2.18 as,

$$\tau_{q|II} = \frac{2\pi}{Q} - \frac{2\Delta}{q} \,. \tag{2.88}$$

2.5.1 Flux Linkage of the Type II Winding Configuration

The maximum or peak value of the flux-linkage for the Type II winding configuration is calculated again in exactly the same manner as that for the Type O and the Type I winding configuration. With the d-axis of the coil aligned with the d-axis of the magnets in order to calculate the peak value of the flux-linkage, we again start by finding the flux-linkage of a single turn, with each turn side at an angle of δ from the centre of each coil side. The flux-linkage of a single turn for the Type II winding configuration can thus be calculated as follows,

$$\lambda_{|II}(\delta) = \int_0^{\ell} \int_{-\left(\frac{\pi}{Q}-\frac{\Delta}{q}\right)+\delta}^{\left(\frac{\pi}{Q}-\frac{\Delta}{q}\right)+\delta} \hat{B}_{r_1} \cos(p\phi) r_n d\phi dz \tag{2.89}$$

$$= \frac{r_n \hat{B}_{r_1}}{p} \int_0^{\ell} \left(\sin\left(\left(\tfrac{p\pi}{3q} - \tfrac{p\Delta}{q}\right) - p\delta \right) - \sin\left(-\left(\tfrac{p\pi}{3q} - \tfrac{p\Delta}{q}\right) + p\delta \right) \right) dz \tag{2.90}$$

$$= \frac{r_n \hat{B}_{r_1}}{p} \int_0^{\ell} \left(\sin\left(\left(\tfrac{2\pi}{3} - 2\Delta\right) - p\delta \right) - \sin\left(-\left(\tfrac{2\pi}{3} - 2\Delta\right) + p\delta \right) \right) dz \tag{2.91}$$

$$= \frac{2 r_n \hat{B}_{r_1}}{p} \int_0^{\ell} \sin\left(\tfrac{2\pi}{3} - 2\Delta\right) \cos(p\delta) dz \tag{2.92}$$

$$= \frac{2 r_n \ell \hat{B}_{r_1}}{p} \sin\left(\tfrac{2\pi}{3} - 2\Delta\right) \cos(p\delta) \,. \tag{2.93}$$

Again taking into account the number of turns per coil, as well as the total number of series and parallel connected coils, the total flux-linkage per phase can be calculated as follows,

$$\Lambda_{a,b,c|II} = \left(\frac{q}{a}\right) \left(\frac{qN}{2\Delta}\right) \int_{-\frac{\Delta}{q}}^{\frac{\Delta}{q}} \lambda_{|II}(\delta) \, d\delta \tag{2.94}$$

$$= \left(\frac{q}{a}\right) \left(\frac{qN}{2\Delta}\right) \int_{-\frac{\Delta}{q}}^{\frac{\Delta}{q}} \frac{2 r_n \ell \hat{B}_{r_1}}{p} \sin\left(\tfrac{2\pi}{3} - 2\Delta\right) \cos(p\delta) \, d\delta \tag{2.95}$$

$$= \left(\frac{q}{a}\right) \left(\frac{qN}{2\Delta}\right) \frac{4 r_n \ell \hat{B}_{r_1}}{p^2} \sin\left(\tfrac{2\pi}{3} - 2\Delta\right) \sin\left(\tfrac{p\Delta}{q}\right) \tag{2.96}$$

$$= \frac{2 r_n \ell N k_q \hat{B}_{r_1} \sin\left(\tfrac{2\pi}{3} - 2\Delta\right)}{a} \cdot \frac{\sin\left(\tfrac{\Delta}{k_q}\right)}{\left(\tfrac{\Delta}{k_q}\right)} \tag{2.97}$$

The flux-linkage of the Type II winding configuration can be written into a general format, so that equation (2.77) can be expanded to include the the Type II winding configuration as well. The general flux-linkage equation for the RFAPM machine can thus be written as

$$\Lambda_{a,b,c|O} = \Lambda_{a,b,c|I} = \Lambda_{a,b,c|II} = 2 r_n \ell N \hat{B}_{r_1} k_q k_{w,pitch} k_{w,slot} \tag{2.98}$$

again with the general format of the slot width factor given by (2.76), so that we can write

$$k_{w,slot} = k_{w,slot|O} = k_{w,slot|I} = k_{w,slot|II} = \frac{\sin\left(\frac{\Delta}{k_q}\right)}{\frac{\Delta}{k_q}}\,, \tag{2.99}$$

with the only difference being the winding pitch factor, $k_{w,pitch}$, which for the Type II winding configuration would be equal to

$$k_{w,pitch|II} = \sin\left(\tfrac{2\pi}{3} - 2\Delta\right)\,. \tag{2.100}$$

2.5.2 Conductor Density Distribution of the Type II Winding Configuration

From the winding distribution for phase a of the Type II winding configuration as shown in Figure 2.19 and with the coil-side width equal to $\frac{2\Delta}{q}$, the conductor density distribution will have the form as shown in Figure 2.20. As was mentioned in section 2.3.2, the conductor density distribution allows us to calculate the back-EMF of the machine as well as the three-phase synchronous inductance of the machine.

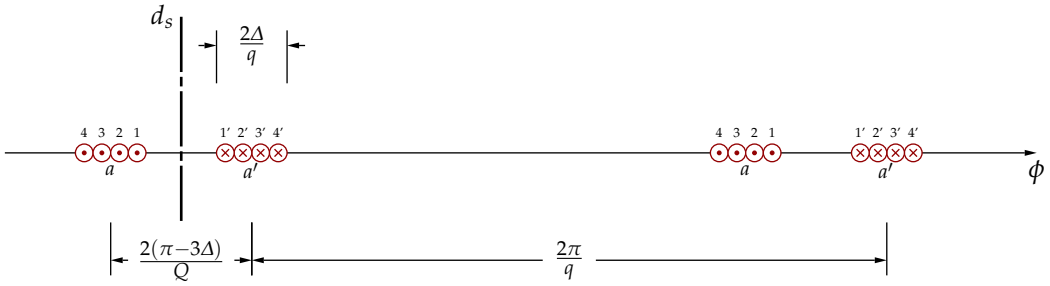

Figure 2.19: The winding distribution and relative coil position for phase a of a RFAPM machine with a Type II winding configuration and $k_q = \frac{1}{2}$.

From Figure 2.20 and with the use of a few trigonometrical identities, the Fourier expansion of the conductor density distribution for phase a can be written similar to (2.78) as

$$n_{a|II}(\phi) = \sum_{m=1}^{\infty} b_{m_{n|II}} \sin(mq\phi) \tag{2.101}$$

with

$$b_{m_{n|II}} = -\frac{2qN}{m\pi\Delta} \sin\left(m(\tfrac{\pi}{3} - \Delta)\right) \sin(m\Delta) \tag{2.102}$$

Once again, as was shown in section 2.4.2, it is possible to write the Fourier series expansion coefficient, $b_{m_{n|II}}$, in terms of a number of winding factors, so that we can write

$$b_{m_{n|II}} = -\frac{2qN}{\pi} \cdot k_{w,m|II} \tag{2.103}$$

with the general winding factor expanding to

$$k_{w,m|II} = k_{w,pitch,m|II} \cdot k_{w,slot,m|II}\,, \tag{2.104}$$

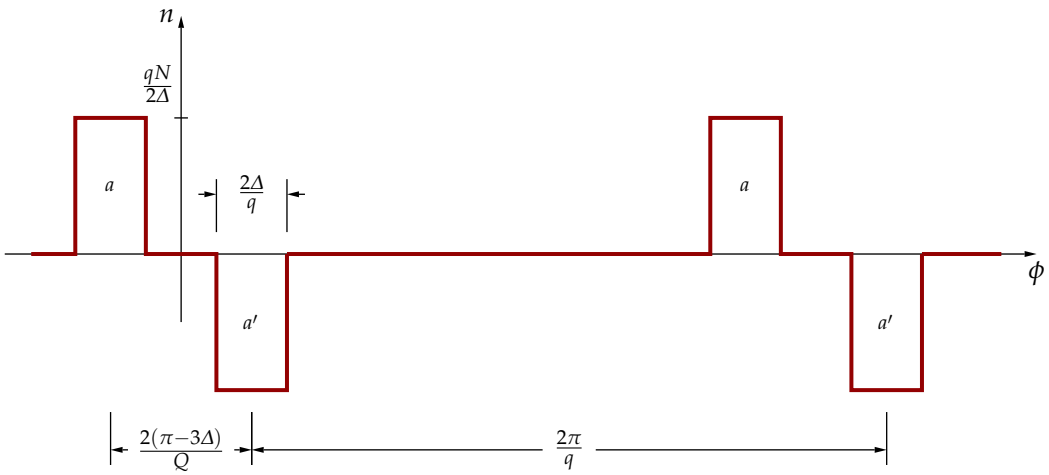

Figure 2.20: The conductor density distribution for phase a of a RFAPM machine with a Type II winding configuration with $k_q = \frac{1}{2}$ and $k_\Delta = \frac{2}{3}$.

with the pitch factor,

$$k_{w,pitch,m|II} = \sin\left(m\left(\tfrac{\pi}{3} - \Delta\right)\right) \tag{2.105}$$

and the "virtual" slot width factor,

$$k_{w,slot,m|II} = k_{w,slot,m|I} = k_{w,slot,m|O} = \frac{\sin(m\Delta)}{m\Delta}\,. \tag{2.106}$$

Furthermore, with the resultant coil pitch equal to twice the resultant pole pitch, i.e. $\tau_{q,res} = 2\tau_{p,res}$, and considering only the fundamental component of the radial flux-density distribution, again only the second harmonic component of the conductor density distribution will contribute to the flux-linkage. Thus with $m = 2$, it follows that

$$k_{w,pitch,m=2|II} = k_{w,pitch|II} \tag{2.107}$$

and

$$k_{w,slot,m=2|II} = k_{w,slot|II}\,. \tag{2.108}$$

2.5.3 Current Density Distribution of the Type II Winding Configuration

In this section, the three-phase current density distribution for the Type II non-overlapping winding configuration will be deduced. The three-phase current density distribution will be used in Chapter 4 to calculate the armature-reaction field for the Type II winding configuration as well as for the calculation of the developed torque of a RFAPM machine with a Type II winding configuration in Chapter 5.

The area of the "virtual stator slot" for a RFAPM machine with Type II winding configuration is again exactly the same as for the Type O and Type I winding configurations. The current density distribution can thus directly be obtained from 2.19 as is shown in Figure 2.21.

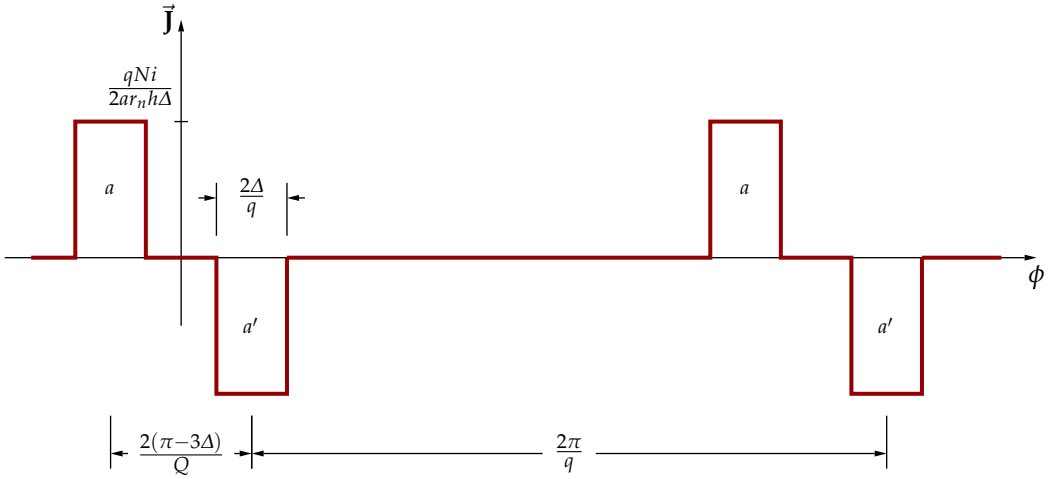

Figure 2.21: The current density distribution for phase a of a Type II winding configuration at $\omega t = 0°$.

The Fourier expansion of the current density distribution for phase a of the concentrated Type II RFAPM machine can be written as

$$J_{z_{a|II}} = \frac{1}{ar_nh} \sum_{m=1}^{\infty} b_{m_{n|II}} \sin(mq\phi) i_a(t) \; . \tag{2.109}$$

Using the same approach as with the Type O, equation (2.51) – and the Type I winding configuration, equation (2.85), the resultant steady state current density distribution for all three phases can be calculated as,

$$J_{z_{|II}} = \begin{cases} -\frac{3qI_pN}{ar_nh\pi} \sum_{m=1}^{\infty} k_{w,m|II} \sin\left(mq\phi + \omega t\right) & \text{for } m = 3k-1,\ k \in \mathbb{N}_1 \\ -\frac{3qI_pN}{ar_nh\pi} \sum_{m=2}^{\infty} k_{w,m|II} \sin\left(mq\phi - \omega t\right) & \text{for } m = 3k-2,\ k \in \mathbb{N}_1 \end{cases} \tag{2.110}$$

as shown for $\omega t = 0°$ in Figure 2.22, $\omega t = 15°$ in Figure 2.23 and $\omega t = 30°$ in Figure 2.24. As was the case for the Type I winding configuration, the $3k-1$ harmonics, which includes the working (second) harmonic is moving to the "right" (i.e. rotating counter clockwise) in these figures.

2.6 Number of Turns per Coils

Before we conclude this chapter, it is important to note that for the different winding configurations under consideration, although the number of turns were always shown as N during the analysis of each winding configuration, the actual number of turns may vary between the different winding configurations. It was shown, that the overlapping (Type O) winding configuration will always have twice the number of coils than either of the non-overlapping winding configurations. This implies that it would theoretically be possible for the non-overlapping windings to have twice the number of turns than for either the Type I or Type II non-overlapping winding configuration. In practise however it turns out to be closer to 1,5 times due to the fact that we require the turns of each coil to be as wide as possible to maximise the flux-linkage. If

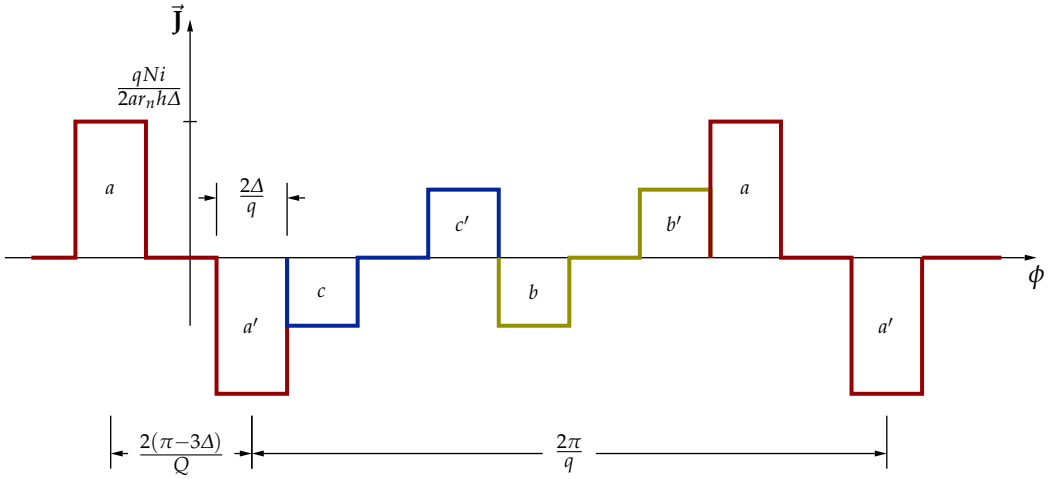

Figure 2.22: The combined current density distribution for phase all three phases of a Type II winding configuration at $\omega t = 0°$.

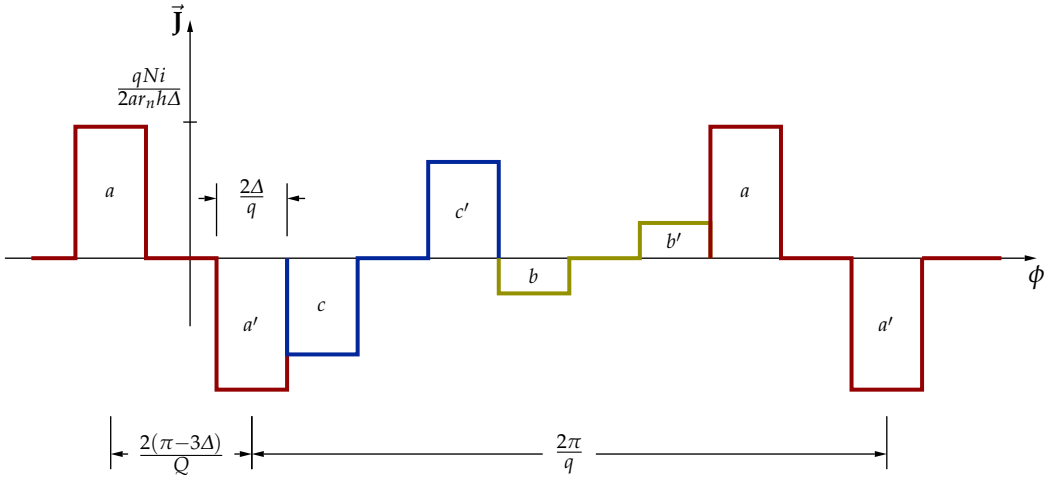

Figure 2.23: The combined current density distribution for phase all three phases of a Type II winding configuration at $\omega t = 15°$.

the turns become too narrow due to an increase in the number of turns, these additional turns will contribute little to the increase in flux-linkage and will only add to the copper losses. The difference in the stator copper losses between the different winding configurations with the end-turn effect for the different winding configurations also taken into account, will be further discussed in Chapter 6.

In order to calculate the number of turns that can fit on a machine, we start by calculating the "virtual slot area", A_{slot}. From (2.36), in terms of the machine parameters,

$$A_{slot} = \frac{2r_n h\Delta}{q} \tag{2.111}$$

with

$$\Delta = k_\Delta \Delta_{max} \tag{2.112}$$

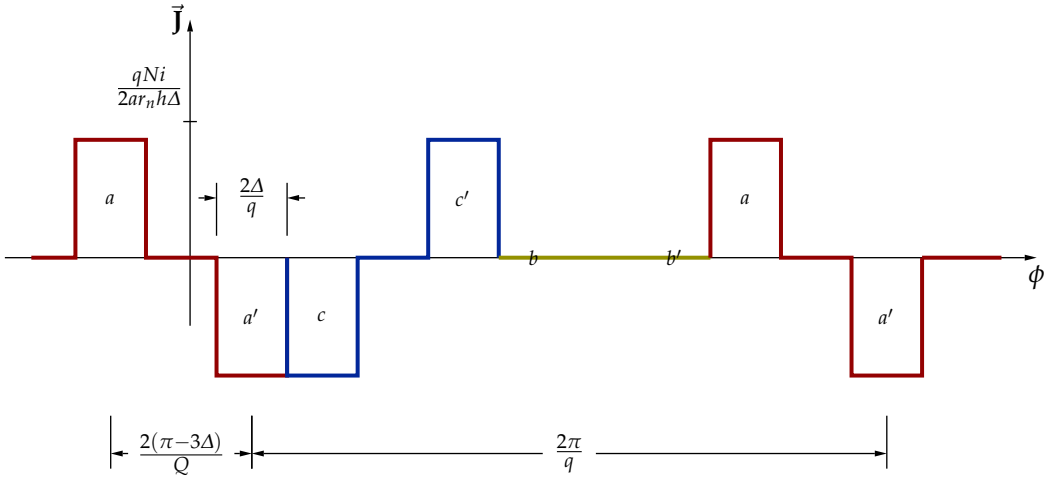

Figure 2.24: The combined current density distribution for phase all three phases of a Type II winding configuration at $\omega t = 30°$.

as was shown in (2.64), and

$$\Delta_{max} = \frac{\pi}{6q} \qquad \text{[mech.]} \tag{2.113}$$

as defined in (2.63).

This implies that the "virtual" slot area in terms of the coil side-width factor, k_Δ, can be written as

$$A_{slot} = \frac{\pi r_n h k_\Delta}{3q} \,. \tag{2.114}$$

With the "virtual" slot area known, the maximum number of turns can be calculated with the area of the copper wire, A_{wire} and the fill factor, k_f, known.

$$N = \frac{A_{slot}}{A_{wire}} k_f \tag{2.115}$$

The fill factor is a function of various aspects, most notably the shape of the wire, i.e. round or rectangular, whether Litz wire is used and the craftsmanship employed. A good estimate of the value is usually known from previous experience.

The thickness of the copper wire used, and hence the cross-sectional area thereof, is usually a trade of between the copper losses allowed for and the copper utilisation with the latter usually dominating. Traditionally a wire current density, J_{wire}, to be in the range of $4-6$ A/mm^2 is considered to be a good trade off between copper utilisation and copper losses. The choice of the current density is also based on how easy or difficult it is to extract the heat out of the stator windings.

For air cored stators, a lower value of current density is recommended, as there is no iron in contact with copper wires to conduct the heat away from the windings. Thus based on the r.m.s. current, I_{rms}, the number of parallel circuits, a, and the selected current density, the cross-sectional area of the copper wire required can be calculated as

$$A_{wire} = \frac{I_{rms}}{a J_{wire}} \,, \tag{2.116}$$

so that with (2.116) and (2.36) substituted into (2.115), the number of turns per coil can be calculated in terms of the various machine parameters as

$$N = \frac{a\pi r_n h k_f k_\Delta J_{wire}}{3qI_{rms}} \,. \tag{2.117}$$

The parameters of two RFAPM non-overlapping, double-layer (Type II) test machines that were built and tested, are given in Appendix E, section E.1 for Stegmann [15] and Stegmann and Kamper [16, 26], and in section E.2 for Groenewald [17]. In this dissertation this data for E.1 will be used for both the analytical and Finite Element (FE) analysis of the RFAPM Type II machine. Although a Type O and a Type I RFAPM machine were not built, the rotors of these two "hypothetical" machines were taken as identical to the Type II machine, with the only difference being in the layout of the stator windings.

With the 32–pole (i.e. 16 pole pairs) rotor being the same for all three machines, it implies that both the Type I and II machines will only employ 8 coils per phase, whilst the Type O machine will have the advantage of using 16 coils per phase. The design in section E.1 of Appendix E uses a coil side-with factor, $k_\Delta = 0{,}74$ which was based on calculation done to maximise the torque and minimise the copper volume of the stator windings, Randewijk *et al.* [14] and Stegmann and Kamper [16, 26]. For comparison purposes it was decided to use the same value for the Type I machine. The Type O machine has the advantage of utilising the maximum available coil side-width available in order maximise its flux-linkage and ultimately the torque produced. The choice of the coil side-width factor, k_Δ, for the Type I and II machines will be discussed in more detail in Chapter 6 together with the difference in end-turn lengths between the three different winding configurations.

Using the same coil side-width factor and the same number of coils per phase for both the Type I and II winding configuration, it implied that the number of turns per phase would also be the same for both. From (2.115) the number of turns per coil for these two winding configurations were calculated at 96 turns each with a current density of $5\,\mathrm{A/mm^2}$ for both winding configurations. For the Type O winding configuration, although k_Δ=1,0 , the maximum allowable coil-side width is half that of the non-overlap winding configuration's maximum coil-side width, due to the fact that twice the number of coils are being used. This resulted in the maximum number of turns per coils being equal to 64 turns, also with a current density value of $5\,\mathrm{A/mm^2}$. In Table 2.1 the key differences between the different winding configurations are highlighted on which the comparative analytical and FEA of Chapters 3, 4 and 5 will be based on.

Table 2.1: Comparison between the number of coils, q, the coil-side width factor, k_Δ, and the number of turns per coil, N, for the different winding configurations with the same rotor geometry and stator current and current density.

	Type O	Type I	Type II
q	16	8	8
k_Δ	1,0	0,74	0,74
N	64	96	96

2.7 Summary and Conclusions

In this chapter the winding factors, conductor density distribution and the three-phase current density distribution for the different winding configurations under consideration were deduced. As distributed windings were not employed for either winding configuration, the winding factors consisted of only a pitch factor and a "slot" factor. Being a slot-less machine the latter could also be called a "coil-side width" factor.

It was seen that due to the fact that for the overlapping winding configuration there is only one coil per pole pair, the fundamental component of the conductor density distribution was the working harmonic. This is in contrast to the working harmonic of the Type I and Type II winding configurations which was seen to be associated with the second harmonic of the conductor density distribution. This is due to of the fact that for both non-overlapping winding configurations, there is only *one* non-overlapping coil for each *two* rotor pole pairs.

For the overlapping winding configuration the coil sequence were also seen to be ABC as opposed to the non-overlapping winding configurations' coil sequence that were ACB – again due to the fact that there is only one non-overlapping coil for each two rotor pole pairs.

In Figures 2.8 to 2.10 it was also clearly shown how the three-phase current density distribution's waveform "moves to the right" (i.e. rotating counter clockwise) at synchronous speed with time. For the Type I and II non-overlapping winding configurations it is however more difficult to see the working (second) harmonic "moving to the right" (i.e. rotating counter clockwise) but was non the less shown in Figures 2.15 to 2.17 and Figures 2.22 to 2.24 for the Type I and Type II winding configurations respectively.

Also in this chapter, the conductor density distribution was derived. This will be used in Chapter 3 to calculate the back-EMF of the machine as well as the three-phase synchronous inductance of the machine in Chapter 4, for the three different winding configuration under consideration.

Finally, the three-phase current density distributions for the three different winding configuration were also derived. This will be used in Chapter 4 to calculate the armature-reaction field, as well as the developed torque of the RFAPM machine for the different winding configurations in Chapter 5.

CHAPTER 3

Magnetostatic Analysis of the Magnetic Fields due to the Permanent Magnets

Finally, two days ago, I succeeded – not on account of my hard efforts, but by the grace of the Lord. Like a sudden flash of lightning, the riddle was solved. I am unable to say what was the conducting thread that connected what I previously knew with what made my success possible.

KARL FRIEDRICH GAUSS

3.1 Introduction

In this chapter the 2-D analytical analysis of the magnetic fields produced by the permanent magnets situated on the double-sided rotor of the RFAPM machine will be discussed. After a short background on the different analysis techniques that exist to model electrical machines, the magnetic field inside the RFAPM machine, produced by the permanent magnets on the double-sided rotor, will be solved from first principles. It will be shown how the permanent magnets' pole arc width influences the fundamental component and total harmonic distortion[1] (THD) of the radial flux-density distribution inside the stator of the machine.

It will also be shown how the flux-linkage and the induced voltage for the different winding configurations can be analytically calculated from the magnetic vector potential for the different winding configurations, using the conductor density distributions derived in Chapter 2. Furthermore, it will be shown that a good approximation of the flux-linkage and induced voltage can be obtained by simply using the fundamental component of the radial flux-density distribution in the centre of the stator region.

[1] Calculated with respect to the space harmonics of the radial flux-density distribution.

3.2 Background on the Magnetic Field Analysis of Electrical Machines

2-D analytical analysis of permanent magnet machines was initially done by modelling the permanent magnet's MMF as current sheets on the surface of the permanent magnets, Boules [27]. The machine was then linearised and the governing quasi-Poisson – and Laplace equations for the permanent magnets and the air-gap regions respectively, were written in terms of the magnetic vector potential, $\vec{\mathbf{A}}$. These equations were then solved in the Cartesian coordinate system from the boundary conditions with the air-gap extended using Carter factors and the stator represented by an equivalent current sheet on the boundary between the air-gap and the stator.

In [28], Boules extended the modelling of permanent magnets, by using the magnetisation vector, $\vec{\mathbf{M}}$, to model both parallel – and radially magnetised permanent magnets. The governing equations were however solved using the scalar vector potential, Ω or φ, in the polar coordinate system. For both these modelling techniques, the recoil permeability of the permanent magnets were take to be unity. In [29], Zhu *et al.* extended the modelling technique further to include the recoil permeability of permanent magnets and applied this theory to slotless machines with radially magnetised permanent magnets. This modelling technique was extended even further in [22] by Zhu *et al.* to include parallel-magnetised permanent magnets and non-overlapping winding configurations.

Holm [24, chap. 5] and Holm *et al.* [21] proposed a way in which the analytical field calculations can be simplified even further and will be explained in section 3.7.2 for to the special case were "$mp = 1$". Holm also reverted back to using the magnetic vector potential for the magnetic field calculations. In this dissertation, this approach will also be used.

For all the above modelling techniques, the rotor – and stator yokes' permeabilities were considered to be infinity. Kumar and Bauer [30] included the rotor – and stator yokes' permeability into the solution for the machine's magnetic field solution by assigning a specific permeability to the iron yokes. This allowed the flux-density in the yokes to be calculated in order to determine the risk of possible yoke saturation to occur. Although Kumar and Bauer's method assumes constant permeability and hence does not take saturation into account, it still is able to give an indication as to whether magnetic saturation is possible. In this dissertation a specific permeability value will also be assigned to the rotor yokes in order to calculate the flux-density inside the yokes and determine the subsequent risk of magnetic saturation occurring inside the rotor yokes.

In Chapter 1 it was mentioned that the RFAPM machine is the dual of the Axial Flux Aircored Permanent Magnet (AFAPM) machine. The first occurrence in the literature on the analytical analysis of AFAPM were in two papers by Virtic *et al.* [31, 32]. The first paper focused on the analytical analysis of the magnetic field caused by the permanent magnets in order to solve the flux-density distribution in the machine and to calculate the back-EMF in the coils produced by the permanent magnets. In the second paper, the flux-density distribution caused by the armature coils were calculated. The torque produced by the machine were then calculate using the Maxwell Stress Tensor.

An AFAPM machine with a double-sided rotor and single side permanent magnets em-

ploying a core-less stator with full-pitched, double-layer windings was analytically analysed by Chan *et al.* [33]. Although a RFAPM dual of this machine was considered, it was found to have a very low radial flux-density distribution with severe flux-leakage between adjacent magnets and as such was not considered further.

All the analytical modelling techniques mentioned above and more were reviewed in Zhu *et al.* [23]. These techniques were subsequently called "subdomain modelling" techniques referring to the different regions or domains into which the machine is subdivided for analysis purposes. Incidentally, this term was first coined in the classical paper by Abdel-Razek *et al.* [34] on the Air-gap Element.

3.3 The Maxwell Equations

We will start our 2-D analytical analysis from first principles with the Maxwell equations. The Maxwell equations,

$$\nabla \times \vec{\mathbf{E}} = -\frac{\partial \vec{\mathbf{B}}}{\partial t}\,, \tag{3.1}$$

$$\nabla \times \vec{\mathbf{H}} = \vec{\mathbf{J}} + \frac{\partial \vec{\mathbf{D}}}{\partial t}\,, \tag{3.2}$$

$$\nabla \cdot \vec{\mathbf{D}} = \rho_v \quad \text{and} \tag{3.3}$$

$$\nabla \cdot \vec{\mathbf{B}} = 0\,. \tag{3.4}$$

These four equations are the mathematical representation in differential form, of Faraday's law, Ampere's law and Gauss's laws on the conservation of electrical and magnetic flux respectively and are the four governing equations that completely describe time-varying electromagnetic fields in free space, Cheng [35, sec. 7.3] and Guru and Hiziroglu [36, sec. 7.4, 7.9 and 7.10].

If the wavelength of the time-varying electromagnetic fields are much larger than the physical dimensions of the device being analysed, the displacement current portion of (3.2), $\frac{\partial \vec{\mathbf{D}}}{\partial t}$, will be negligible compared to the free current density, $\vec{\mathbf{J}}$, Binns *et al.* [37, p. 4], so that equation (3.2) reduces to the original Ampère for, of

$$\nabla \times \vec{\mathbf{H}} = \vec{\mathbf{J}}\,. \tag{1.2'}$$

3.4 Magnetic Materials

The magnetic polarisation, Stratton [38, p. 128], magnetisation vector, Cheng [35, p. 250] or the magnetic moment per unit volume, Guru and Hiziroglu [36, p. 206] for a linear, isotropic medium can be written in terms of the magnetic field intensity as

$$\vec{\mathbf{M}} = \chi_m \vec{\mathbf{H}}\,. \tag{3.5}$$

This allow us to define the magnetic flux-density of the medium in terms of the field intensity, as

$$\begin{aligned}\vec{\mathbf{B}} &= \mu_0\vec{\mathbf{H}} + \vec{\mathbf{M}} && (3.6)\\ &= \mu_0(1+\chi_m)\vec{\mathbf{H}} && (3.7)\\ &= \mu_0\mu_r\vec{\mathbf{H}} && (3.8)\\ &= \mu\vec{\mathbf{H}}\,. && (3.9)\end{aligned}$$

For a permanent magnet material, the magnetisation vector is equal to the sum of the residual magnetisation, and the induced magnetisation, i.e.

$$\begin{aligned}\vec{\mathbf{M}} &= \vec{\mathbf{M}}_0 + \vec{\mathbf{M}}_i && (3.10)\\ &= \vec{\mathbf{M}}_0 + \chi_m\vec{\mathbf{H}}\,, && (3.11)\end{aligned}$$

Boules [28], with specific reference to Stratton [38, p. 129].

The flux-density in the permanent magnet material can thus be calculated as,

$$\begin{aligned}\vec{\mathbf{B}} &= \mu_0\vec{\mathbf{H}} + \mu_0\vec{\mathbf{M}} && (3.12)\\ &= \mu_0\vec{\mathbf{H}} + \mu_0\chi_m\vec{\mathbf{H}} + \mu_0\vec{\mathbf{M}}_0 && (3.13)\\ &= \mu_0(1+\chi_m)\vec{\mathbf{H}} + \mu_0\vec{\mathbf{M}}_0 && (3.14)\\ &= \mu_0\mu_r\vec{\mathbf{H}} + \mu_0\vec{\mathbf{M}}_0 && (3.15)\\ &= \mu\vec{\mathbf{H}} + \mu_0\vec{\mathbf{M}}_0\,. && (3.16)\end{aligned}$$

With the residual magnetisation

$$\vec{\mathbf{M}}_0 = \frac{\vec{\mathbf{B}}_{rem}}{\mu_0}\,, \tag{3.17}$$

the flux-density in the permanent magnet material can also be expressed as

$$\vec{\mathbf{B}} = \mu\vec{\mathbf{H}} + \vec{\mathbf{B}}_{rem}\,, \tag{3.18}$$

as the remanent flux-density is usually the value supplied by the permanent magnet manufacturer in the data sheets and not the residual magnetisation.

3.5 Magnetic Vector Potential

The divergence-free postulate of $\vec{\mathbf{B}}$ by (3.4) assures that $\vec{\mathbf{B}}$ is solenoidal. Consequently $\vec{\mathbf{B}}$ can be expressed as the curl of another vector field, say $\vec{\mathbf{A}}$, Cheng [35, sec. 6.3], i.e.

$$\vec{\mathbf{B}} = \boldsymbol{\nabla}\times\vec{\mathbf{A}}\,. \tag{3.19}$$

The vector field $\vec{\mathbf{A}}$ is called the vector magnetic potential (Cheng [35, sec. 6.3] and Reece and Preston [39, sec. 1.4]) or the magnetic vector potential (Binns *et al.* [37, sec. 1.2.1] and Guru and Hiziroglu [36, sec. 5.6]) or just the vector potential, for short.

In the Cartesian coordinate system, the magnetic vector potential can be written as

$$\vec{\mathbf{A}} = A_x\vec{\mathbf{a}}_x + A_y\vec{\mathbf{a}}_y + A_{z|PM}\vec{\mathbf{a}}_z\,, \tag{3.20}$$

and in the cylindrical coordinate system, as

$$\vec{\mathbf{A}} = A_r\vec{\mathbf{a}}_r + A_\phi\vec{\mathbf{a}}_\phi + A_{z|PM}\vec{\mathbf{a}}_z \ . \tag{3.21}$$

If the current density is only in the z direction, i.e. $J_x = J_y = 0$, it can be shown that the vector potential will also only be in the z direction, i.e. $A_x = A_y = 0$, Reece and Preston [39, sec. 2.1.2].

3.6 The Vector Poisson Equations

3.6.1 The Vector Poisson Equation in the Different Regions of the RFAPM Machine

In order to analyse the RFAPM machine, the machine is divided into several regions or subdomains, Zhu *et al.* [23]. The regions are chosen in such a way that for each region a separate equation can be found to describe the magnetic vector potential everywhere inside that region, as well as a unique set of boundary conditions that exist between the regions, Binns *et al.* [37, sec. 4.3]. The regions must also be chosen in such a way, in what would become clearer in subsequent sections, that the permeability in each region is constant. The magnetic vector potential for each region can be solved more easily if we write it in a vector Poisson equation form for each region, i.e.

$$\boldsymbol{\nabla}^2\vec{\mathbf{A}} = F(r,\phi) \ . \tag{3.22}$$

The only logical way to subdivide the machine is into "ring" regions, with concentric circular boundaries analogous to Atallah *et al.* [6], Zhu *et al.* [29] & [22] and Holm *et al.* [21], to name a few. The different regions for the RFAPM machine is shown in a linear representation in Figure 3.1 with r_n, the nominal radius measured form the centre of the machine to the centre of the stator region. The azimuthal axis of the machine, ϕ, is shown in electrical radians.

The different regions of the RFAPM machine are thus:

I – the inner yoke region
II – the inner yoke permanent magnet region
III – the airgap region (including the air cored stator region)
IV – the outer yoke permanent magnet region
V – the outer yoke region

The governing equations for solving the magnetic vector potential in the different regions of the RFAPM machine, is shown in Table 3.1. These equations will be further expanded in sections 3.6.2 and 3.6.3.

3.6.2 The Vector Poisson Equation in the Non Permanent Magnet Regions

From (3.9), we can write:

$$\vec{\mathbf{H}} = \frac{\vec{\mathbf{B}}}{\mu} \tag{3.23}$$

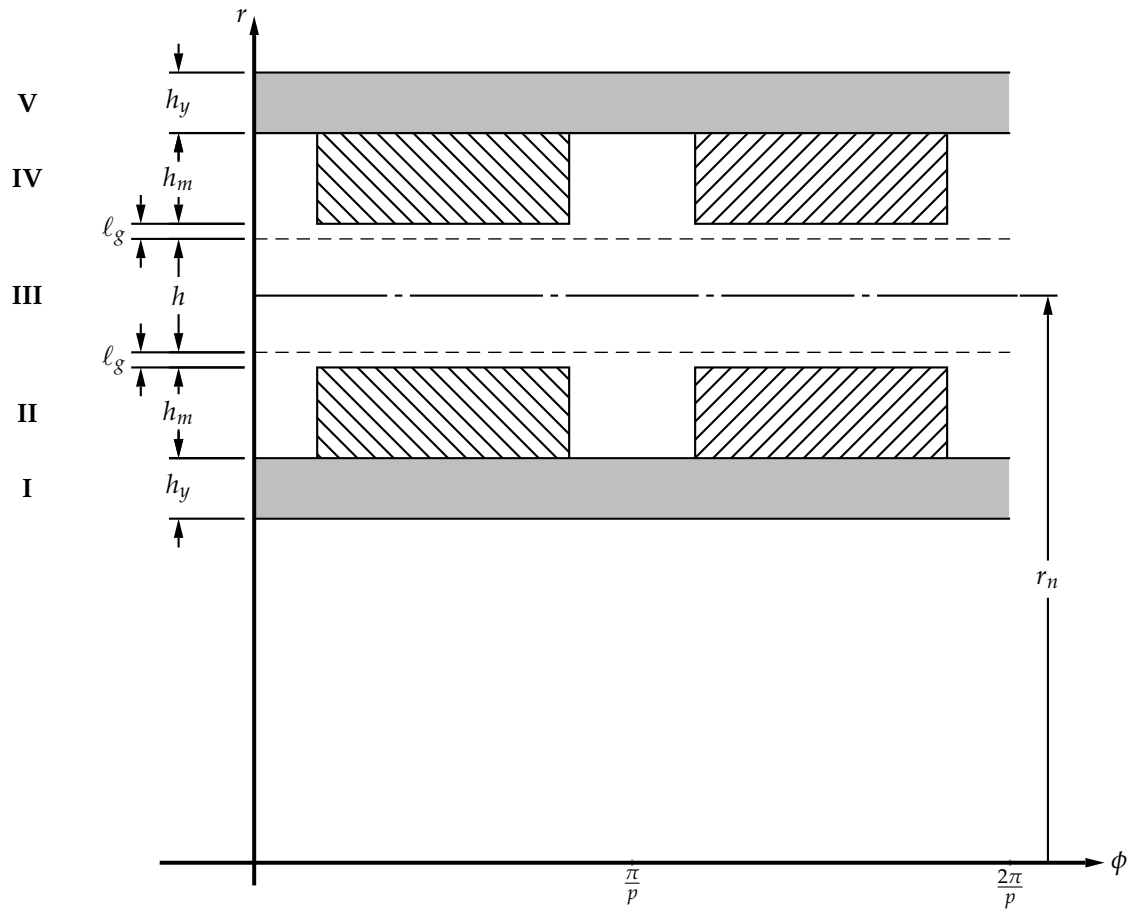

Figure 3.1: A linear representation of the different regions of the RFAPM machine.

Region	Range for r	μ_r	Governing equation
I	$r_n + \frac{h}{2} + \ell_g + h_m + h_y \geq r \geq r_n + \frac{h}{2} + \ell_g + h_m$	μ_y	$\nabla^2 \vec{\mathbf{A}} = 0$
II	$r_n + \frac{h}{2} + \ell_g + h_m \geq r \geq r_n + \frac{h}{2} + \ell_g$	1	$\nabla^2 \vec{\mathbf{A}} = -\mu_0 \left(\nabla \times \vec{\mathbf{M}}_0 \right)$
III	$r_n + \frac{h}{2} + \ell_g \geq r \geq r_n - \frac{h}{2} - \ell_g$	1	$\nabla^2 \vec{\mathbf{A}} = 0$
IV	$r_n - \frac{h}{2} - \ell_g \geq r \geq r_n - \frac{h}{2} - \ell_g - h_m$	1	$\nabla^2 \vec{\mathbf{A}} = -\mu_0 \left(\nabla \times \vec{\mathbf{M}}_0 \right)$
V	$r_n - \frac{h}{2} - \ell_g - h_m \geq r \geq r_n - \frac{h}{2} - \ell_g - h_m - h_y$	μ_y	$\nabla^2 \vec{\mathbf{A}} = 0$

Table 3.1: The governing equations for solving the magnetic vector potential in the different regions of the RFAPM machine when employing permanent magnet excitation.

Substituting this in (1.2′), and assuming that the medium is homogeneous we get

$$\nabla \times \vec{\mathbf{B}} = \mu \vec{\mathbf{J}} \,. \tag{3.24}$$

Now substituting (3.19) into the above equation, it expands to

$$\nabla \times \nabla \times \vec{\mathbf{A}} = \mu \vec{\mathbf{J}} \,, \tag{3.25}$$

or if we further expand the left hand side of the equation,

$$\nabla (\nabla \cdot \vec{\mathbf{A}}) - \nabla^2 \vec{\mathbf{A}} = \mu \vec{\mathbf{J}} \,. \tag{3.26}$$

In order to simplify (3.26) we choose

$$\nabla \cdot \vec{\mathbf{A}} = 0 \,, \tag{3.27}$$

which is called the Coulomb gauge, Binns *et al.* [37, p. 6], so that that (3.26) reduces to

$$\nabla^2 \vec{\mathbf{A}} = -\mu \vec{\mathbf{J}} \,, \tag{3.28}$$

which is called the vector Poisson equation, or simply the Poisson equation for short.

In a current-free region, (3.28) reduces to

$$\nabla^2 \vec{\mathbf{A}} = 0 \,, \tag{3.29}$$

which is known as the Laplace – or homogeneous version of the Poisson equation and can only be solved if the boundary conditions are non– or inhomogeneous, Gockenbach [40, sec. 8.1.8].

For 2-D analysis, with $J_x = J_y = 0$, (3.28) can be written in partial differential form in Cartesian coordinates, as

$$\frac{\partial^2 A_{z|PM}}{\partial x^2} + \frac{\partial^2 A_{z|PM}}{\partial y^2} = -\mu J_z \,, \tag{3.30}$$

or in cylindrical coordinates as

$$\frac{\partial^2 A_{z|PM}}{\partial r^2} + \frac{1}{r}\frac{\partial A_{z|PM}}{\partial r} + \frac{1}{r^2}\frac{\partial^2 A_{z|PM}}{\partial \phi^2} = -\mu J_z \,. \tag{3.31}$$

For the magnetostatic analysis, we ignore the currents in the stator as we are only interested in the flux-density distribution in the airgap as a result of the permanent magnets alone. The windings are effectively "switched off"[1]. Thus for both the yoke regions, regions **I** and **IV** and the stator/airgap region, region **III**, we can take $J_z = 0$. This implies that the Poisson equation (3.31) reduces to a simple Laplace equation,

$$\frac{\partial^2 A_{z|PM}}{\partial r^2} + \frac{1}{r}\frac{\partial A_{z|PM}}{\partial r} + \frac{1}{r^2}\frac{\partial^2 A_{z|PM}}{\partial \phi^2} = 0 \,, \tag{3.32}$$

in all the non-permanent magnet regions.

3.6.3 The Vector Poisson Equation in the Permanent Magnet Regions

A similar approach can be followed for the permanent magnet regions. The only difference between a permanent magnet region and a non permanent magnet region is that in the permanent magnet region the magnetic field intensity is also dependent on the residual magnetisation of the permanent magnets used. Thus from (3.16) and (3.19),

$$\vec{\mathbf{H}} = \frac{\vec{\mathbf{B}} - \mu_0 \vec{\mathbf{M}}_0}{\mu} \tag{3.33}$$

$$= \frac{\nabla \times \vec{\mathbf{A}} - \mu_0 \vec{\mathbf{M}}_0}{\mu} \,. \tag{3.34}$$

[1] In Chapter 4 we will look at the armature reaction fields produces by the stator windings alone with the permanent magnets "switched off".

Substituting the above into (1.2'),

$$\nabla \times \left(\frac{\nabla \times \vec{\mathbf{A}} - \mu_0 \vec{\mathbf{M}}_0}{\mu} \right) = \vec{\mathbf{J}} \,, \tag{3.35}$$

and multiplying through with μ and then expanding the left hand side of the equation, gives

$$\nabla \left(\nabla \cdot \vec{\mathbf{A}} \right) - \nabla^2 \vec{\mathbf{A}} - \mu_0 \left(\nabla \times \vec{\mathbf{M}}_0 \right) = \mu \vec{\mathbf{J}} \,. \tag{3.36}$$

Using the Coulomb gauge again, the above equation simplifies to

$$\nabla^2 \vec{\mathbf{A}} = -\mu \vec{\mathbf{J}} - \mu_0 \left(\nabla \times \vec{\mathbf{M}}_0 \right) \,. \tag{3.37}$$

When working in cylindrical coordinates, radially magnetised permanent magnets will have a residual magnetisation component only in the $\vec{\mathbf{a}}_r$ direction,

$$\vec{\mathbf{M}}_0 = M_{0|_r} \vec{\mathbf{a}}_r \,, \tag{3.38}$$

where as for parallel magnetised permanent magnets, there will also be a $\vec{\mathbf{a}}_\phi$ component.

$$\vec{\mathbf{M}}_0 = M_{0|_r} \vec{\mathbf{a}}_r + M_{0|_\phi} \vec{\mathbf{a}}_\phi \,. \tag{3.39}$$

This implies that in general

$$\begin{aligned} \nabla \times \vec{\mathbf{M}}_0 &= \frac{1}{r} \begin{vmatrix} \vec{\mathbf{a}}_r & r\vec{\mathbf{a}}_\phi & \vec{\mathbf{a}}_z \\ \frac{\partial}{\partial r} & \frac{\partial}{\partial \phi} & \frac{\partial}{\partial z} \\ M_{0|_r} & r M_{0|_\phi} & - \end{vmatrix} \\ &= \frac{1}{r} \left[\frac{\partial (r M_{0|_\phi})}{\partial r} - \frac{\partial M_{0|_r}}{\partial \phi} \right] \vec{\mathbf{a}}_z \qquad (3.40) \\ &= \left[\frac{M_{0|_\phi}}{r} + \frac{\partial M_{0|_\phi}}{\partial \phi} - \frac{1}{r} \frac{\partial M_{0|_r}}{\partial \phi} \right] \vec{\mathbf{a}}_z \,, \qquad (3.41) \end{aligned}$$

which reduces to,

$$\nabla \times \vec{\mathbf{M}}_0 = -\frac{1}{r} \frac{\partial M_0}{\partial \phi} \vec{\mathbf{a}}_z \tag{3.42}$$

with

$$\vec{\mathbf{M}}_{0|_r} = M_0 \,, \tag{3.43}$$

for radially magnetised permanent magnets.

The residual magnetisation distribution for a radially magnetised permanent magnet can be represented by a periodic function as shown in Figure 3.2.

The derivative of the residual magnetisation distribution of the permanent magnets with respect to ϕ will therefore also be periodic and can be determined directly from Figure 3.2 as shown in Figure 3.3. An alternative approach using the equivalent surface magnetisation current distribution to model the permanent magnets as current sheets, Boules [28], is shown in Appendix B.

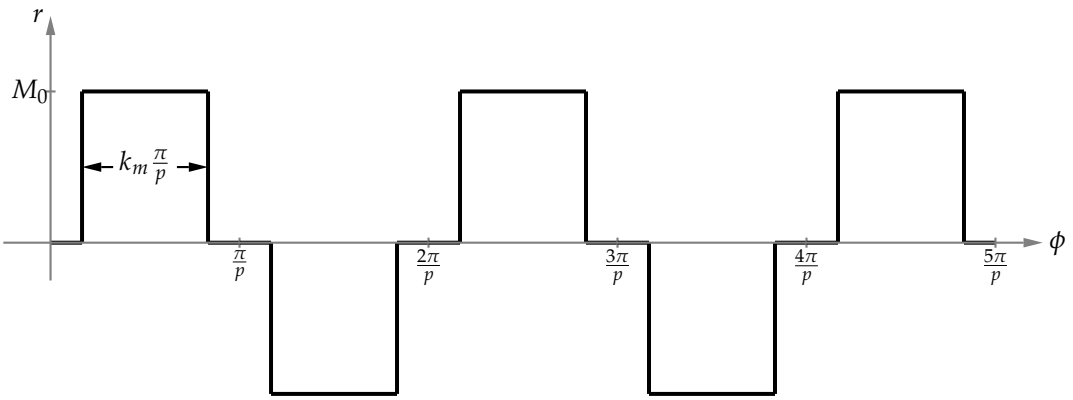

Figure 3.2: The residual magnetisation distribution of a permanent magnet with respect to ϕ.

With

$$f(\phi) = \frac{\partial M_0}{\partial \phi} \tag{3.44}$$

being a periodic function, it can be represented by a Fourier series expansion,

$$f(\phi) = a_0 + \sum_{m=1}^{\infty} \left[a_m \cos(mp\phi) + b_m \sin(mp\phi) \right] . \tag{3.45}$$

Because $f(\phi)$ has no DC component,

$$a_0 = 0 , \tag{3.46}$$

and with $f(\phi)$ being an even function,

$$b_m = 0 , \tag{3.47}$$

therefore only a_m has to be calculated.

The calculation of a_m can further be simplified by setting

$$\beta = \left(\frac{1 - k_m}{2} \right) \frac{\pi}{p} , \tag{3.48}$$

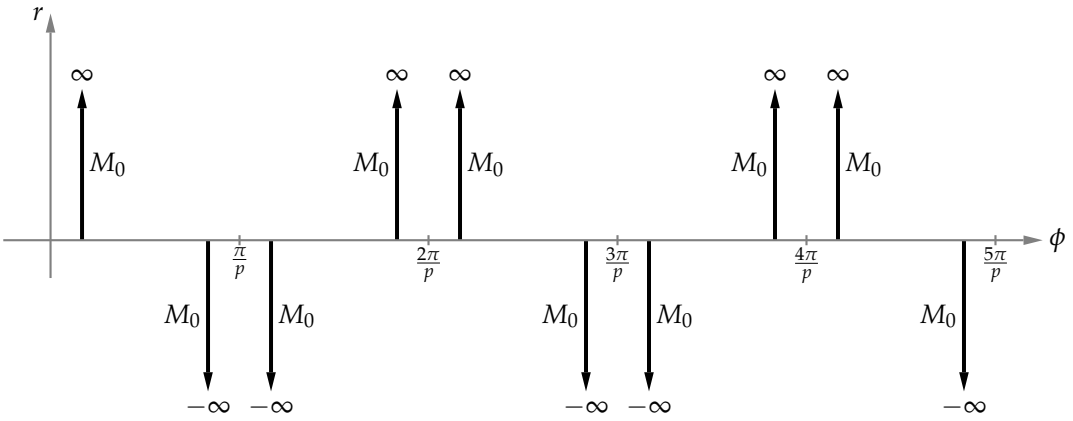

Figure 3.3: The derivative of the residual magnetisation distribution of the permanent magnets with respect to ϕ.

as shown in Figure 3.4, with k_m, the magnet – or pole width defined as a function of the pole pitch, τ_p, as shown in Figure 3.2 with $\tau_p = \frac{\pi}{p}$.

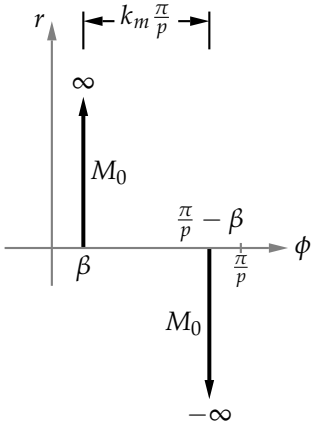

Figure 3.4: The derivative of the remanent flux-density distribution of the permanent magnets with respect to ϕ for one pole.

From Figure 3.4, a_m can now easily be calculated as

$$a_m = \frac{2p}{\pi}\int_0^{\frac{\pi}{p}} f(\phi)\cos(mp\phi)d\phi \tag{3.49}$$

$$= \frac{2p}{\pi}\int_0^{\frac{\pi}{p}} \left[\delta(\phi-\beta)M_0 - \delta\left(\phi - (\tfrac{\pi}{p}-\beta)\right)M_0\right]\cos(mp\phi)d\phi \tag{3.50}$$

$$= \frac{2pM_0}{\pi}\left[\cos(mp\beta) - \cos(m\pi - mp\beta)\right] \tag{3.51}$$

$$= \frac{4pM_0}{\pi}\cos(mp\beta)\ , \tag{3.52}$$

which implies that

$$f(\phi) = \frac{4pM_0}{\pi}\sum_{m=1,3,5,\ldots}^{\infty}\cos(mp\beta)\cos(mp\phi)\ \ , \tag{3.53}$$

or from (3.44),

$$\frac{\partial M_0}{\partial \phi} = \frac{4pM_0}{\pi}\sum_{m=1,3,5,\ldots}^{\infty}\cos(mp\beta)\cos(mp\phi)\ \ . \tag{3.54}$$

Substituting the above into (3.42), yields

$$\nabla \times \vec{\mathbf{M}}_o = -\frac{1}{r}\frac{4pM_0}{\pi}\sum_{m=1,3,5,\ldots}^{\infty}\cos(mp\beta)\cos(mp\phi)\vec{\mathbf{a}}_z \tag{3.55}$$

for radially magnetised permanent magnets.

Then finally by substituting the above into (3.37) with $J_z = 0$ in the PM region, the Poisson equation for region **II** and **IV** for the RFAPM machine is given by

$$\nabla^2\vec{\mathbf{A}} = \mu_0\frac{4pM_0}{\pi r}\sum_{m=1,3,5,\ldots}^{\infty}\cos(mp\beta)\cos(mp\phi)\vec{\mathbf{a}}_z \tag{3.56}$$

or in partial differential format in cylindrical coordinates, as

$$\frac{\partial^2 A_{z|PM}}{\partial r^2} + \frac{1}{r}\frac{\partial A_{z|PM}}{\partial r} + \frac{1}{r^2}\frac{\partial^2 A_{z|PM}}{\partial \phi^2} = \frac{4p\mu_0 M_0}{\pi r}\sum_{m=1,3,5,\ldots}^{\infty}\cos(mp\beta)\cos(mp\phi)\ . \tag{3.57}$$

3.7 Solving the Laplace and Poisson Equations

The Laplace equation consists only of a general (or "homogeneous") solution whereas the Poisson equation consists of a general solution and a particular (or "non-homogeneous") solution.

3.7.1 Finding the General Solution of the Laplace and Poisson Equations

For simple structures such as rectangles and annuli, the general solution to both the Laplace and the Poisson equation can be obtained by the method of separation of variables. The solution for an annulus with periodic boundary conditions will be in the form of harmonic functions. Thus the general solution of (3.32) for all the regions will be of the form,

$$A_{z|PM}(r,\phi) = A_{z,0|PM}(r,\phi) + \sum_{m=1}^{\infty} A_{z,m|PM}(r,\phi)\ , \tag{3.58}$$

Bleecker and Csordas [41, sec. 6.3], with

$$A_{z,0|PM}(r,\phi) = c_0 + d_0\ln(r) \text{ for } m = 0\ , \text{and} \tag{3.59}$$

$$A_{z,m|PM}(r,\phi) = (c_m r^m + d_m r^{-m})(a_m\cos m\phi + b_m \sin m\phi) \text{ for } m \geq 1\ . \tag{3.60}$$

With the flux-density only dependent on the derivatives of the magnetic vector potential and not on the magnitude, Reece and Preston [39, sec. 2.1.2] we can set

$$c_0 = 0\ . \tag{3.61}$$

If there is no DC component,

$$d_0 = 0\ . \tag{3.62}$$

From Zhu *et al.* [29] and [22] it is evident that if $F(r,\phi)$ is an even function, the general solution will also be even, and if $F(r,\phi)$ is odd, the general solution will be odd.

$$A_{z,gen|PM}(r,\phi) = \sum_{m=1,3,5,\ldots}^{\infty}(C_{m|PM}r^{mp} + D_{m|PM}r^{-mp})\cos mp\phi \tag{3.63}$$

3.7.2 Finding the Particular Solution of the Poisson Equation

From (3.17), the governing equation (3.57) for regions **II** and **IV**, can be written in terms of the remanent flux-density of the permanent magnets used as,

$$\frac{\partial^2 A_{z|PM}}{\partial r^2} + \frac{1}{r}\frac{\partial A_{z|PM}}{\partial r} + \frac{1}{r^2}\frac{\partial^2 A_{z|PM}}{\partial \phi^2} = \frac{4pB_{rem}}{\pi r}\sum_{m=1,3,5,\ldots}^{\infty}\cos mp\beta\cos mp\phi\ . \tag{3.64}$$

In order to find the particular solution, one usually makes an intelligent guess as to the form of the particular solution. The solution is then substituted back into the equation being solved to see if it indeed satisfies the equation. The following solution to particular solution was proposed by Zhu *et al.* [29] and [22],

$$A_{z,part|PM}(r,\phi) = \sum_{m=1,3,5,\ldots}^{\infty} G_{m|PM} r \cos mp\phi \; . \tag{3.65}$$

By substituting this solution into the left hand side (LHS) of (3.64),

$$\frac{\partial A_{z|PM}}{\partial r} = \sum_{m=1,3,5,\ldots}^{\infty} G_{m|PM} \cos mp\phi \; , \tag{3.66}$$

$$\frac{\partial^2 A_{z|PM}}{\partial r^2} = 0 \; , \tag{3.67}$$

$$\frac{\partial A_{z|PM}}{\partial \phi} = -\sum_{m=1,3,5,\ldots}^{\infty} mp G_{m|PM} r \sin mp\phi \text{ and} \tag{3.68}$$

$$\frac{\partial^2 A_{z|PM}}{\partial \phi^2} = -\sum_{m=1,3,5,\ldots}^{\infty} (mp)^2 G_{m|PM} r \cos mp\phi \; , \tag{3.69}$$

we are able to verify the validity of the solution. This results in

$$G_{m|PM} = \frac{4pB_{rem} \cos mp\beta}{\pi\,(1-(mp)^2)} \qquad \text{for } mp \neq 1 \; . \tag{3.70}$$

The problem with this particular solution, is that it is not valid for $mp = 1$[1] and thus another solution for the case $mp = 1$ has to be obtained for the permanent magnet region.

In order to simplify the analytical solution, Holm *et al.* [21] proposed that if the B_{rem} were proportional to $\frac{1}{r}$, it would yield a unique particular solution for all values of m. Thus the "new" remanent flux-density value used for the permanent magnet regions is given by the following equation,

$$B'_{rem} = \frac{r_{cm}}{r} B_{rem} \; . \tag{3.71}$$

The error introduced is very small as the magnet's radial thickness, h_m, is much smaller than the radius measured to the centre of the magnets, r_{cm}. Thus with,

$$h_m \ll r_{cm} \tag{3.72}$$

it follows that

$$r \approx r_{cm} \tag{3.73}$$

and

$$B'_{rem} \approx B_{rem} \; . \tag{3.74}$$

[1]This implies that for a two pole machine, i.e. with $p = 1$, this particular solution can not be used to solve the fundamental space harmonic component, i.e. for $m = 1$.

Substituting B'_{rem} for B_{rem} in (3.64) gives

$$\frac{\partial^2 A_{z|PM}}{\partial r^2} + \frac{1}{r}\frac{\partial A_{z|PM}}{\partial r} + \frac{1}{r^2}\frac{\partial^2 A_{z|PM}}{\partial \phi^2} = \frac{4pr_{cm}B_{rem}}{\pi r^2}\sum_{m=1,3,5,\ldots}^{\infty}\cos mp\beta\cos mp\phi \tag{3.75}$$

Again we choose a particular solution,

$$A_{z,part|PM}(r,\phi) = \sum_{m=1,3,5,\ldots}^{\infty} G_{m|PM}\cos mp\phi\ . \tag{3.76}$$

Then by calculating the LHS of (3.75),

$$\frac{\partial A_{z|PM}}{\partial r} = 0\ , \tag{3.77}$$

$$\frac{\partial^2 A_{z|PM}}{\partial r^2} = 0\ , \tag{3.78}$$

$$\frac{\partial A_{z|PM}}{\partial \phi} = -\sum_{m=1,3,5,\ldots}^{\infty} mpG_{m|PM}\sin mp\phi \text{ and} \tag{3.79}$$

$$\frac{\partial^2 A_{z|PM}}{\partial \phi^2} = -\sum_{m=1,3,5,\ldots}^{\infty}(mp)^2 G_{m|PM}\cos mp\phi\ , \tag{3.80}$$

and substituting it back into (3.75), results in

$$G_{m|PM} = -\frac{4r_{cm}B_{rem}\cos mp\beta}{m^2 p\pi}\ . \tag{3.81}$$

which is valid for all $m \geq 0$.

3.8 Boundary Conditions Between the different Regions

In order to solve $C_{m|PM}$ and $D_{m|PM}$ for the different regions, we need to know how the $\vec{\mathbf{B}}$ and $\vec{\mathbf{H}}$ vector field would behave across the boundaries between the different regions, as graphically depicted in Appendix C.

3.8.1 The Magnetic Flux-density at the Boundary Between the different Regions

From the definition of the magnetic flux-density, (3.19), in the cylindrical coordinate system,

$$\vec{\mathbf{B}} = \boldsymbol{\nabla}\times\vec{\mathbf{A}} \tag{3.82}$$

$$= \frac{1}{r}\begin{vmatrix} \vec{\mathbf{a}}_r & r\vec{\mathbf{a}}_\phi & \vec{\mathbf{a}}_z \\ \frac{\partial}{\partial r} & \frac{\partial}{\partial \phi} & \frac{\partial}{\partial z} \\ A_r & rA_\phi & A_{z|PM} \end{vmatrix} \tag{3.83}$$

$$= \frac{1}{r}\left(\frac{\partial A_{z|PM}}{\partial \phi} - r\frac{\partial A_\phi}{\partial z}\right)\vec{\mathbf{a}}_r + \left(\frac{\partial A_r}{\partial z} - \frac{\partial A_{z|PM}}{\partial r}\right)\vec{\mathbf{a}}_\phi + \frac{1}{r}\left(\frac{\partial (rA_\phi)}{\partial r} - \frac{\partial A_r}{\partial \phi}\right)\vec{\mathbf{a}}_z\ . \tag{3.84}$$

For 2-D analysis (with $J_r = J_\phi = 0$) the above equation reduces to

$$\vec{\mathbf{B}} = \frac{1}{r}\frac{\partial A_{z|PM}}{\partial \phi}\vec{\mathbf{a}}_r - \frac{\partial A_{z|PM}}{\partial r}\vec{\mathbf{a}}_\phi \tag{3.85}$$

$$= B_r\vec{\mathbf{a}}_r + B_{\phi|PM}\vec{\mathbf{a}}_\phi\ . . \tag{3.86}$$

Thus for a concentric circular boundary between regions, say, (v) and $(v+1)$,

$$B_{r|PM}^{(v)} = B_{r|PM}^{(v+1)} \tag{3.87}$$

$$\frac{\partial A_{z|PM}^{(v)}}{\partial \phi} = \frac{\partial A_{z|PM}^{(v+1)}}{\partial \phi} \tag{3.88}$$

3.8.2 The Magnetic Field Intensity at the Boundary Between the different Regions

From (3.9), for a linear isotropic non permanent magnet region,

$$\vec{\mathbf{H}} = \frac{\vec{\mathbf{B}}}{\mu}\,, \tag{3.89}$$

and from (3.18), for a linear isotropic permanent magnet region,

$$\vec{\mathbf{H}} = \frac{(\vec{\mathbf{B}} - \vec{\mathbf{B}}_{rem})}{\mu}\,. \tag{3.90}$$

Thus from (3.71) and (3.86) on a boundary between a non permanent magnet region, say, (v) and a permanent magnet region, say, $(v+1)$,

$$H_{\phi|PM}^{(v)} = H_{\phi|PM}^{(v+1)} \tag{3.91}$$

$$\frac{B_{\phi|PM}^{(v)}}{\mu^{(v)}} = \frac{B_{\phi|PM}^{(v+1)}}{\mu^{(v+1)}} - \frac{B_{rem_\phi}}{\mu^{(v+1)}}\,. \tag{3.92}$$

With radially magnetised permanent magnets, the azimuthal component of $\vec{\mathbf{B}}_{rem}$ is zero, so that the above equation reduces to

$$-\frac{1}{\mu^{(v)}}\frac{\partial A_{z|PM}^{(v)}}{\partial r} = -\frac{1}{\mu^{(v+1)}}\frac{\partial A_{z|PM}^{(v+1)}}{\partial r}\,. \tag{3.93}$$

3.9 Solving the Magnetic Vector Potential for all the Regions of RFAPM machine

In the non permanent magnet regions, i.e. regions **I**, **III** and **V**, we have

$$A_{z|PM}(r,\phi) = A_{z_{|gen}}(r,\phi) \tag{3.94}$$

$$= \sum_{m=1,3,5,\ldots}^{\infty}(C_{m|PM}r^{mp} + D_{m|PM}r^{-mp})\cos mp\phi \tag{3.95}$$

so that

$$B_{r|PM}(r,\phi) = \frac{1}{r}\cdot\frac{\partial A_{z|PM}(r,\phi)}{\partial \phi} \tag{3.96}$$

$$= -\frac{1}{r}\cdot\sum_{m=1,3,5,\ldots}^{\infty} mp(C_{m|PM}r^{mp} + D_{m|PM}r^{-mp})\sin mp\phi \tag{3.97}$$

and

$$H_{\phi|PM}(r,\phi) = -\frac{1}{\mu}\cdot\frac{\partial A_{z|PM}(r,\phi)}{\partial r} \tag{3.98}$$

$$= -\frac{1}{\mu}\cdot\sum_{m=1,3,5,\ldots}^{\infty} mp(C_{m|PM}r^{mp-1} - D_{m|PM}r^{-mp-1})\cos mp\phi\,. \tag{3.99}$$

In the permanent magnet region, i.e. for regions **II** and **IV**, we have

$$A_{z|PM}(r,\phi) = A_{z_{|gen}}(r,\phi) + A_{z_{|part}}(r,\phi) \tag{3.100}$$

$$= \sum_{m=1,3,5,\ldots}^{\infty}(C_{m|PM}r^{mp} + D_{m|PM}r^{-mp})\cos mp\phi + \sum_{m=1,3,5,\ldots}^{\infty} G_{m|PM}\cos mp\phi \tag{3.101}$$

$$= \sum_{m=1,3,5,\ldots}^{\infty}(C_{m|PM}r^{mp} + D_{m|PM}r^{-mp} + G_{m|PM})\cos mp\phi \tag{3.102}$$

so that

$$B_{r|PM}(r,\phi) = \frac{1}{r}\cdot\frac{\partial A_{z|PM}(r,\phi)}{\partial \phi} \tag{3.103}$$

$$= -\frac{1}{r}\cdot\sum_{m=1,3,5,\ldots}^{\infty} mp(C_{m|PM}r^{mp} + D_{m|PM}r^{-mp} + G_{m|PM})\sin mp\phi \tag{3.104}$$

and

$$H_{\phi|PM}(r,\phi) = -\frac{1}{\mu}\cdot\frac{\partial A_{z|PM}(r,\phi)}{\partial r} \tag{3.105}$$

$$= -\frac{1}{\mu}\cdot\sum_{m=1,3,5,\ldots}^{\infty} mp(C_{m|PM}r^{mp-1} - D_{m|PM}r^{-mp-1})\cos mp\phi\,. \tag{3.106}$$

3.9.1 On the Inner Boundary of Region I

With $r = r_n - \frac{h}{2} - \ell_g - h_m - h_y$,

$$A^I_{z|PM}(r,\phi) = 0 \tag{3.107}$$

$$\therefore \quad C^I_{m|PM}r^{mp} + D^I_{m|PM}r^{-mp} = 0\,. \tag{3.108}$$

3.9.2 On the Boundary Between Region I and II

With $r = r_n - \frac{h}{2} - \ell_g - h_m$,

$$B^I_r(r,\phi) = B^{II}_r(r,\phi) \tag{3.109}$$

$$\therefore \quad C^I_{m|PM}r^{mp} + D^I_{m|PM}r^{-mp} = C^{II}_{m|PM}r^{mp} + D^{II}_{m|PM}r^{-mp} + G^{II}_{m|PM} \tag{3.110}$$

and

$$H^I_\phi(r,\phi) = H^{II}_\phi(r,\phi) \tag{3.111}$$

$$\therefore \quad \frac{C^I_{m|PM}r^{mp-1} - D^I_{m|PM}r^{-mp-1}}{\mu^I} = \frac{C^{II}_{m|PM}r^{mp-1} - D^{II}_{m|PM}r^{-mp-1}}{\mu^{II}}\,. \tag{3.112}$$

3.9.3 On the Boundary Between Region II and III

With $r = r_n - \frac{h}{2} - \ell_g$,

$$B_r^{II}(r,\phi) = B_r^{III}(r,\phi) \tag{3.113}$$

$$\therefore \quad C_{m|PM}^{II} r^{mp} + D_{m|PM}^{II} r^{-mp} + G_{m|PM}^{II} = C_{m|PM}^{III} r^{mp} + D_{m|PM}^{III} r^{-mp} \tag{3.114}$$

and

$$H_\phi^{II}(r,\phi) = H_\phi^{III}(r,\phi) \tag{3.115}$$

$$\therefore \quad \frac{C_{m|PM}^{II} r^{mp-1} - D_{m|PM}^{II} r^{-mp-1}}{\mu^{II}} = \frac{C_{m|PM}^{III} r^{mp-1} - D_{m|PM}^{III} r^{-mp-1}}{\mu^{III}} \tag{3.116}$$

3.9.4 On the Boundary Between Region III and IV

With $r = r_n + \frac{h}{2} + \ell_g$,

$$B_r^{III}(r,\phi) = B_r^{IV}(r,\phi) \tag{3.117}$$

$$\therefore \quad C_{m|PM}^{III} r^{mp} + D_{m|PM}^{III} r^{-mp} = C_{m|PM}^{IV} r^{mp} + D_{m|PM}^{IV} r^{-mp} + G_{m|PM}^{IV} \tag{3.118}$$

and

$$H_\phi^{III}(r,\phi) = H_\phi^{IV}(r,\phi) \tag{3.119}$$

$$\therefore \quad \frac{C_{m|PM}^{III} r^{mp-1} - D_{m|PM}^{III} r^{-mp-1}}{\mu^{III}} = \frac{C_{m|PM}^{IV} r^{mp-1} - D_{m|PM}^{IV} r^{-mp-1}}{\mu^{IV}} \tag{3.120}$$

3.9.5 On the Boundary Between Region IV and V

With $r = r_n + \frac{h}{2} + \ell_g + h_m$,

$$B_r^{IV}(r,\phi) = B_r^{V}(r,\phi) \tag{3.121}$$

$$\therefore \quad C_{m|PM}^{IV} r^{mp} + D_{m|PM}^{IV} r^{-mp} + G_{m|PM}^{IV} = C_{m|PM}^{V} r^{mp} + D_{m|PM}^{V} r^{-mp} \tag{3.122}$$

and

$$H_\phi^{IV}(r,\phi) = H_\phi^{V}(r,\phi) \tag{3.123}$$

$$\frac{C_{m|PM}^{IV} r^{mp-1} - D_{m|PM}^{IV} r^{-mp-1}}{\mu^{IV}} = \frac{C_{m|PM}^{V} r^{mp-1} - D_{m|PM}^{V} r^{-mp-1}}{\mu^{V}} \tag{3.124}$$

3.9.6 On the Outer Boundary of Region V

With $r = r_n + \frac{h}{2} + \ell_g + h_m + h_y$,

$$A_{z|PM}^{V}(r,\phi) = 0 \tag{3.125}$$

$$\therefore \quad C_{m|PM}^{V} r^{mp} + D_{m|PM}^{V} r^{-mp} = 0 \tag{3.126}$$

3.9.7 The Simultaneous Equations in order to solve the Magnetic Vector Potential and the Magnetic Flux-density

From (3.108), (3.110), (3.112), (3.114), (3.116), (3.118), (3.120), (3.122), (3.124) and (3.126) the following ten equations have to be solved for $m = 1, 3, 5, \rightarrow \infty$,

$$C^{I}_{m|PM} r_i^{mp} + D^{I}_{m|PM} r_i^{-mp} = 0 \tag{3.127}$$

$$C^{I}_{m|PM} r_{ii}^{mp} + D^{I}_{m|PM} r_{ii}^{-mp} - C^{II}_{m|PM} r_{ii}^{mp} - D^{II}_{m|PM} r_{ii}^{-mp} = G^{II}_{m|PM} \tag{3.128}$$

$$\mu^{II} C^{I}_{m|PM} r_{ii}^{mp-1} - \mu^{II} D^{I}_{m|PM} r_{ii}^{-mp-1} - \mu^{I} C^{II}_{m|PM} r_{ii}^{mp-1} + \mu^{I} D^{II}_{m|PM} r_{ii}^{-mp-1} = 0 \tag{3.129}$$

$$C^{II}_{m|PM} r_{iii}^{mp} + D^{II}_{m|PM} r_{iii}^{-mp} - C^{III}_{m|PM} r_{iii}^{mp} - D^{III}_{m|PM} r_{iii}^{-mp} = -G^{II}_{m|PM} \tag{3.130}$$

$$\mu^{III} C^{II}_{m|PM} r_{iii}^{mp-1} - \mu^{III} D^{II}_{m|PM} r_{iii}^{-mp-1} - \mu^{II} C^{III}_{m|PM} r_{iii}^{mp-1} + \mu^{II} D^{III}_{m|PM} r_{iii}^{-mp-1} = 0 \tag{3.131}$$

$$C^{III}_{m|PM} r_{iv}^{mp} + D^{III}_{m|PM} r_{iv}^{-mp} - C^{IV}_{m|PM} r_{iv}^{mp} - D^{IV}_{m|PM} r_{iv}^{-mp} = G^{IV}_{m|PM} \tag{3.132}$$

$$\mu^{IV} C^{III}_{m|PM} r_{iv}^{mp-1} - \mu^{IV} D^{III}_{m|PM} r_{iv}^{-mp-1} - \mu^{III} C^{IV}_{m|PM} r_{iv}^{mp-1} + \mu^{III} D^{IV}_{m|PM} r_{iv}^{-mp-1} = 0 \tag{3.133}$$

$$C^{IV}_{m|PM} r_{v}^{mp} + D^{IV}_{m|PM} r_{v}^{-mp} - C^{V}_{m|PM} r_{v}^{mp} - D^{V}_{m|PM} r_{v}^{-mp} = -G^{IV}_{m|PM} \tag{3.134}$$

$$\mu^{V} C^{IV}_{m|PM} r_{v}^{mp-1} - \mu^{V} D^{IV}_{m|PM} r_{v}^{-mp-1} - \mu^{IV} C^{V}_{m|PM} r_{v}^{mp-1} + \mu^{IV} D^{V}_{m|PM} r_{v}^{-mp-1} = 0 \tag{3.135}$$

$$C^{V}_{m|PM} r_{vi}^{mp} + D^{V}_{m|PM} r_{vi}^{-mp} = 0 \tag{3.136}$$

with

$$r_i = r_n - \frac{h}{2} - \ell_g - h_m - h_y \tag{3.137}$$

$$r_{ii} = r_n - \frac{h}{2} - \ell_g - h_m \tag{3.138}$$

$$r_{iii} = r_n - \frac{h}{2} - \ell_g \tag{3.139}$$

$$r_{iv} = r_n + \frac{h}{2} + \ell_g \tag{3.140}$$

$$r_v = r_n + \frac{h}{2} + \ell_g + h_m \tag{3.141}$$

$$r_{vi} = r_n + \frac{h}{2} + \ell_g + h_m + h_y \tag{3.142}$$

and

$$G^{II}_{m|PM} = -\frac{4(r_n - \frac{h}{2} - \ell_g - \frac{h_m}{2}) B_{rem} \cos m\beta}{m^2 \pi} \tag{3.143}$$

$$G^{IV}_{m|PM} = -\frac{4(r_n + \frac{h}{2} + \ell_g + \frac{h_m}{2}) B_{rem} \cos m\beta}{m^2 \pi} \tag{3.144}$$

By writing equations (3.127) to (3.136) in matrix format, it allows us to solve the $C_{m|PM}$ and $D_{m|PM}$ coefficients for the different regions, for the different values of m, much simpler, as shown in (3.145).

$$
\begin{bmatrix}
r_i^{mp} & r_i^{-mp} & 0 & 0 & 0 & 0 & 0 & 0 & 0 & 0 \\
r_{ii}^{mp} & r_{ii}^{-mp} & -r_{ii}^{mp} & -r_{ii}^{-mp} & 0 & 0 & 0 & 0 & 0 & 0 \\
\mu^{II} r_{ii}^{mp-1} & -\mu^{II} r_{ii}^{-mp-1} & -\mu^{I} r_{ii}^{mp-1} & \mu^{I} r_{ii}^{-mp-1} & 0 & 0 & 0 & 0 & 0 & 0 \\
0 & 0 & r_{iii}^{mp} & r_{iii}^{-mp} & -r_{iii}^{mp} & -r_{iii}^{-mp} & 0 & 0 & 0 & 0 \\
0 & 0 & \mu^{III} r_{iii}^{mp-1} & -\mu^{III} r_{iii}^{-mp-1} & -\mu^{II} r_{iii}^{mp-1} & \mu^{II} r_{iii}^{-mp-1} & 0 & 0 & 0 & 0 \\
0 & 0 & 0 & 0 & r_{iv}^{mp} & r_{iv}^{-mp} & -r_{iv}^{mp} & -r_{iv}^{-mp} & 0 & 0 \\
0 & 0 & 0 & 0 & \mu^{IV} r_{iv}^{mp-1} & -\mu^{IV} r_{iv}^{-mp-1} & -\mu^{III} r_{iv}^{mp-1} & \mu^{III} r_{iv}^{-mp-1} & 0 & 0 \\
0 & 0 & 0 & 0 & 0 & 0 & r_v^{mp} & r_v^{-mp} & -r_v^{mp} & -r_v^{-mp} \\
0 & 0 & 0 & 0 & 0 & 0 & \mu^{V} r_v^{mp-1} & -\mu^{V} r_v^{-mp-1} & -\mu^{IV} r_{vi}^{mp} & \mu^{IV} r_{vi}^{-mp} \\
0 & 0 & 0 & 0 & 0 & 0 & 0 & 0 & r_{vi}^{mp} & r_{vi}^{-mp}
\end{bmatrix}
\cdot
\begin{bmatrix}
C_{m|PM}^{I} \\ D_{m|PM}^{I} \\ C_{m|PM}^{II} \\ D_{m|PM}^{II} \\ C_{m|PM}^{III} \\ D_{m|PM}^{III} \\ C_{m|PM}^{IV} \\ D_{m|PM}^{IV} \\ C_{m|PM}^{V} \\ D_{m|PM}^{V}
\end{bmatrix}
=
\begin{bmatrix}
0 \\ G_{m|PM}^{II} \\ 0 \\ -G_{m|PM}^{II} \\ 0 \\ G_{m|PM}^{IV} \\ 0 \\ -G_{m|PM}^{IV} \\ 0 \\ 0
\end{bmatrix}
\tag{3.145}
$$

3.10 Obtaining the Final Solution of the Magnetic Vector Potential and the Magnetic Flux-density

3.10.1 The Magnetic Vector Potential Solution

The solution of the magnetic vector potential for the whole machine can be obtained by substituting the appropriate values of $C_{m|PM}$ and $D_{m|PM}$ as obtained in (3.145) into (3.95) and (3.102) for the different regions.

$$A_{z|PM}(r,\phi) = \begin{cases} \sum_{m=1,3,5,\ldots}^{\infty} (C^{I}_{m|PM} r^{mp} + D^{I}_{m|PM} r^{-mp}) \cos mp\phi & \text{for Region I} \\ \sum_{m=1,3,5,\ldots}^{\infty} (C^{II}_{m|PM} r^{mp} + D^{II}_{m|PM} r^{-mp} + G^{II}_{m|PM}) \cos mp\phi & \text{for Region II} \\ \sum_{m=1,3,5,\ldots}^{\infty} (C^{III}_{m|PM} r^{mp} + D^{III}_{m|PM} r^{-mp}) \cos mp\phi & \text{for Region III} \\ \sum_{m=1,3,5,\ldots}^{\infty} (C^{IV}_{m|PM} r^{mp} + D^{IV}_{m|PM} r^{-mp} + G^{IV}_{m|PM}) \cos mp\phi & \text{for Region IV} \\ \sum_{m=1,3,5,\ldots}^{\infty} (C^{V}_{m|PM} r^{mp} + D^{V}_{m|PM} r^{-mp}) \cos mp\phi & \text{for Region V} \end{cases} \tag{3.146}$$

3.10.2 The Magnetic Flux-Density Solution

To obtain the solution of the magnetic flux-density for the whole machine is a little bit more difficult. The first step is to obtain the solution for the radial component of the magnetic flux-density. This is done by substituting the appropriate values of $C_{m|PM}$ and $D_{m|PM}$ from (3.145) into (3.97) and (3.104) for the different regions.

$$B_{r|PM}(r,\phi) = \begin{cases} -\frac{1}{r} \cdot \sum_{m=1,3,5,\ldots}^{\infty} mp(C^{I}_{m|PM} r^{mp} + D^{I}_{m|PM} r^{-mp}) \sin mp\phi & \text{for Region I} \\ -\frac{1}{r} \cdot \sum_{m=1,3,5,\ldots}^{\infty} mp(C^{II}_{m|PM} r^{mp} + D^{II}_{m|PM} r^{-mp} + G^{II}_{m|PM}) \sin mp\phi & \text{for Region II} \\ -\frac{1}{r} \cdot \sum_{m=1,3,5,\ldots}^{\infty} mp(C^{III}_{m|PM} r^{mp} + D^{III}_{m|PM} r^{-mp}) \sin mp\phi & \text{for Region III} \\ -\frac{1}{r} \cdot \sum_{m=1,3,5,\ldots}^{\infty} mp(C^{IV}_{m|PM} r^{mp} + D^{IV}_{m|PM} r^{-mp} + G^{IV}_{m|PM}) \sin mp\phi & \text{for Region IV} \\ -\frac{1}{r} \cdot \sum_{m=1,3,5,\ldots}^{\infty} mp(C^{V}_{m|PM} r^{mp} + D^{V}_{m|PM} r^{-mp}) \sin mp\phi & \text{for Region V} \end{cases} \tag{3.147}$$

The next step is to obtain the solution for the azimuthal component of the magnetic flux-density. This is done by once again using the linear relationship between B and H (i.e. $B = \mu H$) and then substituting the appropriate values of $C_{m|PM}$ and $D_{m|PM}$ from (3.145) into (3.99) and (3.106) for the different regions.

$$B_{\phi|PM}(r,\phi) = \begin{cases} -\sum_{m=1,3,5,\ldots}^{\infty} mp(C^{I}_{m|PM} r^{mp-1} - D^{I}_{m|PM} r^{-mp-1}) \cos mp\phi & \text{for Region I} \\ -\sum_{m=1,3,5,\ldots}^{\infty} mp(C^{II}_{m|PM} r^{mp-1} - D^{II}_{m|PM} r^{-mp-1}) \cos mp\phi & \text{for Region II} \\ -\sum_{m=1,3,5,\ldots}^{\infty} mp(C^{III}_{m|PM} r^{mp-1} - D^{III}_{m|PM} r^{-mp-1}) \cos mp\phi & \text{for Region III} \\ -\sum_{m=1,3,5,\ldots}^{\infty} mp(C^{IV}_{m|PM} r^{mp-1} - D^{IV}_{m|PM} r^{-mp-1}) \cos mp\phi & \text{for Region IV} \\ -\sum_{m=1,3,5,\ldots}^{\infty} mp(C^{V}_{m|PM} r^{mp-1} - D^{V}_{m|PM} r^{-mp-1}) \cos mp\phi & \text{for Region V} \end{cases} \quad (3.148)$$

From (3.147) and (3.148) the magnitude of the B can now be obtained as

$$B_{|PM}(r,\phi) = \sqrt{B^2_{r|PM}(r,\phi) + B^2_{\phi|PM}(r,\phi)}\,, \quad (3.149)$$

from which the flux-density contour plot can be obtained as will be shown in the next section.

3.11 Validation of the Magnetic Vector Potential and the Magnetic Flux-density Solutions

In order to test the validity of the analytical solution presented above, the analytical solution was benchmarked against a Finite Element Analysis (FEA) solution using Ansoft's Maxwell® 2D. The benchmarking was performed on the test machine data given in section E.1 of Appendix E.

3.11.1 The Magnetic Vector Potential and the Magnetic Flux-density Contour Plots

A *Matplotlib*, see Hunter [42], contour plot of the analytical solution to the magnetic vector potential solution is shown in Figure 3.5 with the contour plot of the FEA solution using Maxwell® 2D, shown in Figure 3.6. The "filled" or "shaded" contour plots of the magnetic flux-density for the analytical and FEA solutions are shown in Figure 3.7 and 3.8 respectively. The contour plot of the magnetic flux-density for the analytical solution was again done using *Matplotlib* whilst the contour plot of the magnetic flux-density for the FEA solution was obtained directly from Maxwell® 2D.

3.11.2 Radial and Azimuthal Magnetic Flux-density Distribution

It is clearly evident that it is extremely difficult to compare the analytical and FE solutions from the *Matplotlib* and Maxwell® 2D contour plots. In Figure 3.5, the contour plot's scale varies between -12 and +12 mWb/m were as the scale on the contour plot generated by Maxwell® 2D in Figure 3.6 varies between $-13{,}26$ and 13,22 mWb/m. This is even worse for the magnetic flux-density plots. In Figure 3.7 the *Matplotlib* contour plot's scale varies between 0 and $\approx$2,88 T were as the scale on the contour plot generated by Maxwell® 2D in Figure 3.8 varies between ≈ 0 and 1,936 T.

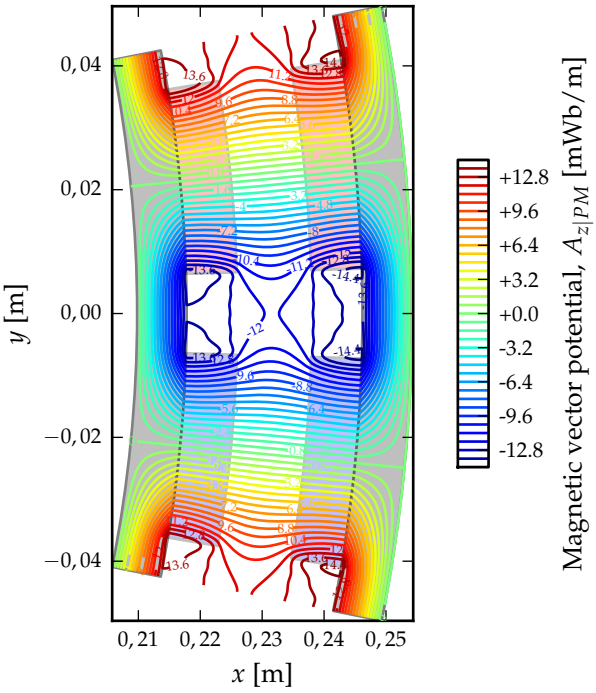

Figure 3.5: Contour plot of the magnetic vector potential obtained analytically.

From the contour plots of the magnetic flux-density, it appears that there is a huge discrepancy in the analytical and FE solutions, especially with regard to the flux-density in the rotor yokes. The higher values of flux-density in the rotor yoke is produced by the analytical solution is due to fact that for the analytical solution a linear relationship between the magnetic

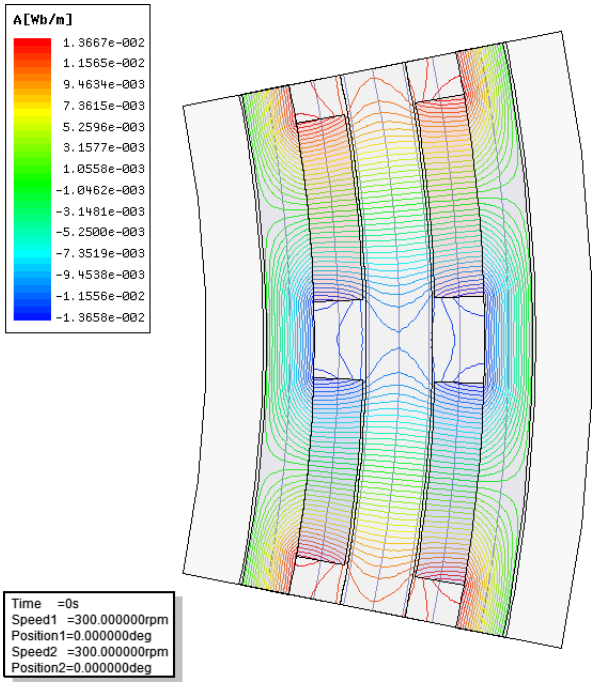

Figure 3.6: Contour plot of the magnetic vector potential simulated in Maxwell® 2D.

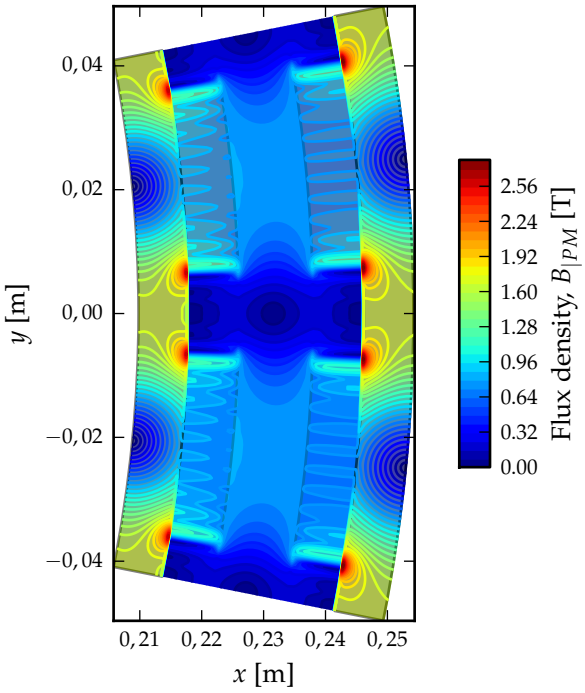

Figure 3.7: Contour plot of the magnetic flux-density obtained analytically.

field intensity, H, and the magnetic field density, B, is assumed. For the FE solution, the actual, non-linear, B–H relationship is used. For our analytical analysis of the RFAPM machine with regard to the induced voltage and torque generated, we are however more interested in the flux-density in the airgap, than in the rotor yokes.

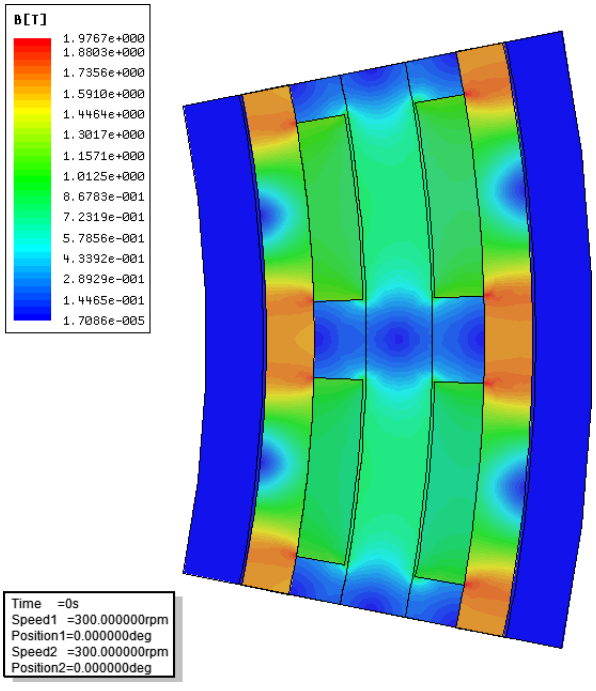

Figure 3.8: Contour plot of the magnetic flux-density simulated in Maxwell® 2D.

If we were to consider only the flux-density in the centre of the airgap, (3.147) and (3.148) reduces to

$$B_{r|PM}(r_n,\phi) = -\frac{1}{r_n}\cdot\sum_{m=1,3,5,\ldots}^{\infty} mp(C^{III}_{m|PM}r_n^{mp} + D^{III}_{m|PM}r_n^{-mp})\sin mp\phi \tag{3.150}$$

and

$$B_{\phi|PM}(r_n,\phi) = -\sum_{m=1,3,5,\ldots}^{\infty} mp(C^{III}_{m|PM}r_n^{mp-1} - D^{III}_{m|PM}r_n^{-mp-1})\cos mp\phi \tag{3.151}$$

for the radial and azimuthal components of the magnetic flux-density respectively.

If we now compare the analytical solution with the FE solution produced by Maxwell® 2D for the radial and azimuthal components of the magnetic flux-density, we can see that the solutions are matching closely as shown in Figures 3.9 and 3.10 respectively, using *Matplotlib*. Also shown in in Figure 3.9 and 3.10 are the radial and azimuthal components of the magnetic flux-density in the centre of the both the inner – and outer magnets. The Fourier series expansion of the analytical solution is only done up to the 27^{th} harmonic. The lack of higher order harmonics is evident in Figure 3.9 which clearly shows that the analytical solution is finding it difficult to track the large step changes in the radial flux-density distribution in the permanent magnets.

An interesting observation, is the computational "noisiness" of the FE solution for the azimuthal flux-density distribution as shown in Figure 3.10. This most probably has to do with the mesh density on the "line" on which the azimuthal flux-density distribution was calculated. With close-up scrutiny of Figure 3.9, the FE solution's segmentation of the radial flux-density distribution in the centre of the stator can also be observed, due to the mesh density on the centreline of the stator.

3.11.3 2-D Analytical Analysis vs. 1-D Analytical Analysis

From Figure 3.9 it can be seen that the radial flux-density in the centre of the magnets (in a radial direction, i.e. at $-5{,}625\,^\circ$ and $5{,}625\,^\circ$) are almost exactly the same inside the airgap as it is inside the permanent magnet on either the inner rotor yoke or the outer rotor yoke. From the 2-D analytical calculations of Test Machine I (see Appendix E.1) as was done in section 3.9, the value of the flux-density inside the airgap, B_g, was calculated as 0,779 T with a fundamental component of 0,824 T.

The question arises, "Can we obtain the same result using simple equivalent magnetic circuit analysis?" A brief introduction to magnetic circuit analysis using permanent magnets is given in Appendix F, with the analysis of a RFAPM machine given in section F.7. In this analysis the assumption was made that fringing could be ignored, i.e. $B_m \approx B_g$, that the permeability of the iron yoke is infinity and that average flux path will be in the centre of the permanent magnets and in the centre of the iron yoke. From the equivalent magnetic circuit analysis, the flux-density inside the airgap, B_g, was calculated as 0,788 T which correlates very closely with the 2-D analysis results.

From this result it is however impossible to predict the exact shape of the flux-density distribution and hence to calculate the fundamental component of the flux-density distribution.

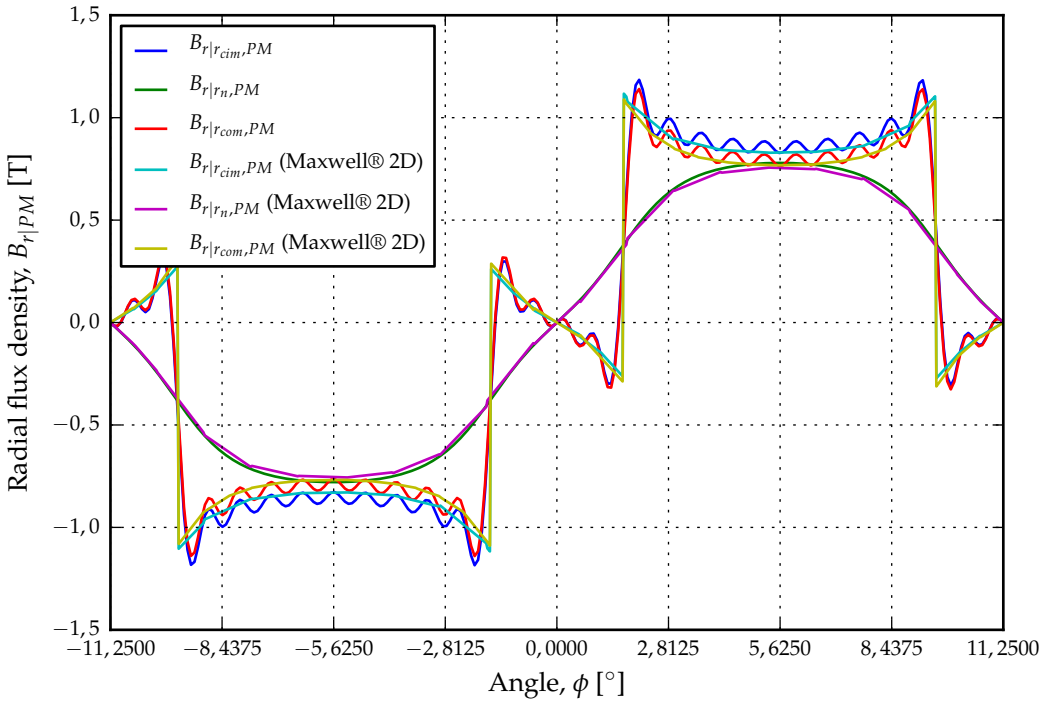

Figure 3.9: The radial flux-density distribution.

This is due to the fact that the 1-D approach of the equivalent magnetic circuit analysis does

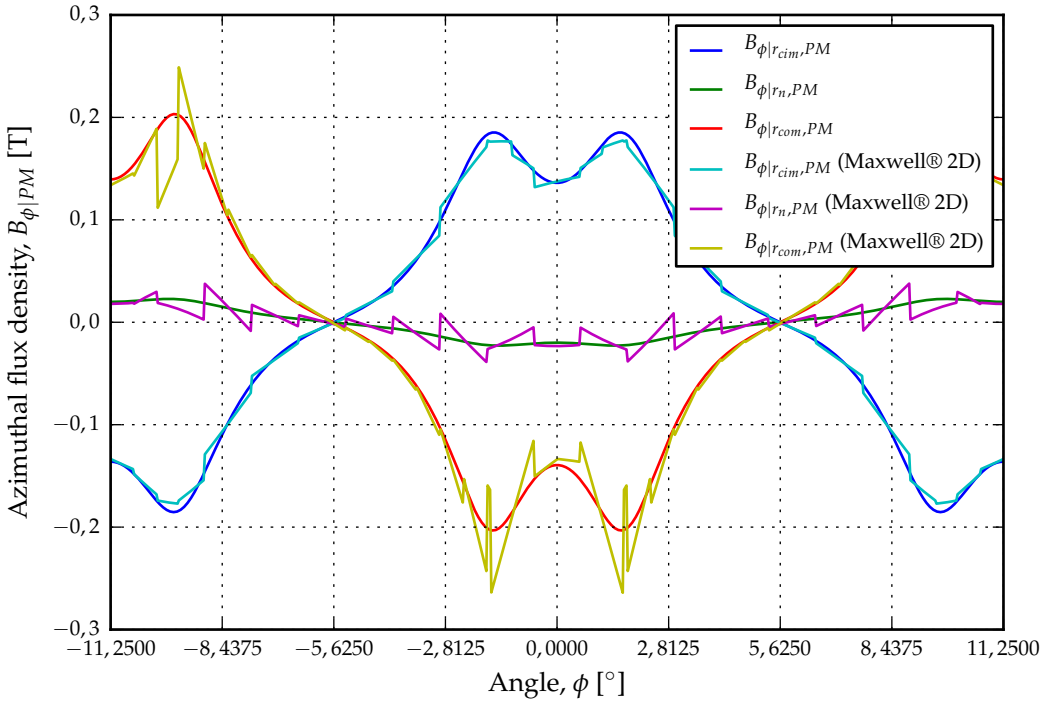

Figure 3.10: The azimuthal flux-density distribution.

not take any cognisance of the magnetic pole width.[1]

In Figure 3.11 the peak value of the radial flux-density and the associated peak value of the fundamental component as a function of k_m, the ration between the pole arc width and the pole pitch, is shown. It can be seen that although the value of the peak radial flux-density increases only slightly with an increase in pole width, the increase in the fundamental component is much larger.

Stegmann and Kamper [26] used the equivalent magnetic circuit analysis technique to calculate the yoke thickness of the rotor. The calculation is based on the assumption that the ratio of the flux-density in the poles and in the yoke is inversely proportional to the ratio of the pole width and yoke thickness, i.e.

$$\frac{B_m}{B_y} = \frac{h_y}{w_p} \tag{3.152}$$

$$= \frac{2ph_y}{\pi r_n k_m} \tag{3.153}$$

assuming that the area under the poles in the air gap is the same as in the magnets, so that the nominal radius, r_n, could be used in the calculation.

Thus from Appendix E.1, the flux-density in the centre of the rotor yoke for Test Machine I can be calculated as 1,55 T. If we however compare this with the results obtained either 2-D analytical analysis, or that obtained using Maxwell® 2D, Figure 3.12 shows that the flux-density in the yokes is not constant and vary from approximately 0,4 T directly behind the magnets to approximately 1,75 T between the magnets.

3.11.4 Harmonic Analysis of the Radial Flux-density

The shape of the radial flux-density, $B_{r|PM}$, distribution throughout the stator region is not completely sinusoidal as the distribution of the flux-density in the centre of the stator, $B_{r|,r_n,PM}$, i.e. at $r{=}r_n$ (see Figure 3.9). In Figure 3.13 the variation in the shape of $B_{r|PM}$ is shown at the outer surface –, $r = r_n + \frac{h}{2}$, the centre –, $r{=}r_n$ and the inner surface of the stator, $r = r_n - \frac{h}{2}$.

The harmonics present in the radial airgap flux-density can be obtained directly from (3.147) without the need to perform a FFT, by setting $r{=}r_n$ and substituting h for m, so that we can write,

$$B_{r,h|r_n,PM} = -\frac{hp}{r_n}(C^{III}_{h|PM} r_n^{hp} + D^{III}_{h|PM} r_n^{-hp}) \,. \tag{3.154}$$

The total harmonic distortion (THD) of the radial flux-density in the airgap can be calculated as follows:

$$\%\text{THD}_{B_{r|r=r_n,PM}} = \frac{\sqrt{\sum_{h=2}^{\infty} B_{r,h}^2}}{B_{r,1}} \times 100\% \tag{3.155}$$

By varying the width of the permanent magnets, the %THD of the radial flux-density can be reduced to such a level that the radial flux-density distribution could be regarded as quasi-sinusoidal. With the magnet width or pole embracing factor, $k_m = 0{,}687\,5$, the %THD reduces

[1] The flux-density values will be exactly the same, whether the magnetic poles span the entire pole pitch or only half the pole pitch.

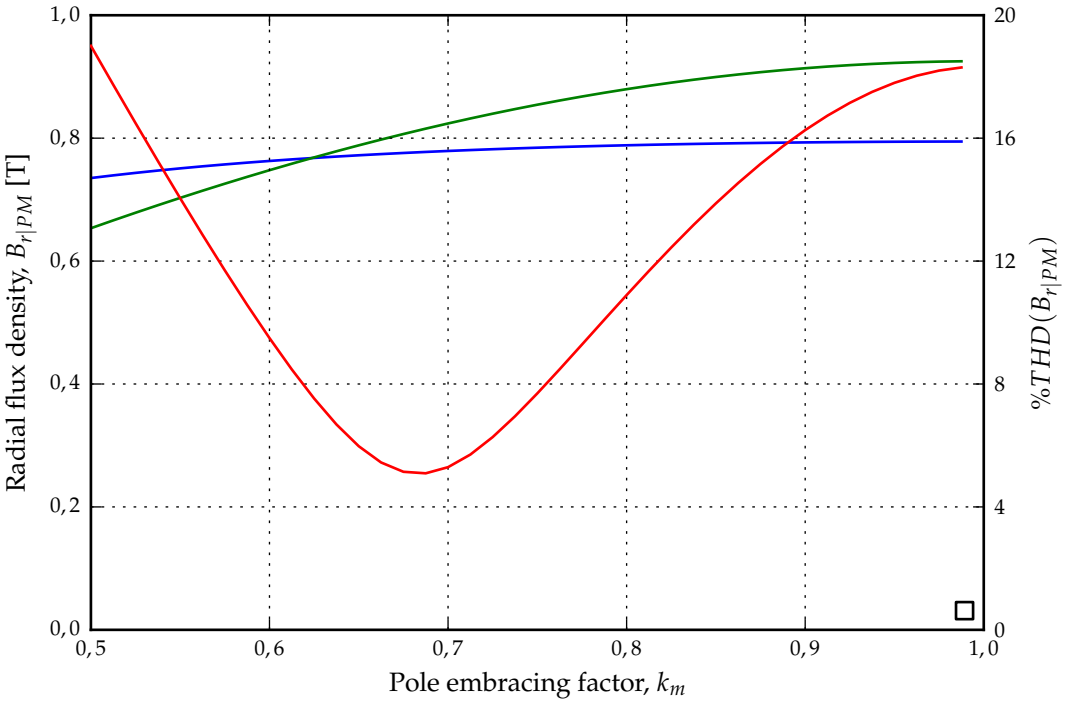

Figure 3.11: The magnitude, fundamental component and %THD of the radial flux-density in the centre of the stator vs. the pole embracing factor.

to its lowest value at just over 5 % as was shown in Figure 3.11 in the previous section, together

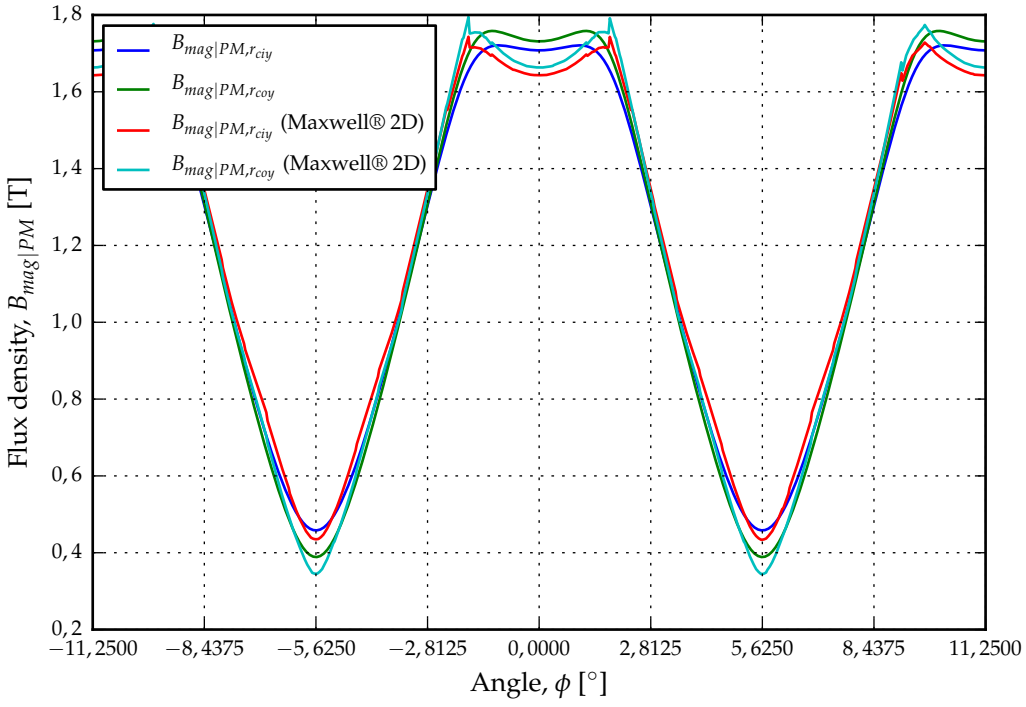

Figure 3.12: The variation in the flux-density in the centre of the rotor yokes.

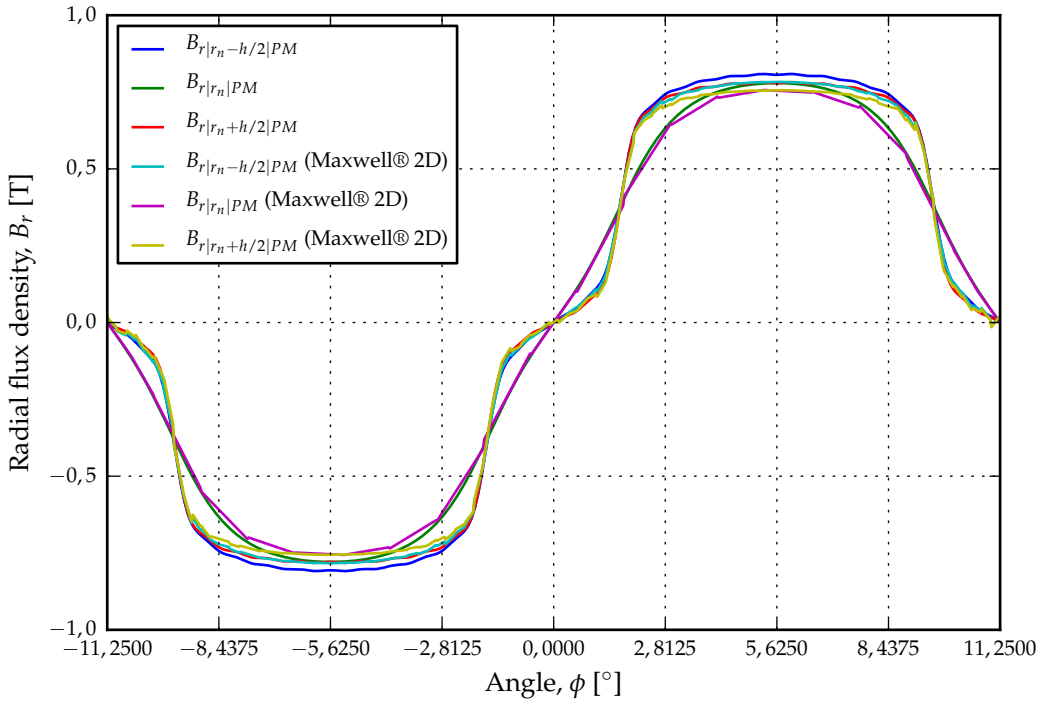

Figure 3.13: The variation in the shape radial flux-density distribution in the stator windings shown on the outer –, centre – and inner radius of the stator for the analytical analysis method compared the the FEA analysis done using Maxwell® 2D.

with the magnitude and fundamental component of the radial flux-density. It was thus decided that a $k_m \approx 0{,}7$ would be a good compromise between a slightly higher fundamental component of the radial flux-density, but still with a rather low %THD value of 5,3 %. This however also implies a slight increase in the cost[1] of the permanent magnet material used.

In Figure 3.14 the harmonic spectrum of the radial flux-density in the middle of the airgap with $k_m = 0{,}7$ is shown. The 5^{th} harmonic although small ($< 5\,\%$) is the most prominent, followed by the 3^{rd} and the 7^{th}.

If we compare this with the harmonic spectrum of radial flux-density as simulated using Maxwell® 2D also shown in Figure 3.14, we can see that it is almost identical, with the fundamental component slightly lower than that of the fundamental component which was analytically calculated. The fundamental component of the analytically calculated radial flux-density distribution were found to be only 3% higher than those of the FEM solution. The reason for this can be attributed to the saturation occurring in the rotor yoke which will result in a higher reluctance value, and hence a lower flux-density value. What is interesting however, is that the % THD is exactly the same for both at 5,3 %, implying that the shape of the flux-density distribution waveforms are similar.

[1] Although not the focus of this dissertation, it would be quite interesting to do an analysis of the trade off between the %THD of the radial flux-density, the cost of the permanent magnets and (say) the torque or torque ripple produced by the machine as a function of k_m. The analytical analysis method presented in the chapter would provide the ideal tool for such an analysis.

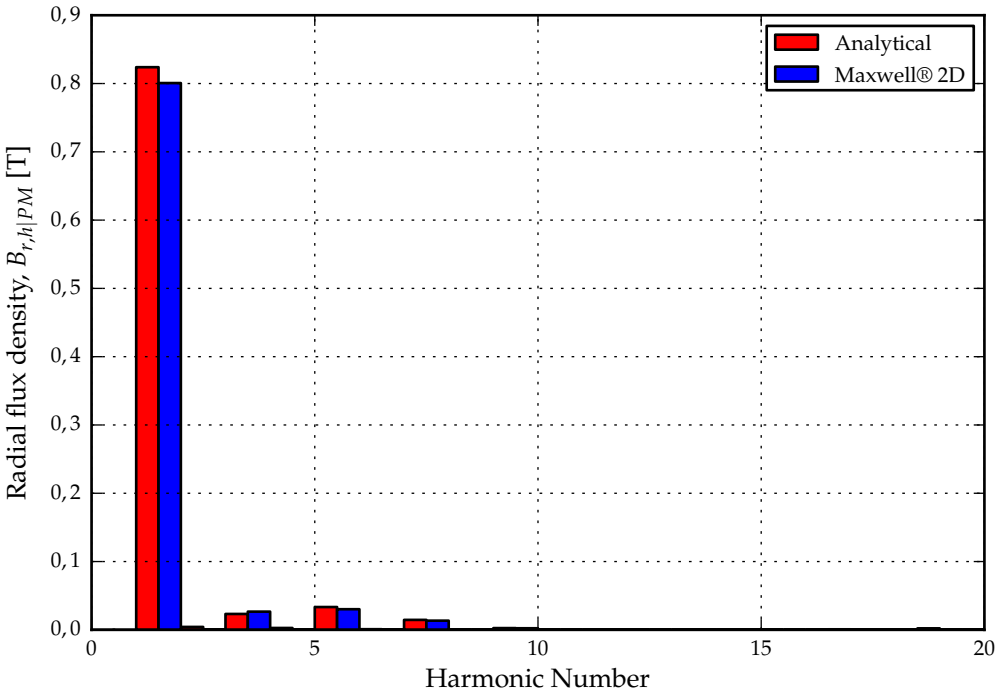

Figure 3.14: The harmonic spectrum of radial flux-density in the centre of the stator winding with $k_m = 0{,}7$.

3.12 The Flux-linkage Calculation for the different Winding Configurations

In Figure 3.15 a single turn of a RFAPM machine is shown. The flux-linkage of this single turn positioned at an arbitrary angle ϕ can be calculated as,

$$\lambda_{1|O,PM}(r,\phi) = \int_S \vec{\mathbf{B}} \cdot d\vec{\mathbf{s}} \tag{3.156}$$

$$= \int_S \boldsymbol{\nabla} \times \vec{\mathbf{A}}_{|PM} \cdot d\vec{\mathbf{s}} \,. \tag{3.157}$$

Applying Stokes' Integral Theorem to (3.157), this equation can be rewritten into a line integral form as,

$$\lambda_{1|O,PM}(r,\phi) = \oint_C \vec{\mathbf{A}}_{|PM} \cdot d\vec{\ell} \tag{3.158}$$

$$= \int_{C_{12}} \vec{\mathbf{A}}_{|PM} \cdot d\vec{\ell} + \int_{C_{23}} \vec{\mathbf{A}}_{|PM} \cdot d\vec{\ell} + \int_{C_{34}} \vec{\mathbf{A}}_{|PM} \cdot d\vec{\ell} + \int_{C_{41}} \vec{\mathbf{A}}_{|PM} \cdot d\vec{\ell} \,. \tag{3.159}$$

With $\vec{\mathbf{A}} = A_{z|PM}\vec{\mathbf{a}}_z$, the line integral reduces to

$$\lambda_{1|O,PM}(r,\phi) = \int_{C_{12}} \vec{\mathbf{A}}_{|PM} \cdot d\vec{\ell} + \int_{C_{34}} \vec{\mathbf{A}}_{|PM} \cdot d\vec{\ell} \tag{3.160}$$

$$= \ell \left(A_{z|PM}\left(r, \phi - \tfrac{\tau_q}{2}\right) - A_{z|PM}\left(r, \phi + \tfrac{\tau_q}{2}\right) \right) , \tag{3.161}$$

with

$$\int_{C_{23}} \vec{\mathbf{A}}_{|PM} \cdot d\vec{\ell} = \int_{C_{41}} \vec{\mathbf{A}}_{|PM} \cdot d\vec{\ell} = 0 \,. \tag{3.162}$$

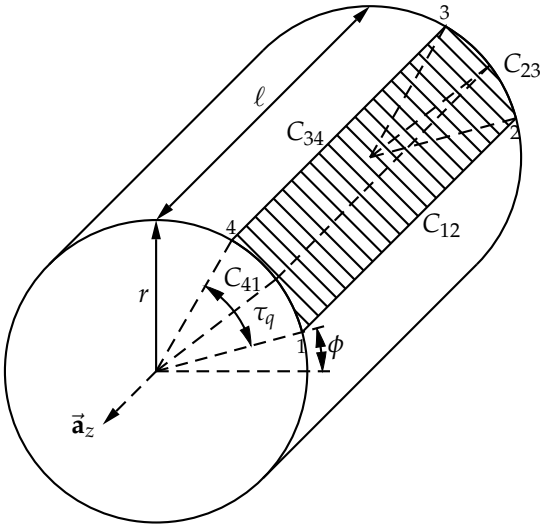

Figure 3.15: Flux-linkage of a single turn.

The maximum flux-linkage will occur when the centre of coils are aligned with the centre of the magnets, or more formally put, when the d-axis of the coil align with the d-axis of the magnets. This will result in

$$A_{z|PM}\left(r,\phi-\tfrac{\tau_q}{2}\right)=-A_{z|PM}\left(r,\phi+\tfrac{\tau_q}{2}\right) \tag{3.163}$$

which enables us to simplify the flux-linkage distribution, (3.161), to

$$\lambda_{1|O,PM}(r,\phi)=2\ell A_{z|PM}(r,\phi)\,. \tag{3.164}$$

3.12.1 The Flux-linkage Calulation for the Type O Winding Configuration

The maximum or peak value of the total flux-linkage per phase for the Type O winding configuration, can now be calculated by multiplying the flux-linkage distribution, (3.164) with the conductor density distribution, (2.26), then integrating over one resultant coil pitch period, and finally multiplying by the total number of series connected circuits[1], $\frac{q}{a}$.

The conductor density distribution that was deduced in section 2.3.2 is only a 1-D approximation in the azimuthal direction and assumes that all the conductors are situated in the centre of the winding, i.e. with $r{=}r_n$. This implies that we only need to use a 1-D representation of the flux-linkage distribution. This is done by setting $r{=}r_n$ in (3.164).

If a more accurate result needs to be obtained, we would have to redefine the conductor density distribution of (2.26) so that it is a 2-D distribution. This 2-D distribution will then have to be multiplied with the 2-D flux-linkage distribution of (3.164) and then integrated, not only over one resultant coil pitch in the azimuthal direction, but also over the entire height of the coil in the radial direction. Holm [24, chap. 5] however showed that the flux-linkage and the resulting back-EMF can be calculated quite accurately by only using the magnetic vector potential in the centre of the windings.

[1] As explained in Appendix A we don't have to divide by the number of parallel circuit as we assume that the current divides equally between the number of parallel branches

The peak value of the flux-linkage per phase, can thus be calculated as follows,

$$\Lambda_{a,b,c|O,PM} = \frac{q}{a}\int_{-\frac{1}{2}\tau_{q,res|O}}^{\frac{1}{2}\tau_{q,res|O}} n_{a|O}(\phi)\lambda_{1|O,PM}(r,\phi)d\phi \tag{3.165}$$

$$= \frac{2q\ell}{a}\int_{-\frac{1}{2}\tau_{q,res|O}}^{\frac{1}{2}\tau_{q,res|O}} n_{a|O}(\phi)A_{z|PM}(r_n,\phi)d\phi\ . \tag{3.166}$$

However, as was mentioned in the previous section, (3.166) and (3.164), this will only be true if the d-axis of the conductor density distribution, (2.26), is aligned with that of the permanent magnets. We therefore need to redefine (3.146) from a cosine series to a sine series in order to facilitate the alignment of the magnetic vector potential with that of the conductor density distribution, as defined in (2.26). We are also only interested in the solution of $A_{z|PM}$ in the stator region, i.e. region III. Furthermore, by substituting 'n' for 'm', we can write

$$A^{III}_{z|PM}(r_n,\phi) = \sum_{n=1}^{\infty} b^{III}_{n_{A_{z|PM}}}\sin(np\phi) \tag{3.167}$$

with

$$b^{III}_{n_{A_{z|PM}}} = a^{III}_{n_{A_{z|PM}}} \tag{3.168}$$

$$= C^{III}_{n|PM}r_n^{np} + D^{III}_{n|PM}r_n^{-np} \tag{3.169}$$

which allows us to write (3.166) as

$$\Lambda_{a,b,c|O,PM} = \frac{2q\ell}{a}\int_{-\frac{1}{2}\tau_{q,res|O}}^{\frac{1}{2}\tau_{q,res|O}} \sum_{m=1}^{\infty} b_{m_{n_{a|O}}}\sin(mq\phi)\sum_{n=1}^{\infty} b^{III}_{n_{A_{z|PM}}}\sin(np\phi)d\phi \tag{3.170}$$

$$= \frac{2q\ell}{a}\sum_{m=1}^{\infty}\sum_{n=1}^{\infty} b_{m_{n_{a|O}}}b^{III}_{n_{A_{z|PM}}}\int_{-\frac{1}{2}\tau_{q,res|O}}^{\frac{1}{2}\tau_{q,res|O}}\sin(mq\phi)\sin(np\phi)d\phi\ . \tag{3.171}$$

The integral term evaluates to zero except where $n = m$, where it evaluates to $\frac{\pi}{2q}$. This implies that (3.171) can be simplified to

$$\Lambda_{a,b,c|O,PM} = \frac{N\ell}{\pi a}\sum_{m=1}^{\infty} b_{m_{n_{a|O}}}b^{III}_{m_{A_{z|PM}}}\ , \tag{3.172}$$

or from (2.30) in terms of the winding factor as

$$\Lambda_{a,b,c|O,PM} = -\frac{2qN\ell}{a}\sum_{m=1}^{\infty} k_{w,m|O}b^{III}_{m_{A_{z|PM}}}\ . \tag{3.173}$$

With the rotor rotating at a constant speed of ω_{mech}, we can write,

$$\lambda_{a|O,PM}(t) = \Lambda_{a,b,c|O,PM}\cos\left(p\omega_{mech}t\right)\ , \tag{3.174}$$

$$\lambda_{b|O,PM}(t) = \Lambda_{a,b,c|O,PM}\cos\left(p\omega_{mech}t - \tfrac{2\pi}{3}\right)\ \text{and} \tag{3.175}$$

$$\lambda_{c|O,PM}(t) = \Lambda_{a,b,c|O,PM}\cos\left(p\omega_{mech}t - \tfrac{4\pi}{3}\right)\ . \tag{3.176}$$

The analytically calculated flux-linkages above is virtually identical to that obtain using FEA in Maxwell® 2D as shown in Figure 3.16. The problem however with (3.173), if we compare it to the more simpler (2.98), is that although the former equation is very accurate, it is

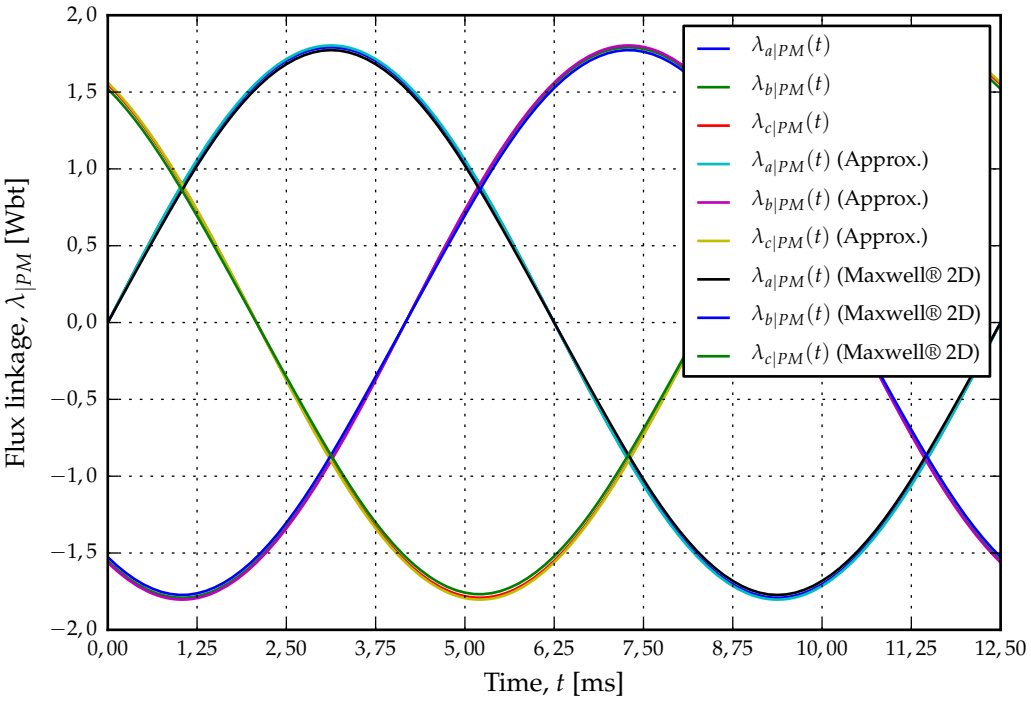

Figure 3.16: Comparison of the flux-linkage calculations for the Type O winding configuration.

not a simple – but computational intensive design equation. There also seem to be no relation between the two equations. There is also no clear evidence that (2.98) is indeed a good approximation of (3.173).

However on closer inspection, if we compare (3.169) with (3.146) and (3.147) and remembering (3.154) with $n = h$, we see that

$$\lambda_{a|O,PM}(r) = -\frac{2qN\ell}{a}\sum_{h=1}^{\infty} k_{w,h|O}\left(-\frac{rB_{r,h}}{hp}\right) \tag{3.177}$$

and if we are only interested in the peak fundamental component, i.e. with $h = 1$ and setting $r{=}r_n$, it allows us to express

$$\Lambda_{a,b,c|O,PM} \approx \frac{2r_n\ell N}{a} k_q k_{w,m=1|O} B_{r,1} \tag{3.178}$$

with

$$B_{r,1} = \hat{B}_{r_1} \tag{3.179}$$

which is identical to (2.24)

The approximated flux-linkage calculations are also shown in Figure 3.16 and correlate extremely well with the more accurate analytical calculation method.

3.12.2 The Flux-linkage Calculation for Type I Winding Configuration

The peak value of the flux-linkage for a Type I winding configuration can be calculated in exactly the same manner as was done in section 3.12.1 for the Type O winding configuration,

so that (3.171) becomes,

$$\Lambda_{a,b,c|I,PM} = \frac{2q\ell}{a}\sum_{m=1}^{\infty}\sum_{n=1}^{\infty} b_{m_{n|I}} b^{III}_{n_{A_{z|PM}}} \int_{-\frac{1}{2}\tau_{q,res|I}}^{\frac{1}{2}\tau_{q,res|I}} \sin(mq\phi)\sin(np\phi)d\phi \,. \tag{3.180}$$

With $\frac{q}{p}{=}k_q{=}\frac{1}{2}$, it implies that the integral in (3.180) will only evaluate to $\frac{\pi}{2q}$ when $n = 2m$, similar to that mentioned in section 2.4.2, but now including only the even harmonics. Thus, with (2.80) redefined to

$$b_{\ddot{m}_{n|I}} = -\frac{2qN}{\pi}\cdot k_{w,\ddot{m}|I} \tag{3.181}$$

and with

$$\ddot{m} = 2m \,. \tag{3.182}$$

(3.180) reduces to

$$\Lambda_{a,b,c|I,PM} = -\frac{2qN\ell}{a}\sum_{m=1}^{\infty} k_{w,\ddot{m}|I} b^{III}_{n_{A_{z|PM}}} \tag{3.183}$$

when

$$\ddot{m} = n \,. \tag{3.184}$$

Thus, with the rotor turning at a constant speed of ω_{mech}, the flux-linkage of each phase in terms of (3.183), can be written as

$$\lambda_{a|I,PM}(t) = \Lambda_{a,b,c|I,PM}\cos\left(p\omega_{mech}t\right) \,, \tag{3.185}$$

$$\lambda_{b|I,PM}(t) = \Lambda_{a,b,c|I,PM}\cos\left(p\omega_{mech}t - \tfrac{2\pi}{3}\right) \text{ and} \tag{3.186}$$

$$\lambda_{c|I,PM}(t) = \Lambda_{a,b,c|I,PM}\cos\left(p\omega_{mech}t - \tfrac{4\pi}{3}\right) \,. \tag{3.187}$$

The flux-linkages calculated above is again virtually identical to that obtain using FEA in Maxwell® 2D as shown in Figure 3.17.

Similar to equation (3.178), a good approximation of equation (3.183), when considering only the fundamental component of the radial flux-density, would be

$$\Lambda_{a,b,c|I,PM} \approx \frac{2r_n\ell N}{a} k_q k_{w,2|I} B_{r,1} \,, \tag{3.188}$$

with only the second harmonics of the winding factor being considered, as was discussed in section 2.4.2 and is shown in Figure 3.17.

3.12.3 The Flux-linkage Calculation for Type II Winding Configuration

Again, for a Type II winding configuration, the peak value of the total flux-linkage per phase can be calculated similarly to (3.183), so that,

$$\Lambda_{a,b,c|II,PM} = -\frac{2qN\ell}{a}\sum_{m=1}^{\infty} k_{w,\ddot{m}|II} b^{III}_{n_{A_{z|PM}}} \tag{3.189}$$

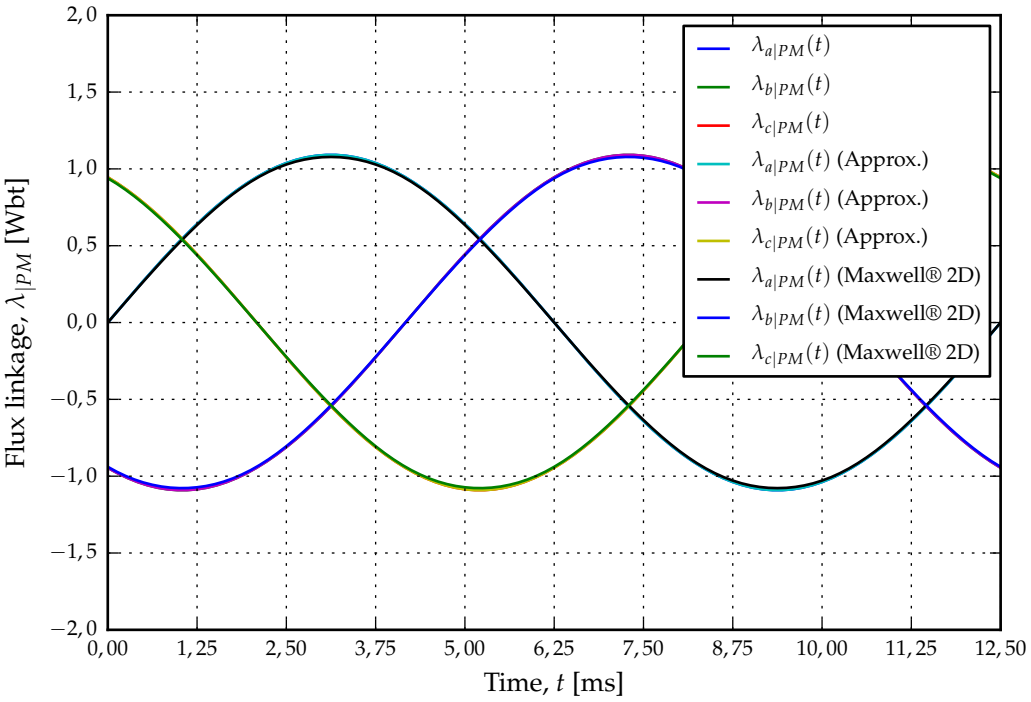

Figure 3.17: Comparison of the flux-linkage calculations for the Type I winding configuration.

and, assuming a constant rotor speed of ω_{mech}, it allows us to write the flux-linkages of each phase as

$$\lambda_{a|II,PM}(t) = \Lambda_{a,b,c|II,PM}\cos\left(p\omega_{mech}t\right) , \tag{3.190}$$

$$\lambda_{b|II,PM}(t) = \Lambda_{a,b,c|II,PM}\cos\left(p\omega_{mech}t - \tfrac{2\pi}{3}\right) \text{ and} \tag{3.191}$$

$$\lambda_{c|II,PM}(t) = \Lambda_{a,b,c|II,PM}\cos\left(p\omega_{mech}t - \tfrac{4\pi}{3}\right) . \tag{3.192}$$

The time plots of the flux-linkages is again virtually identical to the FEA results obtain using Maxwell® 2D as is shown in Figure 3.18.

The approximation of $lambda_{a,b,c|II,PM}$ when only considering the fundamental component of the radial flux-density, similar to that done in (3.178) and (3.188), can be expressed as

$$\Lambda_{a,b,c|II,PM} \approx \frac{2r_n\ell N}{a}k_q k_{w,2|II}B_{r,1} , \tag{3.193}$$

with only the second harmonics of the winding factor being considered, as was discussed in section 2.5.2 and is shown in Figure 3.18.

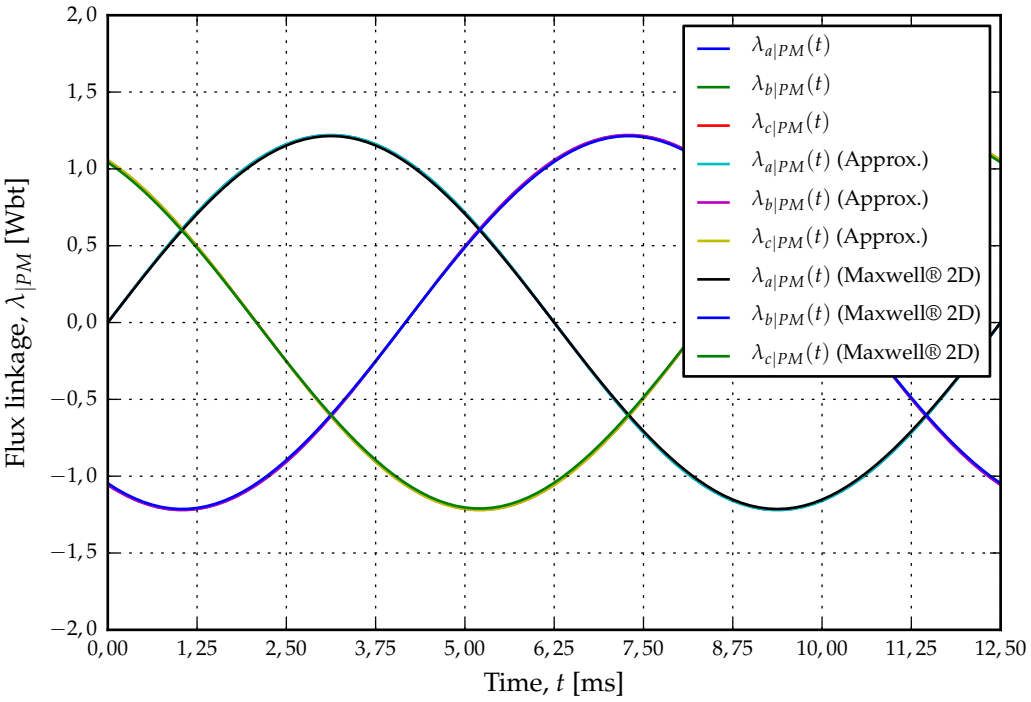

Figure 3.18: Comparison of the flux-linkage calculations for the Type II winding configuration.

3.13 The Back-EMF Calculation for the different Winding Configurations

3.13.1 The Back-EMF Calculation for the Type O Winding Configurations

The open circuit voltages or back-EMF can be calculated directly from the flux-linkages by noting that

$$e(t) = \frac{\lambda t}{dt} \,. \tag{3.194}$$

Thus for the Type O winding configuration, we will have

$$\begin{aligned} e_{a|O,PM} &= \frac{\lambda_{a|O,PM}(t)}{dt} && (3.195)\\ &= -p\omega_{mech}\Lambda_{a|O,PM}\sin\left(p\omega_{mech}t\right) && (3.196)\\ &= E_{a,b,c|O,PM}\sin\left(p\omega_{mech}t\right) && (3.197) \end{aligned}$$

with

$$\begin{aligned} E_{a,b,c|O,PM} &= -p\omega_{mech}\Lambda_{a|O,PM} && (3.198)\\ &\approx -\frac{2q\omega_{mech}r_n\ell N}{a}k_{w,1|O}B_{r,1} && (3.199) \end{aligned}$$

and

$$\begin{aligned} e_{b|O,PM} &= E_{a,b,c|O,PM}\sin\left(p\omega_{mech}t - \tfrac{2\pi}{3}\right) && (3.200)\\ e_{b|O,PM} &= E_{a,b,c|O,PM}\sin\left(p\omega_{mech}t - \tfrac{4\pi}{3}\right) \,. && (3.201) \end{aligned}$$

The three-phase open circuit voltages for the Type O winding configuration is shown in Figure 3.19, where it is compared with the open circuit voltages simulated in Maxwell® 2D using FEA. It is evident that there is some difference between the two sets of results and that the FEA results contains a lot of harmonics.

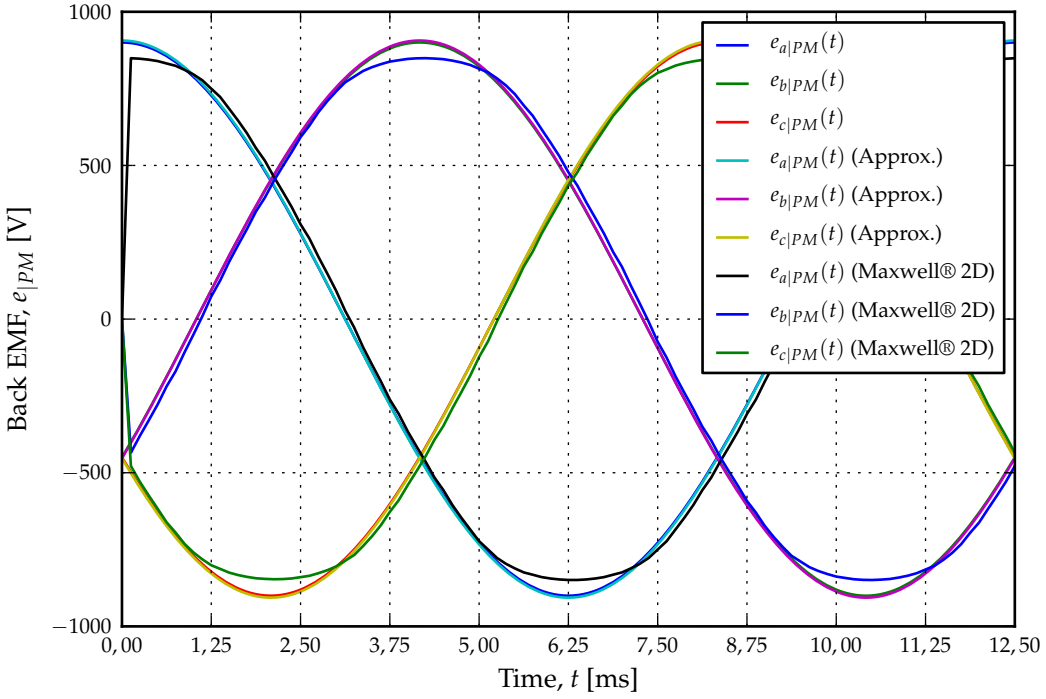

Figure 3.19: Comparison of the back-EMF calculations for the Type O winding configuration.

The FFT result of the FEA voltages is shown in Figure 3.20. Although the third and fifth harmonics are slightly larger than the rest, the harmonics are quite evenly spread. The % THD of the the FEA simulated voltages amounts to 14,53 % which is quite substantial.

The problem with the analytical calculations for the flux-linkage and the induced voltages is that it assumes that the radial flux-density in the centre of the stator is constant through out the entire stator region, which in fact it is not, as was shown in Figure 3.13.

Although the analytical calculations of the radial flux-density is similar to that calculated in Maxwell® 2D using FEA, the solution obtained in (3.147) is not a closed-form solution. It would be possible to perform numerical integration on the radial flux-density solutions over the entire stator height in order to obtain a more accurate analytically calculated flux-linkage and hence induced voltage result. This would however not be useful as "design equation" nor a "control equation", for the Double-sided Rotor RFAPM machine and hence the derivation of a set of approximated analytical equations is proposed.

3.13.2 The Back-EMF Calculation for the Type I Winding Configurations

For the Type I winding configuration, the three-phase open-circuit induced voltages can be approximated with the following equations,

$$e_{a|I,PM} = E_{a,b,c|I,PM} \sin\left(p\omega_{mech}t\right) \tag{3.202}$$

$$e_{b|I,PM} = E_{a,b,c|I,PM} \sin\left(p\omega_{mech}t - \tfrac{2\pi}{3}\right) \tag{3.203}$$

$$e_{b|I,PM} = E_{a,b,c|I,PM} \sin\left(p\omega_{mech}t - \tfrac{4\pi}{3}\right) \tag{3.204}$$

with

$$E_{a,b,c|I,PM} \approx -\frac{2q\omega_{mech}r_n\ell N}{a} k_{w,2|I} B_{r,1} \; . \tag{3.205}$$

The analytical solution for the three-phase, open-circuit induced voltages for the Type I winding configuration are shown in Figure 3.21 together with the Maxwell® 2D simulated waveforms.

3.13.3 The Back-EMF Calculation for the Type II Winding Configurations

The analytical approximation of the three-phase open-circuit induced voltages for the Type II winding configuration, can be given by the following set of equations,

$$e_{a|II,PM} = E_{a,b,c|II,PM} \sin\left(p\omega_{mech}t\right) \tag{3.206}$$

$$e_{b|II,PM} = E_{a,b,c|II,PM} \sin\left(p\omega_{mech}t - \tfrac{2\pi}{3}\right) \tag{3.207}$$

$$e_{b|II,PM} = E_{a,b,c|II,PM} \sin\left(p\omega_{mech}t - \tfrac{4\pi}{3}\right) \tag{3.208}$$

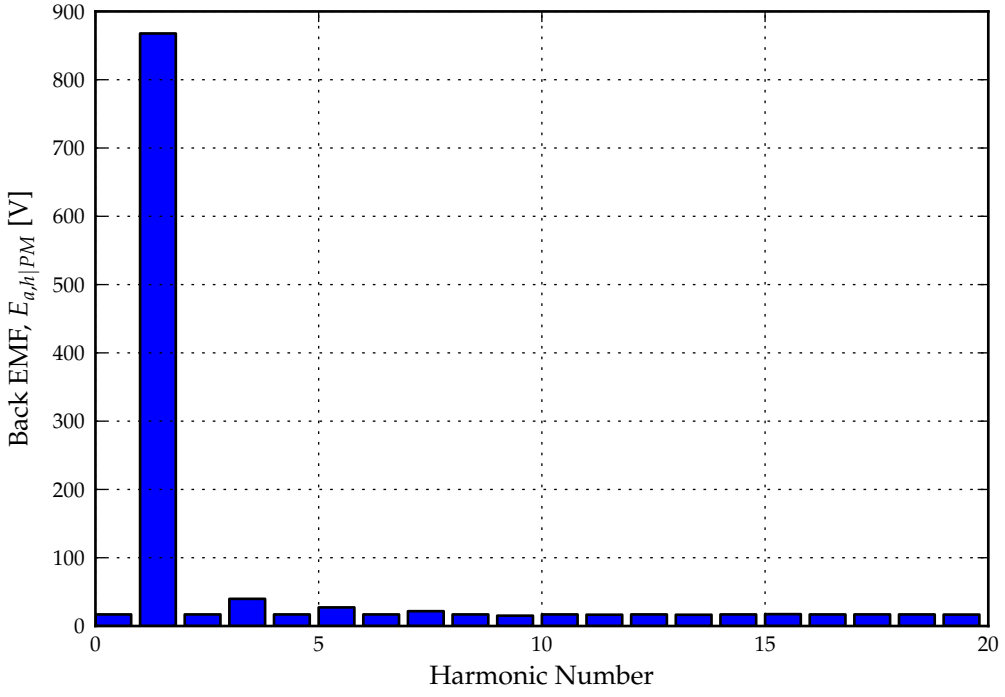

Figure 3.20: The harmonic spectrum for the back-EMF obtained from the Maxwell® 2D FEA results for the Type O winding configuration.

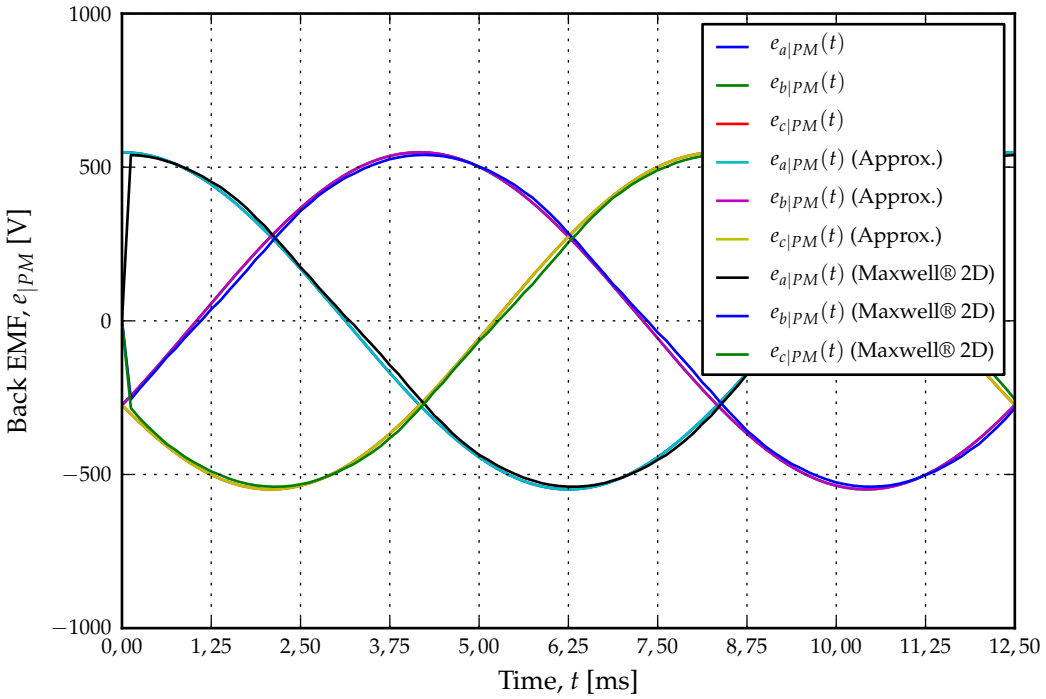

Figure 3.21: Comparison of the back-EMF calculations for the Type I winding configuration.

with

$$E_{a,b,c|II,PM} \approx -\frac{2q\omega_{mech}r_n\ell N}{a}k_{w,2|II}B_{r,1}\,. \tag{3.209}$$

These approximated waveforms together with the Maxwell® 2D simulated waveforms are shown in Figure 3.22.

3.14 Definition of the General Voltage Constant for the RFAPM Machine

In section 3.13, the existence of a common factor in the simplified, or approximated, back-EMF equation for the Type O, Type I and Type II could be observed. This allows us to define, for the RFAPM machine, a voltage constant, k_E, similar to that done for traditional sinusoidal permanent magnet AC (or commonly referred to as brushless DC) machines, Mohan [43, Chapter 10]. The peak value of the back-EMFs for the Type O, Type I and Type II winding configurations can thus be defined as,

$$\hat{E}_{f|O} = k_{E|O}\omega_{mech}\,, \tag{3.210}$$

$$\hat{E}_{f|I} = k_{E|I}\omega_{mech} \quad \text{and} \tag{3.211}$$

$$\hat{E}_{f|II} = k_{E|II}\omega_{mech} \tag{3.212}$$

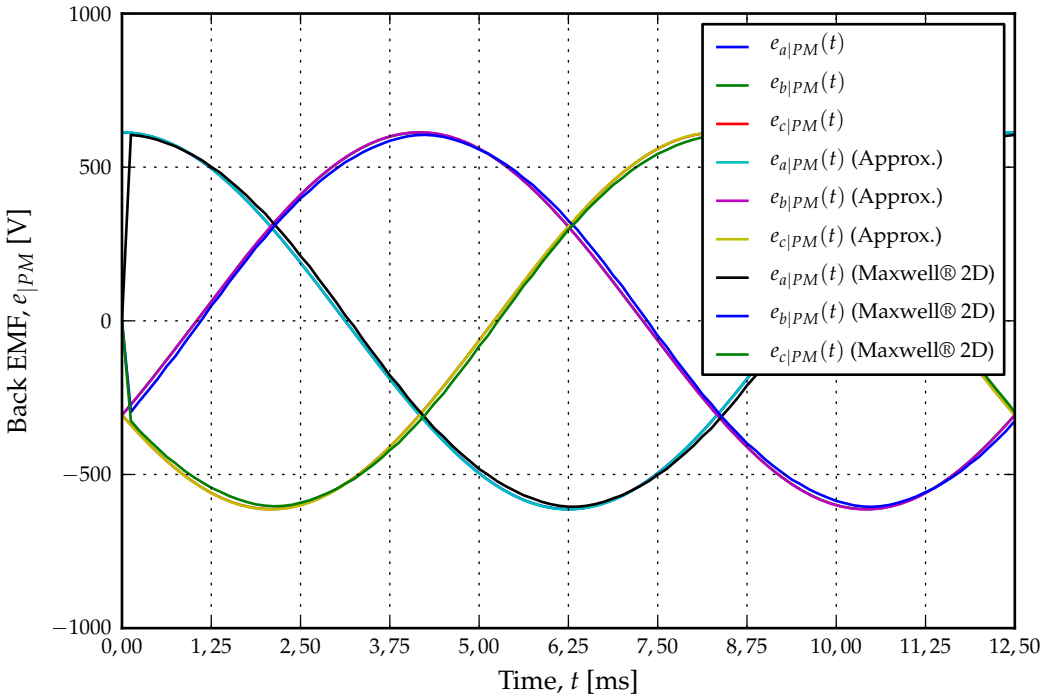

Figure 3.22: Comparison of the back-EMF calculations for the Type II winding configuration.

respectively, with the back-EMF values

$$\hat{E}_{f|O} = E_{a,b,c|O,PM}\,, \tag{3.213}$$

$$\hat{E}_{f|I} = E_{a,b,c|I,PM} \quad \text{and} \tag{3.214}$$

$$\hat{E}_{f|II} = E_{a,b,c|II,PM} \tag{3.215}$$

and the voltage constants,

$$k_{E|O} = \frac{2qr_n\ell N}{a} k_{w,1|O} B_{r,1}\,, \tag{3.216}$$

$$k_{E|I} = \frac{2qr_n\ell N}{a} k_{w,2|I} B_{r,1} \quad \text{and} \tag{3.217}$$

$$k_{E|II} = \frac{2qr_n\ell N}{a} k_{w,2|II} B_{r,1} \tag{3.218}$$

with the units of the voltage constants equal to V/rad/s.

The only difference in the definition of the voltage constant between the different winding configuration is that for the overlapping (Type O) winding configuration, the fundamental space harmonic component of the winding factor is used, as opposed to the second order space harmonics component of the winding factor for the two non-overlapping winding configurations.

3.15 Summary and Conclusions

In this chapter it was shown how the electromagnetic field produced by the permanent magnets of a RFAPM machine can be calculated in 2-D using subdomain analysis. The radial- and

azimuthal flux-density distributions inside the stator region were almost exactly the same as that produced using Maxwell® 2D. The slightly higher (approximately 3 %) value can be attributed to the fact that for the analytical subdomain analysis method the permeability of the iron yoke were taken to be constant, thus ignoring saturation in the yokes. This could clearly be seen in the flux-density contour plots where the highest analytical value was in the order of 2,7 T whereas the highest Maxwell® 2D values were calculated to be just below 2,0 T.

Furthermore was it shown, that by adjusting the pole arc width of the permanent magnets, the radial flux-density distribution in the centre of the airgap could be made quasi-sinusoidal. The ability to quickly simulate the radial flux-density for any array of magnetic pole width values, compared to the time it would take to perform the same task using FEA, illustrates the power of the analytical analysis technique. We were able to sweep the pole embracing factor, k_m , from 0,5 to 1,0 in 40 intervals steps to obtain the value of k_m which would produce the lowest %THD for the radial flux-density in the centre of the air-gap in a matter of seconds, as compared to a FEA sweep which would take a few hours. Also the FEA solution requires successive redrawing of the RFAPM model and to be comparable it requires the model to be redrawn 40 times for each value of k_m which can be quite computational intensive, unless the FEA solution is properly scripted. Also, to change an azimuthal dimension in Maxwell® 2D is much more difficult than to change a radial dimension due to the segmentation of arcs being used by Maxwell® 2D. One has to be careful of the segmentation of the machine to ensure that neighbouring arcs not overlapping.

In the calculation of the flux-linkage and the induced voltage (or back-EMF) for the different winding configurations under consideration, it was found that by using only the fundamental component of the radial flux-density distribution in the centre of the stator, an extremely good approximation of the flux-linkage and back-EMF could be obtained, especially for the non-overlapping, Type I and Type II, winding configurations.

Furthermore, it is interesting to note that if we compare (3.199), (3.205) and (3.209) with one another, the magnitude of the back-EMF is directly proportional to the number of coils per phase, q and the winding factor. Without considering the winding factor, it would at first appear that the magnitude of the back-EMF for the non-overlapping windings will always be at least half of that of the overlapping winding. However if we compare Figure 3.19, Figure 3.21 and Figure 3.22 we see that this is clearly not the case. Furthermore, if we remember that the Type O winding configuration uses full-pitch windings compared to the fractional pitch windings employed by the non-overlapping winding configurations, it is clear that the slot width or coil-side width factor, $k_{w,slot}$, plays a very important factor in machines with non-overlapping winding configurations. This will be discussed in more detail in Chapter 6.

Finally, in this chapter, the voltage constants for the the different winding configurations of the RAPM machine were deduced. The voltage constants for the different winding configurations are essentially the same, with the only difference that for the overlapping winding configuration, the fundamental space harmonic component of the winding factor needs to be used, as opposed to the second order space harmonic component of the winding factor for the non-overlapping winding configurations. The voltage constant is similar to the voltage constant of a permanent magnet DC machine. This is the reason why permanent magnet AC machines are sometimes referred to as “Brushless DC” machines.

CHAPTER 4

Magnetostatic Analysis of the Armature Reaction Fields

In mathematics you don't understand things. You just get used to them.

JOHANN VON NEUMANN

4.1 Introduction

The analytical analysis of the armature reaction field, using subdomain analysis, was first done by Zhu and Howe [7] for a slotted stator machine. The analysis was later extended, in Zhu *et al.* [22], to include slotless machines. Both these papers made use of the magnetic scalar potential to solve the reaction field produced by the stator. Atallah *et al.* [6], on the other hand, used of the magnetic vector potential to solve the reaction fields of slotless PM machines. In this chapter, the magnetic vector potential, similar to Atallah *et al.*, will also be used. By calculating the magnetic vector potential, the flux-linkage for the windings can easily be calculated as was shown in section 3.12.

With the permanent magnets effectively "switched off" during the armature reaction calculation, the calculated flux-linkages can be used to obtain the inductances of the different winding configurations, similar to the method showed in Holm [24, chap. 6]. The inductances calculation will be done assuming a sinusoidal phase current so that only the space-harmonics of the windings will be considered. The variation in the inductance due to the time harmonics of the phase current, will thus be ignored. Unfortunately the analytical method used in the calculation of the phase winding inductances does not take the end-turn effect into consideration, as it is essentially a 2D analysis method. The additional inductance due to the end-turns can be calculated with the use of empirical formulas, as was investigated by Rossouw [44]. This will, however, be left for future work and will not form part of the analysis done in this chapter.

4.2 The Governing Equations

With the current density distribution known, as was calculated in Chapter 2, it is possible to solve the magnetic field caused by the stator windings. In order to do this, we once again need to solve the magnetic vector potential, using a similar process to that done in Chapter 3. Once again we subdivide the RFAPM machine into different regions similar to that shown in Figure 3.1. The only difference now is that permanent magnets are ignored, so that the "new" regions **II** and **IV** includes the airgaps on either side of the stator windings respectively. The different regions to be solved and their governing equations for the calculation of the magnetic vector potential, are shown in Table 4.1.

Region	Range for r	μ_r	Governing equation
I	$r_n + \frac{h}{2} + \ell_g + h_m + h_y \geq r \geq r_n + \frac{h}{2} + \ell_g + h_m$	μ_y	$\nabla^2 \vec{\mathbf{A}}_{\|AR} = 0$
II	$r_n + \frac{h}{2} + \ell_g + h_m \geq r \geq r_n + \frac{h}{2}$	1	$\nabla^2 \vec{\mathbf{A}}_{\|AR} = 0$
III	$r_n + \frac{h}{2} \geq r \geq r_n - \frac{h}{2}$	1	$\nabla^2 \vec{\mathbf{A}}_{\|AR} = -\mu J_z$
IV	$r_n - \frac{h}{2} \geq r \geq r_n - \frac{h}{2} - \ell_g - h_m$	1	$\nabla^2 \vec{\mathbf{A}}_{\|AR} = 0$
V	$r_n - \frac{h}{2} - \ell_g - h_m \geq r \geq r_n - \frac{h}{2} - \ell_g - h_m - h_y$	μ_y	$\nabla^2 \vec{\mathbf{A}}_{\|AR} = 0$

Table 4.1: The governing equations for the different regions during stator excitation.

4.3 Finding the General Solutions for all the Regions

Similar to sections 3.7.1 and 3.7.2 we again need to find the general solution for each region, as well as the particular solution for the stator region, i.e. region **III**. Both the general – and the particular solution will consist of the same space – and time harmonics present in the current density distribution.[1]. From (2.51), the general solution for regions **I**–**V** will therefore have the form,

$$A_{z,gen|AR}(r,\phi) = \begin{cases} \sum_{m=1}^{\infty} \left(C_{m|AR} r^{mq} + D_{m|AR} r^{-mq}\right) \sin(mq\phi + \omega t) & \text{for } m = 3k-2,\ k \in \mathbb{N}_1 \\ \sum_{m=2}^{\infty} \left(C_{m|AR} r^{mq} + D_{m|AR} r^{-mq}\right) \sin(mq\phi - \omega t) & \text{for } m = 3k-1,\ k \in \mathbb{N}_1 \end{cases}, \tag{4.1}$$

and the particular solution for region **III** will have the form,

$$A_{z,part|AR}(r,\phi) = \begin{cases} \sum_{m=1}^{\infty} G_{m|AR} \sin(mq\phi + \omega t) & \text{for } m = 3k-2,\ k \in \mathbb{N}_1 \\ \sum_{m=2}^{\infty} G_{m|AR} \sin(mq\phi - \omega t) & \text{for } m = 3k-1,\ k \in \mathbb{N}_1 \end{cases}. \tag{4.2}$$

[1]This implies either $J_{z|O}$ for the Type O winding configuration, $J_{z|I}$ for the Type I winding configuration or $J_{z|II}$ for the Type II winding configuration

From Table 4.1 it is clear that the solution to the governing equations, consist of only Laplace and Poisson equations and are therefore not time dependant. Thus the following shorthand notation will be used for (4.1) and (4.2) in order to simplify the writing,

$$A_{z,gen|AR}(r,\phi) = \sum_{m=1}^{\infty} (C_{m|AR} r^{mq} + D_{m|AR} r^{-mq}) \sin(mq\phi \pm \omega t) \tag{4.3}$$

and

$$A_{z,part|AR}(r,\phi) = \sum_{m=1}^{\infty} G_{m|AR} \sin(mq\phi \pm \omega t)\ . \tag{4.4}$$

4.4 Finding the Particular Solutions for Region III

The current density distributions of the Typ O –, the Type I – and the Type II winding configurations, equations (2.51), (2.85) and (2.110) respectively, all have the same basic form. The general format of the expanded governing equation for region **III** can therefore be written the following form,

$$\frac{\partial^2 A_{z|AR}}{\partial r^2} + \frac{1}{r}\frac{\partial A_{z|AR}}{\partial r} + \frac{1}{r^2}\frac{\partial^2 A_{z|AR}}{\partial \phi^2} = -\mu_0 J_z \tag{4.5}$$

$$= -\frac{3\mu_0 q I_p N}{a r_n h \pi} \sum_{m=1}^{\infty} k_{w,m} \sin\big(mq\phi \pm \omega t\big) \tag{4.6}$$

$$\tag{4.7}$$

Substituting the particular solution of (4.4) into (4.6), we get

$$-\frac{1}{r^2}(mq)^2 \sum_{m=1}^{\infty} G_{m|AR} \sin(mq\phi \pm \omega t) = -\frac{3\mu_0 q I_p N}{a r_n h \pi} \sum_{m=1}^{\infty} k_{w,m} \sin\big(mq\phi \pm \omega t\big) \tag{4.8}$$

so that

$$G_{m|AR}(r) = \frac{3\mu_0 I_p N r^2}{a\pi r_n h q m^2} k_{w,m} \tag{4.9}$$

which now, unlike (3.81), is a also a function of r, the radial component. We will subsequently see that in order to solve the boundary condition equations involving $H_\phi(r,\phi)$, we will need to calculate $\frac{dG_{m|AR}(r)}{r}$. Thus, in order to simply the writing, we define,

$$G'_{m|AR}(r) = \frac{dG_{m|AR}(r)}{dr} \tag{4.10}$$

$$= \frac{6\mu_0 I_p N r}{a\pi r_n h q m^2} k_{w,m}\ . \tag{4.11}$$

4.5 Boundary Equations in order to solve the Armature Reaction Fields

In all the regions, except for region **III**, we have

$$A_{z|AR}(r,\phi) = A_{z,gen|AR}(r,\phi) \tag{4.12}$$

$$= \sum_{m=1}^{\infty} (C_{m|AR} r^{mq} + D_{m|AR} r^{-mq}) \sin(mq\phi \pm \omega t) \tag{4.13}$$

so that

$$B_{r|AR}(r,\phi) = \frac{1}{r}\cdot\frac{\partial A_{z|AR}(r,\phi)}{\partial\phi} \tag{4.14}$$

$$= \frac{1}{r}\cdot\sum_{m=1}^{\infty} mq(C_{m|AR}r^{mq} + D_{m|AR}r^{-mq})\cos(mq\phi \pm \omega t) \tag{4.15}$$

and

$$H_{\phi|AR}(r,\phi) = -\frac{1}{\mu}\cdot\frac{\partial A_{z|AR}(r,\phi)}{\partial r} \tag{4.16}$$

$$= -\frac{1}{\mu}\cdot\sum_{m=1}^{\infty} mq(C_{m|AR}r^{mq-1} - D_{m|AR}r^{-mq-1})\sin(mq\phi \pm \omega t)\ . \tag{4.17}$$

However in region **III** we have

$$A_{z|AR}(r,\phi) = A_{z,gen|AR}(r,\phi) + A_{z,part|AR}(r,\phi) \tag{4.18}$$

$$= \sum_{m=1}^{\infty}(C_{m|AR}r^{mq} + D_{m|AR}r^{-mq})\sin(mq\phi) + \sum_{m=1}^{\infty} G_{m|AR}(r)\sin(mq\phi \pm \omega t) \tag{4.19}$$

$$= \sum_{m=1}^{\infty}\Big(C_{m|AR}r^{mq} + D_{m|AR}r^{-mq} + G_{m|AR}(r)\Big)\sin(mq\phi \pm \omega t) \tag{4.20}$$

so that

$$B_{r|AR}(r,\phi) = \frac{1}{r}\cdot\frac{\partial A_{z|AR}(r,\phi)}{\partial\phi} \tag{4.21}$$

$$= \frac{1}{r}\cdot\sum_{m=1}^{\infty} mq\Big(C_{m|AR}r^{mq} + D_{m|AR}r^{-mq} + G_{m|AR}(r)\Big)\cos(mq\phi \pm \omega t) \tag{4.22}$$

and

$$H_{\phi|AR}(r,\phi) = -\frac{1}{\mu}\cdot\frac{\partial A_{z|AR}(r,\phi)}{\partial r} \tag{4.23}$$

$$= -\frac{1}{\mu}\cdot\sum_{m=1}^{\infty} mq\Big(C_{m|AR}r^{mq-1} - D_{m|AR}r^{-mq-1} + \tfrac{1}{mq}G'_{m|AR}(r)\Big)\sin(mq\phi \pm \omega t)\ . \tag{4.24}$$

4.5.1 The Boundary Equations on the Inner Boundary of Region I

With $r = r_n - \frac{h}{2} - \ell_g - h_m - h_y$,

$$A^I_{z|AR}(r,\phi) = 0 \tag{4.25}$$

$$\therefore \quad C^I_{m|AR}r^{mq} + D^I_{m|AR}r^{-mq} = 0 \tag{4.26}$$

4.5.2 The Boundary Equations on the Boundary Between Region I and II

With $r = r_n - \frac{h}{2} - \ell_g - h_m$,

$$B^I_{r|AR}(r,\phi) = B^{II}_{r|AR}(r,\phi) \tag{4.27}$$

$$\therefore \quad C^I_{m|AR} r^{mq} + D^I_{m|AR} r^{-mq} = C^{II}_{m|AR} r^{mq} + D^{II}_{m|AR} r^{-mq} \tag{4.28}$$

and

$$H^I_{\phi|AR}(r,\phi) = H^{II}_{\phi|AR}(r,\phi) \tag{4.29}$$

$$\therefore \quad \frac{C^I_{m|AR} r^{mq-1} - D^I_{m|AR} r^{-mq-1}}{\mu^I} = \frac{C^{II}_{m|AR} r^{mq-1} - D^{II}_{m|AR} r^{-mq-1}}{\mu^{II}} \tag{4.30}$$

4.5.3 The Boundary Equations on the Boundary Between Region II and III

With $r = r_n - \frac{h}{2} - \ell_g$,

$$B^{II}_{r|AR}(r,\phi) = B^{III}_{r|AR}(r,\phi) \tag{4.31}$$

$$\therefore \quad C^{II}_{m|AR} r^{mq} + D^{II}_{m|AR} r^{-mq} = C^{III}_{m|AR} r^{mq} + D^{III}_{m|AR} r^{-mq} + G_{m|AR}(r) \tag{4.32}$$

and

$$H^{II}_{\phi|AR}(r,\phi) = H^{III}_{\phi|AR}(r,\phi) \tag{4.33}$$

$$\therefore \quad \frac{C^{II}_{m|AR} r^{mq-1} - D^{II}_{m|AR} r^{-mq-1}}{\mu^{II}} = \frac{C^{III}_{m|AR} r^{mq-1} - D^{III}_{m|AR} r^{-mq-1} + \frac{1}{mq} G'_{m|AR}(r)}{\mu^{III}} \tag{4.34}$$

4.5.4 The Boundary Equations on the Boundary Between Region III and IV

With $r = r_n + \frac{h}{2} + \ell_g$,

$$B^{III}_{r|AR}(r,\phi) = B^{IV}_{r|AR}(r,\phi) \tag{4.35}$$

$$\therefore \quad C^{III}_{m|AR} r^{mq} + D^{III}_{m|AR} r^{-mq} + G_{m|AR}(r) = C^{IV}_{m|AR} r^{mq} + D^{IV}_{m|AR} r^{-mq} \tag{4.36}$$

and

$$H^{III}_{\phi|AR}(r,\phi) = H^{IV}_{\phi|AR}(r,\phi) \tag{4.37}$$

$$\therefore \quad \frac{C^{III}_{m|AR} r^{mq-1} - D^{III}_{m|AR} r^{-mq-1} + \frac{1}{mq} G'_{m|AR}(r)}{\mu^{III}} = \frac{C^{IV}_{m|AR} r^{mq-1} - D^{IV}_{m|AR} r^{-mq-1}}{\mu^{IV}} \tag{4.38}$$

4.5.5 The Boundary Equations on the Boundary Between Region IV and V

With $r = r_n + \frac{h}{2} + \ell_g + h_m$,

$$B^{IV}_{r|AR}(r,\phi) = B^{V}_{r|AR}(r,\phi) \tag{4.39}$$

$$\therefore \quad C^{IV}_{m|AR} r^{mq} + D^{IV}_{m|AR} r^{-mq} = C^{V}_{m|AR} r^{mq} + D^{V}_{m|AR} r^{-mq} \tag{4.40}$$

and

$$H^{IV}_{\phi|AR}(r,\phi) = H^{V}_{\phi|AR}(r,\phi) \tag{4.41}$$

$$\frac{C^{IV}_{m|AR} r^{mq-1} - D^{IV}_{m|AR} r^{-mq-1}}{\mu^{IV}} = \frac{C^{V}_{m|AR} r^{mq-1} - D^{V}_{m|AR} r^{-mq-1}}{\mu^{V}} \tag{4.42}$$

4.5.6 The Boundary Equations on the Outer Boundary of Region V

With $r = r_n + \frac{h}{2} + \ell_g + h_m + h_y$,

$$A^{V}_{z|AR}(r,\phi) = 0 \tag{4.43}$$

$$\therefore \quad C^{V}_{m|AR} r^{mq} + D^{V}_{m|AR} r^{-mq} = 0 \tag{4.44}$$

4.6 Simultaneous Equations to solve for the Armature Reaction Fields

From (4.26), (4.28), (4.30), (4.32), (4.34), (4.36), (4.38), (4.40), (4.42) and (4.44) the following ten equations have to be solved for $m = 1 \to \infty$,

$$C^{I}_{m|AR} r_i^{mq} + D^{I}_{m|AR} r_i^{-mq} = 0 \tag{4.45}$$

$$C^{I}_{m|AR} r_{ii}^{mq} + D^{I}_{m|AR} r_{ii}^{-mq} - C^{II}_{m|AR} r_{ii}^{mq} - D^{II}_{m|AR} r_{ii}^{-mq} = 0 \tag{4.46}$$

$$\mu^{II} C^{I}_{m|AR} r_{ii}^{mq-1} - \mu^{II} D^{I}_{m|AR} r_{ii}^{-mq-1} - \mu^{I} C^{II}_{m|AR} r_{ii}^{mq-1} + \mu^{I} D^{II}_{m|AR} r_{ii}^{-mq-1} = 0 \tag{4.47}$$

$$C^{II}_{m|AR} r_{iii}^{mq} + D^{II}_{m|AR} r_{iii}^{-mq} - C^{III}_{m|AR} r_{iii}^{mq} - D^{III}_{m|AR} r_{iii}^{-mq} = G_{m|AR}(r_{iii}) \tag{4.48}$$

$$\mu^{III} C^{II}_{m|AR} r_{iii}^{mq-1} - \mu^{III} D^{II}_{m|AR} r_{iii}^{-mq-1} - \mu^{II} C^{III}_{m|AR} r_{iii}^{mq-1} + \mu^{II} D^{III}_{m|AR} r_{iii}^{-mq-1} = \mu^{II} \frac{G'_{m|AR}(r_{iii})}{mq} \tag{4.49}$$

$$C^{III}_{m|AR} r_{iv}^{mq} + D^{III}_{m|AR} r_{iv}^{-mq} - C^{IV}_{m|AR} r_{iv}^{mq} - D^{IV}_{m|AR} r_{iv}^{-mq} = -G_{m|AR}(r_{iv}) \tag{4.50}$$

$$\mu^{IV} C^{III}_{m|AR} r_{iv}^{mq-1} - \mu^{IV} D^{III}_{m|AR} r_{iv}^{-mq-1} - \mu^{III} C^{IV}_{m|AR} r_{iv}^{mq-1} + \mu^{III} D^{IV}_{m|AR} r_{iv}^{-mq-1} = -\mu^{IV} \frac{G'_{m|AR}(r_{iv})}{mq} \tag{4.51}$$

$$C^{IV}_{m|AR} r_v^{mq} + D^{IV}_{m|AR} r_v^{-mq} - C^{V}_{m|AR} r_v^{mq} - D^{V}_{m|AR} r_v^{-mq} = 0 \tag{4.52}$$

$$\mu^{V} C^{IV}_{m|AR} r_v^{mq-1} - \mu^{V} D^{IV}_{m|AR} r_v^{-mq-1} - \mu^{IV} C^{V}_{m|AR} r_v^{mq-1} + \mu^{IV} D^{V}_{m|AR} r_v^{-mq-1} = 0 \tag{4.53}$$

$$C^{V}_{m|AR} r_{vi}^{mq} + D^{V}_{m|AR} r_{vi}^{-mq} = 0 \tag{4.54}$$

with

$$r_i = r_n - \frac{h}{2} - \ell_g - h_m - h_y \tag{4.55}$$

$$r_{ii} = r_n - \frac{h}{2} - \ell_g - h_m \tag{4.56}$$

$$r_{iii} = r_n - \frac{h}{2} \tag{4.57}$$

$$r_{iv} = r_n + \frac{h}{2} \tag{4.58}$$

$$r_v = r_n + \frac{h}{2} + \ell_g + h_m \tag{4.59}$$

$$r_{vi} = r_n + \frac{h}{2} + \ell_g + h_m + h_y \tag{4.60}$$

and $G_{m|AR}$ and $G'_{m|AR}$ as defined in (4.9) and (4.11) respectively.

By replacing $k_{w,m}$ with $k_{w,m|O}$, $k_{w,m|I}$ or $k_{w,m|II}$, the simultaneous equations to solve the armature reaction fields for the Type O, Type I and II winding configuration respectively, can be obtained. In (4.61), the equations of (4.45) to (4.54) are written in matrix format. This allows us to solve the C_m and D_m coefficients for the different regions and for the different values of m much easier, for the armature reactions fields of the different winding configurations.

4.7 Obtaining the Solution to the Magnetic Vector Potential and Magnetic Flux-Density

4.7.1 The Magnetic Vector Potential Solution

The final solution for the magnetic vector potential due to the armature reaction, for the different regions of the machine, is thus obtained by substituting the appropriate values of $C_{m|AR}$ and $D_{m|AR}$ as obtained in (4.61) into (4.13) and (4.20), as shown in (4.62).

$$
\begin{bmatrix}
r_{i}^{mq} & r_{i}^{-mq} & 0 & 0 & 0 & 0 & 0 & 0 \\
r_{ii}^{mq} & r_{ii}^{-mq} & -r_{ii}^{mq} & -r_{ii}^{-mq} & 0 & 0 & 0 & 0 \\
\mu^{II} r_{ii}^{mq-1} & -\mu^{II} r_{ii}^{-mq-1} & -\mu^{I} r_{ii}^{mq-1} & \mu^{I} r_{ii}^{-mq-1} & 0 & 0 & 0 & 0 \\
0 & 0 & r_{iii}^{mq} & r_{iii}^{-mq} & -r_{iii}^{mq} & -r_{iii}^{-mq} & 0 & 0 \\
0 & 0 & \mu^{III} r_{iii}^{mq-1} & -\mu^{III} r_{iii}^{-mq-1} & -\mu^{II} r_{iii}^{mq-1} & \mu^{II} r_{iii}^{-mq-1} & 0 & 0 \\
0 & 0 & 0 & 0 & r_{iv}^{mq} & r_{iv}^{-mq} & -r_{iv}^{mq} & -r_{iv}^{-mq} \\
0 & 0 & 0 & 0 & \mu^{IV} r_{iv}^{mq-1} & -\mu^{IV} r_{iv}^{-mq-1} & -\mu^{III} r_{iv}^{mq-1} & \mu^{III} r_{iv}^{-mq-1} \\
0 & 0 & 0 & 0 & 0 & 0 & r_{v}^{mq} & r_{v}^{-mq} \\
0 & 0 & 0 & 0 & 0 & 0 & \mu^{V} r_{v}^{mq-1} & -\mu^{V} r_{v}^{-mq-1} \\
0 & 0 & 0 & 0 & 0 & 0 & r_{vi}^{mq} & r_{vi}^{-mq} \\
0 & 0 & 0 & 0 & 0 & 0 & \mu^{IV} r_{v}^{mq-1} & -\mu^{IV} r_{v}^{-mq-1}
\end{bmatrix}
\begin{bmatrix}
C_{m|AR}^{I} \\
D_{m|AR}^{I} \\
C_{m|AR}^{II} \\
D_{m|AR}^{II} \\
C_{m|AR}^{III} \\
D_{m|AR}^{III} \\
C_{m|AR}^{IV} \\
D_{m|AR}^{IV} \\
C_{m|AR}^{V} \\
D_{m|AR}^{V}
\end{bmatrix}
=
\begin{bmatrix}
0 \\
0 \\
0 \\
G_{m|AR}(r_{iii}) \\
\frac{\mu^{II}}{mq} G'_{m|AR}(r_{iii}) \\
-G_{m|AR}(r_{iv}) \\
-\frac{\mu^{IV}}{mq} G'_{m|AR}(r_{iv}) \\
0 \\
0 \\
0
\end{bmatrix}
\tag{4.61}
$$

$$A_{z|AR}(r,\phi) = \begin{cases} \sum_{m=1}^{\infty} \left(C^{I}_{m|AR} r^{mq} + D^{I}_{m|AR} r^{-mq}\right) \sin(mq\phi \pm \omega t) & \text{for Region I} \\ \sum_{m=1}^{\infty} \left(C^{II}_{m|AR} r^{mq} + D^{II}_{m|AR} r^{-mq}\right) \sin(mq\phi \pm \omega t) & \text{for Region II} \\ \sum_{m=1}^{\infty} \left(C^{III}_{m|AR} r^{mq} + D^{III}_{m|AR} r^{-mq} + G_{m|AR}(r)\right) \cdot \sin(mq\phi \pm \omega t) & \text{for Region III} \\ \sum_{m=1}^{\infty} \left(C^{IV}_{m|AR} r^{mq} + D^{IV}_{m|AR} r^{-mq}\right) \sin(mq\phi \pm \omega t) & \text{for Region IV} \\ \sum_{m=1}^{\infty} \left(C^{V}_{m|AR} r^{mq} + D^{V}_{m|AR} r^{-mq}\right) \sin(mq\phi \pm \omega t) & \text{for Region V} \end{cases} \tag{4.62}$$

4.7.2 The Magnetic Flux-Density Solution

To obtain the final solution of the magnetic flux-density, for the different regions of the RFAPM machine, due to armature reaction, is a little bit more difficult. This is done by substituting the appropriate values of $C_{m|AR}$ and $D_{m|AR}$ from (4.61) into (4.15) and (4.22) to obtain the radial component of the magnetic flux-density, as shown in (4.63).

$$B_{r|AR}(r,\phi) = \begin{cases} -\frac{1}{r} \cdot \sum_{m=1}^{\infty} mq \left(C^{I}_{m|AR} r^{mq} + D^{I}_{m|AR} r^{-mq}\right) \cos(mq\phi \pm \omega t) & \text{for Region I} \\ -\frac{1}{r} \cdot \sum_{m=1}^{\infty} mq \left(C^{II}_{m|AR} r^{mq} + D^{II}_{m|AR} r^{-mq}\right) \cos(mq\phi \pm \omega t) & \text{for Region II} \\ -\frac{1}{r} \cdot \sum_{m=1}^{\infty} mq \left(C^{III}_{m|AR} r^{mq} + D^{III}_{m|AR} r^{-mq} + G_{m|AR}(r)\right) \cdot \cos(mq\phi \pm \omega t) & \text{for Region III} \\ -\frac{1}{r} \cdot \sum_{m=1}^{\infty} mq \left(C^{IV}_{m|AR} r^{mq} + D^{IV}_{m|AR} r^{-mq}\right) \cos(mq\phi \pm \omega t) & \text{for Region IV} \\ -\frac{1}{r} \cdot \sum_{m=1}^{\infty} mq \left(C^{V}_{m|AR} r^{mq} + D^{V}_{m|AR} r^{-mq}\right) \cos(mq\phi \pm \omega t) & \text{for Region V} \end{cases} \tag{4.63}$$

Assuming a linear relationship between the flux-density, B, and the magnetic field intensity, H, (i.e. $B = \mu H$) the azimuthal component of the magnetic flux-density, due to armature reaction, for the different regions of the RFAPM machine can be obtained by, again, substituting the appropriate values of $C_{m|AR}$ and $D_{m|AR}$ from (4.61) into (4.17) and (4.24) as shown in (4.64).

$$B_{\phi|AR}(r,\phi) = \begin{cases} -\sum_{m=1}^{\infty} mq\left(C^{I}_{m|AR}r^{mq-1} - D^{I}_{m|AR}r^{-mq-1}\right)\sin(mq\phi \pm \omega t) & \text{for Region I} \\ -\sum_{m=1}^{\infty} mq\left(C^{II}_{m|AR}r^{mq-1} - D^{II}_{m|AR}r^{-mq-1}\right)\sin(mq\phi \pm \omega t) & \text{for Region II} \\ -\sum_{m=1}^{\infty} mq\left(C^{III}_{m|AR}r^{mq-1} - D^{III}_{m|AR}r^{-mq-1} + \frac{1}{mq}G'_{m|AR}(r)\right)\cdot \sin(mq\phi \pm \omega t) & \text{for Region III} \\ -\sum_{m=1}^{\infty} mq\left(C^{IV}_{m|AR}r^{mq-1} - D^{IV}_{m|AR}r^{-mq-1}\right)\sin(mq\phi \pm \omega t) & \text{for Region IV} \\ -\sum_{m=1}^{\infty} mq\left(C^{V}_{m|AR}r^{mq-1} - D^{V}_{m|AR}r^{-mq-1}\right)\sin(mq\phi \pm \omega t) & \text{for Region V} \end{cases} \tag{4.64}$$

From (4.63) and (4.64) the magnitude of the magnetic flux-density can now be obtained as follows

$$B_{|AR}(r,\phi) = \sqrt{B^2_{r|AR}(r,\phi) + B^2_{\phi|AR}(r,\phi)}\,. \tag{4.65}$$

The magnetic flux-density contour plots will be discussed in the following sections and are shown in Appendix G together with the magnetic vector potential contour plots.

4.8 Validation of the Type O Winding Configuration Solution

4.8.1 Magnetic Field Solutions of the Type O Winding Configuration

The *Matplotlib* contour plot of the analytically calculated magnetic vector potential, is shown in Figure G.1[1], with the FEA solution obtained from Maxwell® 2D shown in Figure G.2. In Figure G.3 the *Matplotlib* contour plot of the analytically calculated magnetic flux-density is shown, whilst the FEA solution obtained from Maxwell® 2D, is shown in Figure G.4.

As was mentioned in section 3.11.1, it is very difficult to compare the analytical solution with the FEA solution from the contour plots. The best way to do it, is to take slices through the machine at different radius values and compare the radial – and azimuthal flux-density distributions between the analytical and FEA results on these "cut lines". This is shown in Figure 4.1 and Figure 4.2, where the radial – and azimuthal magnetic flux-density distributions for the analytically and FEA solution obtained using Maxwell® 2D, are compared.

4.8.2 Flux-linkage Calculation of the Type O Winding Configuration

The peak value of the total flux-linkage due to the armature reaction can be calculated in exactly the same way as was done in section 3.12 for the calculation of the peak value of the total flux-linkage per phase due to the permanent magnets. This implies that equation (3.164), which was derived for the flux-linkage in a single turn in terms of the magnetic vector potential caused by the permanent magnets, could be rewritten as

$$\lambda_{1|O,AR}(r,\phi) = 2\ell A_{z|O,AR}(r,\phi)\,, \tag{4.66}$$

[1]The magnetic vector potential en magnetic flux-density contour plots are shown in Appendix G on pages 163 and page 164 respectively.

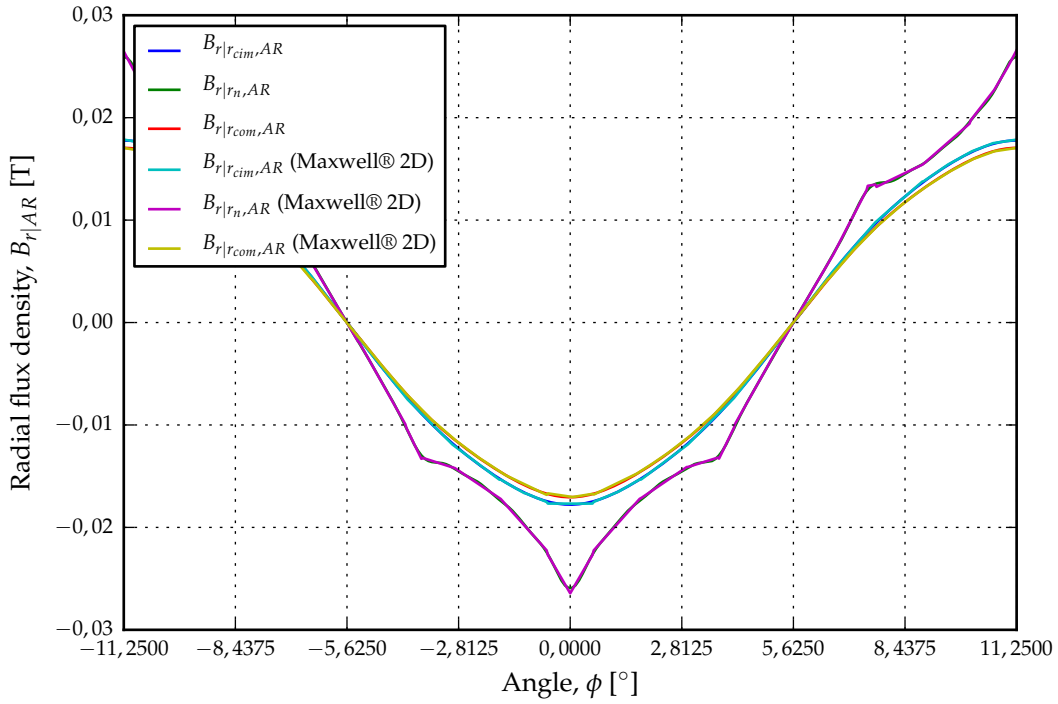

Figure 4.1: Radial Flux-Density Distribution

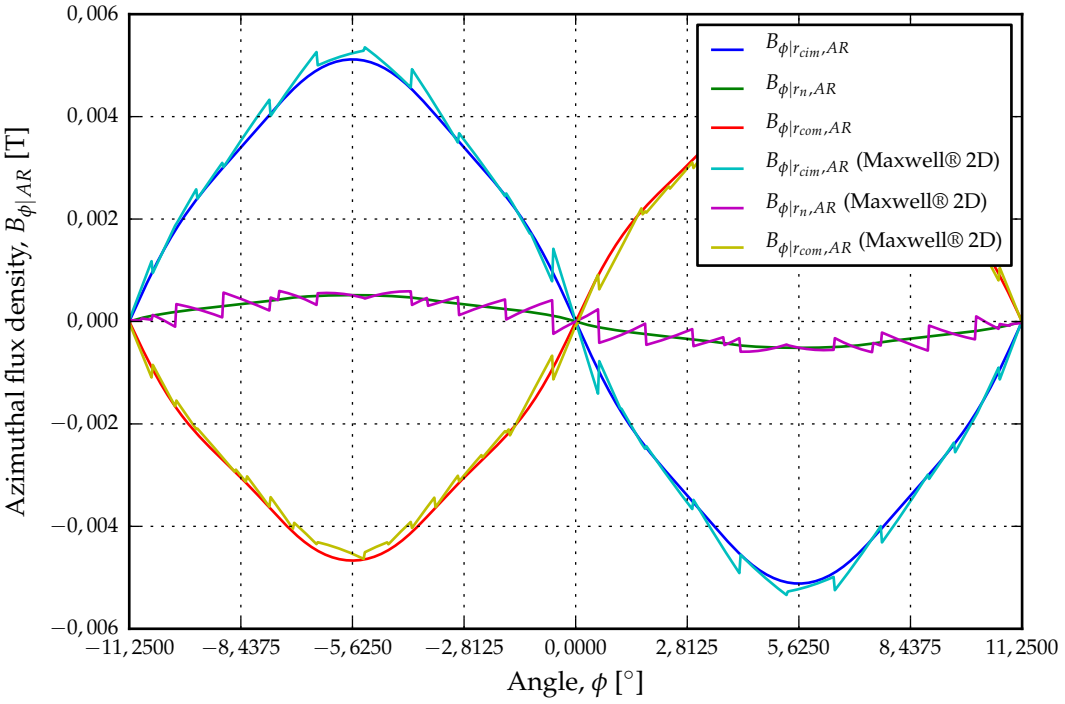

Figure 4.2: Azimuthal Flux-Density Distribution

with $A_{z|O,AR}(r,\phi)$ the vector potential caused only by the three-phase currents flowing in the windings with the permanent magnets "switched off".

The total flux-linkage per phase can thus be calculated by multiplying the flux-linkage distribution in (4.66) with the conductor density distribution given in (2.26) (see also Figure 2.5); then integrating over one resultant coil pitch period and finally multiplying by the number of series connected circuits[1], $\frac{q}{a}$. Also, as discussed in section 3.12.1, we assume that the magnetic vector potential throughout the windings is equal to the magnetic vector potential at the centre of the windings, at $r{=}r_n$.

$$\Lambda_{a,b,c|O,AR} = \frac{q}{a}\int_{-\frac{\tau_{q|O}}{2}}^{\frac{\tau_{q|O}}{2}} n_{a|O}(\phi)\lambda_{1|O,AR}(r_n,\phi)d\phi \tag{4.67}$$

$$= \frac{2q\ell}{a}\int_{-\frac{\tau_{q|O}}{2}}^{\frac{\tau_{q|O}}{2}} n_{a|O}(\phi)A_{z|O,AR}(r_n,\phi)d\phi \tag{4.68}$$

From (4.62) and only using the solution for the vector potential in the stator region, i.e. region III, for a Type O winding configuration and substituting 'n' for 'm', we can write

$$A^{III}_{z|O,AR}(r_n,\phi) = \sum_{m=1}^{\infty} b^{III}_{m_{A_{z|O,AR}}}\sin(nq\phi) \tag{4.69}$$

with

$$b^{III}_{m_{A_{z|O,AR}}} = C^{III}_{m|AR}r_n^{mq} + D^{III}_{m|AR}r_n^{-nq} + G_{m|O,AR}(r_n) \tag{4.70}$$

and from (4.9), using the winding factor, $k_{w,m|O}$, for the Type O winding configuration as defined in (2.31), $G_{m|O,AR}(r_n)$ can be expanded to

$$G_{m|O,AR}(r_n) = \frac{3\mu_0 I_p N r_n}{a\pi hqn^2}k_{w,n|O}\,. \tag{4.71}$$

From (2.26) and (4.69), (4.68) can now be written as

$$\Lambda_{a,b,c|O,AR} = \frac{2q\ell}{a}\int_{-\frac{\tau_{q|O}}{2}}^{\frac{\tau_{q|O}}{2}}\sum_{m=1}^{\infty} b_{m_{a|O}}\sin(mq\phi)\sum_{m=1}^{\infty} b^{III}_{m_{A_{z|O,AR}}}\sin(nq\phi)d\phi \tag{4.72}$$

$$= \frac{2q\ell}{a}\sum_{m=1}^{\infty}\sum_{m=1}^{\infty} b_{m_{a|O}}b^{III}_{m_{A_{z|O,AR}}}\int_{-\frac{\tau_{q|O}}{2}}^{\frac{\tau_{q|O}}{2}}\sin(mq\phi)\sin(nq\phi)d\phi\,. \tag{4.73}$$

With the coil-pitch of the Type O winding configuration, $\tau_{q|O} = \frac{\pi}{q}$, the integral term evaluates to zero except where $m = n$ when it evaluates to $\frac{\pi}{2q}$. This implies that (4.73) can be simplified to

$$\Lambda_{a,b,c|O,AR} = \frac{\pi\ell}{a}\sum_{m=1}^{\infty} b_{m_{a|O}}b^{III}_{m_{A_{z|O,AR}}}\,, \tag{4.74}$$

or from (2.30) in terms of the winding factors, as

$$\Lambda_{a,b,c|O,AR} = \frac{2qN\ell}{a}\sum_{m=1}^{\infty} k_{w,m|O}b^{III}_{m_{A_{z|O,AR}}}\,, \tag{4.75}$$

[1] As explained in Appendix A we don't have to divide by the number of parallel circuits as we assume that the current divides equally between the number of parallel branches

The peak value of the total flux-linkage per phase, $\Lambda_{a,b,c|O,AR}$, for the Type O winding configuration, using the same rotor configuration as given in Appendix E, section E.1, is calculated as

$$\Lambda_{a,b,c|O,AR} = 48{,}045 \text{ mWbt} . \tag{4.76}$$

If we compare the peak value of the flux-linkage in (4.76) with the results in Table 4.2 were the flux-linkage of each space-harmonic component were calculated separately, we can see that the main contribution of the flux-linkage results from the fundamental space-harmonic component. This implies that (4.75) may be simplified to

$$\Lambda_{a,b,c|O,AR} \approx \frac{2qN\ell}{a} k_{w,m=1|O} b^{III}_{m=1_{A_{z|O,AR}}} \tag{4.77}$$

$$\approx 47{,}827 \text{ mWbt} . \tag{4.78}$$

which would yield a good approximation of the flux-linkage for the Type O winding configuration.

Due to the fact that the N48 Neodymium-Boron-Iron (NdBFe) surface mounted permanent magnets that are used in the RFAPM machine's recoil permeability, $\mu_{recoil} \approx \mu_0$, see also [45], the flux-linkage will be the same regardless of the rotor position. The magnitude of the flux-linkage will thus only depend on the value of the phase current, so that for a perfectly balanced three-phase stator current, we can write,

$$\lambda_{a|O,AR}(t) = \Lambda_{a,b,c|O,AR} \cos(\omega t) \tag{4.79}$$

$$\lambda_{b|O,AR}(t) = \Lambda_{a,b,c|O,AR} \cos(\omega t - \tfrac{2\pi}{3}) \quad \text{and} \tag{4.80}$$

$$\lambda_{c|O,AR}(t) = \Lambda_{a,b,c|O,AR} \cos(\omega t - \tfrac{4\pi}{3}) . \tag{4.81}$$

In Figure 4.3 the analytically calculated flux-linkages for the Type O winding configuration is compared with that calculated by Maxwell® 2D, using FEA. The difference between the

Table 4.2: The flux-linkage component for each space-harmonic of the Type O winding configuration.

Space harmonic, m	$\Lambda_{a,b,c\|O,AR,m}$ [mWbt]
1	47,827
2	–
3	–
4	–
5	0,157
6	–
7	0,045
8	–
9	–
10	–
11	0,008
12	–
13	0,004

analytically calculated flux-linkage values and that of the FEA values can be contributed to the fact that only a 1–D conductor density distribution was used together with the assumption that the average magnetic vector potential distribution values in the windings remains equal to the values in the centre of the windings.

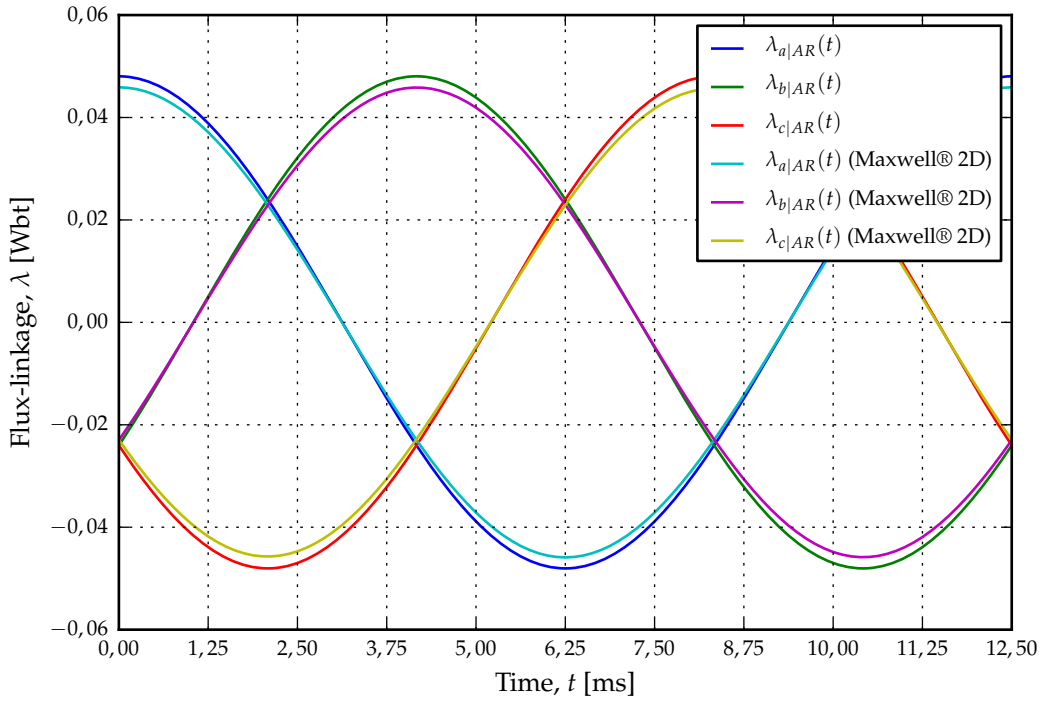

Figure 4.3: Flux-linkages for phase a, b and c for the Type O winding configuration.

4.8.3 Stator Inductance Calculation of the Type O Winding Configuration

With the flux-linkages for the Type O winding configuration known, it is now possible to calculate the inductances of the stator windings for this winding configuration. If we assume the machine to be perfectly symmetrical, the self inductance for each phase as well as the mutual inductance between any two phases will be exactly the same. This implies that the inductance matrix, in terms of the flux-linkage for each phase winding (with the magnets "switched off") and the phase current, can be written as,

$$\begin{bmatrix} \lambda_{a|O,AR} \\ \lambda_{b|O,AR} \\ \lambda_{c|O,AR} \end{bmatrix} = \begin{bmatrix} L_{|O} & M_{|O} & M_{|O} \\ M_{|O} & L_{|O} & M_{|O} \\ M_{|O} & M_{|O} & L_{|O} \end{bmatrix} \begin{bmatrix} i_a \\ i_b \\ i_c \end{bmatrix} \tag{4.82}$$

with L_O the self inductance of each phase winding and $M_{|O}$ the mutual inductance between any two phase windings.

For a balanced, three-phase supply (in the case of motor operation), or for a balanced, three-phase load (in the case of generator operation) the inductance matrix in terms of the flux-

linkages and three-phase currents, can be reduced to

$$\begin{bmatrix} \lambda_{a|O,AR} \\ \lambda_{b|O,AR} \\ \lambda_{c|O,AR} \end{bmatrix} = \begin{bmatrix} L_{|O} - M_{|O} & 0 & 0 \\ 0 & L_{|O} - M_{|O} & 0 \\ 0 & 0 & L_{|O} - M_{|O} \end{bmatrix} \begin{bmatrix} i_a \\ i_b \\ i_c \end{bmatrix} \tag{4.83}$$

or simply as

$$\begin{bmatrix} \lambda_{a|O,AR} \\ \lambda_{b|O,AR} \\ \lambda_{c|O,AR} \end{bmatrix} = \begin{bmatrix} L_{s|O} & 0 & 0 \\ 0 & L_{s|O} & 0 \\ 0 & 0 & L_{s|O} \end{bmatrix} \begin{bmatrix} i_a \\ i_b \\ i_c \end{bmatrix} \tag{4.84}$$

with $L_{s|O}$ the three-phase synchronous inductance of the machine.

Assuming a sinusoidal current and flux-linkage, the synchronous inductance, $L_{s|O}$, can be thus be approximated by

$$L_{s|O} = \frac{\Lambda_{a,b,c|O,AR}}{I_p} , \tag{4.85}$$

with I_p the peak value of the phase current, see (2.43) to (2.45). This implies that for the test machine in Appendix E, section E.1, the three-phase stator inductance, $L_{s|O}$, for the Type O winding configuration, with the end-turn effect ignored, would be equal to

$$L_{s|O} = 6{,}55 \text{ mH} . \tag{4.86}$$

4.9 Validation of the Type I Winding Configuration Solution

4.9.1 Magnetic Field Solutions of the Type I Winding Configuration

The *Matplotlib* contour plot of the magnetic vector potential is shown in Figure G.5 with the FEA solution obtained from Maxwell® 2D shown in Figure G.6. In Figure G.7 the *Matplotlib* contour plot of the analytical solution to the magnetic flux-density is shown. The FEA solution obtained from Maxwell® 2D shown in Figure G.8.

In Figure 4.4 and Figure 4.5 which shows the *Matplotlib* plots of the radial – and azimuthal flux-density distributions respectively, the analytically calculated flux-density values are compared with the results obtained from the Maxwell® 2D FEA simulation.

4.9.2 Flux-linkage Calculation of the Type I Winding Configuration

The flux-linkage for the Type I winding configuration can be calculated in a similar fashion as for the Type O winding configuration. The flux-linkage in a single coil turn, due to the magnetic vector potential caused only by the current flowing in the windings, again with the permanent magnets "switched off", can be written as,

$$\lambda_{1|I,AR}(r,\phi) = 2\ell A_{z|O,AR}(r,\phi) . \tag{4.87}$$

The total flux-linkage per phase can be calculated by multiplying the flux-linkage distribution in (4.87) with the conductor density distribution given by (2.78)[1]; then integrating over one coil pitch period and finally multiplying by the number of series connected circuits[2], $\frac{q}{a}$.

[1] Graphically illustrated in Figure 2.13
[2] See explanation in Appendix A.

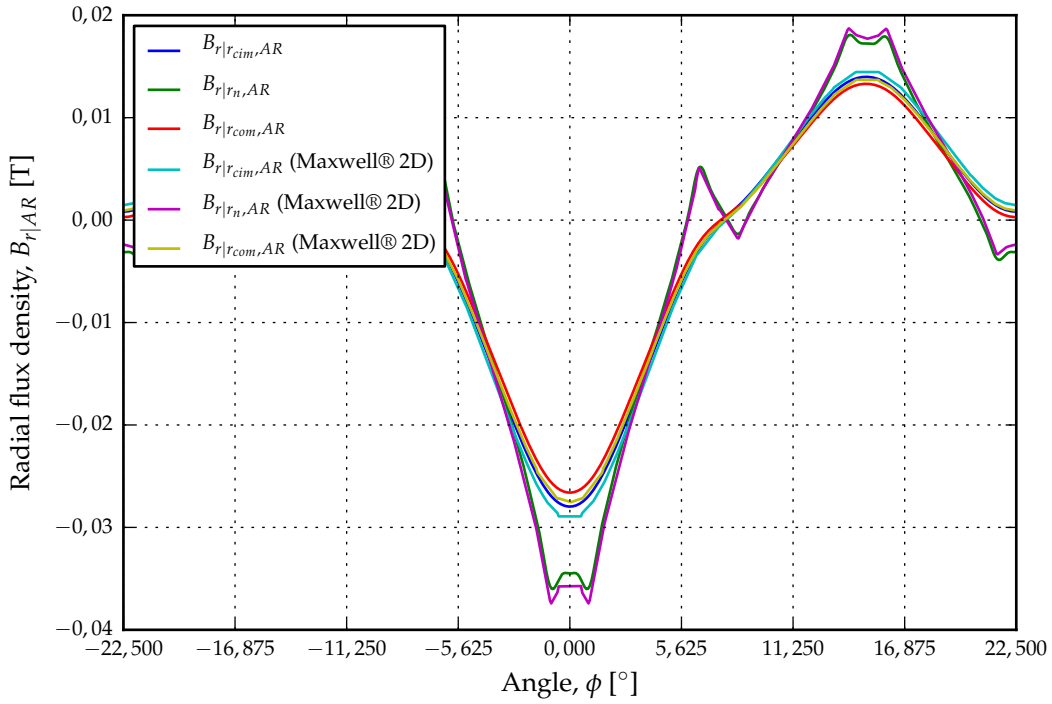

Figure 4.4: Radial flux-density distribution for the Type II winding configuration due to armature reaction.

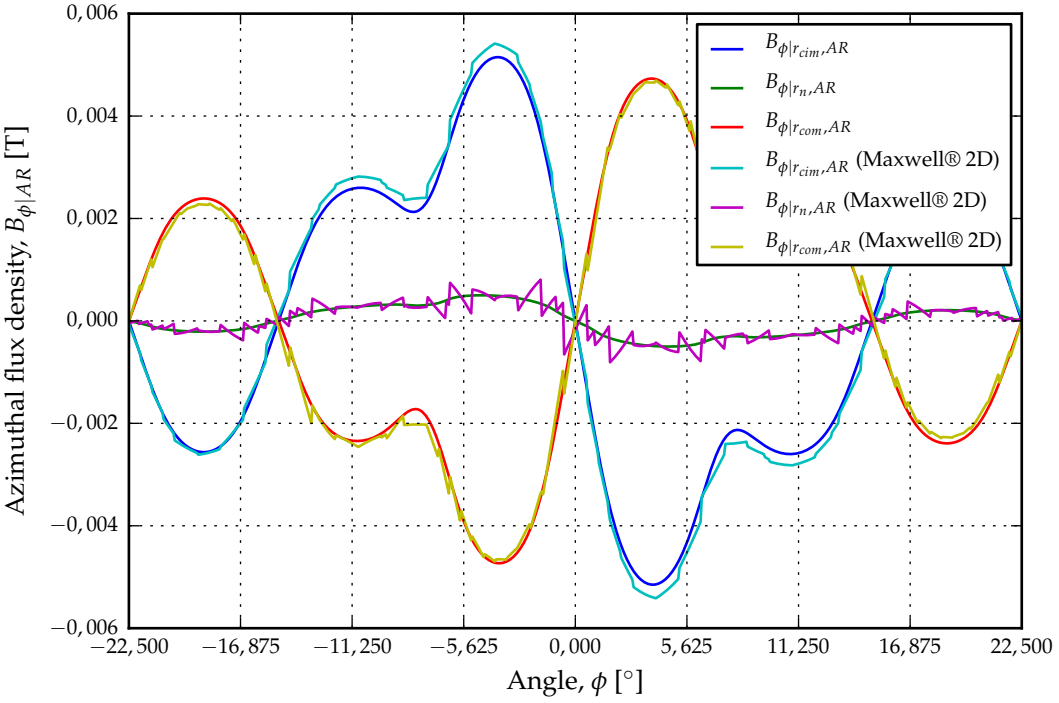

Figure 4.5: Azimuthal flux-density distribution for the Type II winding configuration due to armature reaction.

Again, with the 1–D conductor density distribution taken at $r{=}r_n$, we can assume that the flux-density distribution in the centre of the windings, at $r{=}r_n$, is the same through out. This implies that the peak value of the flux-density distribution for the Type I winding configuration can be calculated as,

$$\Lambda_{a,b,c|I,AR} = \frac{q}{a}\int_{-\frac{\tau_{q|I}}{2}}^{\frac{\tau_{q|I}}{2}} n_{a|I}(\phi)\lambda_{1|I,AR}(r_n,\phi)d\phi \tag{4.88}$$

$$= \frac{2q\ell}{a}\int_{-\frac{\tau_{q|I}}{2}}^{\frac{\tau_{q|I}}{2}} n_{a|I}(\phi)A_{z|I,AR}(r_n,\phi)d\phi\,. \tag{4.89}$$

From (2.78) and (4.62) and substituting 'n' for 'm', we can write

$$A^{III}_{z|I,AR}(r_n,\phi) = \sum_{m=1}^{\infty} b^{III}_{m_{A_{z|I,AR}}}\sin(nq\phi) \tag{4.90}$$

with

$$b^{III}_{m_{A_{z|I,AR}}} = C^{III}_{m|AR}r_n^{mq} + D^{III}_{m|AR}r_n^{-nq} + G_{m|I,AR}(r_n) \tag{4.91}$$

and, from (4.9), using the winding factor for the Type I winding configuration as defined in (2.81), the value of $G_{m|I,AR}(r_n)$ will expand to

$$G_{m|I,AR}(r_n) = \frac{3\mu_0 I_p N r_n}{a\pi hqn^2}k_{w,n|I}\,. \tag{4.92}$$

From (2.78) and (4.90), equation (4.89) can now be written as

$$\Lambda_{a,b,c|I,AR} = \frac{2q\ell}{a}\int_{-\frac{\tau_{q|I}}{2}}^{\frac{\tau_{q|I}}{2}}\sum_{m=1}^{\infty} b_{m_{m_{a|I}}}\sin(mq\phi)\sum_{m=1}^{\infty} b^{III}_{m_{A_{z|I,AR}}}\sin(nq\phi)d\phi \tag{4.93}$$

$$= \frac{2q\ell}{a}\sum_{m=1}^{\infty}\sum_{m=1}^{\infty} b_{m_{m_{a|I}}}b^{III}_{m_{A_{z|I,AR}}}\int_{-\frac{\tau_{q|I}}{2}}^{\frac{\tau_{q|I}}{2}}\sin(mq\phi)\sin(nq\phi)d\phi\,. \tag{4.94}$$

With the coil-pitch of the Type I winding configuration, $\tau_{q|I} = \frac{\pi}{Q}$, the integral term in (4.94) evaluates to zero except where $m = n$, when it evaluates once again to $\frac{\pi}{2q}$, so that (4.94) can be simplified to,

$$\Lambda_{a,b,c|I,AR} = \frac{\pi\ell}{a}\sum_{m=1}^{\infty} b_{m_{m_{a|I}}}b^{III}_{m_{A_{z|I,AR}}}\,. \tag{4.95}$$

This has the same form as the flux-linkage equation of the Type O winding configuration calculated in (4.74), but differs slightly from the flux-linkage of the Type I windings due to effect of the permanent magnets, as calculated in (3.183). For the latter, only the second order space-harmonics were present, but for armature reaction, the first, fifth, seventh, eleventh and thirteenth harmonics are also present as shown in Table 4.3. Only the space-harmonic flux-linkage values up to the thirteenth harmonic are shown and are calculated from (4.95) for the Type I winding configuration.[1].

[1]Again the same rotor configuration as in Appendix E, section E.1 was used

Table 4.3: The flux-linkage component for each space-harmonic for the Type I winding configuration.

Space harmonic, m	$\Lambda_{a,b,c\|I,AR,m}$ [mWbt]
1	23,195
2	17,487
3	–
4	2,936
5	0,392
6	–
7	0,024
8	–
9	–
10	0,052
11	0,022
12	–
13	0,013

The total flux-linkage per phase for the Type I winding configuration, using (4.95), is calculated as $\Lambda_{a,b,c|I,AR}$=44,165 mWbt. If we compare this with the values in Table 4.3 as well as with the result for the Type O winding configuration given in Table 4.2, we can see that the fundamental space-harmonic is not dominant and that the peak value of flux-linkage per phase has to be takes as the sum of all the space-harmonics components. The flux-linkage calculation method for the armature reaction for the Type I winding configuration also differs from the method used to calculate the flux-linkage due to the permanent magnets acting alone (see (3.188)) where the flux-linkage were approximated by using only the second space-harmonic (or working harmonic) value.

As mentioned in section 4.8.2, due to the fact that surface mounted permanent magnets are used with a relative recoil permeability close to unity, the peak value of the flux-linkage will be the same regardless of the rotor position. The magnitude of the flux-linkage will thus only depend on the value of the phase current in each phase winding, so that for a perfectly balanced, three-phase stator current, we can write,

$$\lambda_{a|I,AR}(t) = \Lambda_{a,b,c|I,AR}\cos(\omega t) \tag{4.96}$$

$$\lambda_{b|I,AR}(t) = \Lambda_{a,b,c|I,AR}\cos(\omega t - \tfrac{2\pi}{3}) \quad \text{and} \tag{4.97}$$

$$\lambda_{c|I,AR}(t) = \Lambda_{a,b,c|I,AR}\cos(\omega t - \tfrac{4\pi}{3})\,. \tag{4.98}$$

In Figure 4.6 the analytically calculated flux-linkage waveform for the Type I winding configuration is compared with the waveform obtained from FEA simulations using Maxwell® 2D. Here the analytically calculated flux-linkages are a much closer match than for the values obtained for Type O winding configuration that was shown in Figure 4.3.

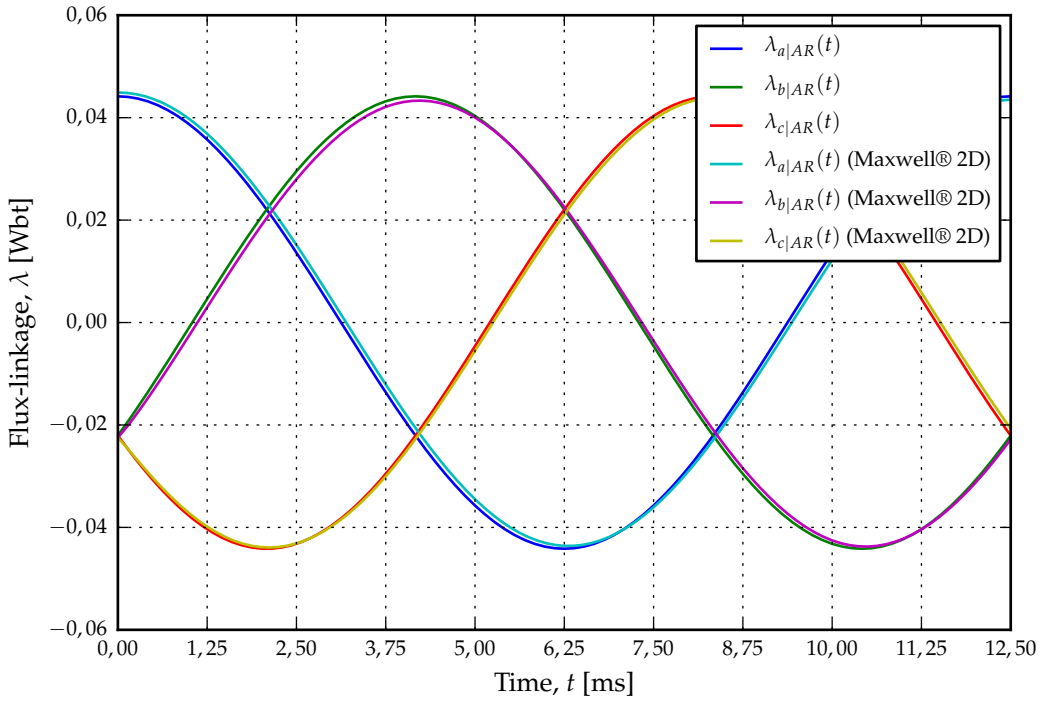

Figure 4.6: Flux-linkages for phase a, b and c for the Type I winding configuration.

4.9.3 Stator Inductance Calculation of the Type I Winding Configuration

Again assuming perfectly balanced, three-phase, sinusoidal currents and flux-linkages, the inductance matrix can be approximated, similarly to section 4.8.3, in terms of the three-phase currents and flux-linkages, as

$$\begin{bmatrix} \lambda_{a|I,AR} \\ \lambda_{b|I,AR} \\ \lambda_{c|I,AR} \end{bmatrix} = \begin{bmatrix} L_{s|I} & 0 & 0 \\ 0 & L_{s|I} & 0 \\ 0 & 0 & L_{s|I} \end{bmatrix} \begin{bmatrix} i_a \\ i_b \\ i_c \end{bmatrix} \tag{4.99}$$

with the three-phase stator inductance

$$L_{s|I} = \frac{\Lambda_{a,b,c|I,AR}}{I_p} \, . \tag{4.100}$$

This implies that for the test machine in Appendix E, section E.1 with non-overlapping, single-layer (Type I) winding configuration, the synchronous inductance, with the end-turn effect ignored, would be equal to

$$L_{s|I} = 6{,}02 \text{ mH} \, . \tag{4.101}$$

4.10 Validation of the Type II Winding Configuration Solution

4.10.1 Magnetic Field Solutions of the Type II Winding Configuration

The *Matplotlib* contour plot of the magnetic vector potential is shown in Figure G.9 with the FEA result from Maxwell® 2D shown in Figure G.10. In Figure G.11 the contour plot of the magnetic flux-density is shown with the FEA result from Maxwell® 2D shown in Figure G.12.

In Figure 4.7 and Figure 4.8 *Matplotlib* plots of the radial and azimuthal flux-density analytical calculations are compared with Maxwell® 2D finite element calculations.

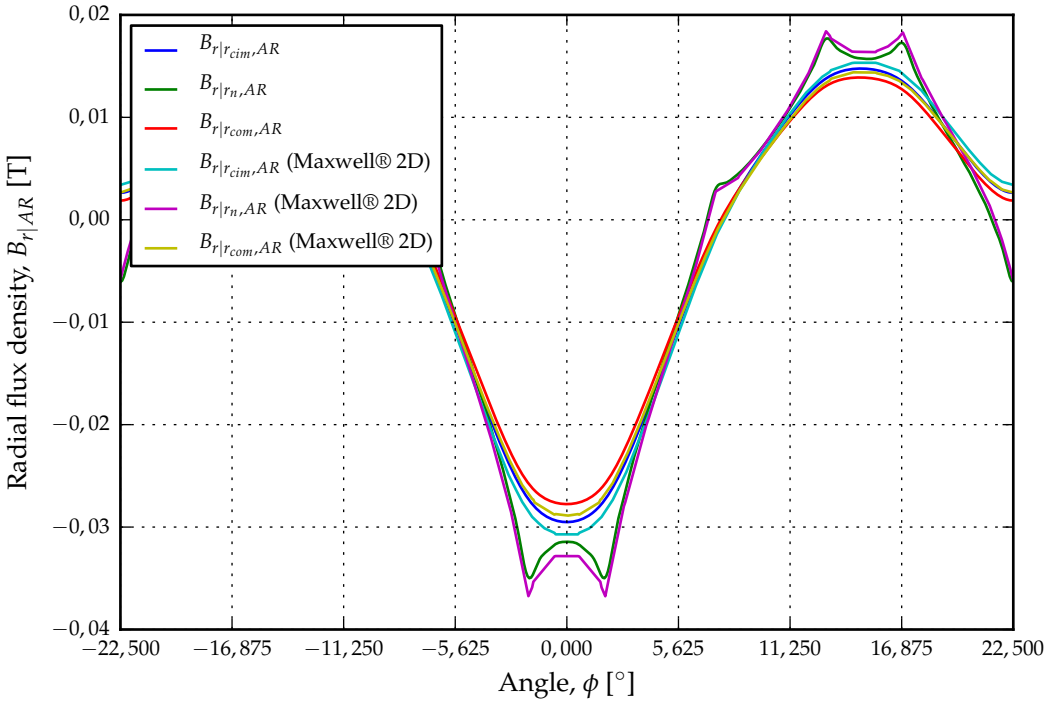

Figure 4.7: Radial Flux-Density Distribution

4.10.2 Flux-linkage Calculation of the Type II Winding Configuration

The flux-linkage calculations for the Type II winding configuration will be similar to that of the Type I winding configuration, so that

$$\Lambda_{a,b,c|II,AR} = \frac{\pi\ell}{a}\sum_{m=1}^{\infty} b_{m_{m_{a|II}}} b^{III}_{m_{A_{z|II,AR}}} \tag{4.102}$$

with

$$b^{III}_{m_{A_{z|II,AR}}} = C^{III}_{m|AR} r_n^{mq} + D^{III}_{m|AR} r_n^{-nq} + G_{m|II,AR}(r_n) \tag{4.103}$$

and

$$G_{m|II,AR}(r_n) = \frac{3\mu_0 I_p N r_n}{a\pi hqn^2} k_{w,n|I}\,. \tag{4.104}$$

The peak value of flux-linkage per phase for the Type II winding configuration can thus be calculated as $\lambda_{a|II,AR,m}$ =57,885 mWbt. If we compared the peak value to the values of the individual space-harmonic components given in Table 4.4, or with the approximation for the flux-linkage due to the permanent magnets alone, (3.193), it is clear neither the first nor the second harmonic is dominant and that all the space-harmonics needs to be taken into account for the accurate calculation of the total flux-linkage per phase for armature reaction.

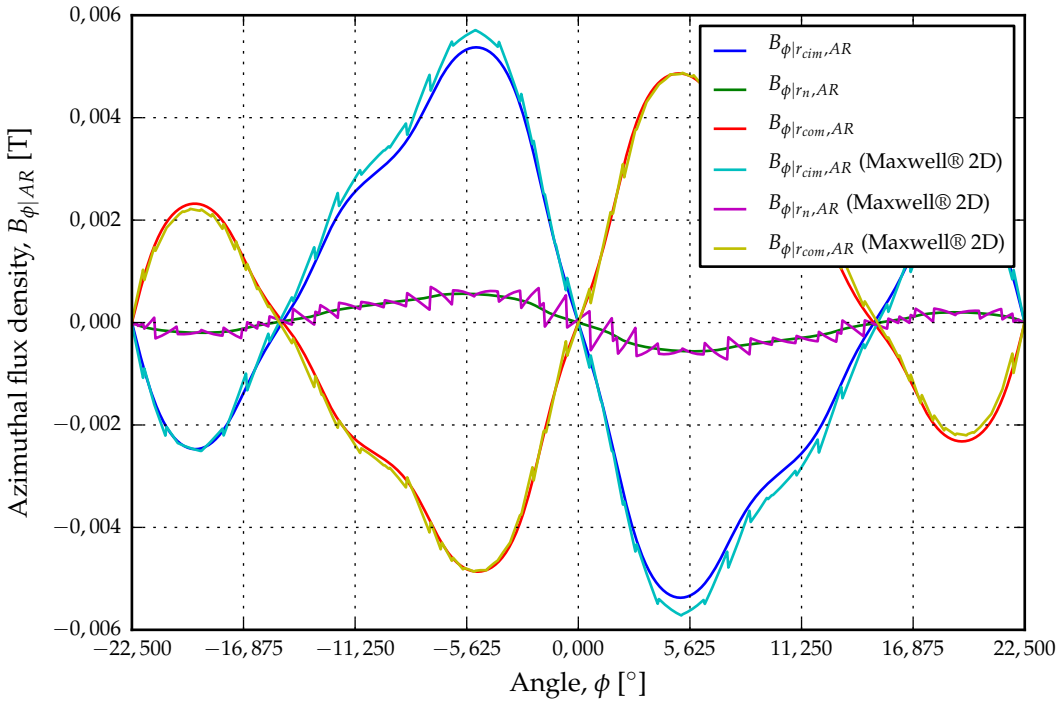

Figure 4.8: Azimuthal Flux-Density Distribution

Table 4.4: The flux-linkage components for each space-harmonic for the Type II winding configuration.

Space harmonic, m	$\lambda_{a\|II,AR,m}$ [mWbt]
1	34,854
2	21,873
3	–
4	0,908
5	0,038
6	–
7	0,096
8	–
9	–
10	0,007
11	0,061
12	–
13	0,030

For a perfectly balanced, three-phase, sinusoidal stator current, we will be able to write,

$$\lambda_{a|II,AR}(t) = \Lambda_{a,b,c|II,AR}\cos(\omega t) \tag{4.105}$$

$$\lambda_{b|II,AR}(t) = \Lambda_{a,b,c|II,AR}\cos(\omega t - \tfrac{2\pi}{3}) \quad \text{and} \tag{4.106}$$

$$\lambda_{c|II,AR}(t) = \Lambda_{a,b,c|II,AR}\cos(\omega t - \tfrac{4\pi}{3})\,. \tag{4.107}$$

In Figure 4.9 the analytically calculated flux-linkages waveforms for the Type II winding configuration are compared with FEA simulated waveforms, using Maxwell® 2D.

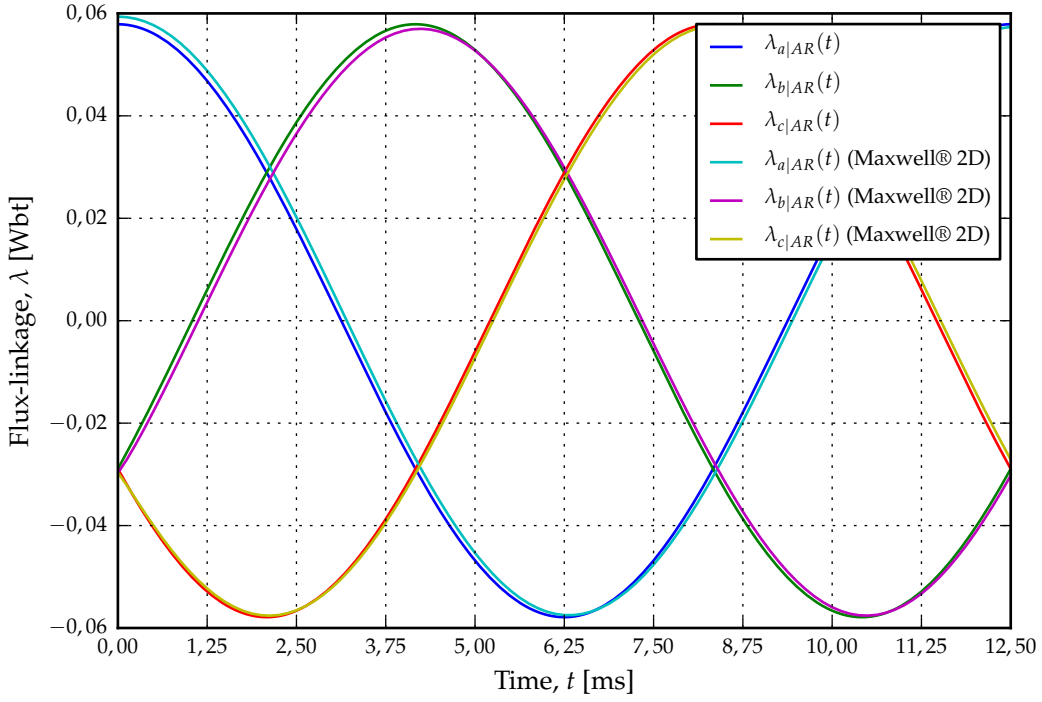

Figure 4.9: Flux-linkages for phase a, b and c for the Type II winding configuration.

4.10.3 Stator Inductance Calculation of the Type II Winding Configuration

Assuming perfectly balanced, three-phase, sinusoidal currents and flux-linkages, the inductance matrix can be approximated, similar to sections 4.8.3 and 4.9.3, in terms of the three-phase currents and flux-linkages, as

$$\begin{bmatrix} \lambda_{a|II,AR} \\ \lambda_{b|II,AR} \\ \lambda_{c|II,AR} \end{bmatrix} = \begin{bmatrix} L_{s|II} & 0 & 0 \\ 0 & L_{s|II} & 0 \\ 0 & 0 & L_{s|II} \end{bmatrix} \begin{bmatrix} i_a \\ i_b \\ i_c \end{bmatrix} \tag{4.108}$$

with the three-phase stator inductance

$$L_{s|II} = \frac{\Lambda_{a,b,c|II,AR}}{II_p} \, . \tag{4.109}$$

This implies that for the test machine in Appendix E, section E.1 with a non-overlapping, double-layer (Type II winding configuration, the synchronous inductance, with the end-turn effect ignored, would be equal to

$$L_{s|II} = 7{,}896 \text{ mH} \, . \tag{4.110}$$

4.11 Summary and Conclusions

In this chapter the flux-linkages for the different winding configuration from the solution of the magnetic vector potential in the centre of the stator region. The flux-linkage values were found to be almost identical to FEA simulation results. With the flux-linkages virtually sinusoidal and in-phase with the sinusoidal phase currents, the synchronous inductances were easy to calculate for the different winding configurations.

For the Type O winding configuration, it was possible to simplify the flux-linkage equation and hence the synchronous inductance equation, due to the dominant first order space-harmonic in the flux-linkage solution. The flux-linkage equation for the Type I and Type II winding configuration, however, could not be simplified, although it would be possible to only consider the dominant first, second and fourth order space-harmonics components.

From the calculation of the synchronous inductances, the value of the Type II winding configuration's synchronous inductance was, as expected, significantly higher ($\approx 31\,\%$) than that of the Type I winding configuration's synchronous inductance, due to its wider coils and hence higher flux-linkage value. The interesting finding, however, was that the synchronous inductance of the Type II winding configuration was also higher ($\approx 21\,\%$) than that of the Type O winding configuration, in spite of the fact that the Type II winding configuration has only half the number of coils per phase. The higher synchronous inductance however can be attributed to the higher number of turns per coil (see section 2.6).

Finally it must be emphasized that the calculation of the synchronous inductances for the different winding configurations excluded the additional inductance that would be caused by the end-turn windings. A method for including these additional end-turn inductances (whether it can be done analytically or empirically), will be left for future work.

CHAPTER 5

Torque Calculation

In speaking of the Energy of the field, however, I wish to be understood literally. All energy is the same as mechanical energy, whether it exists in the form of motion or in that of elasticity, or in any other form. The energy in electromagnetic phenomena is mechanical energy.

JAMES CLERK MAXWELL, 1876

5.1 Introduction

The average torque produced by an electrical machine under steady state conditions be expressed as the average power delivered (for motor operation) or absorbed by the machine (for generator operation) divided by the angular speed of the machine,

$$T_{mech} = \frac{P_{mech}}{\omega_{mech}} \,. \tag{5.1}$$

The calculation of the ripple torque under steady state conditions requires the detailed calculation of the magnetic field produced by the rotor and stator in order to calculate the electromagnetic forces vectors acting on the different parts of the electrical machine. From the different force vector, the resultant torque, including the ripple torque component, produce by the machine can be calculated. The four major methods used for calculating these electromagnetic forces, see Benhama *et al.* [46], are

- the Lorentz method
- the Maxwell stress tensor (MST) method
- the classical virtual work method and
- the Coulomb virtual work (CVW) method.

From the above methods, only the Lorentz method and the MST method can be used to calculate the torque analytically. These two methods are not usually preferred for FEA. The

problem with the Lorentz method is that it can only calculate the electromagnetic forces that act upon the current carrying conductors. This makes it unsuitable for the calculation of cogging torque, or for the calculation of reluctance torque. The Lorentz method is therefore not usually implemented in commercial FE packages. A variation of the Lorentz method was proposed by Kabashima *et al.* [47] which calculates an equivalent current density flowing in a thin layer of thickness around the magnetised element under consideration. In a comparison between the equivalent current density method, the equivalent magnetic charge method, the classical virtual work method and the MST method, Muller [48] found that the accuracy of the equivalent current density method is heavily reliant on the accuracy of the permeability of the magnetic material under consideration.

A generalised equivalent magnetising current method, based on the equivalent current density calculation method, has recently been proposed by Choi *et al.* [49]. The generalised equivalent magnetising current method addresses the problem of calculating the force acting on a magnetised body that is not completely surrounded by air. The MST method suffers form exactly the same problem. Also when working in 3D, the surface integration required by the MST method is a lot more complex to perform compared to the classical virtual work method and the Coulomb virtual work method.

The classical virtual work method, or the more refined version of the classical virtual work method that makes use of co-energy calculations, is only suited for FEA programs. The CVW method is an enhancement of the classical virtual work method, Coulomb [50] and [51] and also uses the co-energy in its calculations. The CVW is the method employed by Ansys' Maxwell® 2D, Lebedev *et al.* [52], to calculate force and hence torque values.

As the RFAPM machine is an air cored machine, either the Lorentz method, or the MST method could be used for an analytical solution of the torque, with the analytical analysis limited to two dimensions only.

5.2 Average Torque Calculation

The average torque can be calculated directly from the equivalent circuit of the RFAPM machine as shown in Figure 5.1. In order to correlate the equivalent circuit with the work done in Chapters 3 and 4, it is important to note that E_{af} in Figure 5.1, is the RMS value of the back-EMFs as defined in equations (3.210) to (3.212), for phase a.

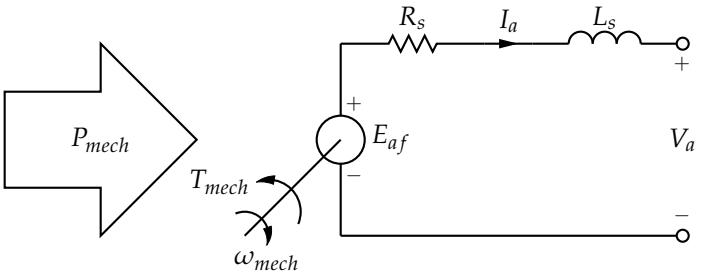

Figure 5.1: The equivalent circuit of the RFAPM machine.

Similarly, L_s corresponds to the inductance calculated in (4.85), (4.100) and (4.109) for the Type O, Type I or the Type II winding configurations respectively. Thus with,

$$X_s = \omega L_s \,, \tag{5.2}$$

we can say that $X_s I_a$ is equal to the voltage induced in the stator windings[1], due to the phase current, I_a, flowing in the windings. In order to simplify the torque calculations, Kamper *et al.* [13] and Randewijk *et al.* [14], we assume that the phase current, I_a is in phase with E_a. From the phasor diagram shown in Figure 5.2, for generator operation, we can see that the phase current, I_a, is actually 180° degrees out of phase with the back EMF, E_a, hence power is being delivered by the machine with the torque produced being negative.

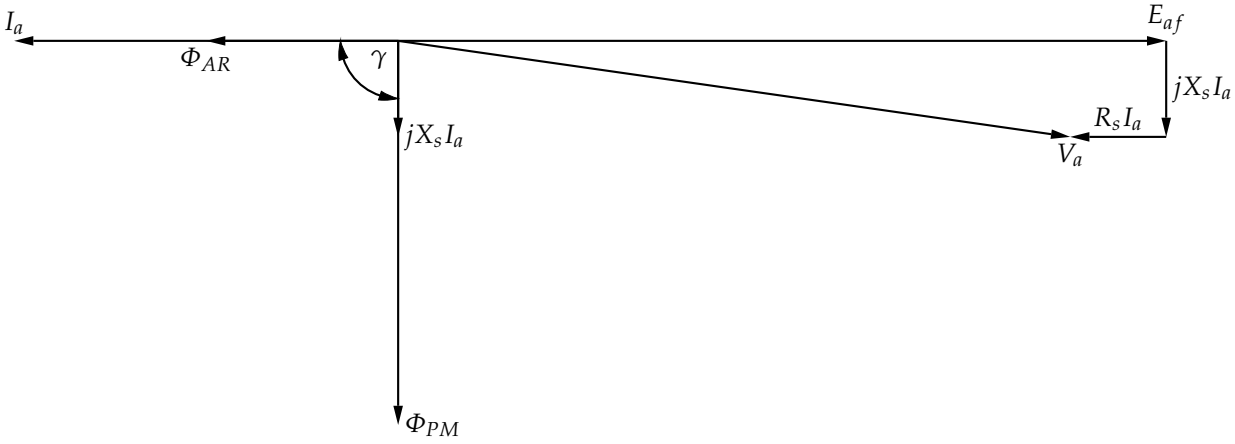

Figure 5.2: The phasor diagram of phase a of the RFAPM machine with I_a and E_a in phase for generator operation *(not to scale)*.

The phasor diagram for motor operation is shown in Figure 5.3. Here, with I_a and E_a in phase, power will be absorbed by the machine and the power delivered will be positive.

This allows us to define the torque produced by the RFAPM machine, while taking cognisance of the direction of power flow, as

$$T_{mech} = \frac{3E_{af}I_a}{\omega_{mech}} \,, \tag{5.3}$$

with I_a the RMS values of the phase current for phase a. From (3.210), (3.211) and (3.212), the average torque can be expressed in terms of the approximated amplitude of the back-EMF voltages, so that we can write,

$$T_{mech|O} = \tfrac{3}{2}k_{E|O}\hat{I}_a \tag{5.4}$$

$$T_{mech|I} = \tfrac{3}{2}k_{E|I}\hat{I}_a \tag{5.5}$$

$$T_{mech|II} = \tfrac{3}{2}k_{E|II}\hat{I}_a \tag{5.6}$$

for the Type O, Type I and Type II winding configurations respectively, with $\hat{I}_a$ the amplitude of the phase current for phase a.

[1] Assuming a perfectly sinusoidal phase current.

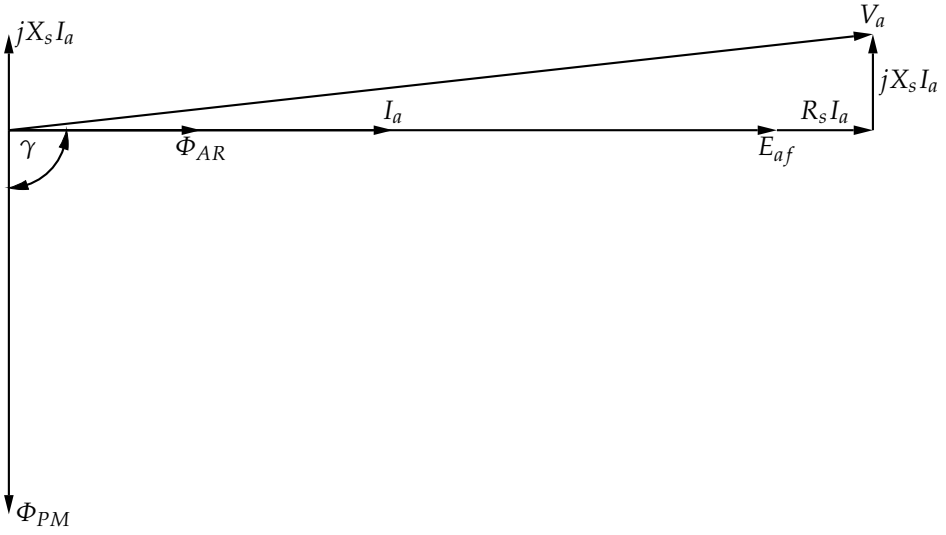

Figure 5.3: The phasor diagram of phase a of the RFAPM machine with I_a and E_a in phase for motor operation *(not to scale)*.

For both motor and generator operation, the angle, γ, between the magnetic axis of the rotor, Φ_{PM}, and that of the stator, Φ_{AR}, must be maintained at 90°, for equations (5.4), (5.5) and (5.6) to be true. This is usually achieved by field orientated control for either motor or generator mode of operation. As mentioned in Chapter 2, the Φ_{PM} and Φ_{AR} axes correspond to the d-axes, d_r and d_s respectively as shown in Figures 2.1, 2.11 and 2.18 for the Type O, Type I and Type II winding configurations respectively.

With $\gamma = 90°$, we can also define the torque for a Double-sided Rotor RFAPM machine generically in terms of the peak value of the stator current space vector, $\hat{I}_s$, Slemon [20] and Mohan [43], as

$$T_{mech} = k_T \hat{I}_s \tag{5.7}$$

with the torque constants defined as

$$k_{T|O} = k_{E|O} = \frac{2qr_n\ell N}{a} k_{w,1|O} B_{r,1} \,, \tag{5.8}$$

$$k_{T|I} = k_{E|I} = \frac{2qr_n\ell N}{a} k_{w,2|I} B_{r,1} \quad \text{and} \tag{5.9}$$

$$k_{T|II} = k_{E|II} = \frac{2qr_n\ell N}{a} k_{w,2|II} B_{r,1} \tag{5.10}$$

from (3.216), (3.217) and (3.218) for the Type O, Type I and the Type II windings respectively, and the stator current space vector

$$\hat{I}_s = \tfrac{3}{2}\hat{I}_a \,. \tag{5.11}$$

We can see that the torque constants are exactly the same as the voltage factors defined in Chapter 3, with the only difference that the units for the torque constants are Nm/A versus the V/rad/s used for the voltage factors. This is consistent with the definition of the voltage and torque constant for Sinusoidal Permanent Magnet AC (commonly referred to as brushless

DC) Machines, given by Mohan [43, Chapter 10]. This implies that the same control principles applicable to brussless DC machines, can be used for the control of the Double-side Rotor RFAPM machine.

5.3 Ripple Torque Calculation using the Lorentz Method

The Lorentz method provides a quick and easy way to calculate the torque ripple under steady steady state conditions. With ω_m constant, the torque is calculated by using only the analytical solution for the magnetic fields produced by the permanent magnets in the stator region, together with the current density distribution function of the stator windings, Holm [24].

From Lorentz's law, the volumetric force density, as defined by Muller [48], can be calculated as follows

$$\vec{\mathbf{f}}_v = \vec{\mathbf{J}} \times \vec{\mathbf{B}} \,. \tag{5.12}$$

With the current density distribution in the stator region,

$$\vec{\mathbf{J}}_z = J_z \vec{\mathbf{a}}_z \tag{5.13}$$

only defined in the axial or z-axis direction and the flux density defined only in the radial and azimuthal, or r – and ϕ-axis directions, (5.12) can be written as

$$\vec{\mathbf{f}}_v = -J_z B_\phi \vec{\mathbf{a}}_r + J_z B_r \vec{\mathbf{a}}_\phi \tag{5.14}$$

$$= f_r \vec{\mathbf{a}}_r + f_\phi \vec{\mathbf{a}}_\phi \tag{5.15}$$

Only the azimuthal component of the volumetric force density, f_ϕ will contribute to "useful" torque. The volumetric torque density distribution developed by the electrical machine will thus be equal to

$$\vec{\boldsymbol{\rho}}_v = \vec{\mathbf{r}} \times \vec{\mathbf{f}}_v \tag{5.16}$$

$$= r J_z B_r \vec{\mathbf{a}}_z \,. \tag{5.17}$$

with $\vec{\mathbf{r}}$ the radial vector from the centre of the machine.

The nett electromagnetic or mechanical torque, T_{mech}, can then be calculated by integrating the volumetric torque density distribution over the entire stator volume, so that

$$T_{mech} = \int_v \rho_{v,z} \, dv \tag{5.18}$$

$$= \ell \int_{r_n - \frac{h}{2}}^{r_n + \frac{h}{2}} \int_0^{2\pi} r^2 J_z B_r \, d\phi \, dr \,. \tag{5.19}$$

5.3.1 The Simplified Lorentz Method for the Ripple Torque Calculation

The calculation of to the torque and specifically the torque ripple in the machine can be simplified, if we, once again, assume that the radial flux-density in the centre of the stator windings, i.e. at radius $r{=}r_n$, can be considered to be constant throughout the whole stator region. This implies that (5.19) can be simplified to

$$T_{mech} = r_n^2 h \ell \int_0^{2\pi} J_z B^{III}_{r,m|r=r_n,PM} \, d\phi \,. \tag{5.20}$$

This assumption was also made in both sections 3.12 and 3.13 where both the flux-linkage and back EMF due to the permanent magnets were calculated respectively and yielded good correlation with the results obtained using Maxwell® 2D.

5.3.1.1 The Simplified Lorentz Method for the Ripple Torque Calculation for the Type O Winding Configuration

From (2.51), for the three phase current density distribution of the Type O winding configuration and substituting "n" for "m" and "$p\omega_{mech}$" for "ω" we have

$$J_{z_{|O}} = \begin{cases} -\frac{3qI_pN}{ar_nh\pi}\sum_{n=1}^{\infty} k_{w,n|O}\sin\left(nq\phi + p\omega_{mech}t\right) & \text{for } n{=}3k{-}2,\ k\in\mathbb{N}_1 \\ -\frac{3qI_pN}{ar_nh\pi}\sum_{n=2}^{\infty} k_{w,n|O}\sin\left(nq\phi - p\omega_{mech}t\right) & \text{for } n{=}3k{-}1,\ k\in\mathbb{N}_1 \end{cases}. \tag{5.21}$$

For our analysis we will, similar to that used in Chapter 4, adopt the following short hand notation for (5.21)

$$J_{z_{|O}} = -\frac{3qI_pN}{ar_nh\pi}\sum_{n=1}^{\infty} k_{w,n|O}\sin\left(nq\phi \pm \omega_{mech}t\right) \tag{5.22}$$

in order to reduce the writing.

From the three phase current density distribution shown in Figure 2.8, it is clear that the d–, or magnetic axis of (5.22), is located at 0° [electr.], whereas the d–, or magnetic axis of the radial magnetisation distribution, as shown in Figure 3.2, is located a 90° [electr.].

Thus from (3.147), the rotating radial flux-density in the centre of the stator windings with $r{=}r_n$ written in terms of the speed of rotation, ω_{mech} and the relative angle between the d-axis of the rotor (i.e. the rotating radial flux-density) and stator (i.e. the rotating three phase current density distribution), γ, can be give by the following equation

$$B^{III}_{r|r=r_n,PM}(r_n,\phi) = -\sum_{m=1,3,5,\ldots}^{\infty} B^{III}_{r,m|r=r_n,PM}\cos(mp\phi + mp\omega_{mech}t + m\gamma) \tag{5.23}$$

with

$$B^{III}_{r,m|r=r_n,PM} = -\frac{mp}{r_n}\left(C^{III}_{m|PM}r_n^{mp} + D^{III}_{m|PM}r_n^{-mp}\right). \tag{5.24}$$

However, with the requirement that $\gamma{=}90°$ [elect.] as was mentioned in section 5.2, (5.23) can be simplified to

$$B^{III}_{r|PM}(r_n,\phi) = \sum_{m=1,3,5,\ldots}^{\infty} B^{III}_{r,m|r=r_n,PM}\sin(mp\phi + mp\omega_{mech}t), \tag{5.25}$$

which will be equal to the rotating radial flux-density for generator operation. For motor operation, the rotating radial flux-density will just be the negative of (5.25).

The simplified torque equation, using the Lorentz method, can thus be obtained by substituting (5.21) and (5.25) into (5.20):

$$T_{mech|O} = -\frac{3qr_n\ell NI_p}{a\pi}\int_0^{2\pi}\sum_{n=1}^{\infty}k_{w,n|O}\sin\left(nq\phi \pm p\omega_{mech}t\right)\cdot \sum_{m=1,3,5,\ldots}^{\infty}B^{III}_{r,m|r=r_n,PM}\sin(mp\phi + mp\omega_{mech}t)\,d\phi \tag{5.26}$$

$$= -\frac{3qr_n\ell NI_p}{a\pi}\sum_{n=1}^{\infty}\sum_{m=1,3,5,\ldots}^{\infty}k_{w,n|O}B^{III}_{r,m|r=r_n,PM}\cdot \int_0^{2\pi}\sin\left(nq\phi \pm p\omega_{mech}t\right)\sin(mp\phi + mp\omega_{mech}t)\,d\phi \tag{5.27}$$

With $p{=}q$, the integral term evaluates to zero everywhere except where $n{=}m$. This allows us to define a function, say S_m,

$$S_m = \begin{cases}\cos\left((m{-}1)p\omega_{mech}t\right) & \text{for } m{=}6k{+}1,\ k\in\mathbb{N}_0\\ \sin\left((m{+}1)p\omega_{mech}t\right) & \text{for } m{=}6k{-}1,\ k\in\mathbb{N}_1\end{cases} \tag{5.28}$$

so that (5.27) can be simplifies to:

$$T_{mech|O} = -\frac{3qr_n\ell NI_p}{a}\sum_{m=1,5,7\ldots}^{\infty}k_{w,m|O}B^{III}_{r,m|r=r_n,PM}S_m\ . \tag{5.29}$$

If we only consider the fundamental component of the winding factor and the radial flux density, i.e at $m{=}1$, we find that $S_m{=}1$ and equation (5.29) simplifies to be equal to (5.4) as expected.

In Figure 5.4, a *Matplotlib* plot of the torque waveform, for the Type O winding configuration as a function of time, calculated using the simplified Lorentz method, compared with the torque waveform obtained using Maxwell® 2D, together with the calculated average torque component. From the plot it is clear that although the average torque value calculated using the simplified Lorentz method and that obtained using Maxwell® 2D are almost equal,[1] the shape of the torque ripple waveform is however totally different.

5.3.1.2 The Simplified Lorentz Method for the Ripple Torque Calculation for the Type I Winding Configuration

The simplified Lorentz method yields the following equation for the torque develped by the Type I winding configuration,

$$T_{mech|I} = \frac{-3qr_n\ell NI_p}{a}\sum_{m=1,3,5,\ldots}^{\infty}k_{w,2m|I}B^{III}_{r,m|r=r_n,PM}S_m\ . \tag{5.30}$$

Considering only the fundamental component of the radial flux density, i.e for $m{=}1$, (5.30) simplifies, as would be expected, to (5.5). It is also interesting to note that with $k_q{=}\frac{q}{p}{=}\frac{1}{2}$, only the even harmonic components of the winding factor, $k_{w,m|I}$, contribute to the torque ripple.

[1] The average torque value of the Type O winding configuration calculated using the simplified Lorentz method is $\approx 5\,\%$ higher than that obtained from the FEA using Maxwell® 2D.

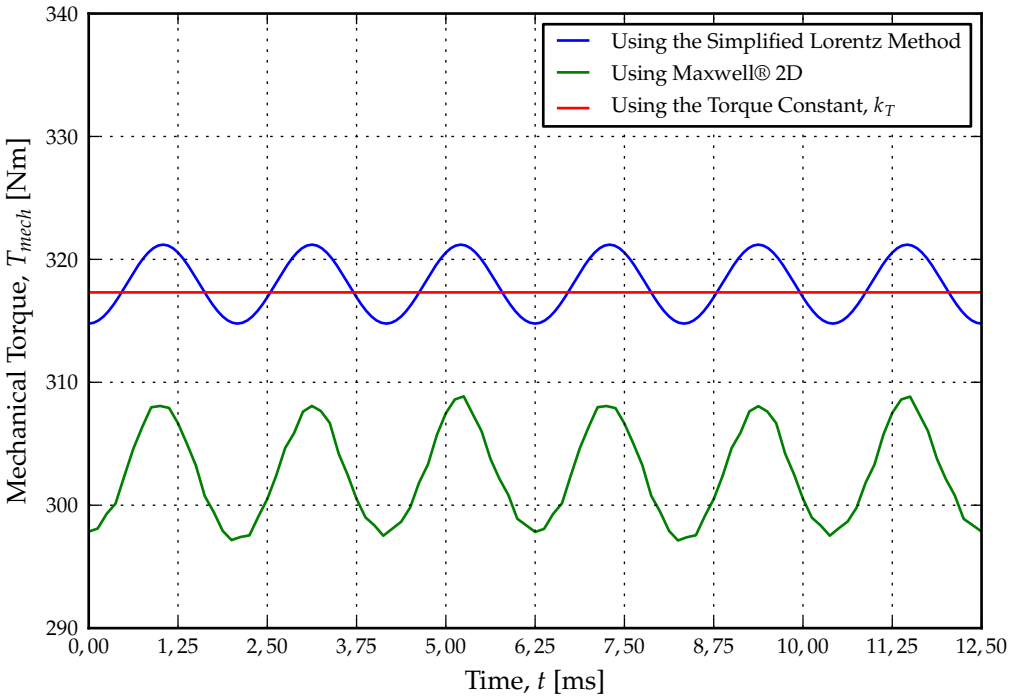

Figure 5.4: The torque waveform using the simplified Lorentz method for the Type O winding configuration compared to the Maxwell® 2D simulation.

Figure 5.5 shows the torque waveforms as a function of time calculated with the simplified Lorentz method, obtained using FEA in Maxwell® 2D, as well as the simplified average torque component. Once again it can be seen that although the average values of the torque waveforms compare well[1], the shape of the torque waveforms differs.

5.3.1.3 The Simplified Lorentz Method for the Ripple Torque Calculation for the Type II Winding Configuration

The torque waveform calculated using the simplified Lorentz method, for the Type II winding configuration can be given by the following equation,

$$T_{mech|II} = \frac{-3qr_n\ell NI_p}{a}\sum_{m=1,3,5,\ldots}^{\infty} k_{w,2m|II}B^{III}_{r,m|r=r_n,PM}S_m \,. \tag{5.31}$$

(5.31) also simplifies to (5.6) at the fundamental component of the radial flux-density, i.e. with m=1. Similar to the Type I winding configuration, when k_q=$\frac{q}{p}$=$\frac{1}{2}$, only the even harmonic components of the winding factor, $k_{w,m|II}$, contribute to the torque ripple.

In Figure 5.6, the output torque waveforms, all as a function of time, is shown for the simplified Lorentz method calculation, together with torque waveform obtained in FEA, using Maxwell® 2D, as well as the simplified average torque component. Again, the average value of the torque waveform calculated using the simplified Lorentz method, closely matches the

[1]The average value of the torque for the Type I winding configuration using the simplified Lorentz method is only $\approx$ 1,0 % higher than that calculated using Maxwell® 2D.

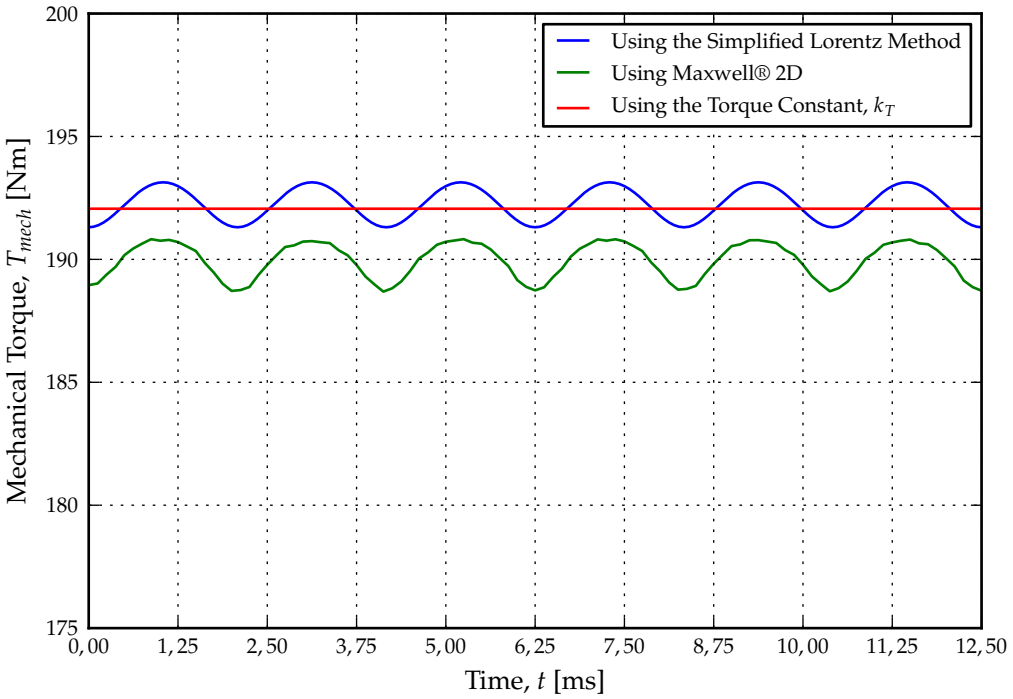

Figure 5.5: The torque waveform using the simplified Lorentz method for the Type I winding configuration compared to the Maxwell® 2D simulation.

average of the simulated Maxwell® 2D waveform[1], with only the shape of the waveforms that differs.

5.3.1.4 Conclusions Regarding the Simplified Lorentz Method for the Ripple Torque Calculation

Although (5.20) yields three elegant looking equations, (5.29), (5.30) and (5.31) that closely matches (5.4), (5.5) and (5.6) for the Type O, Type I and Type II winding configurations respectively, the shape of the torque waveform obtained using these equations does not compare favourably with the waveforms of the torque simulated in Maxwell® 2D. This can be attributed to the radial flux density which is not constant throughout the stator region.

In Figure 5.7, the analytically calculated radial flux-density, as calculated using (3.147)[2], is compared with the simulated radial flux-density values obtained using Maxwell® 2D. Where can clearly see that the flux-density distribution varies from sinusoidal in the centre of the stator windings, to trapezoidal on the inner and outer boundary between the stator windings and the two air gaps.

5.3.2 The Exact Lorentz Method for the Ripple Torque Calculations

From the conclusion of the section 5.3.1.4, it stands to reason that the torque could be calculated more accurately using the analytical solution for the radial flux density obtained in (3.147) as a

[1]The average value of the torque for the Type II winding configuration using the simplified Lorentz method is only $\approx$ 1,3 % higher than that calculated using Maxwell® 2D.
[2]Only using the equation for Region III, i.e. the stator region.

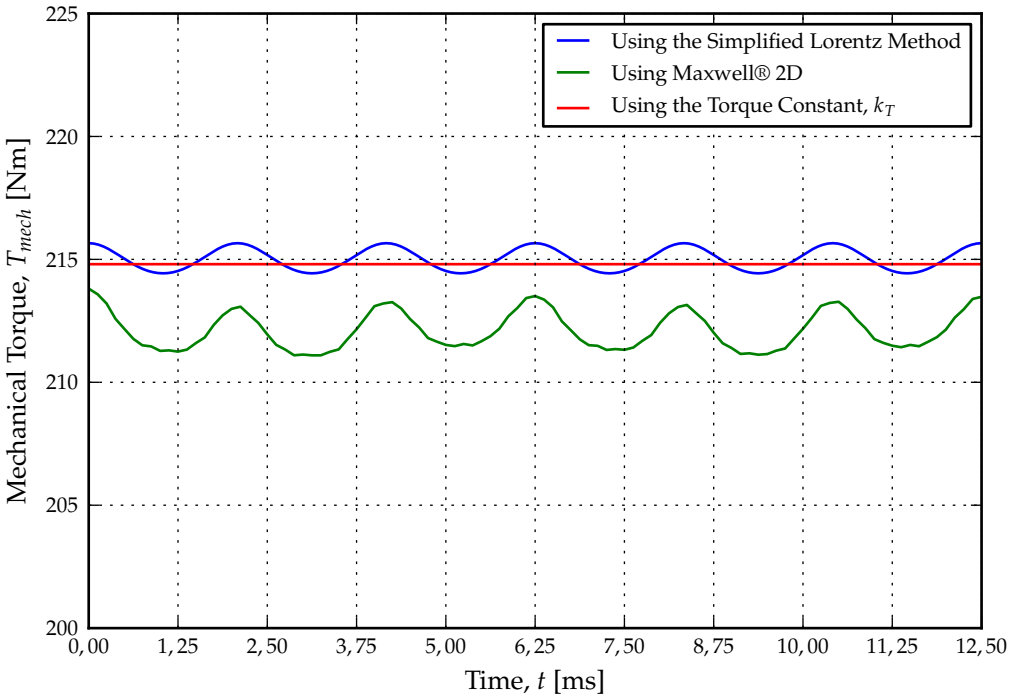

Figure 5.6: The torque waveform using the simplified Lorentz method for the Type I winding configuration compared to the Maxwell® 2D simulation.

function of the radius, r, instead of only considering the solution at $r{=}r_n$.

$$B^{III}_{r|PM}(r,\phi) = \sum_{m=1,3,5,\ldots}^{\infty} B^{III}_{r|PM} \sin(mp\phi + mp\omega_{mech}t) \tag{5.32}$$

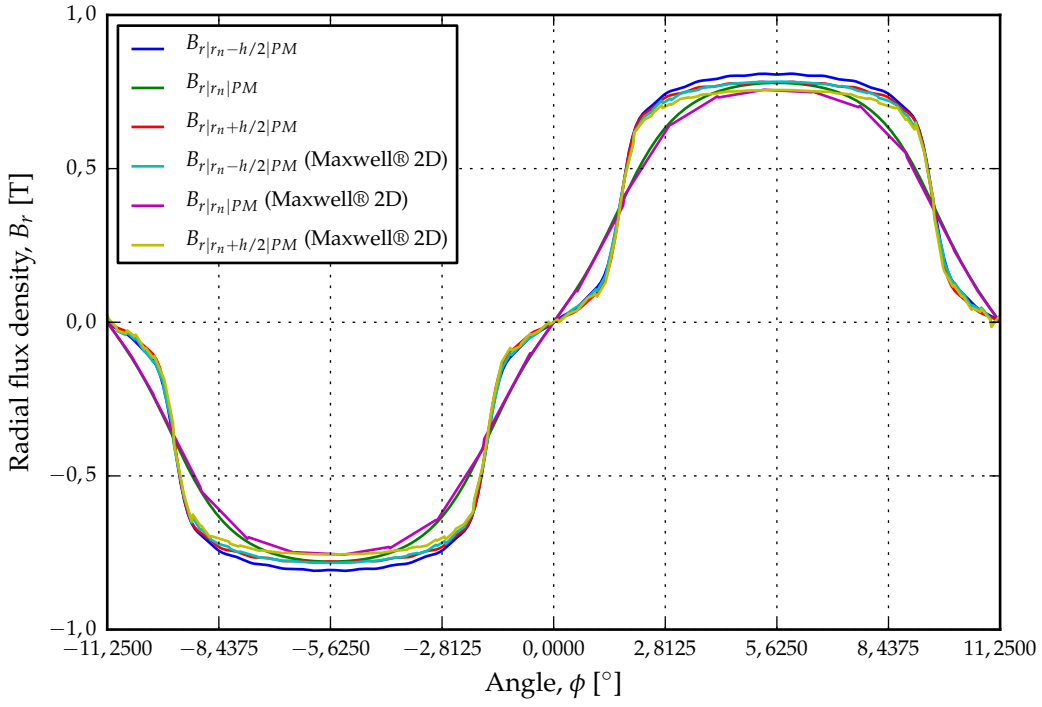

Figure 5.7: The radial flux-density in at the top, centre and bottom of the stator windings.

with

$$B^{III}_{r|PM} = -\frac{mp}{r}\left(C^{III}_{m|PM}r^{mp} + D^{III}_{m|PM}r^{-mp}\right). \tag{5.33}$$

As were are only interested in the solution to the radial flux-density in the stator region, i.e. Region III, only coefficients $C^{III}_{m|PM}$ and $D^{III}_{m|PM}$ needs to be considered. The solution for the radial flux density is then integrated over the entire stator region as is required for the exact solution using the Lorentz method, see (5.19).

5.3.2.1 The Exact Lorentz Method for the Ripple Torque Calculation for the Type O Winding Configuration

Substituting (5.21) and (5.32) into (5.19), the following equation is obtained

$$\begin{aligned} T_{mech|O} = -\frac{3q\ell NI_p}{ar_n h\pi}\int_{r_n-\frac{h}{2}}^{r_n+\frac{h}{2}}\int_0^{2\pi} & \sum_{n=1}^{\infty} k_{w,n|O}\sin\left(nq\phi \pm p\omega_{mech}t\right)\cdot \\ & \sum_{m=1,3,5,\ldots}^{\infty} mpr\left(C^{III}_{m|PM}r^{mp} + D^{III}_{m|PM}r^{-mp}\right) \\ & \sin(mp\phi + mp\omega_{mech}t)\,d\phi\,dr\,, \end{aligned} \tag{5.34}$$

which can be rewritten as

$$\begin{aligned} T_{mech|O} = -\frac{3q\ell NI_p}{ar_n h\pi}\sum_{n=1}^{\infty}\sum_{m=1,3,5,\ldots}^{\infty} k_{w,n|O}\int_{r_n-\frac{h}{2}}^{r_n+\frac{h}{2}} & mpr\left(C^{III}_{m|PM}r^{mp} + D^{III}_{m|PM}r^{-mp}\right)dr\cdot \\ & \int_0^{2\pi}\sin\left(nq\phi \pm p\omega_{mech}t\right)\sin(mp\phi + mp\omega_{mech}t)\,d\phi\,. \end{aligned} \tag{5.35}$$

Integrating with respect to r yields

$$\begin{aligned} T_{mech|O} = \frac{3q\ell NI_p}{ar_n h\pi}\sum_{n=1}^{\infty}\sum_{m=1,3,5,\ldots}^{\infty} k_{w,n|O}\, mp & \left[\frac{C^{III}_{m|PM}r^{mp+2}}{mp+2} - \frac{D^{III}_{m|PM}r^{-mp+2}}{mp-2}\right]_{r_n-\frac{h}{2}}^{r_n+\frac{h}{2}}\cdot \\ & \int_0^{2\pi}\sin\left(nq\phi \pm p\omega_{mech}t\right)\sin(mp\phi + mp\omega_{mech}t)\,d\phi \end{aligned} \tag{5.36}$$

and noting that the integral with respect to ϕ only has a solution when $n{=}m$, the solution to the exact analytical torque calculation using the Lorentz methods reduces to

$$T_{mech|O} = -\frac{3q\ell NI_p}{ar_n h}\sum_{m=1,3,5,\ldots}^{\infty} k_{w,m|O}R_m S_m \tag{5.37}$$

with

$$R_m = \int_{r_n-\frac{h}{2}}^{r_n+\frac{h}{2}} r^2\cdot\frac{mp(C^{III}_{m|PM}r^{mp} + D^{III}_{m|PM}r^{-mp})}{r}\,dr \tag{5.38}$$

$$= mp\left[\frac{C^{III}_{m|PM}r^{mp+2}}{mp+2} - \frac{D^{III}_{m|PM}r^{-mp+2}}{mp-2}\right]_{r_n-\frac{h}{2}}^{r_n+\frac{h}{2}} \tag{5.39}$$

and S_m as defined in (5.28).

In Figure 5.8 the output torque waveform obtained using (5.37) is shown compared to that obtained using Maxwell® 2D. It can be seen that the torque ripple component has the same shape and magnitude for both the analytical and FEM solutions. This implies that the harmonic contents of both should be similar. This is confirmed in Figure 5.9, where the harmonic components of the analytical solution is compared to the solution obtained using Maxwell® 2D.

It is interesting to note the dominance of the sixth order harmonics for both solutions (i.e 6, 12 and 18). Maxwell® 2D is also sporting a second order harmonic which, is absent in the analytical solution, but this will be discussed in more detail in section 5.3.2.3.

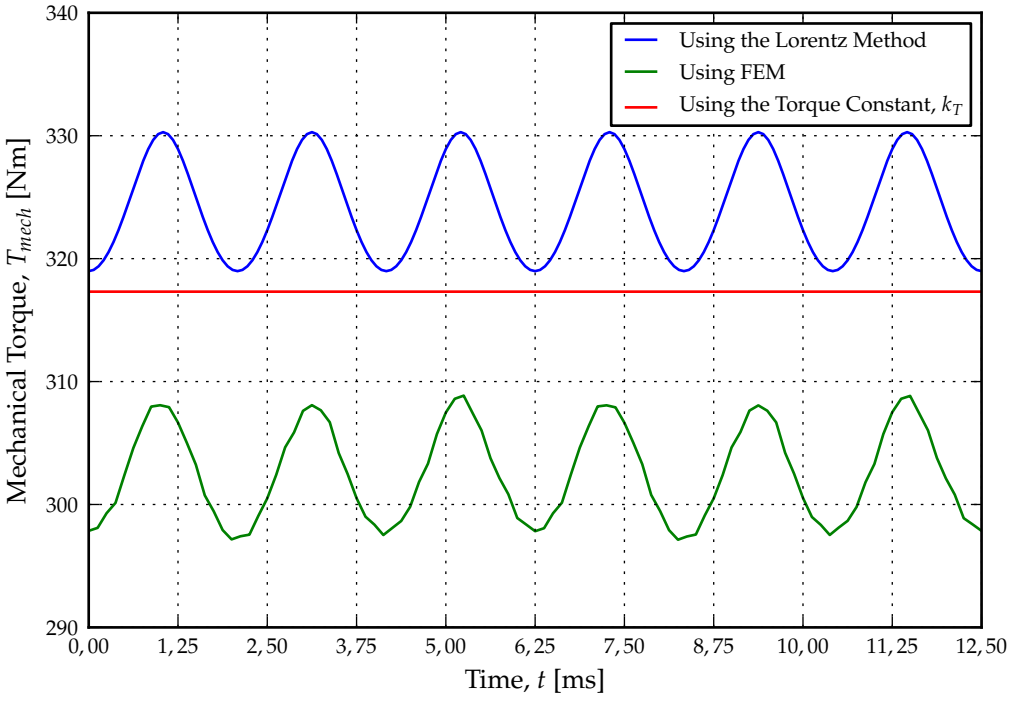

Figure 5.8: The torque ripple waveforms for the Type O winding configuration.

5.3.2.2 The Exact Lorentz Method for the Ripple Torque Calculation for the Type I Winding Configuration

Using the same approach as in section 5.3.2.1 above, the torque calculation for the Type I winding configuration will yield the following equation,

$$T_{mech|I} = -\frac{3q\ell N I_p}{a r_n h} \sum_{m=1,3,5,\ldots}^{\infty} k_{w,2m|I} R_m S_m \tag{5.40}$$

with S_m and R_m as defined in (5.28) and (5.39) respectively.

In Figure 5.10 the output torque waveform of a RFAPM machine with a Type I winding configuration, calculated using the Lorentz method is compared with the simulated torque waveform obtained using Maxwell® 2D, as well as with the average torque calculated using equation (5.5).

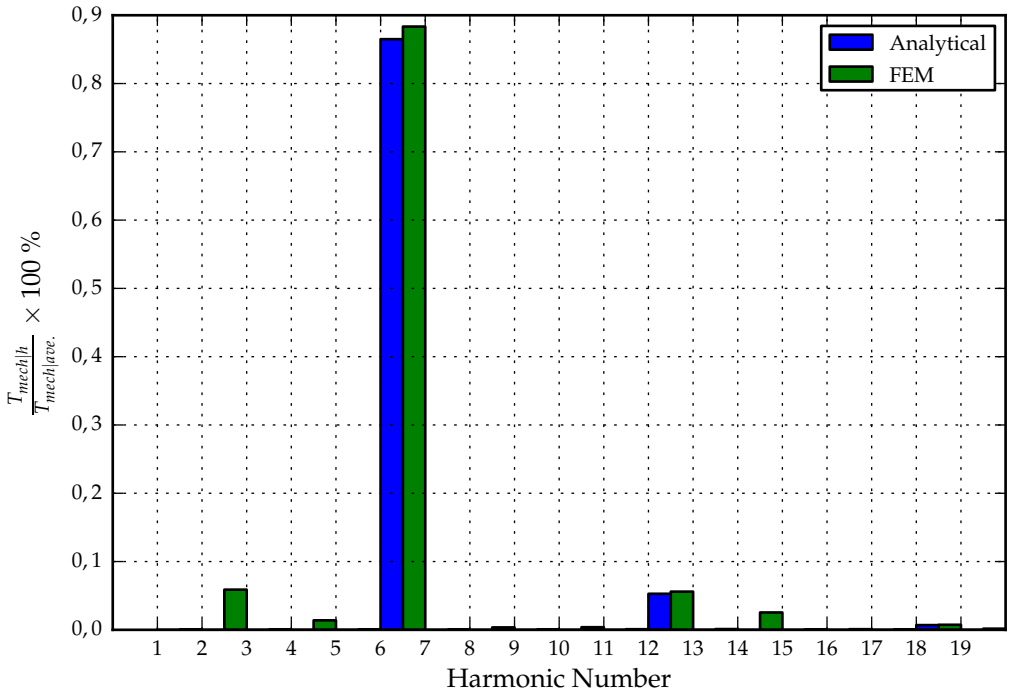

Figure 5.9: A FFT of the torque ripple harmonics for the Type O winding configuration.

Figure 5.10 shows that, although the average torque value of the analytically calculated torque waveform using the Lorentz method is slightly higher than that of the torque calculated

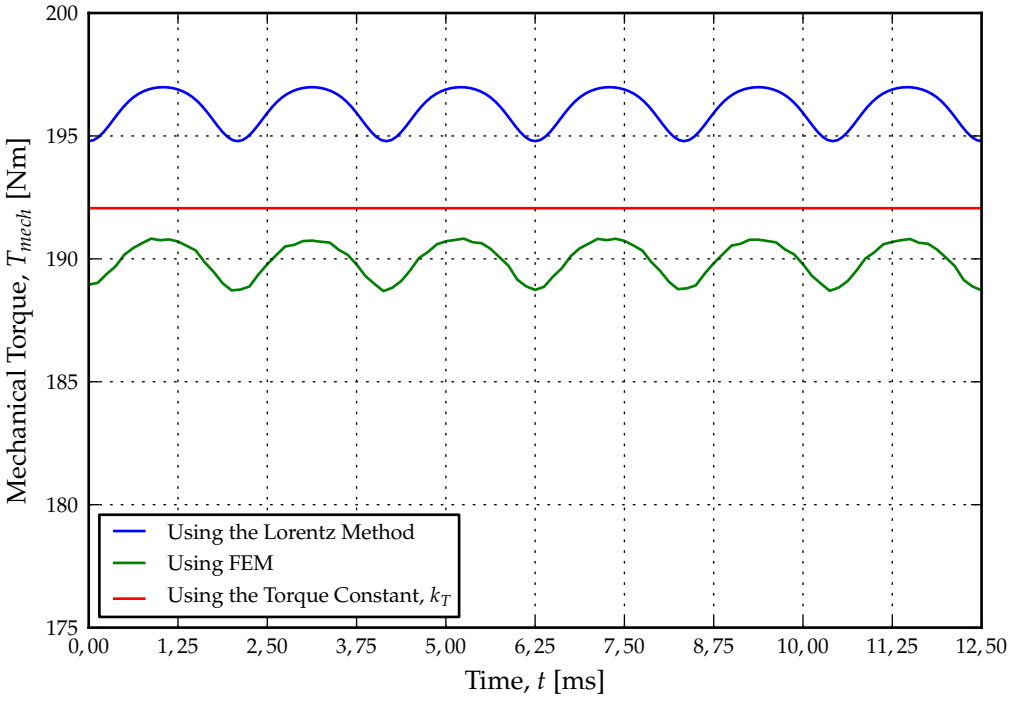

Figure 5.10: The torque ripple waveforms for the Type I winding configuration.

using Maxwell® 2D, the shape of the torque ripple is almost exactly the same. This is confirmed by the harmonic content of the two solutions, as shown in Figure 5.11.

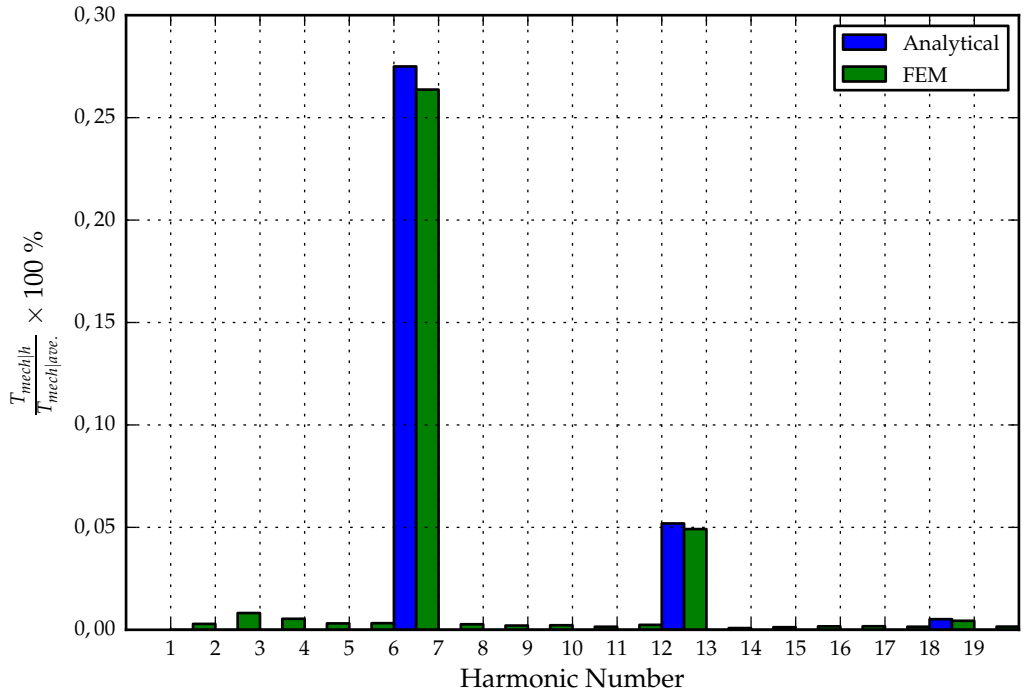

Figure 5.11: A FFT of the torque ripple harmonics for the Type I winding configuration.

5.3.2.3 The Exact Lorentz Method for the Ripple Torque Calculation for the Type II Winding Configuration

Again using the same approach as in section 5.3.2.1, the torque calculation for the Type I winding configuration is given by the following equation,

$$T_{mech|II} = -\frac{3q\ell N I_p}{a r_n h} \sum_{m=1,3,5,\ldots}^{\infty} k_{w,2m|II} R_m S_m \tag{5.41}$$

with S_m and R_m once again as defined in (5.28) and (5.39) respectively.

In Figure 5.12 the analytically calculated torque waveform using the Lorentz method is compared with that using Maxwell® 2D. Once again the Lorentz method yield a slightly higher average value compared to the Maxwell® 2D simulation. The shape of the torque ripple is almost exactly the same, except for a second order harmonic component present in the Maxwell® 2D solution as shown in Figure 5.14. This second order harmonic was also present in torque waveform of the Maxwell® 2D simulation for the Type O winding configuration, shown in Figure 5.9, but not in torque waveform of the Type I winding configuration, shown Figure 5.11.

Torque result of the Type II winding configuration differs the most compared to the Maxwell® 2D simulation. In order to validate the the Type II winding configuration's torque result,

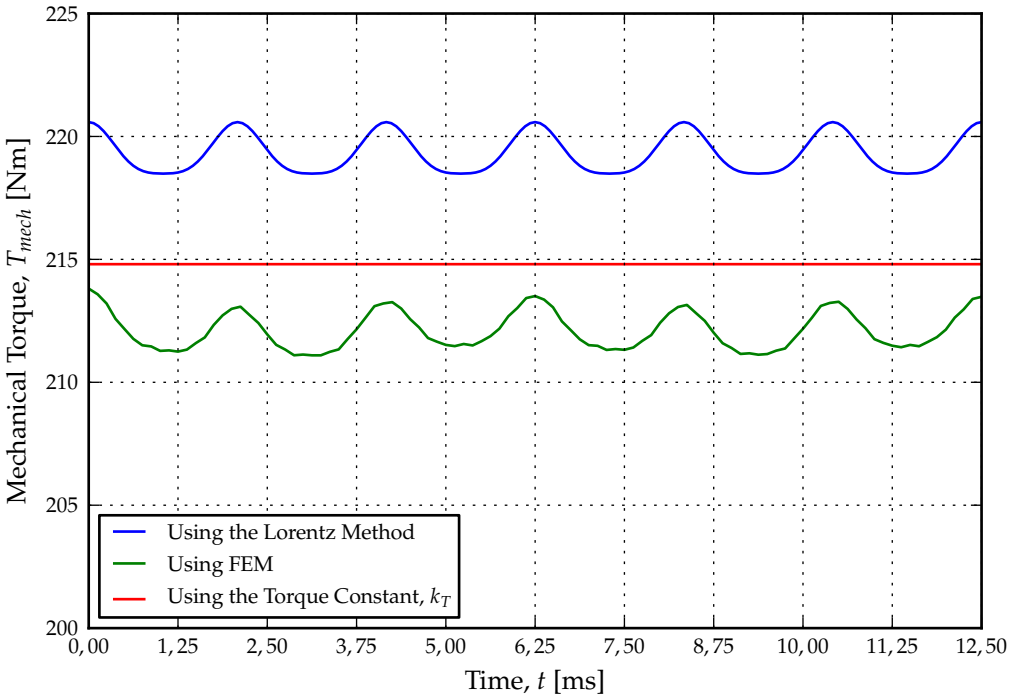

Figure 5.12: The torque ripple waveforms for the Type II winding configuration.

another FEM simulation was done in SEMFEM, see Gerber *et al.* [18]. SEMFEM, short for Stellenbosch Electrical Machines Finite Element Method, is based on Abdel-Razek *et al.* [53] and utilises a combination of FEA and an air gap element (AGE) for the simulation of electrical machines. The AGE is an analytical description of the air gap of the machine and results in a faster solution of the magnetic fields in the machine for a transient analysis as it is not necessary to continuously re-mesh the air gap(s) between the rotor and stator of the machine being analysed.

In Figure 5.13 the torque waveform of the analytically calculated and the torque waveform obtained using Maxwell® 2D and SEMFEM are shown. We can clearly see that the two FEM solutions are almost exactly the same, given the resolution of the vertical (y) axis. In Figure 5.14, the FFT of the torque waveform simulated using SEMFEM is shown. The SEMFEM solution confirms that there is indeed no second order harmonic present in the torque waveform of the Type II winding configuration. From communications with Ansoft/Ansys support, the reason for the second order harmonic in the torque waveform of Maxwell® 2D simulation for the Type II winding configuration can be attributed to "computational oscillations" due to the Master and Slave boundaries touching the coils of the machine.

In Figure 5.14, the FFT of the torque waveform obtained using a "tweaked" Maxwell® 2D FEA model of the Type II winding configuration is also shown. In this "tweaked" Maxwell® 2D FEA model, the coil sides of the Type II windings that were originally touching the Master and Slave boundaries, were shifted by 0,05 radians away from the Master and Slave boundaries. This unfortunately reduces the flux-linkage of the windings marginally and result in a slightly lower average torque value. The most important aspect however, is that the second order "computational oscillation" disappeared.

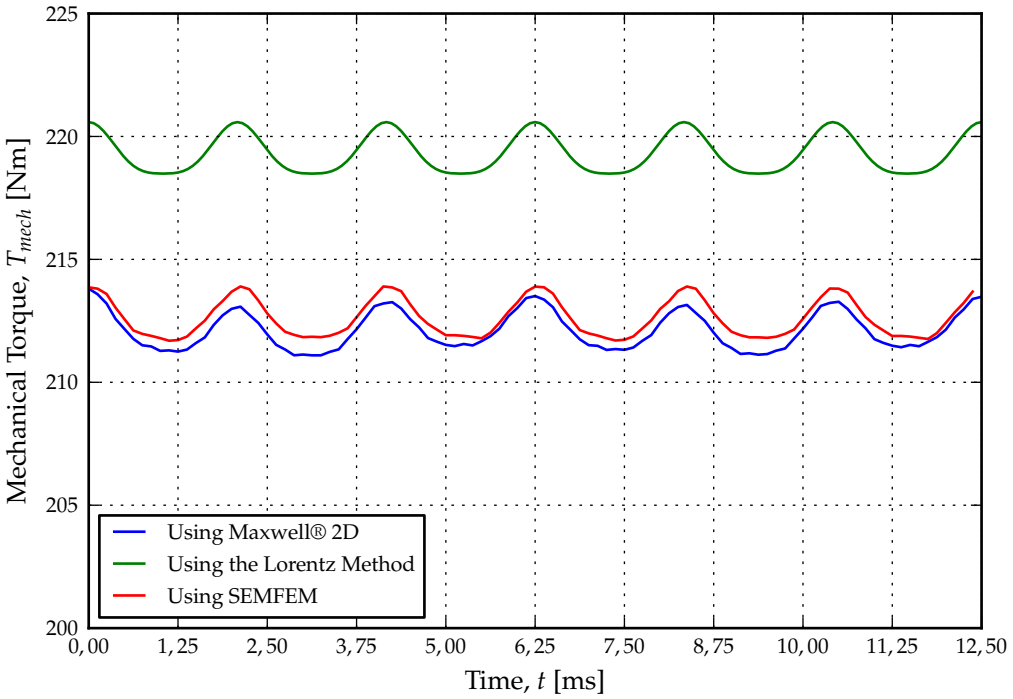

Figure 5.13: The torque ripple waveforms for the Type II winding configuration.

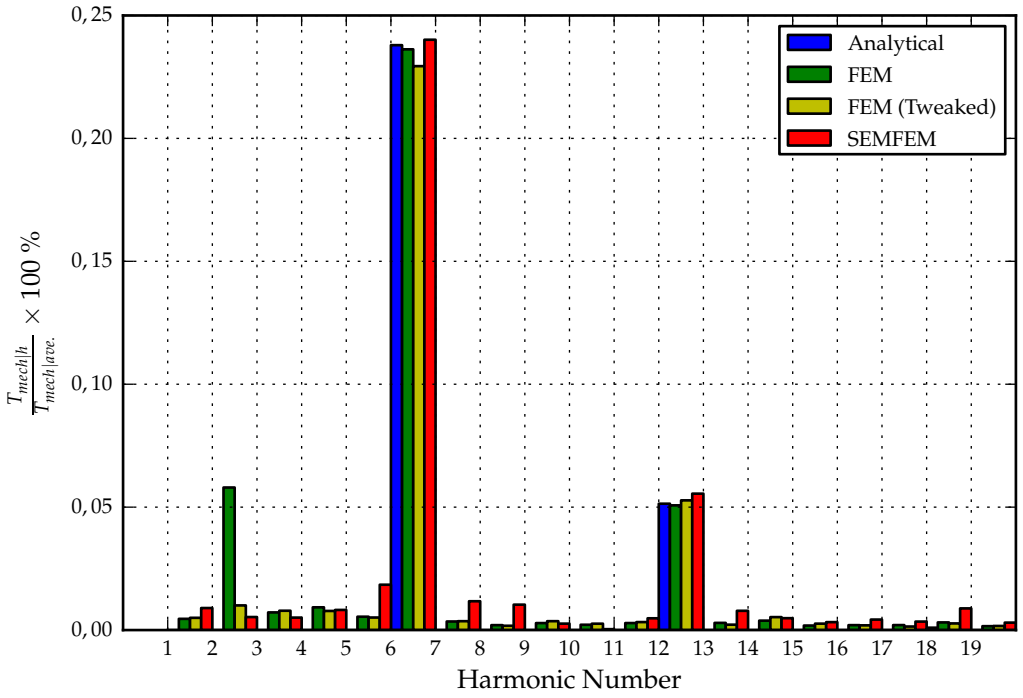

Figure 5.14: A FFT of the torque ripple harmonics for the Type II winding configuration.

5.4 The Effect of a Reduced Subdomain Model on the Torque Calculations

In this chapter, the torque produced by the different winding configurations were analytically calculated using different calculation methods. All the torque calculation methods however relied on the radial flux-density solution obtained in Chapter 3 using the subdomain analysis method. The subdomain model used in Chapter 3, assumed a constant value of 1 000 for the relative permeability in the rotor yokes as the subdomain method is a linear approximated to the magnetic field solution. In this section we will investigate the effect of increasing the permeability of the rotor yoke to infinity, have on the torque calculation results.

5.4.1 Using a Subdomain Model with the Permeability in the Rotor Yoke taken as Constant

In Table 5.1 the torque results for the three different winding configurations, calculated with the different analysis methods, i.e. the simplified average torque calculation of section 5.2, the simplified Lorentz method discussed in section 5.3.1 and the "exact" Lorentz method of section 5.3.2, are shown. These calculated torque value a shown together with the torque values obtained from the FEM results using Maxwell® 2D and SEMFEM[1]. All the analytical calculations were done assuming a constant value of 1 000 for the permeability in the rotor yokes.

The "simplified average torque calculation method", calculates the average torque component from the torque constants, as defined in (5.8), (5.9) and (5.10) for the Type O, Type I and Type II winding configurations respectively. The torque constant uses the peak value of the radial flux-density distribution in the centre of the stator windings and assumes that the back-EMF and phase current are not only sinusoidal, but also in phase.

The "simplified Lorentz" method also uses the fundamental component of the radial flux-density in the centre of the stator region for the torque calculation, but considers the space harmonics components of the current density distribution of the different winding configurations as well. The ripple torque calculated, using the simplified Lorentz method is therefore only that component of the total ripple torque that can be associated with the space harmonics of the current density distribution.

The "exact" Lorentz method uses the complete solution of the radial flux-density distribution over the entire stator area, in order to calculate ripple torque component due to the combined effect of the variation in the radial flux-density distribution in the stator region and the variation in the current density distribution.

5.4.2 Using a Subdomain model with the Permeability in the Rotor Yoke taken as Infinity

In Table 5.2 the differences between the different torque calculation methods are shown with the yoke's relative permeability approximated as being infinity (∞) instead of 1 000 to calculate the radial flux-density distribution using the subdomain analysis method. By doing this, the number of governing equations that needs to be solved reduces from five to three, as shown

[1]SEMFEM is only used to model the Type II winding configuration.

Calculation Method	Machine Type	Average	Ripple	%Ripple	%THD
Simplified Average Torque $\mu_{r\|yoke} = 1000$	O	310,29 Nm	–	–	–
	I	192,03 Nm	–	–	–
	II	214,55 Nm	–	–	–
Simplified Lorentz $\mu_{r\|yoke} = 1000$	O	313,05 Nm	6,33 Nm	2,02 %	0,51 %
	I	192,24 Nm	1,83 Nm	0,95 %	0,24 %
	II	215,02 Nm	1,23 Nm	0,57 %	0,14 %
Lorentz $\mu_{r\|yoke} = 1000$	O	319,27 Nm	11,13 Nm	3,49 %	0,87 %
	I	196,08 Nm	2,19 Nm	1,12 %	0,28 %
	II	219,32 Nm	2,10 Nm	0,96 %	0,24 %
Maxwell® 2D	O	302,47 Nm	11,74 Nm	3,88 %	0,89 %
	I	189,94 Nm	2,13 Nm	1,24 %	0,27 %
	II	212,12 Nm	2,71 Nm	1,28 %	0,25 %
"Tweaked"	II	211,58 Nm	2,32 Nm	1,10 %	0,24 %
SEMFEM	O	–	–	–	–
	I	–	–	–	–
	II	212,62 Nm	2,21 Nm	1,04 %	0,25 %

Table 5.1: Comparison between the result of the various torque calculation methods.

in appendix H. This results in the coefficients matrix that needs to be solved for each value of m reducing from a 10×10 matrix to a 6×6 matrix, without compromising the accuracy of the results significantly. Although the analytical calculation method is already two orders of magnitude faster than the FEM solution using Maxwell® 2D[1], the reduced matrix solution did not prove to be much faster[2] using Python™.

Calculation Method	Machine Type	Average	Ripple	%Ripple	%THD
Simplified Average Torque $\mu_{r\|yoke} = \infty$	O	310,95 Nm	–	–	–
	I	192,44 Nm	–	–	–
	II	215,00 Nm	–	–	–
Simplified Lorentz $\mu_{r\|yoke} = \infty$	O	313,69 Nm	6,32 Nm	2,01 %	0,50 %
	I	192,65 Nm	1,83 Nm	0,95 %	0,23 %
	II	215,47 Nm	1,23 Nm	0,57 %	0,14 %
Lorentz $\mu_{r\|yoke} = \infty$	O	319,94 Nm	11,13 Nm	3,48 %	0,86 %
	I	196,49 Nm	2,19 Nm	1,12 %	0,28 %
	II	219,78 Nm	2,10 Nm	0,95 %	0,24 %

Table 5.2: Analytical results with the permeability of the rotor yoke taken as infinity.

[1] Approximately, ≈ 6 s for the analytical solution versus ≈ 890 s for the Maxwell® 2D solution
[2] It was only ≈ 1 s faster – both measured using the `time` function in *IPython*

From Table 5.2 we can see that as a result of the permeability of the rotor yoke being regarded as infinity, the MMF drop across the rotor yokes have effectively been ignored, so that the radial flux-density values as well as the calculated average torque values will being slightly higher than the values showed in Table 5.1. The difference is only in the order of 0,2 % which is so small that we can safely ignore the reluctance of the rotor yoke in our torque ripple calculations.

5.5 Investigating the Effect of Rotor Yoke Saturation on the Analytical Torque Calculation

In section 3.11.4 it was mentioned that the fundamental component of the analytically calculated radial flux-density distribution was 3 % higher than of the FEA solution. This was attributed to saturation in the rotor yokes as could be observed in the flux-density contour plot of Figure 3.8. In this section, we will investigate the effect of saturation in the rotor yokes region on the torque calculations. Our investigation will be limited to the Type II winding configuration.

We decided to again use the machine data of Test Machine I in section E.1 of Appendix E but with the rotor yoke thickness of 20 mm instead of 8 mm. From the FEA solution using Maxwell® 2D, we saw that peak flux-density values in the centre of rotor yokes reduced from ≈1,7 T to ≈0,67 T. The FEA solution to the torque output were however only slightly higher, as shown in Figure 5.15, compared to the FEA solution shown in Figure 5.12 with a saturated 8 mm thick rotor yokes.

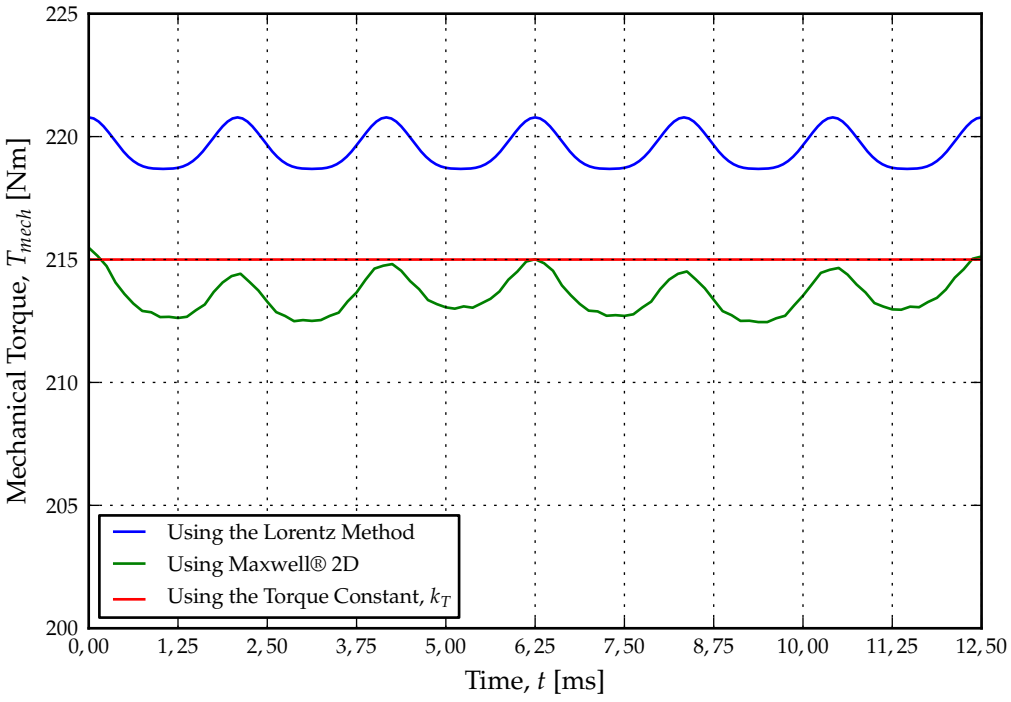

Figure 5.15: The torque ripple waveforms for the Type II winding configuration with a rotor yoke thickness of 20 mm.

From Figure 5.15 and Figure 5.12 it is clear that saturation of the rotor yokes reduces the output torque of this Type II RFAPM machine with only an ≈0,5 %. There is however still a difference in the analytically calculated torque output and that calculated using FEA. This clearly implies that the difference in the torque calculation can not be attributed to rotor yoke saturation.

5.6 Investigating the Effect of the Recoil Permeability of the Permanent Magnets on the Analytical Torque Calculation

With saturation of the rotor yokes ruled out as a possible cause to the difference between the FEA solution and analytically calculated solution to the radial flux-density distribution in the stator region, it was decided to investigate the effect the approximation of the recoil permeability to unity, in our subdomain model, have on the accuracy of the analytically calculated radial flux-density. We again made used of the machine data of Test Machine I in section E.1 of Appendix E, but now, not only with a rotor yoke thickness equal to 20 mm, but also with the N48 NdBFe permanent magnets' coercivity modified from 1 050 000 A/m to 1 114 084 A/m to effectively change the value of the relative recoil permeability of the permanent magnets to unity in our FEA simulation.

The result of the FEA solution to the torque, as well as the analytically calculated value of the torque using the exact Lorentz method, are shown in Figure 5.16 with both solution assuming a relative recoil permeability for the permanent magnets of unity. We can see that both solutions to the torque are an allmost exact match. The lower value of the radial flux-density in the FEA solutions where the the recoil permeability were not taken as unity, could thus attributed to larger inter-pole leakage flux due to the slightly higher recoil permeability of the permanent magnets compared to the permeability in the surrounding air gaps and stator region.

5.7 Summary and Conclusions

In this chapter, different calculation methods were employed to calculate the torque produced by a Double-sided Rotor RFAPM machine. A torque constant, k_T, for the RFAPM was derived. This torque constant is equal to the voltage constant, k_E, defined in section 3.14. The torque constant relates the torque produced by the RFAPM machine to the peak value of stator current space vector. In order for this to be valid, the phase current and the back-EMF of the RFAPM machine needs to be in phase. This requires the machine to be operated under field orientated control to ensure that the d-axis of the rotor and the d-axis of the stator are orthogonal (i.e. at 90°) to one another. The similarity to a DC machine, where the armature – and the field flux are also orthogonal to one another and where the torque is directly proportional to the armature current, is the reason why the Double-side Rotor RFAPM machine can therefore also be classified as a classical brushless DC machine.

The average, steady state torque produced by the RFAPM machine, can therefore be calculated from the torque constant. The accuracy of the torque constant (and hence the voltage constant) is directly proportional to the accuracy of radial flux-density value used in the calcu-

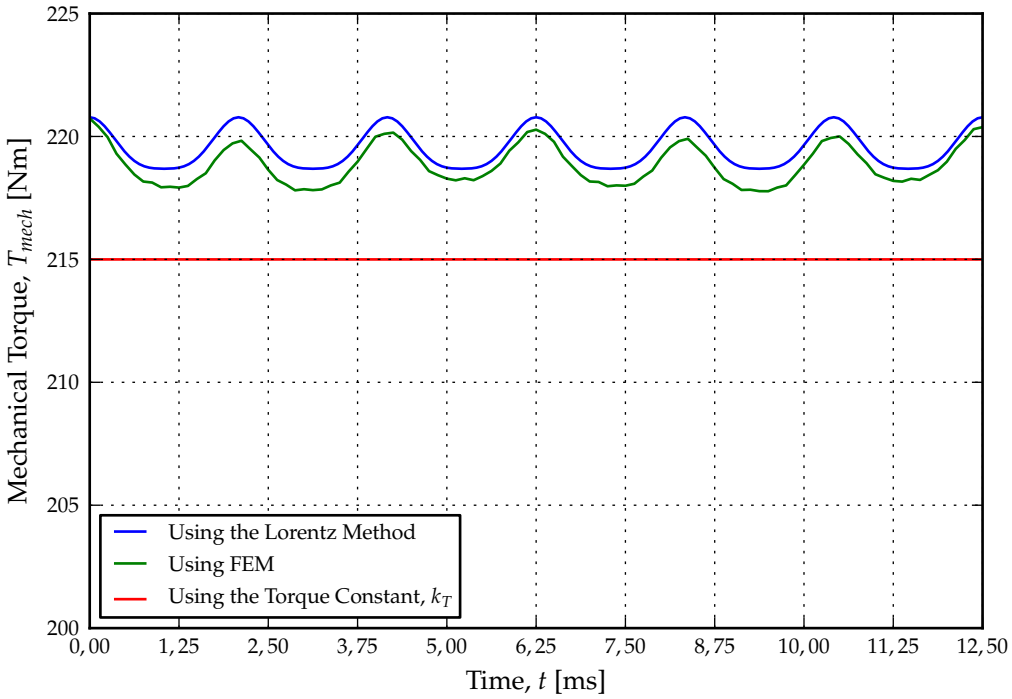

Figure 5.16: The torque ripple waveforms for the Type II winding configuration with a rotor yoke thickness of 20 mm and a relative recoil permeability for the permanent magnets in Maxwell® 2D, $mu_{r,recoil} = 1$.

lation of torque constant. By using the peak value of the fundamental component of the radial flux-density distribution in the centre of the stator region as calculated in Chapter 3, the average torque values for the RFAPM machine with either a Type O, Type I or Type II winding configuration, could be calculated to within ≈1 % of the average value for the torque obtained using FEA. Based on the the simplicity of the calculation, the accuracy of the average torque result is truly remarkable and emphasises the importance of the calculation of the pole width angle to minimise the %THD in the radial flux-density distribution, as discussed in Chapter 3.

The simple Lorentz calculation method used to calculate the torque ripple component was in essence just a way to see what the effect of the stator slotting is. The simplified Lorentz calculation method assumed that the radial flux-density distribution in the stator region is constant and sinusoidal. In order to accurately calculate the ripple torque component, the complete solution to the radial flux-density distribution in the stator region from the subdomain analysis method has to be used. This is to account for the variation in the radial flux-density distribution in the stator region.

It was found that the torque ripple component could be calculated very accurately using the Lorentz method when compared to FEA results. The Lorentz method also gave very accurate torque ripple result with a simplified subdomain model being employed that assumes the rotor yokes' permeability to be infinity. It was however found that the average value of the the torque calculated using the Lorentz method was ≈3,3 % higher than the average calculated using FEA. This coincided with the fact that the radial flux-density values, calculated using the subdomain method, and used in the Lorentz method calculation was found in Chapter 3 to be

$\approx$3 % higher. The difference in the radial flux-density values were initially attributed to the fact that the subdomain analysis method is a linear approximation to the solution of the magnetic fields and does not take the saturation of the rotor yokes into account.

On closer inspection however, it was found that the main difference in the torque calculated analytically using the Lorentz method and that calculated using FEA were not as a result of the rotor yoke saturation, but due to the fact that the subdomain analysis method assumes the recoil permeability of the permanent magnets to be unity. With the reason for this difference between the analytically calculated results and that using FEA known, it was decided to leave the solution to this problem for further research, as the analytical solution at hand is a adequate engineering solution for the time being.

CHAPTER 6

Machine Performance Comparison as a Function of Winding Configuration Including the End-turns Effects

There are no foolish questions and no man becomes a fool until he has stopped asking questions

CHARLES P. STEINMETZ

6.1 Introduction

The end-turns of a coil are defined as those parts of the coil that connect the two coil-sides of the coil in order to maintain electrical continuity. The end-turns do not contribute to the induced voltage in the coil, nor do they partake in producing any torque. In this chapter the end-turns effect of the different winding configurations, i.e. Type O, Type I and Type II, on the performance of the RFAPM machine will examined. This will be done in order to obtain a more realistic performance comparison between the different winding configurations, than possible with the 2-D analytical analysis, done in Chapters 3 to 5. The empirical analysis of the end-turns done in this chapter, is an enhancement of the analysis done in Randewijk *et al.* [14] which in turn was based on the analysis done by Rossouw and Kamper [25] and Kamper *et al.* [13] on the end-turn effect in Axial Flux Permanent Magnet (AFPM) machines with air-cored, non-overlapping, concentrated stator windings.

Although the end-turns will add to the machine's synchronous inductances, as was calculated in Chapter 4, this effect will be ignored. This is due to the fact that for the Type O, Type I and Type II air-cored winding configurations, the slight increase in the inductance due to the end-turns will be minimal and will have almost no effect on the performance of the machine.

We will rather focus on the effect the end-turns have on the winding resistance, as this has a direct influence on the losses in different winding configurations and hence the efficiency of the RFAPM machine. The end-turn length adds to the total length of the coil and thus also adds to the resistance of the coil.

In this chapter the performance of the RFAPM machine will be measured in terms of the amount of torque produced by the Type I and Type II non-overlapping windings configurations, compared to the Type O overlapping winding configuration used as benchmark. Although technically not a performance issue, the effect of the end-turn length on the total copper volume of the different winding configurations and thus on the cost of the machine, will also be discussed.

6.2 Simple Torque Comparison

Before analysing the effect of the end-turns, we will consider a simple comparison for the average torque produced by a RFAPM machine, as a function of various winding configuration parameters. From (5.7) and (5.11), the general format of the steady state torque equation for the RFAPM machine can be written as

$$T_{mech} = \tfrac{3}{2} k_T I_p \tag{6.1}$$

$$= \tfrac{3}{\sqrt{2}} k_T I_{rms} \tag{6.2}$$

with the general torque constant, from (5.8), (5.9) and (5.10),

$$k_T = \frac{2qr_n\ell N}{a} k_w \hat{B}_{r_1} \, , \tag{6.3}$$

and the winding factor,

$$k_w = k_{w,slot} k_{w,pitch} \, . \tag{6.4}$$

For the same rotor design, the peak value of the fundamental component of the radial flux-density, $\hat{B}_{r_1}$, will be the same for all three winding configurations. If we further ensure that the nominal radius, r_n, and the active stator length, ℓ are also the same for the Type O, Type I and Type II winding configurations, the difference in torque produced for the different winding configurations will depend solely on the differences in the stator designs. It is clear that for the stator designs of the Type O, Type I and Type II winding configurations, the is torque directly proportional to the number of coils per phase, q; the number of turns per coil, N; and the winding factor, k_w; and inversely proportional to the number of parallel circuits, a.

To summarise briefly from Chapter 2, the winding factor consists of the coil slot-width factor,

$$k_{w,slot} = \frac{\sin(\frac{\Delta}{k_q})}{\frac{\Delta}{k_q}} \tag{6.5}$$

and the coil pitch factor

$$k_{w,pitch} = 1 \quad \text{– Type O} \tag{6.6}$$
$$= \sin(\tfrac{\pi}{3}) \quad \text{– Type I} \tag{6.7}$$
$$= \sin(\tfrac{2\pi}{3} - 2\Delta) \quad \text{– Type II ,} \tag{6.8}$$

with Δ, half the coil-side with angle[1] and k_q, the coil factor equal to $\frac{q}{p}$.

The numerical values of the winding factors for the Type O, Type I and Type II winding configurations are given in Table 6.1, using the machine parameters for Test Machine I from Appendix E, section E.1. Table 6.1 also shows, the number of coils, q, the coil factor, k_q, the coil-side width factor, k_Δ and the number of turns per coil, N, for the different winding configurations.

Table 6.1: Comparison between the Type O, Type I and Type II winding configurations with the same rotor geometry, stator current and stator current density.

	Type O	Type I	Type II
q	16	8	8
k_q	1	0,5	0,5
k_Δ	1,0	0,74	0,74
N	64	96	96
$k_{w,slot}$	0,955	0,903	0,903
$k_{w,pitch}$	1,0	0,866	0,969

In order to obtain a comparison between the torque produced by the RFAPM machine for the Type O, Type I and Type II winding configurations, we start by substituting (2.117), the equation for the number of turns per coil into (6.3) and expanding (5.7) so that we can write

$$T_{mech} = \sqrt{2}\pi r_n^2 h\ell k_f k_\Delta J_{wire} k_w \hat{B}_{r_1} \tag{6.9}$$
$$= \sqrt{2}\pi r_n^2 h\ell k_f k_\Delta J_{wire} k_{w,slot} k_{w,pitch} \hat{B}_{r_1} \tag{6.10}$$
$$= \sqrt{2}6 r_n^2 h\ell k_f k_q J_{wire} \sin\Big(\frac{k_\Delta \pi}{6k_q}\Big) k_{w,pitch} \hat{B}_{r_1} \tag{6.11}$$
$$= C_1 K_1 \tag{6.12}$$

with

$$C_1 = \sqrt{2}6 r_n^2 h\ell k_f J_{wire} \hat{B}_{r_1} \tag{6.13}$$

defined as a constant factor, common to the torque expression for the Type O, Type I and Type II winding configurations and

$$K_1 = k_q \sin\Big(\frac{k_\Delta \pi}{6k_q}\Big) k_{w,pitch} \tag{6.14}$$

[1]The coil-side width angle was defined in Chapter 3 as 2Δ.

defined as a variable factor based on the differences in the different stators' winding design parameters. Assuming that the current density is the same for the Type O, Type I and Type II winding configurations, we only need to consider K_1 when comparing the developed torque for the different winding configurations as is shown in Table 6.2.

Table 6.2: A comparison between normalised developed torque for the Type O, Type I and Type II winding configurations with the same rotor geometry and stator current density.

	Type O	Type I	Type II
K_1	0,5	0,303	0,339
Normalised Torque	100 %	60,59 %	67,76 %

From Table 6.2, we can see that the torque produced by the two non-overlapping winding configurations does not compare well with that of the Type O winding configuration. This comparison is however very simplistic as it does not take into account the losses in the copper windings associated with the torque delivery. In the next section, section 6.3, we will first calculate the end-turn lengths for the different winding configurations and then in section 6.4 we will calculate the total copper loss of the windings, taking the effect of the end-turn length, into account.

6.3 End-turn Length Calculation

The end-turn lengths for the Type O, Type I and Type II winding configurations will be estimated from their respective 3-D winding geometries.

6.3.1 End-turn Length Calculation for the Type O Winding Configuration

In Figure 6.1, the 3-D representation of a typical coil of an overlapping winding configuration is shown. Although drawn as a solid copper bar, it actually consists of a bundle of conductors.

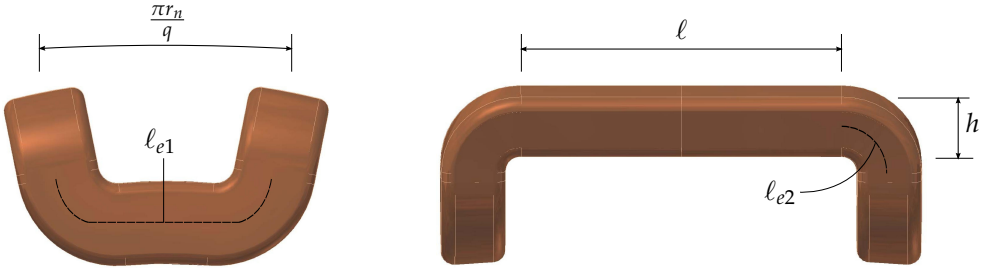

Figure 6.1: A typical coil used in an overlapping winding configuration.

From Figure 6.1 it can be seen that the end-turn length of each coil[1], $\ell_{e|O}$, for the Type O winding configuration, is equal to

$$\ell_{e|O} = \ell_{e1} + 2\ell_{e2} \,, \tag{6.15}$$

with ℓ_{e1} and $2\ell_{e2}$ two sections of the end-turn length as defined in Figure 6.1.

It is however quite difficult to calculate ℓ_{e1} and ℓ_{e2} accurately and therefore a conservative estimation of the different sections of the end-turn length can be approximated by

$$\ell_{e1} \approx \frac{\pi r_n}{q} \quad \text{and} \tag{6.16}$$

$$\ell_{e2} \approx h \tag{6.17}$$

with r_n the nominal radius measured from the centre of the machine to the centre of the windings, q the number coils per phase and h the stator height. This implies that the end-turn length can therefore be approximated by

$$\ell_{e|O} \approx \frac{\pi r_n}{q} + 2h \,. \tag{6.18}$$

6.3.2 End-turn Length Calculation for the Type I Winding Configuration

The 3-D representation of a typical coil used in a Type I winding configuration is shown in Figure 6.2.

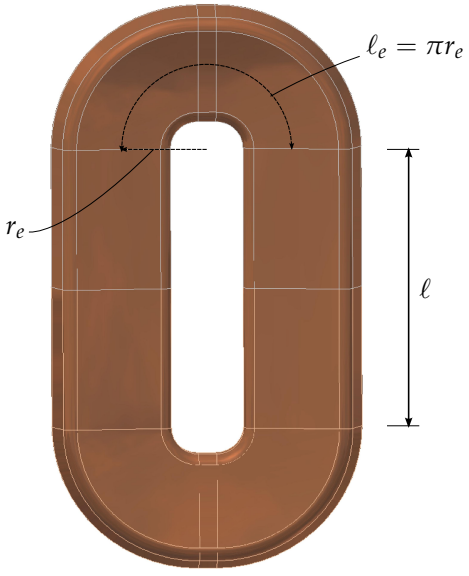

Figure 6.2: A typical coil used in a non-overlapping Type I and Type II winding configuration.

The average end-turn conductor radius, from Figure 2.11 for the Type I winding configuration can be approximated as

$$r_{e|I} \approx \frac{\pi r_n}{2Q} \,. \tag{6.19}$$

[1]The end-turn length defined in this dissertation is the average end-turn length between the centres of the coil's two coil-sides.

A good approximation of the end-turn length, $\ell_{e|I}$ can therefore by calculated as follows,

$$\ell_{e|I} \approx \pi r_{e|I} \tag{6.20}$$

$$\approx \frac{\pi^2 r_n}{2Q} \tag{6.21}$$

with Q the total number of coils for all three-phases, i.e. $Q = 3q$.

This assumes that the shape of the end-turn winding approximates a half-circle, which is a good approximation for a machine with a large number short pitched coils. This would imply that the average bending radius of the coil conductors is approximately equal to the radius of the end-turn conductors.

6.3.3 End-turn Length Calculation for the Type II Winding Configuration

The 3-D representation of the Type I coil shown in Figure 6.2 is just as applicable for the Type II winding configuration. Although this would be regarded as a more conservative estimation of the end-winding length, we could again assume that the end-turn winding approximates a half-circle and that the average bending radius of coil conductors can be taken as equal to the radius of the end-turn conductors.

From Figure 2.18 it can be seen that for the Type II winding configuration, the average end-turn conductor radius $r_{e|II}$ will be slightly larger compared to the Type I winding configuration and will be equal to

$$r_{e|II} \approx r_n\left(\frac{\pi}{Q} - \frac{\Delta}{q}\right), \tag{6.22}$$

with Δ, half the coil-side width angle, so that the end-turn length can be calculated as

$$\ell_{e|II} \approx \pi r_e \tag{6.23}$$

$$\approx \pi r_n\left(\frac{\pi}{Q} - \frac{\Delta}{q}\right) \tag{6.24}$$

$$\approx \frac{\pi r_n(\pi - 3\Delta)}{Q}. \tag{6.25}$$

6.4 Copper Loss Calculation

The main loss component that would effect the performance of the RFAPM machine is the copper losses in the stator windings. This is graphically depicted in Figure 6.3 with the power flow shown for generator operation. The copper losses will be the only loss component considered for our analysis. The reason is due to the fact, that with the RFAPM machine being an air-cored machine, there are no core-losses in the stator of the machine. Furthermore, due to the relatively low flux densities produced be the stator coils, see Chapter 4, we can safely ignore the core-losses in the rotor caused by the stator MMF harmonics. Also, Arkadan *et al.* [5] and Holm [24, sec. 7.6] calculated the eddy current losses in high speed toothless stator machines with Litz wire winding and found that these losses were very small, compared to the stator back (or yoke) iron losses. It is therefore safe to assume that the eddy-current losses in the air-cored stator windings, using Litz wire, can be ignored.

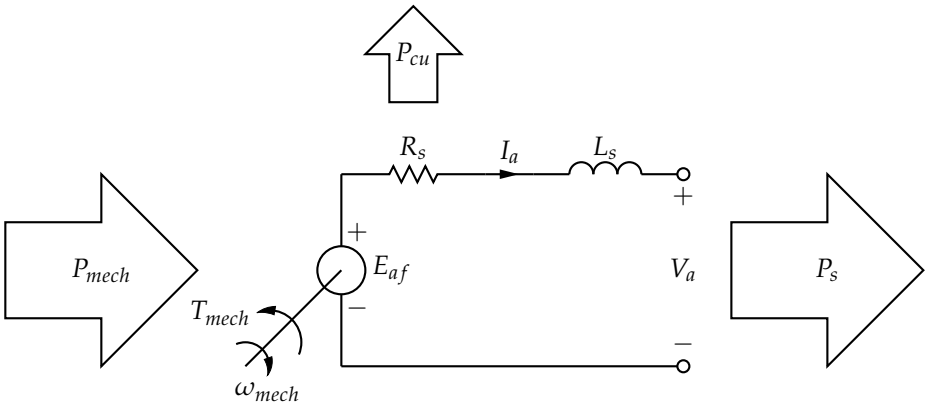

Figure 6.3: The equivalent circuit of the RFAPM machine together with the main power flow components..

In order to calculate the equivalent stator resistance per phase, R_s, we first need to calculate the average coil-turn length,

$$\ell_n = 2(\ell + \ell_e) \tag{6.26}$$

with ℓ, the active stator length[1] and ℓ_e, the end-turn length as calculated in the previous section. The equivalent resistance of each coil can now be calculated as follows,

$$R_{coil} = N\frac{\rho_{Cu}\ell_n}{A_{wire}} \tag{6.27}$$

with N the number of turns per phase; A_{wire} the area of the copper conductors and ρ_{Cu} the resistivity of copper. With the number of conductors per phase, q, and the number of parallel circuits, a, known, the equivalent resistance per phase can now be calculated as,

$$R_s = \frac{qR_{coil}}{a^2}\,. \tag{6.28}$$

This allows us to calculate the total stator copper loss as

$$P_{Cu} = 3R_s I_{rms}^2 \tag{6.29}$$

$$= 3\frac{qN\rho_{Cu}\ell_n}{a^2 A_{wire}} I_{rms}^2 \tag{6.30}$$

$$= 3\frac{qN\rho_{Cu}\ell_n}{a} J_{wire} I_{rms} \tag{6.31}$$

or from (2.116), only in terms of the current density, J_{wire}, instead of J_{wire} and I_{rms},

$$P_{Cu} = \pi r_n \ell_n h k_f k_\Delta \rho_{Cu} J_{wire}^2 \tag{6.32}$$

$$= 2\pi r_n(\ell + \ell_e) h k_f k_\Delta \rho_{Cu} J_{wire}^2 \tag{6.33}$$

$$= C_2 K_2 \tag{6.34}$$

[1]The active stator length is also sometimes referred to as the active copper length, or the active stack length in electrical machines that utilises laminated iron-cored stators.

with

$$C_2 = 2\pi r_n h k_f \rho_{Cu} J_{wire}^2 \tag{6.35}$$

defined as a constant factor, common to the different winding configurations and

$$K_2 = (\ell + \ell_e) k_\Delta \tag{6.36}$$

defined as a variable factor based on the differences between the different winding configurations in terms of the nominal turn length, that includes the end-turn length of each coil and the relative coil-side width factor, k_Δ.

In Table 6.3, a comparison between the Type O, Type I and Type II winding configuration is given with the stator current density, J_{wire}, considered the same for all the winding configurations. If we compare this to Table 6.2 we can see that the relative torque-to-copper-loss ratio of the non-overlapping Type I and Type II winding configurations compares favourably[1] to the overlapping (Type O) winding configuration. However, the ratio for both the Type I and Type II are still slightly lower thant the "1,0 " ration of the overlapping winding configuration.

Table 6.3: Comparison between stator copper losses for the different winding configurations with the same rotor geometry and stator current density.

	Type "O"	Type "I"	Type "II"
K_2	0,141 6	0,091 5	0,100 7
Normalised Copper Losses	100 %	64,67 %	71,15 %

The comparison given in Table 6.3 was based on using the same value for the current density, in each of the three winding configuration. In the next section we will discuss the performance comparison between the different winding configurations based on a fixed stator copper-loss value in the Type O, Type I and Type II winding configurations.

6.5 Performance Comparison with Fixed Copper-loss Value

In this section we will compare the performance of the RFAPM machine with the different winding configurations, presuming that the stator copper losses in the Type I and Type II winding configurations are equal to that of the Type O winding configuration, $P_{Cu|O}$. From (6.33) the current density in the Type I winding configuration can thus be calculated as

$$J_{wire|I} = \sqrt{\frac{P_{Cu|O}}{2\pi r_n (\ell + \ell_{e|I}) h k_f k_\Delta \rho_{Cu}}} \tag{6.37}$$

and in the Type II winding configuration as

$$J_{wire|II} = \sqrt{\frac{P_{Cu|O}}{2\pi r_n (\ell + \ell_{e|II}) h k_f k_\Delta \rho_{Cu}}} \,. \tag{6.38}$$

[1]The Torque to copper-loss ratio is calculated at 0,937 and 0,952 for the Type I and Type II winding configurations respectively.

With the current densities in the different winding configurations not equal any more, it requires us to redefine (6.11) as

$$T_{mech} = C_1' K_1' \tag{6.39}$$

with

$$C_1' = \sqrt{2} 6 r_n^2 h \ell k_f \hat{B}_{r_1} \tag{6.40}$$

the revised constant factor, common to each of the different winding configurations and

$$K_1' = k_q \sin\left(\frac{k_\Delta \pi}{6k_q}\right) k_{w,pitch} J_{wire} \tag{6.41}$$

the revised variable factor, unique to each of the three different winding configurations, based on the differences in the winding designs. If follows that (6.33) also needs to be redefined, so that

$$P_{Cu} = C_2' K_2' \tag{6.42}$$

with

$$C_2' = 2\pi r_n h k_f \rho_{Cu} \tag{6.43}$$

defined as the revised constant factor common to the different winding configurations and

$$K_2' = (\ell + \ell_e) k_\Delta J_{wire}^2 \tag{6.44}$$

the revised variable factor based on the differences between the three different winding configurations.

Other than the fact that the non-overlapping (Type I and II) winding configurations hold the advantage in shorter end-turn lengths, these winding configurations also have the advantage that their coil-side widths can be varied, compared to the overlapping (Type O) winding configuration, where the coil-side width is usually kept at the maximum coil-side width value.[1] The coil-side width factor, k_Δ, as defined in (2.64), will be used as the abscissae against which the performance parameters will be plotted for the Type I and Type II winding configurations.

From equations (6.33) and (6.44), we can see that with the active stator length, ℓ, the same for all three winding configurations, the performance difference between the different winding configurations will be more pronounced in a short stator machine, i.e. with $\ell \approx \ell_e$, than in a long stator machine, i.e. with $\ell \gg \ell_e$. In order to illustrate this, we will define the ratio ξ as the ratio between the active stator length, ℓ, and the nominal stator radius, r_n, so that

$$\xi = \frac{\ell}{r_n} . \tag{6.45}$$

The performance comparison graphs that will be presented in the follow pages, will be done for different values of ξ. With the nominal stator radius constant, it implies that the comparison will effectively be done for different "per unit" stator length values[2], expressed in terms of the nominal stator radius taken as "base length". The machine parameters used, except for the stator length, are based on the double-layer (Type II) machine data shown in Appendix E, section E.2.

[1] This is best illustrated in the difference between Figure 2.1, Figure 2.11 and Figure 2.18.
[2] This is also sometimes referred to as the aspect ratio of an electrical machine.

6.5.1 Current Density Comparison

In Figure 6.4 the current density for the Type I and II winding configurations are shown as a function of the coil-side width that would yield the same copper loss as the Type O winding configuration with the current density, $J_{wire} = 5\,\mathrm{A/mm^2}$ and the coil-side width factor, $k_\Delta = 1{,}0$. With the different winding configurations all working at the same phase current of 7,33 A, we can see that the Type I and Type II winding configurations are able to operate at a much higher current density for the same amount of copper losses. Even with the coil-side width factor at 100 %, the current density in the non-overlapping winding configurations will be slightly higher that the $5\,\mathrm{A/mm^2}$ at which the Type O winding configuration is operating at, due to the lower end-turn length and hence lower coil –, or phase resistance. We can also see that for different stator lengths, i.e. different values of ξ, there is not much difference in the current density values for a specific value of k_Δ.

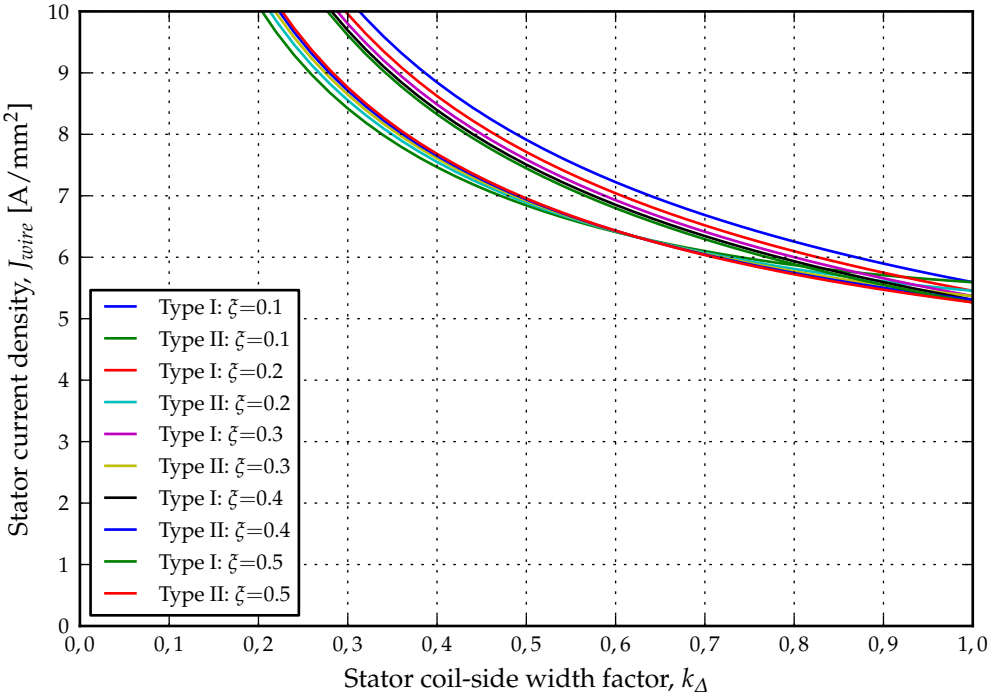

Figure 6.4: The current density versus the coils-side width for the non-overlapping winding configuration stators with different values of ξ.

6.5.2 Torque Comparison

The current density curves showed in Figure 6.4 however, needs to be put in perspective with the relative output torque curves for the non-overlapping winding configurations, as shown in Figure 6.5. We can see that for $\xi = 0{,}1$, i.e. for a short stator machine, the double-layer non-overlapping winding configuration (Type II) can deliver almost 90 % of the torque of a overlapping winding configuration, but at a relative coil-side width of only $\approx 80\,\%$. We can furthermore see that although the end-turn length of the double-layer winding configuration

is slightly more than that of the single-layer winding configuration (Type I), and thus will have a lower current density for the same amount of copper losses, see Figure 6.4, it still is able to produce more torque due to its wider coil pitch configuration.

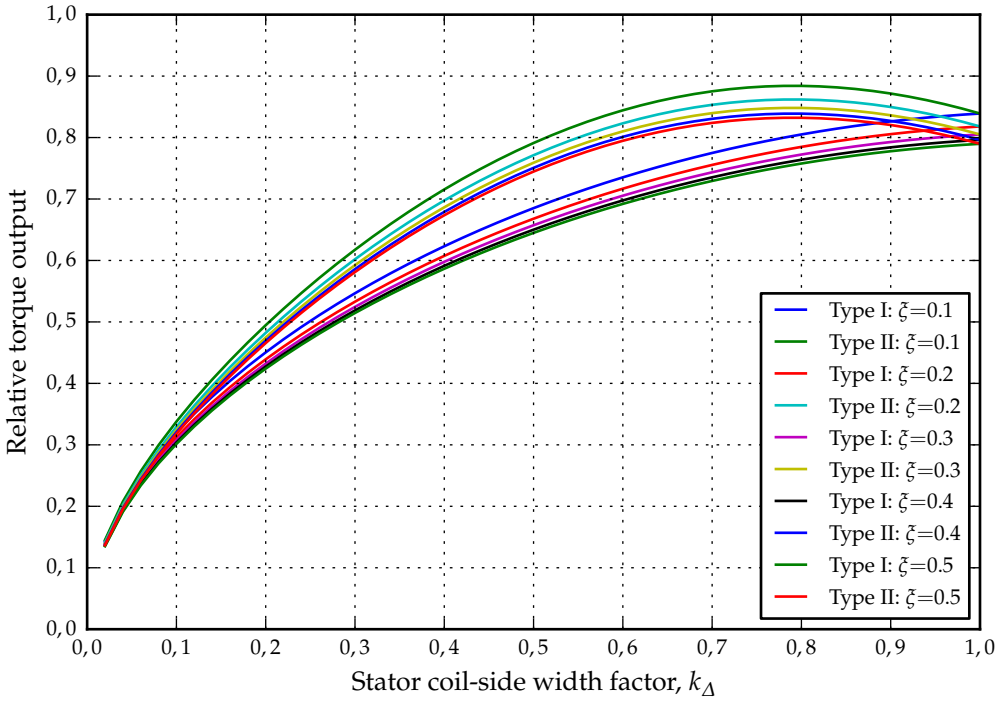

Figure 6.5: The current density versus the coils-side width for the non-overlapping winding configuration stators with different values of ξ.

6.5.3 Copper Volume Comparison

The advantage of the non-overlapping winding configurations in terms of a shorter end-turn lengths, coupled with the fact of being able to vary their coil-side widths, result in a much lower copper volume, V_{Cu}, when compared to the overlapping winding configuration. The total copper volume for the different winding configurations can be calculated as

$$V_{Cu} = 2(\ell + \ell_e)NA_{wire} \tag{6.46}$$

or in terms of the phase current and current density, as

$$V_{Cu} = \frac{2(\ell + \ell_e)NI_{rms}}{aJ_{wire}} \,. \tag{6.47}$$

In Figure 6.6 the relative copper volume of the two non-overlapping winding configurations with respect to that of the overlapping winding configuration is shown. We can clearly see that the copper volume of the double-layer (Type II) winding configuration is always higher, e.g. at $k_\Delta = 0{,}7$ for a $\xi = 0{,}1$ (i.e. short stator) machine, the copper volume is 15 % higher. For longer stator machines (i.e. a higher ξ value) the difference becomes less.

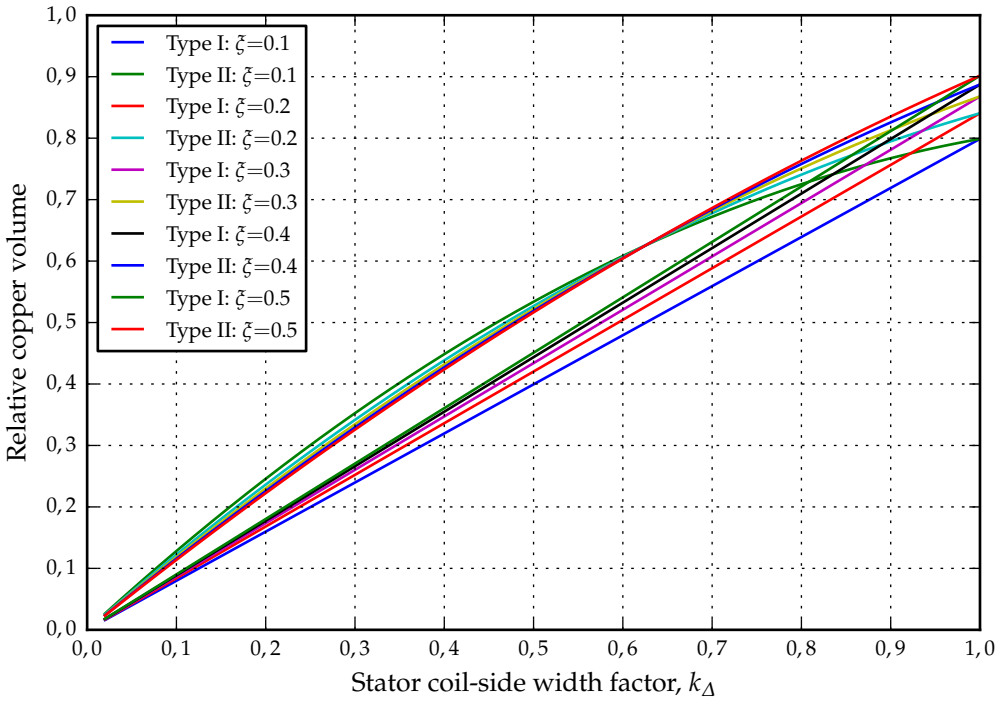

Figure 6.6: The current density versus the coils-side width for the non-overlapping winding configuration stators with different values of ξ.

From Figure 6.6 we can also see that even with a $k_\Delta = 1{,}0$, i.e. the coil-side width at an absolute maximum, the copper volume for the double– and single-layer winding configurations are essentially the same, but still less than that of the overlapping winding configuration. This is due to the reduced end-turn length of the non-overlapping winding configurations. It is also clear that for higher ξ values (i.e. the longer the stator becomes) the less the difference between the overlapping and non-overlapping winding's copper volumes become, due the the fact that $\ell \gg \ell_e$.

A further decrease in the copper volume can be obtained by decreasing the coil-side width. For the single-layer (Type I) winding configuration, the relationship between the copper volume and coil-side width is linear, where as for the double-layer (Type II) winding configuration, the relationship is more parabolic. In Figure 6.5 we saw that the maximum torque produced by the double-layer windings were obtained at $k_\Delta \approx 0{,}8$. At this value of k_Δ, the copper volume of the double-layer windings is ≈ 75 % (depending on the value of ξ) of the overlapping winding configuration's copper volume. At this value of k_Δ, the single-layer winding configuration produced less torque however, but also requires less copper.

In Figure 6.7 the torque produced per copper volume as a function of k_Δ is shown. The interesting thing to note is that except for $\xi = 0{,}1$ and $0{,}2$, the torque per copper volume rations for the other values of ξ at k_Δ between $0{,}7$ and $0{,}8$ are virtually the same for both the non-overlapping winding configurations and yields an approximate 5 % to 15 % better result than for the overlapping winding configuration.

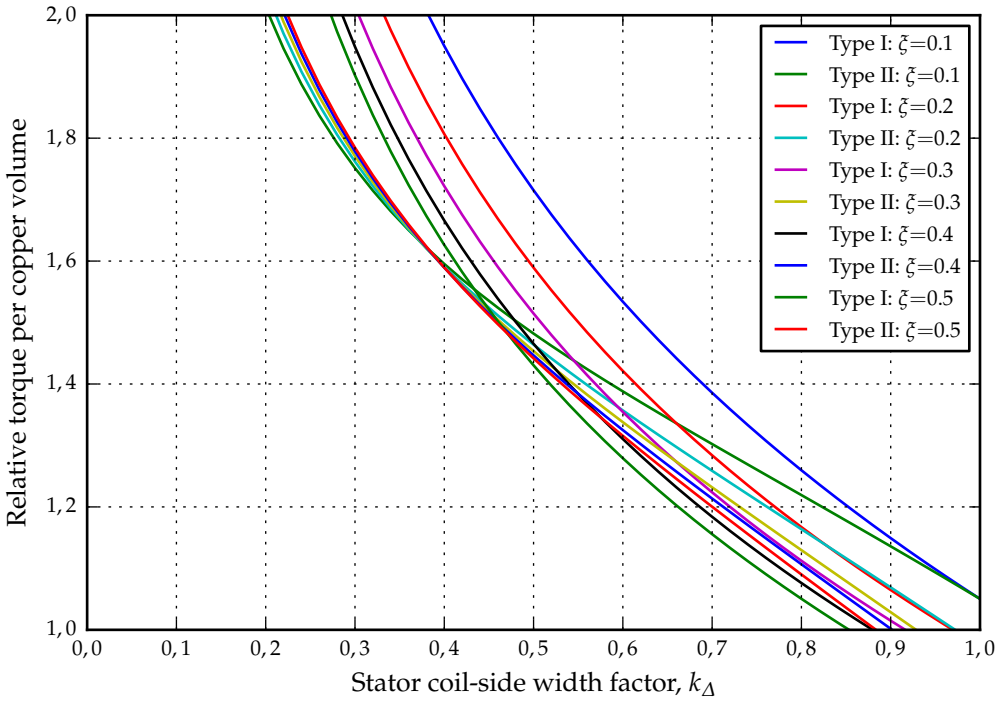

Figure 6.7: The current density versus the coils-side width for the non-overlapping winding configuration stators with different values of ξ.

6.6 Summary and Conclusions

In this chapter we have discussed the effects the end-turn lengths of the Type O, Type I and Type II winding configurations have on the performance of the RFAPM machine. Due to the longer end-turn length of the overlapping winding configuration compared to that of the non-overlapping winding configurations, the overlapping winding configuration has to operate at a lower stator current density in order to produce the same amount of stator copper losses. The single-layer (Type I) configuration has the lowest end-turn length, resulting in it being able to operate at a slightly higher current density than that of the double-layer (Type I) winding configuration, for the same amount of stator copper losses.

With the copper losses the same for all three winding configurations, the increase in current density for the non-overlapping winding configurations result in their maximum torque being much closer to that of the overlapping winding configuration than initially predicted in Table 6.2. This was shown in Figure 6.5 with the double-layer winding configuration holding the edge over the single-layer winding configuration.

It is however in the torque per copper volume ratio where the non-overlapping winding configurations really outperformed the overlapping winding configuration. This was especially prevalent for "pancake like" short stator machines, i.e. low values of ξ, where the end-turn effect is more dominant, as shown in Figure 6.7.

CHAPTER 7

Conclusions and Recommendations

The greatest reward lies in making the discovery; recognition can add little or nothing to that.

FRANZ ERNST NEUMANN

7.1 Introduction

The work presented in this dissertation focused on the complete analytical analysis of the Double-sided Rotor Radial Flux Air-cored Permanent Magnet (RFAPM) machine. The Double-sided Rotor RFAPM machine is a new type of electrical machine that was first introduced by Randewijk *et al.* [14] in 2007. Two subsequent articles on the RFAPM machine were published by Stegmann and Kamper [16, 26] and focused specifically on the design aspect of the Double-sided Rotor RFAPM machine pertaining to their use in medium power wind generator applications.

The aim of this research was to obtain a detailed analytical solution of the electromagnetic fields inside the RFAPM machine. Of specific interest was an analytical solution that could quickly and accurately calculate the radial flux-density in the stator region of the RFAPM machine. This was required to determine the influence, the permanent magnet pole arc width have on the shape of the radial flux-density distribution.

Furthermore, an analytical solution to the steady state induced phase voltages (or back-EMF) as well as the average steady state torque of the RFAPM machine in terms of key machine parameters were required that would be suitable for implementation in an optimisation algorithm. The reason for this was to reduce the reliance of the RFAPM machine optimisation on extremely slow FEM solutions, as well as to supplement the design procedure presented in Stegmann and Kamper [26] for wind generator applications.

An analytical solution for the ripple torque produced by the RFAPM machine was also required. The reason for this was to address the severe torque oscillation problems experienced

in the FEM calculation of the ripple torque component of the RFAPM machine as mentioned by Gerber *et al.* [18], especially when using Maxwell® 2D and to a lesser extend with SEMFEM. In order to solve the oscillation problems in the FEM torque calculation, the mesh in the air gap and stator region had to be refined considerable, resulting in very long simulation times. It was also debatable if the final solution was indeed correct, or still contained some "computational noise".

The research also considered the pro's and con's of using single-layer, non-overlapping, concentrated (Type I) winding configuration as well as the usually more preferred, double-layer, non-overlapping, concentrated (Type II) winding configuration, that was used by Stegmann and Kamper [16, 26]. An obvious advantage of the Type I winding configuration over the Type II winding configuration, is its shorter end-turn length. However its short coil-pitch length implies a lower back-EMF value and hence a lower torque value. I was also decided to benchmark these non-overlapping winding configurations with a classical overlapping (Type O) winding configuration, albeit difficult to implement in the Double-side Rotor RFAPM machine, due to the overlapping end-turn windings. The reason for this comparison was to prove the effectiveness of non-overlapping winding configurations for the RFAPM machine, compared to the more traditional overlapping winding configuration found in classical electrical machine text books.

7.2 Dissertation Contribution and Original Content

In this dissertation, the following new and original contributions were made:

- A complete set of winding factors for the concentrated, overlapping (Type O) –; the concentrated, single-layer, non-overlapping (Type I) – and the concentrated, double-layer, non-overlapping (Type II) winding configuration were derived. The winding factors include the space harmonic components. It was shown that if the flux-density distribution in the stator region is sinusoidal, only the fundamental space harmonic component of the winding factor for the Type O winding configuration will contribute to the flux-linkage. For the non-overlapping, Type I and Type II winding configurations, only the second order space harmonic component of the winding factor will contribute to the flux-linkage.

- A subdomain analytical model of the RFAPM machine was developed whereby the magnetic vector potential as well as the radial – and azimuthal flux-densities in the RFAPM machine could be calculated. It was shown how a sweep of the permanent magnets' pole arc width, using the analytical subdomain model, could be done to quickly determine the optimum value of the pole arc width angle that would result in the lowest percentage Total Harmonic Distortion (%THD) value for the radial flux-density distribution in the centre of the stator region.

- With the radial flux-density distribution in the centre of the stator region considered to be quasi-sinusoidal, a voltage constant and torque constant for the RFAPM machine were derived. The voltage constant, k_E, gives the relationship between the back-EMF and the speed of the RFAPM machine. The torque constant, k_T, which is equal to the voltage

constant and gives the relationship between the torque produced by the RFAPM machine and the peak value of stator current space vector.

- An equation was derived from the analytical subdomain model of the RFAPM machine using of the Lorentz method, whereby the torque ripple component produced by the Type O, Type I and Type II winding configurations could be calculated quickly and fairly accurately. We were also able to distinguish between the ripple torque component caused by the winding layout, and that caused by the variation in the radial flux-density distribution in the stator region.

- A comprehensive comparison of the Type O, Type I and Type II winding configurations was done relating to the effect, the end-turn windings of the different winding configurations have on the performance of the RFAPM machine, in terms of torque, copper losses and copper volume.

7.3 Conclusions

The linear subdomain model of the Double-sided Rotor RFAPM machine as presented in this dissertation, provide a sufficiently accurate analytical model of the RFAPM machine from which the radial flux-density, flux-linkage, back-EMF and the developed torque of the machine can be calculated much faster, especially when compared to a FEA solution. With the subdomain model of the RFAPM, the optimum pole arc width of the permanent magnet, that would yield the lowest %THD for the radial flux-density distribution in the stator windings, can be calculated within a matter of seconds. This is a further prove to value this subdomain model has as a design tool for RFAPM machines.

The importance of having a quasi-sinusoidal radial flux-density distribution in the stator region of the RFAPM machine can not be over emphasised, as it provides us with a simple voltage – and a torque constant, similar to that of a normal sinusoidal permanent magnet AC or "brushless DC" machine. These constants simplify, not only the design aspect of RFAPM machine, but also from an application aspect, in that it provides the engineer with a set of simplified equations for the RFAPM machine's back-EMF and developed torque in terms of the rotational speed and phase current, respectively. However, as was mentioned in Chapter 5, the torque constant will only be valid with the back-EMF and phase current in phase. This is achieved using field orientated control.

In this dissertation the accuracy of the subdomain model for the RFAPM machine, as well as the accuracy of the voltage – and torque constant were benchmarked against a FEA simulation of a RFAPM machine that was designed for a small, low speed, direct drive wind generator by Stegmann [15]. The parameters for this machine (Test Machine I) is given in section E.1 of Appendix E.

The same benchmarking was also done against a FEA simulation of a RFAPM machine that was designed by Groenewald [17], as direct replacement for an Internal Combustion Engine (ICE) in an Electric Vehicle (EV) project at Stellenbosch University. The parameters for this machine (Test Machine II) is given in Appendix E, section E.2. The results of the benchmarking tests showing the analytically calculated waveforms together with the waveforms obtained

using FEA in Maxwell® 2D, are shown in Appendix I. From the comparison for the radial and azimuthal flux-density in section I.2, the flux-linkage and back-EMF comparison in section I.3 and the comparison of the armature reaction fields in section I.4, it is clear that the analytical model derived in this dissertation for the RFAPM machine, is indeed valid.

However in the comparison between the analytically calculated ripple torque and the solution provided by Maxwell® 2D as shown in Figure I.9, it obvious that the Maxwell® 2D solution is clearly wrong. This can also be seen from the harmonic spectrum of the torque waveforms as shown in Figure I.10. The torque waveform of the Maxwell® 2D solution should only contain 6^{th} order harmonics, similar to that of the analytical solution, as was shown in equation (5.28).

This emphasises the problems experience with the FEA modelling of RFAPM machines. For the FEA model of Test Machine II, the mesh element size in the different regions of the machine was chosen, using exactly the same relationship between the machine dimensions and that of element size as was done for Test Machine I.

7.4 Recommendations for Future Work

The analytical analysis method presented in this dissertation, although sufficiently accurate, can be improved further, by taking the recoil permeability of the permanent magnets into consideration. The method can also be extended to include parallel-magnetised permanent magnets, instead of only radially-magnetised permanent magnets. Furthermore, the effect of the end-windings can be added to the calculation of the synchronous inductances.

In this dissertation, all the scripting to perform the analytical analysis, as well the Maxwell® 2D simulations, was done using Python™. The Python™ scripts that were used, are briefly discussed in Appendix J. At the moment the Python™ scripts make use of a Command Line User Interface (CLUI) which, although very powerful, are not very user friendly.

It is recommended that a Qt based Graphical User Interface (GUI), e.g. PyQt4[1] or PySide[2], be developed for the Python™ scripts, for people unfamiliar with Python™. The integration of OpenOpt[3], a numerical optimisation package written in Python™, into the GUI should also be investigated, in order create an analytical based design tool for the design and optimisation of RFAPM machines.

[1] http://www.riverbankcomputing.co.uk/software/pyqt
[2] http://www.pyside.org/
[3] http://openopt.org

Appendices

APPENDIX A

Series–parallel coil combination

A.1 Introduction

When calculating the total flux-linkage of series–parallel combination of coils, it is important not to note that the flux-linkages does not add together as inductances would. This is best explained using an example as shown in Figure A.1 for a phase grouping of a number of coils in, say, phase a of an hypothetical machine.

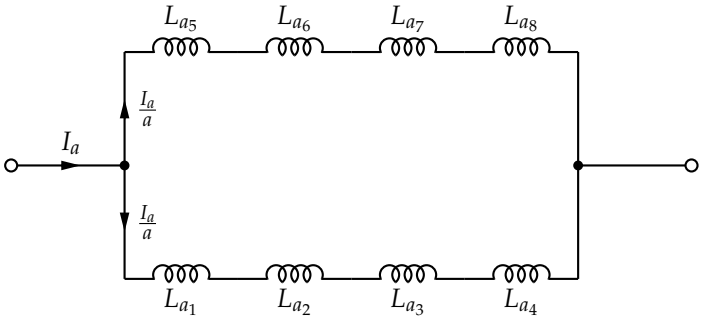

Figure A.1: Hypothetical per phase interconnected coil layout of a electrical machine.

A.2 Total inductance

The inductance of each coil in the phase grouping can be calculated as

$$L_{aj} = \frac{\Lambda_{aj}}{\hat{I}_{aj}} \quad \text{with } j = 1 \dots q \tag{A.1}$$

$$= \frac{a\Lambda_{aj}}{\hat{I}_a}\,, \tag{A.2}$$

with $\hat{I}_a$ the peak value of the phase current I_a and assuming that the phase current divides equally between the two branches due to all the coils having the same inductance and hence the same flux-linkage, Λ_{aj}.

The total inductance of phase a can now be calculated as follows

$$L_a = \frac{\frac{q}{a} \cdot L_{aj}}{a} \tag{A.3}$$

$$= \frac{qL_{aj}}{a^2} \,. \tag{A.4}$$

A.3 Total flux-linkage

From (A.4) it is easy to make the wrong conclusion regarding the total flux-linkage. It must be emphasised that the total flux-linkage for phase a,

$$\Lambda_a \neq \frac{q\Lambda_{aj}}{a^2} \,. \tag{A.5}$$

Substituting (A.2) into (A.4), we get

$$L_a = \frac{q\frac{a\Lambda_{aj}}{\hat{I}_a}}{a^2} \tag{A.6}$$

$$= \frac{q\Lambda_{aj}}{a\hat{I}_a} \tag{A.7}$$

$$\therefore \qquad L_a\hat{I}_a = \frac{q\Lambda_{aj}}{a} \tag{A.8}$$

so that we can write

$$\Lambda_a = \frac{q\Lambda_{aj}}{a} \tag{A.9}$$

which is the total flux-linkage "seen" by phase a.

APPENDIX B

The Surface Magnetisation Current Density Equivalance

The effect of the magnetisation vector is equivalent to a volumetric – combined with a surface magnetisation current density, Cheng [35, sec. 6.6]. If the magnetisation vector is uniform inside the permanent magnet material, as is the case for a radial magnetised permanent magnet in cylindrical coordinates, the currents of the neighbouring atomic dipoles that flow in opposite directions inside the permanent magnet will effectively cancel out, leaving no net current in the interior but only on the surface of the permanent magnets.

The equivalent surface magnetisation current distribution of the permanent magnets is shown in Figure B.1 and can be calculated as follows,

$$\vec{\mathbf{J}}_{ms} = \vec{\mathbf{M}} \times \vec{\mathbf{a}}_n \tag{B.1}$$

$$= M_0 \vec{\mathbf{a}}_r \times \vec{\mathbf{a}}_\theta \tag{B.2}$$

$$= M_0 \vec{\mathbf{a}}_z \, . \tag{B.3}$$

In this dissertation the derivative of the residual magnetisation distribution is used, as shown in Figure 3.3 and not the equivalent surface magnetisation current distribution as shown in Figure B.1. This comparison merely shows that they are indeed equivalent. We can also see that this equivalent surface magnetisation current distribution is basically equivalent to the current sheets used in the analysis of permanent magnet machines employed by Boules [28].

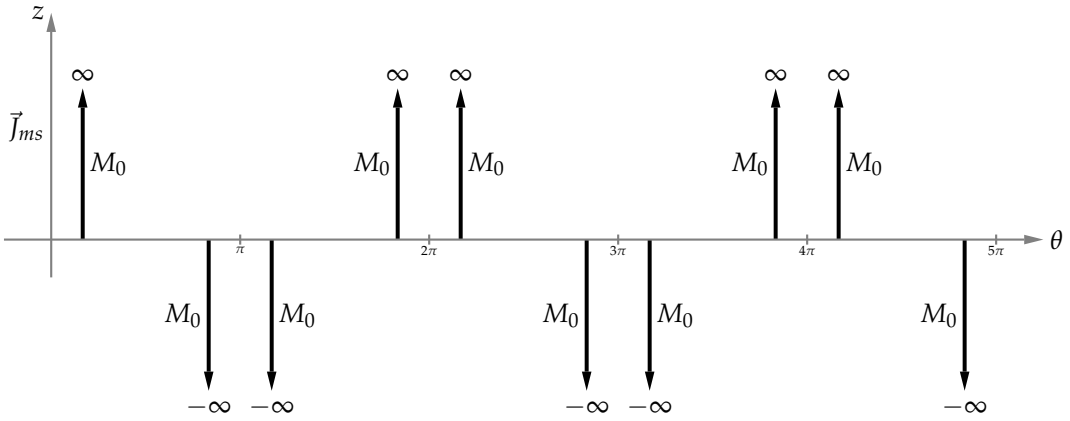

Figure B.1: The equivalent surface magnetisation current distribution with respect to θ.

APPENDIX C

Boundary conditions

C.1 For the magnetic flux density

If we write (3.4) in integral form,

$$\oint_s \vec{\mathbf{B}} \cdot d\vec{\mathbf{s}} = 0 \tag{C.1}$$

and we choose the Gaussian surface s in the form of a flat cylinder (e.g. a pillbox) with an infinity small thickness, to span across the boundary between to regions, we can expand (C.1) to

$$\int_{s_1} \vec{\mathbf{B}} \cdot d\vec{\mathbf{s}} + \int_{s_2} \vec{\mathbf{B}} \cdot d\vec{\mathbf{s}} = 0\,, \tag{C.2}$$

with s_1 the top portion of the Guassian surface and s_2 the bottom portion of the Guassian surface.

With $s_1 = s_2$, the above equation reduces to

$$B_{1_n} = B_{2_n}\,, \tag{C.3}$$

Figure C.1 or in vector form,

$$\vec{\mathbf{a}}_n \cdot (\vec{\mathbf{B}}_1 - \vec{\mathbf{B}}_2) = 0\,, \tag{C.4}$$

which implies that the normal components of the flux density is continuous across a boundary, Cheng [35, sec. 6.10].

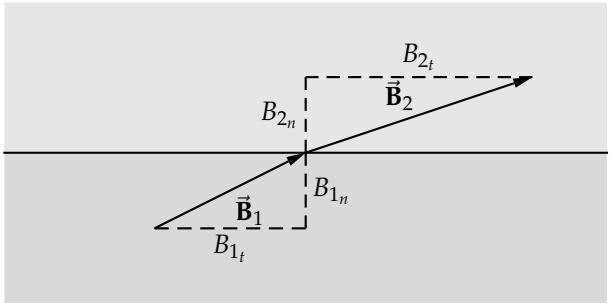

Figure C.1: The boundary condition of $\vec{\mathbf{B}}$ across an interface boundary.

Thus from the general solution for the magnetic vector potential, the fluxdensity can be calculated in the Cartesian coordiante systems as follows

$$\vec{\mathbf{B}} = \boldsymbol{\nabla} \times \vec{\mathbf{A}} \tag{C.5}$$

$$= \begin{vmatrix} \vec{\mathbf{a}}_x & \vec{\mathbf{a}}_y & \vec{\mathbf{a}}_z \\ \frac{\partial}{\partial x} & \frac{\partial}{\partial y} & \frac{\partial}{\partial z} \\ A_x & A_y & A_z \end{vmatrix} \tag{C.6}$$

$$= \left(\frac{\partial A_z}{\partial y} - \frac{\partial A_y}{\partial z}\right)\vec{\mathbf{a}}_x + \left(\frac{\partial A_x}{\partial z} - \frac{\partial A_z}{\partial x}\right)\vec{\mathbf{a}}_y + \left(\frac{\partial A_y}{\partial x} - \frac{\partial A_x}{\partial y}\right)\vec{\mathbf{a}}_z \,. \tag{C.7}$$

For 2D analysis (with $J_x = J_y = 0$), this reduces to

$$\vec{\mathbf{B}} = \frac{\partial A_z}{\partial y}\vec{\mathbf{a}}_x - \frac{\partial A_z}{\partial x}\vec{\mathbf{a}}_y \,. \tag{C.8}$$

Thus if the boundary between region (say) (v) and $(v+1)$ is parallel with the x-axis,

$$B_y^{(v)} = B_y^{(v+1)} \tag{C.9}$$

$$\frac{\partial A_z^{(v)}}{\partial x} = \frac{\partial A_z^{(v+1)}}{\partial x} \tag{C.10}$$

In the cylindrical coordinate system,

$$\vec{\mathbf{B}} = \boldsymbol{\nabla} \times \vec{\mathbf{A}} \tag{C.11}$$

$$= \frac{1}{r}\begin{vmatrix} \vec{\mathbf{a}}_r & r\vec{\mathbf{a}}_\theta & \vec{\mathbf{a}}_z \\ \frac{\partial}{\partial r} & \frac{\partial}{\partial \theta} & \frac{\partial}{\partial z} \\ A_r & rA_\theta & A_z \end{vmatrix} \tag{C.12}$$

$$= \frac{1}{r}\left(\frac{\partial A_z}{\partial \theta} - r\frac{\partial A_\theta}{\partial z}\right)\vec{\mathbf{a}}_r + \left(\frac{\partial A_r}{\partial z} - \frac{\partial A_z}{\partial r}\right)\vec{\mathbf{a}}_\theta + \frac{1}{r}\left(\frac{\partial (rA_\theta)}{\partial r} - \frac{\partial A_r}{\partial \theta}\right)\vec{\mathbf{a}}_z \,. \tag{C.13}$$

For 2D analysis (with $J_r = J_\theta = 0$) the above equation reduces to

$$\vec{\mathbf{B}} = \frac{1}{r}\frac{\partial A_z}{\partial \theta}\vec{\mathbf{a}}_r - \frac{\partial A_z}{\partial r}\vec{\mathbf{a}}_\theta \,. \tag{C.14}$$

Thus for a concentric circular boundarie between regions, say, (v) and $(v+1)$,

$$B_r^{(v)} = B_r^{(v+1)} \tag{C.15}$$

$$\frac{\partial A_z^{(v)}}{\partial \theta} = \frac{\partial A_z^{(v+1)}}{\partial \theta} \tag{C.16}$$

C.2 For the magnetic field intensity

If we write (1.2') in differential form,

$$\oint_c \vec{\mathbf{H}} \cdot d\vec{\ell} = \int_s \vec{\mathbf{J}} \cdot d\vec{\mathbf{s}} \tag{C.17}$$

with c the contour spanning the surface s. If we choose c to span accross the boundary between two regions and we make the thickness infinite small, and if we further assume that the surface current density on the boundary is zero, we can write

$$\int_{c_1} \vec{\mathbf{H}} \cdot d\vec{\ell} + \int_{c_2} \vec{\mathbf{H}} \cdot d\vec{\ell} = 0 \tag{C.18}$$

with c_1 the top portion of the contour and c_2 the bottom portion of the contour.

With $c_1 = c_2$ the above equation reduces to,

$$\therefore \quad H_{1_t} = H_{2_t} \,, \tag{C.19}$$

see Figure C.2, or in vector format for the general case,

$$\vec{\mathbf{a}}_n \times (\vec{\mathbf{H}}_1 - \vec{\mathbf{H}}_2) = \vec{\mathbf{J}}_s \,, \tag{C.20}$$

which implies that the tangential component of the magnetic field intensity is continuous across a boundary if and only if the free surface current density on the boundary is zero.

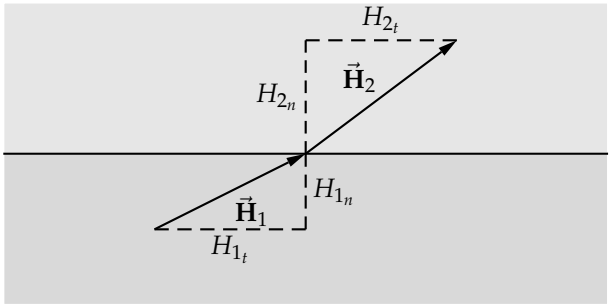

Figure C.2: The boundary condition of $\vec{\mathbf{H}}$ across an interface boundary.

From (3.9), for a linear isotropic non permanent magnet region,

$$\vec{\mathbf{H}} = \frac{\vec{\mathbf{B}}}{\mu} \,, \tag{C.21}$$

and from (3.18), for a linear isotropic permanent magnet region,

$$\vec{\mathbf{H}} = \frac{(\vec{\mathbf{B}} - \vec{\mathbf{B}}_{rem})}{\mu} \,. \tag{C.22}$$

Thus from (3.71) and (C.14) on a boundary between a non permanent magnet region, say, (v) and a permanent magnet region, say, $(v+1)$,

$$H_\theta^{(v)} = H_\theta^{(v+1)} \tag{C.23}$$

$$\frac{B_\theta^{(v)}}{\mu^{(v)}} = \frac{B_\theta^{(v+1)}}{\mu^{(v+1)}} - \frac{B_{rem_\theta}}{\mu^{(v+1)}} \,. \tag{C.24}$$

With radial magnetised permanent magnets, the azimutial component of $\vec{\mathbf{B}}_{rem}$ is zero, so that the above equation reduses to

$$\frac{1}{\mu^{(v)}}\frac{\partial A_z^{(v)}}{\partial r} = \frac{1}{\mu^{(v+1)}}\frac{\partial A_z^{(v+1)}}{\partial r} \,. \tag{C.25}$$

APPENDIX D

Doing Fourier Analysis in Degrees

D.1 Working with electrical degrees

The Fourier series expansion for a_m is calculated as follows,

$$a_m = \frac{4}{T}\int_0^{\frac{T}{2}} f(t)\cos(m\omega_0 t)dt\ . \tag{D.1}$$

The Fourier series of an angular distribution, can also directly be calculated, by setting,

$$\theta = \omega_0 t\ , \tag{D.2}$$

$$\frac{d\theta}{dt} = \omega_0\ , \tag{D.3}$$

$$\therefore \quad dt = \frac{d\theta}{\omega_0} \tag{D.4}$$

$$= T\frac{d\theta}{2\pi} \tag{D.5}$$

with

$$\omega_0 = \frac{2\pi}{T}\ . \tag{D.6}$$

This also affects the integration boundaries, so that,

$$\omega_0 t\big|_{t=0} = 0 \tag{D.7}$$

and

$$\omega_0 t\big|_{t=\frac{T}{2}} = \pi\ , \tag{D.8}$$

resulting in

$$a_m = \frac{4}{2\pi}\int_0^{\pi} f(\theta)\cos(m\theta)d\theta \tag{D.9}$$

D.2 Working with mechanical degrees

The same can also be done when working in mechanical degrees, by setting:

$$\theta = \frac{\omega_0 t}{p}\,, \tag{D.10}$$

$$\frac{d\theta}{dt} = \frac{\omega_0}{p}\,, \tag{D.11}$$

$$\therefore \quad dt = p\frac{d\theta}{\omega_0} \tag{D.12}$$

$$= pT\frac{d\theta}{2\pi}\,, \tag{D.13}$$

with

$$\omega_0 = \frac{2\pi}{pT}\,. \tag{D.14}$$

Again the integration boundaries change, so that

$$\omega_0 t\big|_{t=0} = 0 \tag{D.15}$$

and

$$\omega_0 t\big|_{t=\frac{T}{2}} = \frac{\pi}{p}\,. \tag{D.16}$$

resulting in

$$a_m = \frac{4p}{2\pi}\int_0^{\frac{\pi}{p}} f(\theta)\cos(mp\theta)d\theta \tag{D.17}$$

APPENDIX E

Test Machine Data

E.1 Test Machine I

For more information regarding this machine refer to Stegmann [15] and Stegmann and Kamper [16, 26].

p	=	16		– *the total number of pole (magnets) pairs on the inner/outer rotor yoke*
k_q	=	$\frac{1}{2}$		– *coils-per-phase to pole-pair ratio*
q	=	pk_q		– *number of coils per phase*
	=	8		
Q	=	$3q$		– *total number of coils*
	=	24		
k_m	=	0,7		– *the magnet angle to pole-pitch angle ratio*
r_n	=	232	[mm]	– *nominal stator radius*
l	=	76	[mm]	– *active stack/copper length*
w	=	22,473	[mm]	– *coil side width*
Δ	=	$\frac{w}{2r_n}$		– *coil side width angle*
	=	$48{,}433 \cdot 10^{-3}$	[rad]	
	=	2,775	[°]	
Δ_{max}	=	$\frac{\pi}{2Q}$		– *maximum coil side-width angle*
	=	$65{,}45 \cdot 10^{-3}$	[rad]	
	=	3,75	[°]	
k_Δ	=	$\frac{\Delta}{\Delta_{max}}$		– *coil side-width factor*
	=	0,74		
h	=	10,0	[mm]	– *height/thickness of the stator coils*
h_m	=	8,2	[mm]	– *magnet height/thickness*

h_y	=	8,0	[mm]	– *yoke height/thickness*
ℓ_g	=	1,0	[mm]	– *air gap length*
N	=	96		– *number of turns per coil*
a	=	1		– *number of parallel branches*
n	=	300	[rpm]	– *rated speed*
f	=	$\frac{np}{120}$		– *rated frequency*
	=	80,0	[Hz]	
H_c	=	1 050 000	[A/m]	– *the maximum coercivity force*
B_{rem}	=	1,4	[T]	– *the remanent flux density of the permanent magnets*
I_p	=	7,33	[A]	– *rated peak current value per phase*

E.2 Test Machine II

For more information regarding this machine refer to Groenewald [17].

p	=	12		– *the total number of pole (magnets) pairs on the inner/outer rotor yoke*
k_q	=	$\frac{1}{2}$		– *coils-per-phase to pole-pair ratio*
q	=	pk_q		– *number of coils per phase*
	=	6		
Q	=	$3q$		– *total number of coils*
	=	18		
k_m	=	$\frac{2}{3}$		– *the magnet angle to pole-pitch angle ratio*
r_n	=	125	[mm]	– *nominal stator radius*
l	=	80	[mm]	– *active stack/copper length*
w	=	13,96	[mm]	– *coil side width*
Δ	=	$\frac{w}{2r_n}$		– *coil side width angle*
	=	$55{,}84 \cdot 10^{-3}$	[rad]	
	=	3,2	[°]	
Δ_{max}	=	$\frac{\pi}{2Q}$		– *maximum coil side-width angle*
	=	$87{,}266 \cdot 10^{-3}$	[rad]	
	=	5,0	[°]	
k_Δ	=	$\frac{\Delta}{\Delta_{max}}$		– *coil side-width factor*
	=	0,64		
h	=	8,0	[mm]	– *height/thickness of the stator coils*
h_m	=	4,0	[mm]	– *magnet height/thickness*
h_y	=	5,0	[mm]	– *yoke height/thickness*
ℓ_g	=	2,0	[mm]	– *air gap length*
N	=	33		– *number of turns per coil*
a	=	6		– *number of parallel branches*
n	=	4800	[rpm]	– *rated speed*

f	=	$\frac{np}{120}$		– *rated frequency*
	=	960,0	[Hz]	
H_c	=	923 000	[A/m]	– *the maximum coercivity force*
B_{rem}	=	1,4	[T]	– *the remanent flux density of the permanent magnets*
I_p	=	152,08	[A]	– *rated peak current value per phase*

APPENDIX F

Permanent Magnetic Circuit Analysis

F.1 Introduction

In this appendix magnetic circuit analysis of circuits with permanent magnets will be discussed. In the literature magnetic circuit analysis is also sometimes referred to as 1-D analytical analysis, Zhu *et al.* [23].

F.2 Permanent Magnet Fundamentals

All materials are composed of atoms with a positively charged nucleus and a number of orbiting negatively charged electrons, Cheng [35, chap. 6]. The orbiting electrons cause a "circulation current" and form microscopic magnetic dipoles. In the absence of an external magnetic field, the magnetic dipoles of most materials, except that of permanent magnets, have random orientation resulting in no net magnetic moment. The application of an external magnetic field causes both an alignment of the magnetic moments of the spinning electrons and an induced magnetic moment due to the change in the orbital motion of the electrons.

At a macroscopic level, a magnetic material is usually represented by a magnetisation vector, $\vec{\mathbf{M}}$, which is defined as the vector sum of the magnetic dipole moments per unit volume on a microscopic level. It can be proved that the magnetisation vector is equivalent to both a volumetric current density

$$\vec{\mathbf{J}}_m = \boldsymbol{\nabla} \times \vec{\mathbf{M}} \tag{F.1}$$

and a surface current density

$$\vec{\mathbf{J}}_{ms} = \vec{\mathbf{M}} \times \vec{\mathbf{a}}_n \, . \tag{F.2}$$

If the magnetisation vector of a material is uniform inside the material, the currents of the neighbouring atomic dipoles that flow in opposite directions will cancel, leaving no net

current in the interior. This implies that inside the material, the curl of the constant $\vec{\mathbf{M}}$ will be zero and from (F.1), $\vec{\mathbf{J}}_m$ will be zero. A uniformly magnetised permanent magnet can therefor be represented by an equivalent surface current density or a fictitious winding, N_m carring a current i_m so that the MMF produced by the permanent magnet,

$$\mathcal{F} = N_m i_m \tag{F.3}$$

$$= H_m h_m \tag{F.4}$$

with H_m the coercivity of the permanent magnet and h_m the height or thickness of the permanent magnet, Fitzgerald *et al.* [19, chap. 1 & 3].

F.3 Magnetic Circuit Analysis with Coil Excitation

To start the analysis, we will only consider a magnetic circuit with a single coil excitation, Figure F.1.

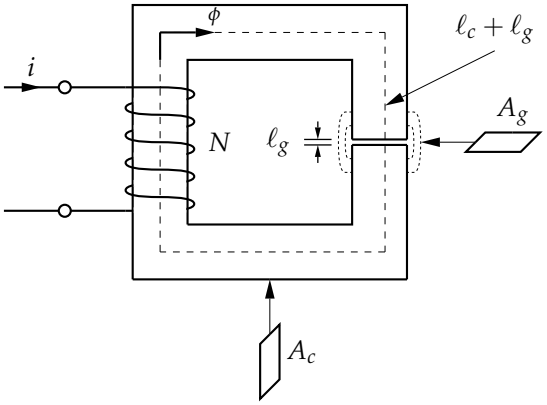

Figure F.1: Magnetic circuit with coil excitation.

Basic magnetic circuit analysis is usually done using Ampère's law. Applying Ampère's law to the above circuit yield:

$$H_c \ell_c + H_g \ell_g = Ni \tag{F.5}$$

If the relative permeability of the iron core tends towards infinity, i.e. $\mu_{r_c} \to \infty$ or $\mu_{r_c} \gg 1$, the magnetic field intensity in the airgap can now easily be calculated from (F.5).

$$H_g = \frac{Ni}{\ell_g} \tag{F.6}$$

With,

$$B_g = \mu_0 H_g \,, \tag{F.7}$$

the airgap fluxdensity will be equal to:

$$B_g = \mu_0 \frac{Ni}{\ell_g} \tag{F.8}$$

F.4 Magnetic Circuit Analysis with PM Excitation

We now replace a portion of the iron core with a permanent magnet as shown in Figure F.2.

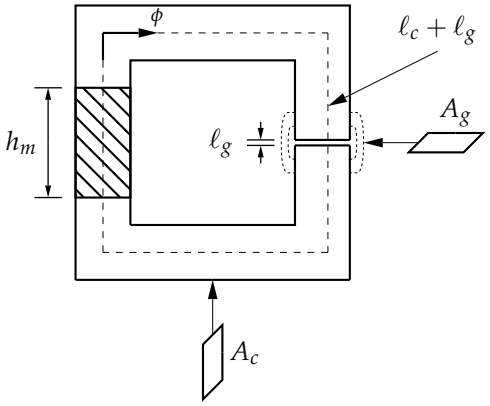

Figure F.2: Magnetic circuit with permanent magnet excitation.

According to Ampère's law:

$$H_m h_m + H_c \ell_c + H_g \ell_g = 0 \tag{F.9}$$

If we once again take the permeability of the iron core as striving toward infinity, (F.9) reduces to,

$$H_m h_m + H_g \ell_g = 0\,, \tag{F.10}$$

which is impossible to solve as both H_m and H_g are unknowns.

However in terms of flux, we know that,

$$\Phi_m = \Phi_g \tag{F.11}$$

because all the flux that goes through the magnet must pass through the airgap.

$$\therefore \quad B_m A_m = B_g A_g \tag{F.12}$$

Unfortunately the relationship between the fluxdensity and the magnetic field intensity in the magnet are as such undefined as opposed to the simple relationship that excists in the airgap, (F.7).

F.5 NdFeB Permanent Magnets

The advantages of using "Rare-earth" permanent magnets, e.g. Samarium-Cobalt ($SmCo_5$) or Neodymium-Iron-Boron (NdFeB), are not only that they have a much higher coercivity than Alnico magnets but also that they have a linear demagnetisation curve. The demagnetisation curve for NdFeB magnets can thus be represented by a straight line as shown in Figure F.3.

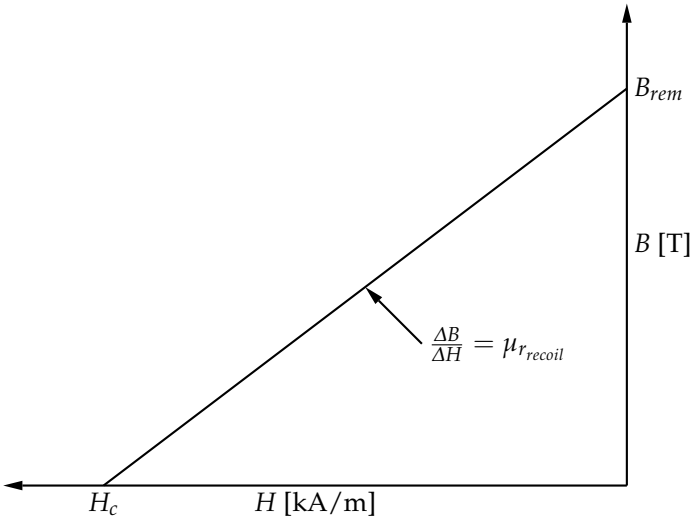

Figure F.3: Demagnetisation curve for NdFeB magnets.

For N48 NdFeB magnets, this straight line approxamation is however only valid at 20°C, [45]. For higher temperatures, a higher temperature grade magnets, e.g. N48H, should be used which has a linear demagnetisation curve up to 50°C, [54].

The recoil permeability, μ_{recoil}, of a permanent magnet is defined as

$$\mu_{recoil} = \mu_0 \mu_{r_{recoil}} \tag{F.13}$$

$$= \frac{\Delta B}{\Delta H} \, . \tag{F.14}$$

For a NdFeB permanent magnet with a linear demagnetisation curve, the recoil permeability will thus be equal[1] to,

$$\mu_{recoil} = \frac{B_{rem}}{H_c} \, , \tag{F.15}$$

with the equation for the demagnetisation line given by

$$B_m = \mu_{recoil} H_m + B_{rem} \, . \tag{F.16}$$

From the specifications for the different grade NdFeB magnets as given in Table F.1, the linear equation for the different grades of NdFeB magnets kan easily be found.

F.6 Magnetic Circuit Analysis with PM Excitation Continue...

From (F.7), the magnetic field intensity in the airgap can be written as

$$H_g = \frac{B_g}{\mu_0} \, , \tag{F.17}$$

and from (F.16), the magnetic field intensity in the permanent magnet can be written as

$$H_m = \frac{B_m - B_{rem}}{\mu_0 \mu_{r_{recoil}}} \, . \tag{F.18}$$

[1]The symbol used for the magnetic field intensity in F.4 is the same as that used for the magnetic coersivity.

Table F.1: Specification of different NdFeB magnets.

Grade	B_{rem} [mT]	H_{cb} [kA/m]	H_{cj} [kA/m]	$(BH)_{max}$ [kJ/m^3]	T_w
N27	1030–1080	≥ 796	≥ 955	199–23	80 °C
N30	1080–1130	≥ 796	≥ 955	223–247	80 °C
N33	1130–1170	≥ 836	≥ 955	247–271	80 °C
N35	1170–1220	≥ 868	≥ 955	263–287	80 °C
N38	1220–1250	≥ 899	≥ 955	287–310	80 °C
N40	1250–1280	≥ 907	≥ 955	302–326	80 °C
N42	1280–1320	≥ 915	≥ 955	318–342	80 °C
N45	1320–1380	≥ 923	≥ 955	342–366	80 °C
N48	1380–1420	≥ 923	≥ 876	366–390	80 °C
N50	1400–1450	≥ 796	≥ 876	382–406	60 °C
N52	1430–1480	≥ 796	≥ 876	398–422	60 °C

Substituting (F.17) and (F.18) into (F.10) to solve the Ampère's law equation, yield:

$$\begin{aligned} \frac{B_g}{\mu_0} \cdot \ell_g &= -\left(\frac{B_m - B_{rem}}{\mu_0 \mu_{r_{recoil}}}\right) \cdot h_m \\ \therefore \qquad B_g &= \left(\frac{B_{rem} - B_m}{\mu_{r_{recoil}}}\right) \cdot \left(\frac{h_m}{\ell_g}\right) \end{aligned} \tag{F.19}$$

From (F.12), if the area of the airgap and that of the magnets are the same, i.e. if we ignore fringing, $B_g = B_m$ which implies that (F.19) can further be simplified to,

$$B_g = \frac{B_{rem}}{\left(1 + \mu_{r_{recoil}} \cdot \frac{\ell_g}{h_m}\right)}, \tag{F.20}$$

which is similar to (2.14) in [1] except that here we have a double airgap.

From (F.20) the fluxdensity in the airgap can now easily be calculated from the specifications of the NdFeB magnet used and the airgap length.

Alternatively, (F.20) allows one to calcualte the required length, or thickness, of the NdFeB magnet required for a required airgap fluxdensity as follows:

$$h_m = \frac{\ell_g \mu_{r_{recoil}}}{\left(\frac{B_{rem}}{B_g} - 1\right)} \tag{F.21}$$

F.7 Magnetic Circuit Analysis for the RFAPM Machine.

In Figure F.4 the magnetic equivalent circuit for one pole pair of a RFAPM machine is shown. The equivalent circuit differs slightly from the simplified one shown in Figure F.2.

The RFAPM machine have two airgap, two sets of magnets as well as a set of air cored windings. This implies that for the RFAPM machine (F.20) will change to,

$$B_g = \frac{B_{rem}}{\left(1 + \mu_{r_{recoil}} \cdot \frac{2\ell_g + h}{2h_m}\right)}, \tag{F.22}$$

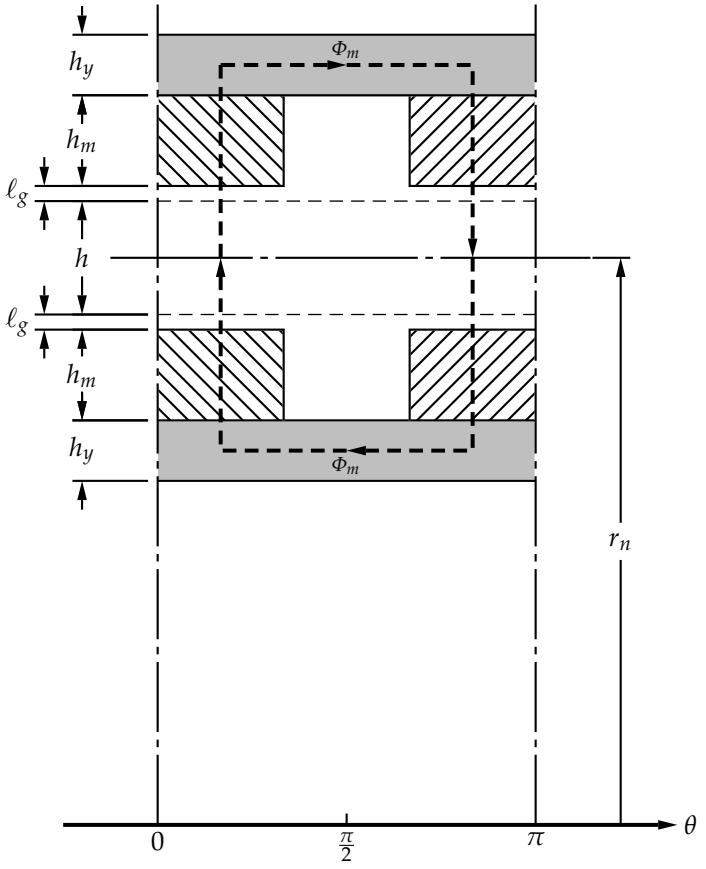

Figure F.4: Magnetic circuit of the RFAPM machine for one pole pair.

and (F.21) to

$$h_m = \frac{(\ell_g + \frac{h}{2})\mu_{r_{recoil}}}{\left(\frac{B_{rem}}{B_g} - 1\right)} \,. \tag{F.23}$$

From this figure, using (F.19) the fluxdensity in the airgap for test machine I, see Appendix E.1, can be calculated as,

$$B_g = 0{,}788 \text{ T} \,, \tag{F.24}$$

and that for test machine II, see Appendix E.2, as,

$$B_g = 0{,}498 \text{ T} \,. \tag{F.25}$$

Appendix G

Armature reaction contour field plots

G.1 Overlapping, Type O, winding configuration

G.1.1 Magnetic vector potential

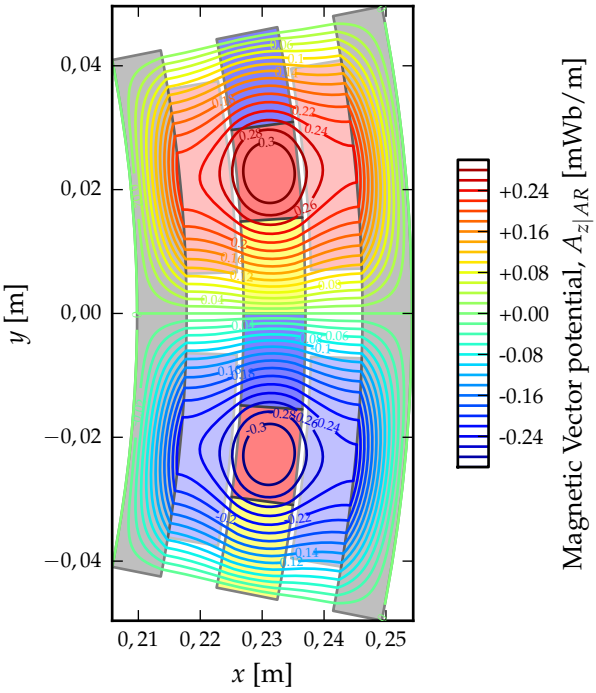

Figure G.1: Contour plot of the magnetic vector potential.

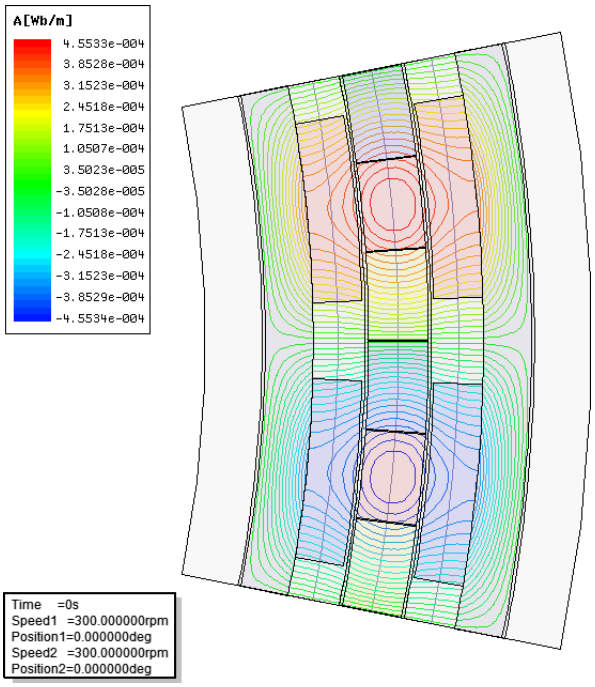

Figure G.2: Contour plot of the magnetic vector potential as simulated in Maxwell® 2D.

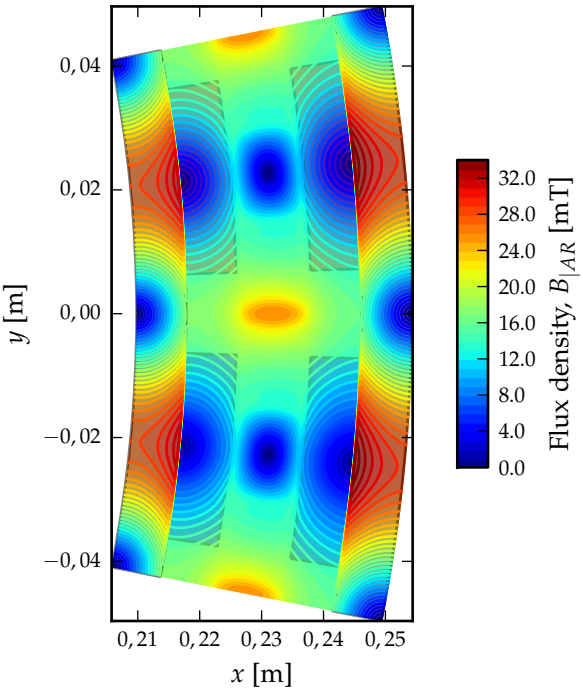

Figure G.3: Contour plot of the magnetic flux density.

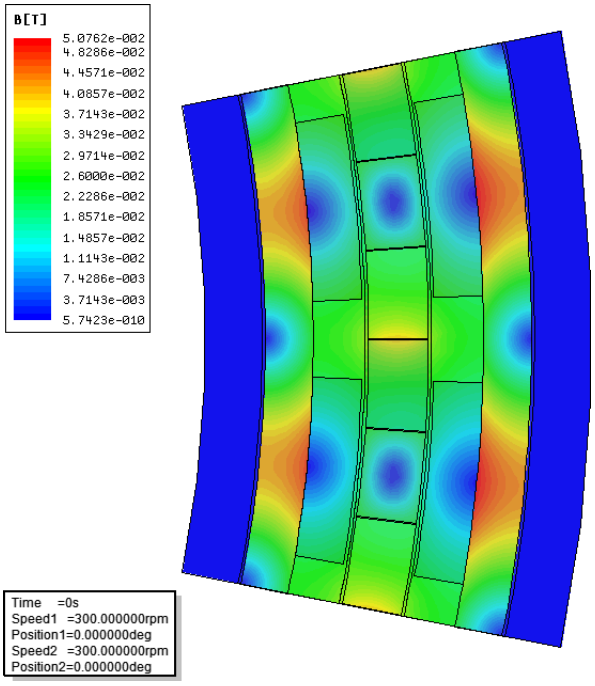

Figure G.4: Contour plot of the magnetic flux density as simulated in Maxwell® 2D.

G.2 Non-overlapping, Type I, winding configuration

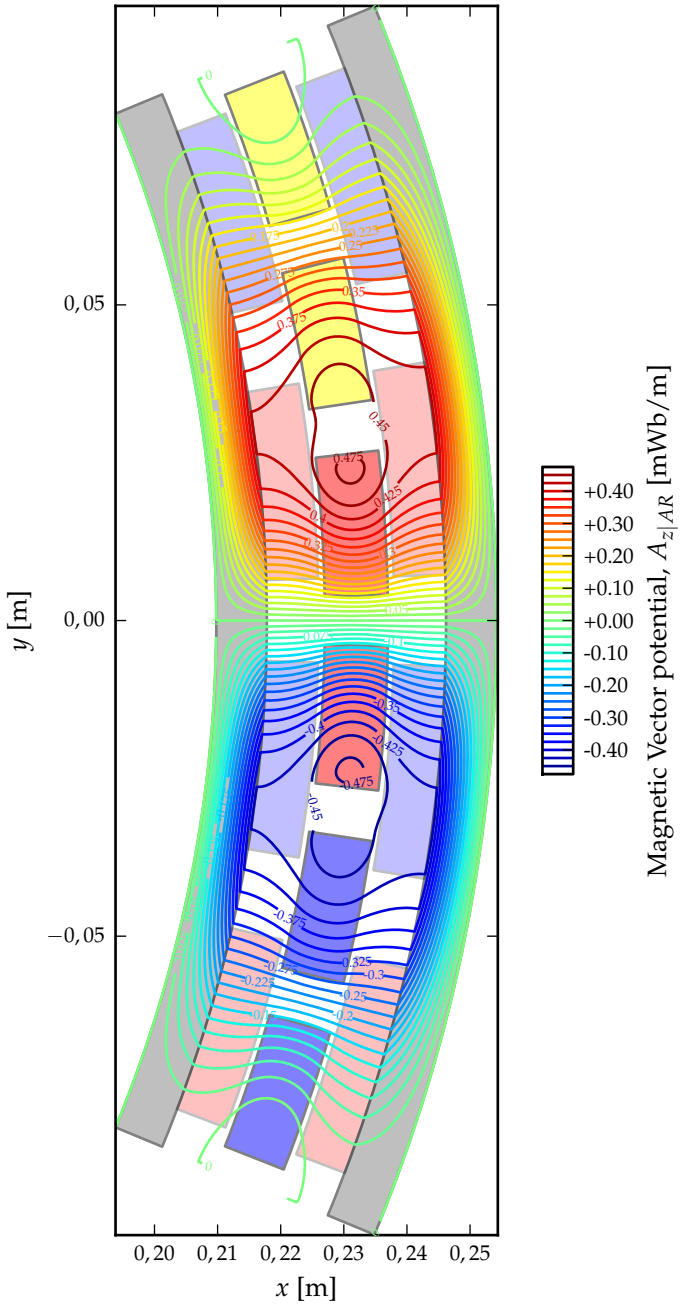

Figure G.5: Contour plot of the magnetic vector potential

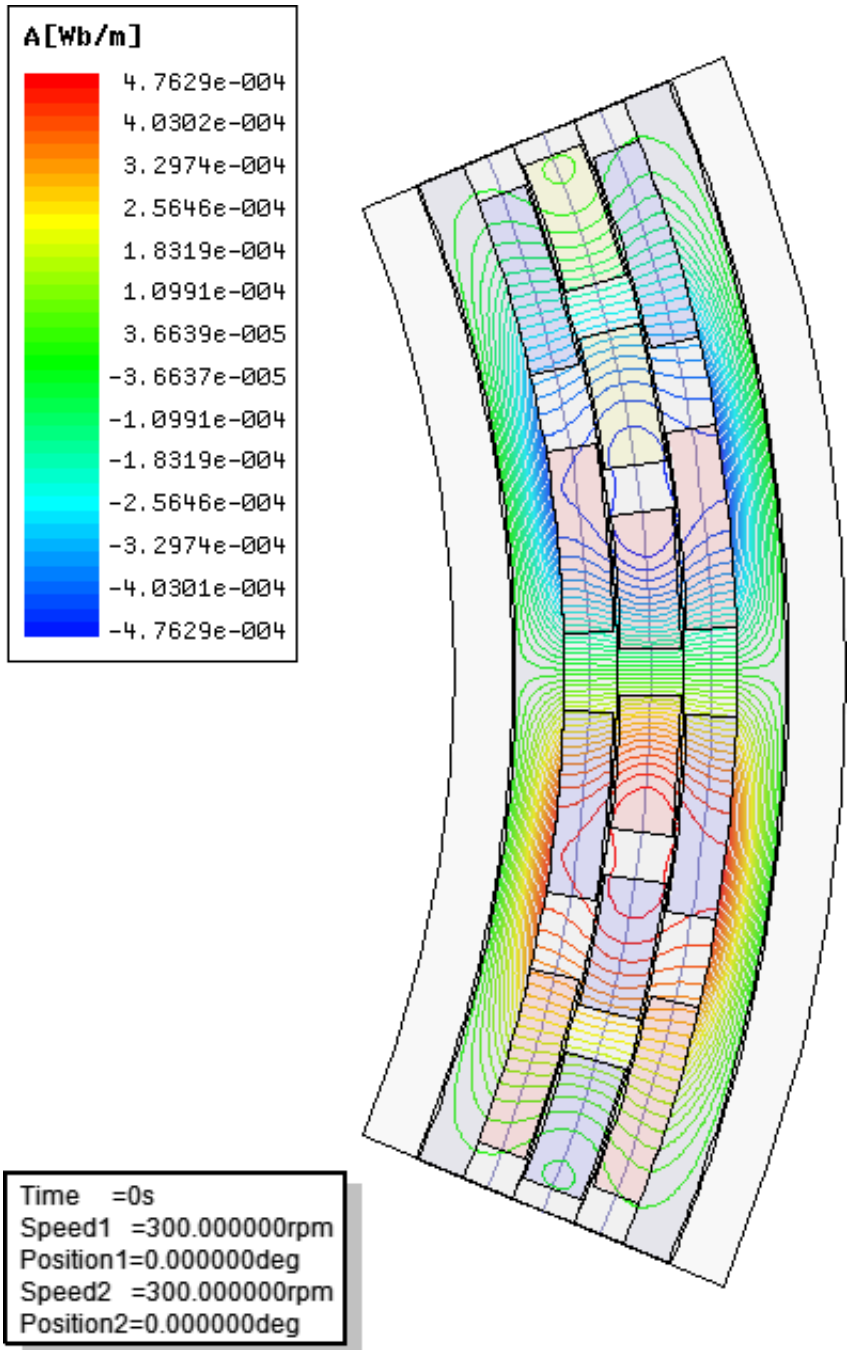

Figure G.6: Contour plot of the magnetic vector potential as simulated in Maxwell® 2D.

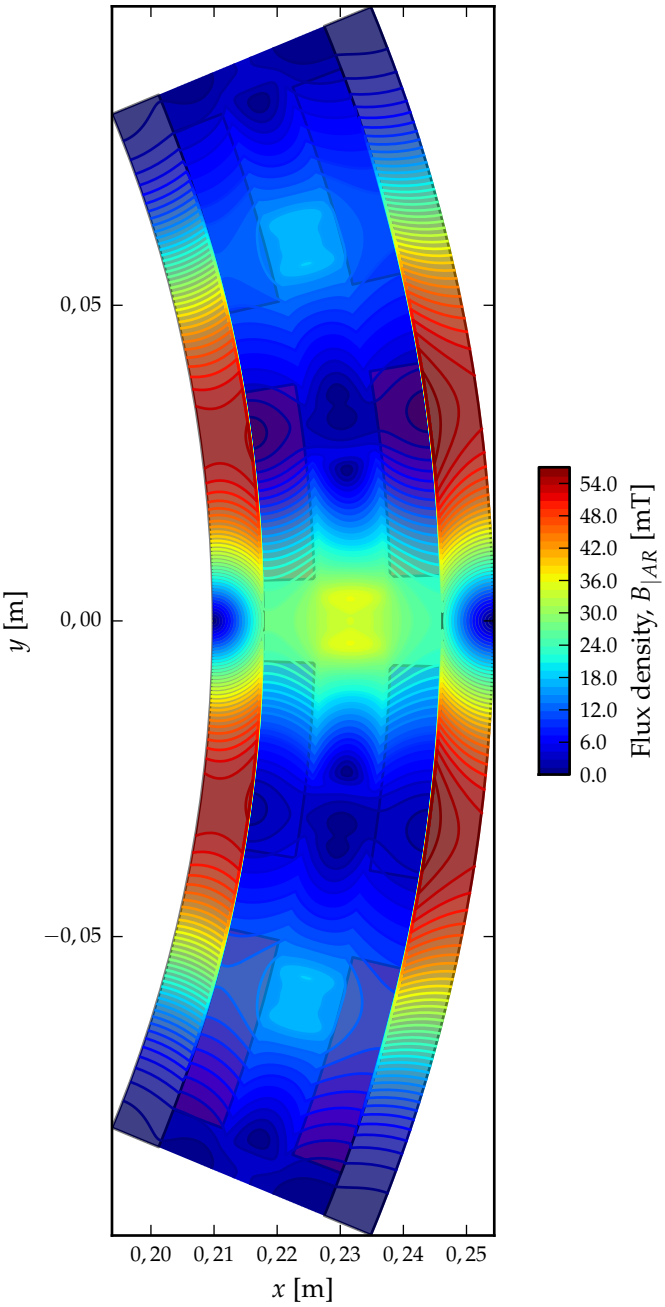

Figure G.7: Contour plot of the magnetic flux density

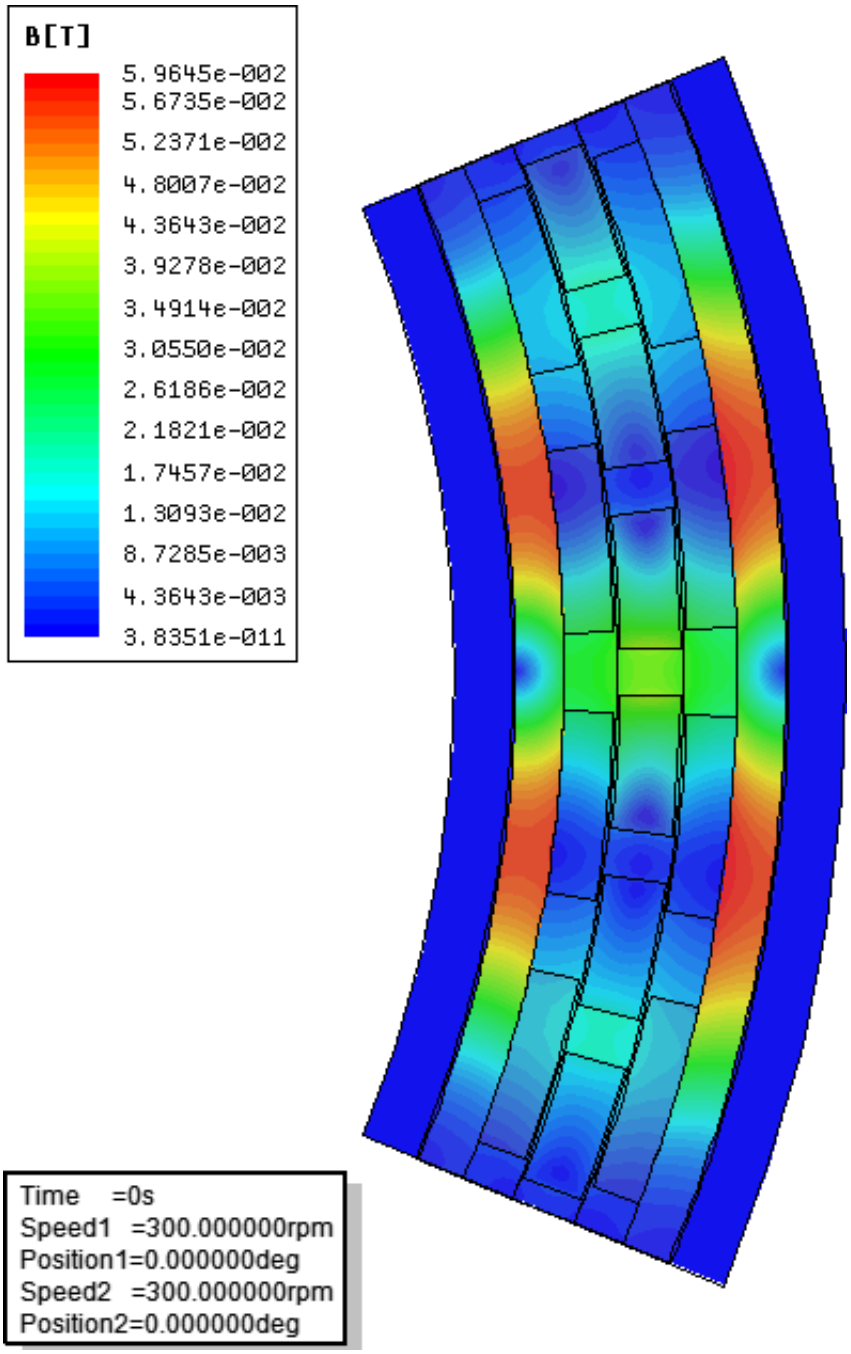

Figure G.8: Contour plot of the magnetic flux density as simulated in Maxwell® 2D.

G.3 Non-overlapping, Type II, winding configuration

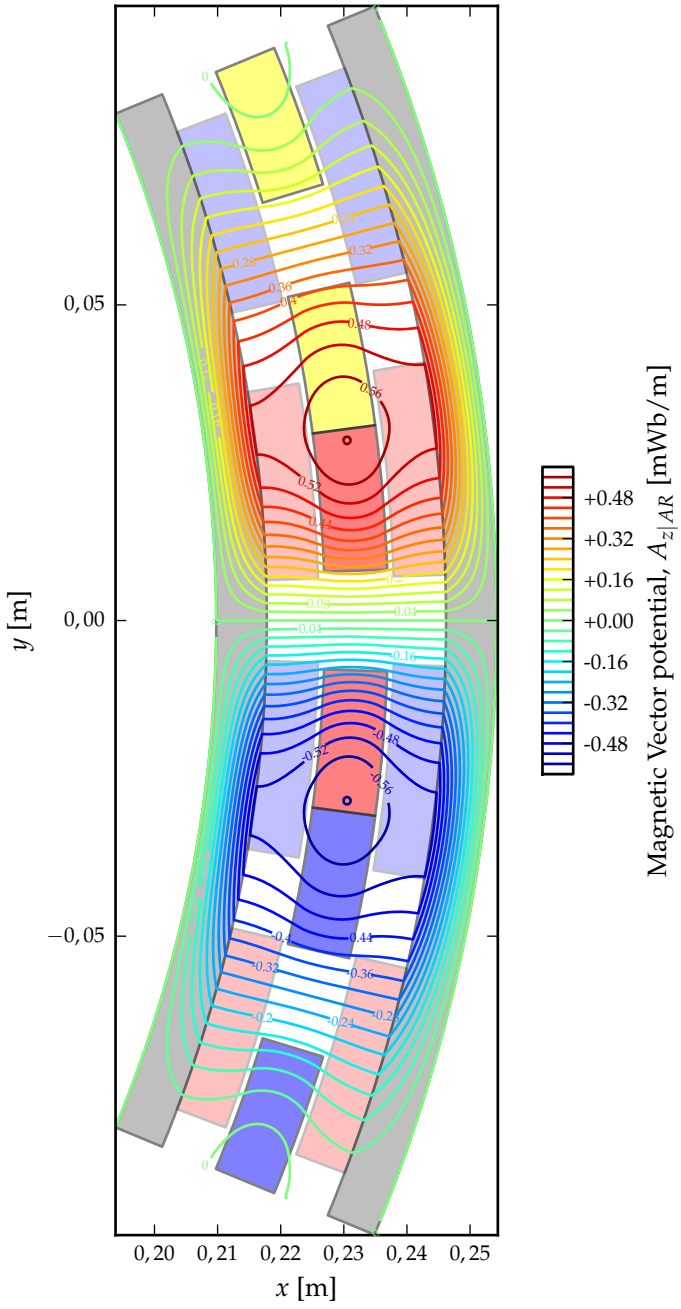

Figure G.9: Contour plot of the Magnetic Vector Potential.

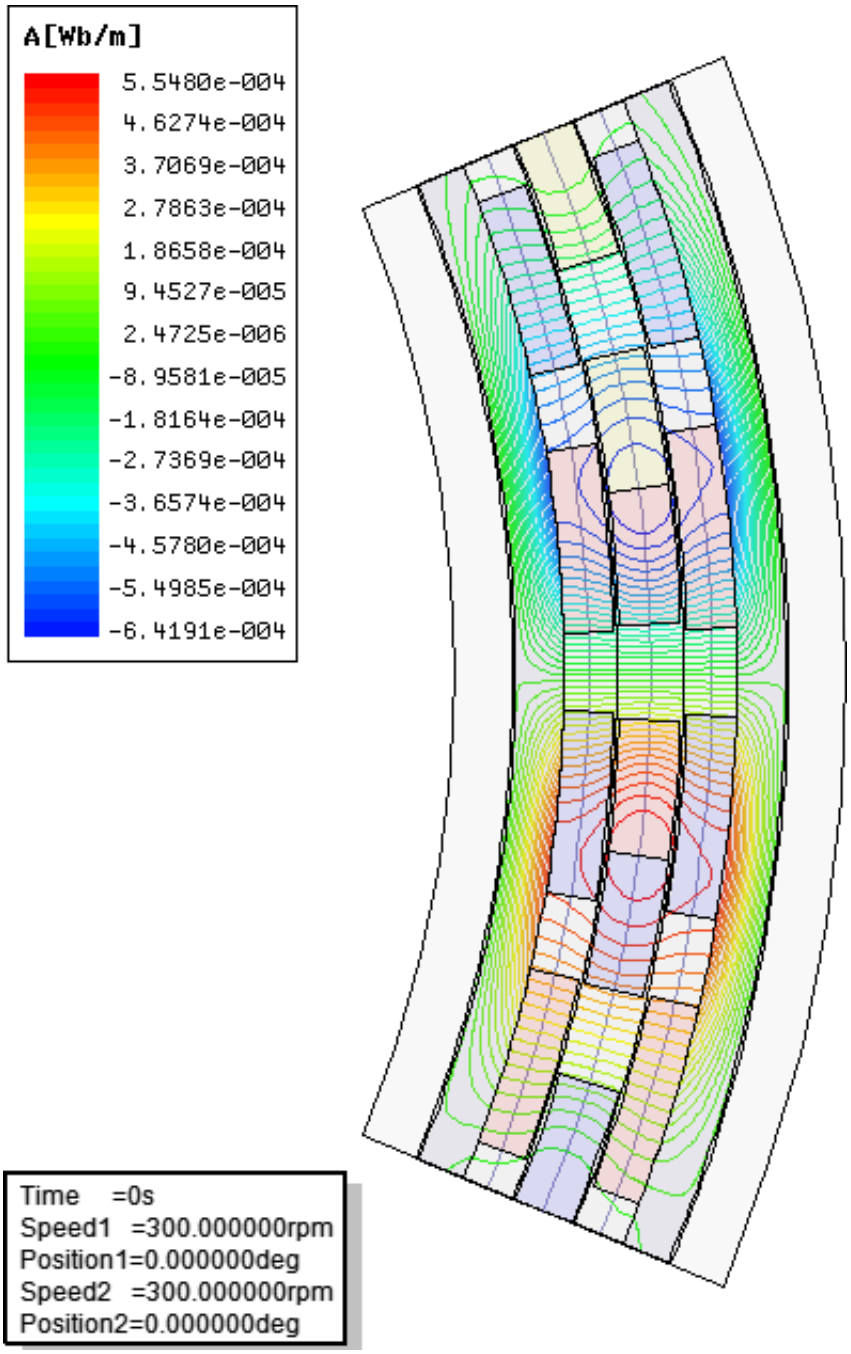

Figure G.10: Contour plot of the magnetic vector potential as simulated in Maxwell® 2D.

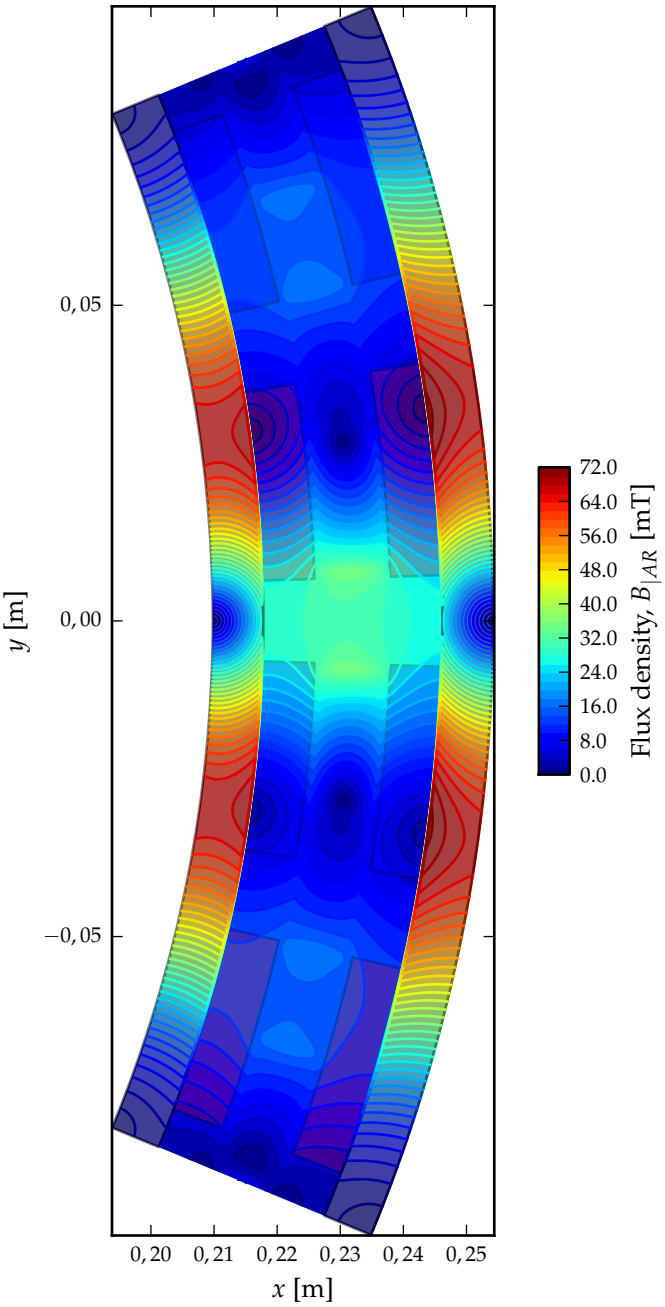

Figure G.11: Contour plot of the magnetic flux density.

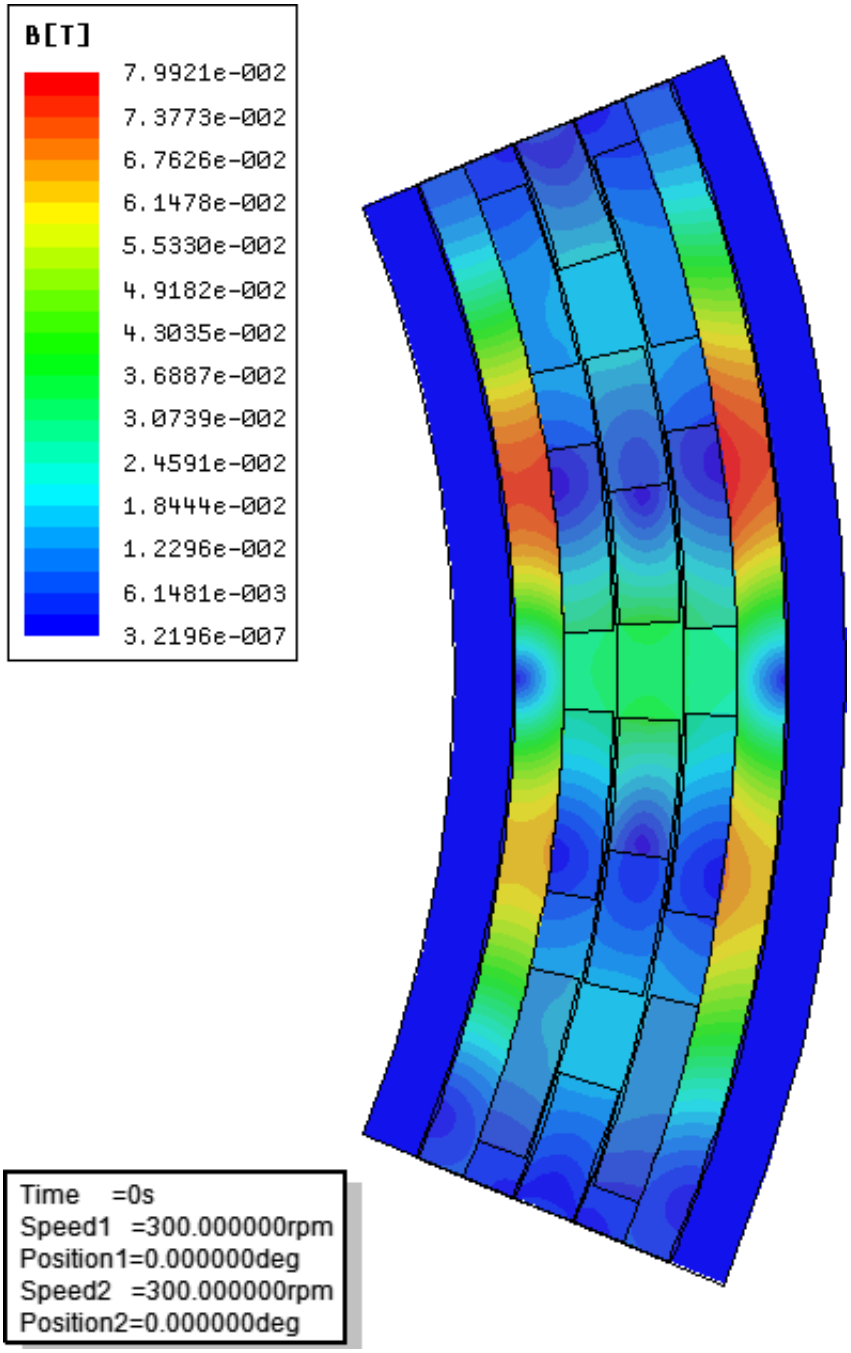

Figure G.12: Contour plot of the magnetic flux density as simulated in Maxwell® 2D.

APPENDIX H

Simplified Analytical Analysis

H.1 Solving for all the regions of RFAPM machine simultaneously

H.1.1 Introduction

By taking the permeability of the yoke iron $\approx \infty$, we only need to solve for regions II, III and IV.

H.1.2 On the boundary between region I and II

With $r = r_n - \frac{h}{2} - \ell_g - h_m$,

$$H_\phi^{II}(r,\phi) = 0 \tag{H.1}$$

$$\therefore \quad C_{m|PM}^{II} r^{mp-1} - D_{m|PM}^{II} r^{-mp-1} = 0 \tag{H.2}$$

H.1.3 On the boundary between region II and III

With $r = r_n - \frac{h}{2} - \ell_g$,

$$B_r^{II}(r,\phi) = B_r^{III}(r,\phi) \tag{H.3}$$

$$\therefore \quad C_{m|PM}^{II} r^{mp} + D_{m|PM}^{II} r^{-mp} + G_{m|PM}^{II} = C_{m|PM}^{III} r^{mp} + D_{m|PM}^{III} r^{-mp} \tag{H.4}$$

and

$$H_\phi^{II}(r,\phi) = H_\phi^{III}(r,\phi) \tag{H.5}$$

$$\therefore \quad \frac{C_{m|PM}^{II} r^{mp-1} - D_{m|PM}^{II} r^{-mp-1}}{\mu^{II}} = \frac{C_{m|PM}^{III} r^{mp-1} - D_{m|PM}^{III} r^{-mp-1}}{\mu^{III}} \tag{H.6}$$

H.1.4 On the boundary between region III and IV

With $r = r_n + \frac{h}{2} + \ell_g$,

$$B_r^{III}(r,\phi) = B_r^{IV}(r,\phi) \tag{H.7}$$

$$\therefore \quad C_{m|PM}^{III} r^{mp} + D_{m|PM}^{III} r^{-mp} = C_{m|PM}^{IV} r^{mp} + D_{m|PM}^{IV} r^{-mp} + G_{m|PM}^{IV} \tag{H.8}$$

and

$$H_\phi^{III}(r,\phi) = H_\phi^{IV}(r,\phi) \tag{H.9}$$

$$\therefore \quad \frac{C_{m|PM}^{III} r^{mp-1} - D_{m|PM}^{III} r^{-mp-1}}{\mu^{III}} = \frac{C_{m|PM}^{IV} r^{mp-1} - D_{m|PM}^{IV} r^{-mp-1}}{\mu^{IV}} \tag{H.10}$$

H.1.5 On the boundary between region IV and V

With $r = r_n + \frac{h}{2} + \ell_g + h_m$,

$$H_\phi^{IV}(r,\phi) = 0 \tag{H.11}$$

$$C_{m|PM}^{IV} r^{mp-1} - D_{m|PM}^{IV} r^{-mp-1} = 0 \tag{H.12}$$

H.1.6 Simultaneous equations to solve

From (H.2), (H.4), (H.6), (H.8), (H.10) and (H.12) the following ten equations have to be solved for $m = 1, 3, 5, \to \infty$,

$$C_{m|PM}^{II} r_{ii}^{mp-1} - D_{m|PM}^{II} r_{ii}^{-mp-1} = 0 \tag{H.13}$$

$$C_{m|PM}^{II} r_{iii}^{mp} + D_{m|PM}^{II} r_{iii}^{-mp} - C_{m|PM}^{III} r_{iii}^{mp} - D_{m|PM}^{III} r_{iii}^{-mp} = -G_{m|PM}^{II} \tag{H.14}$$

$$\mu^{III} C_{m|PM}^{II} r_{iii}^{mp-1} - \mu^{III} D_{m|PM}^{II} r_{iii}^{-mp-1} - \mu^{II} C_{m|PM}^{III} r_{iii}^{mp-1} + \mu^{II} D_{m|PM}^{III} r_{iii}^{-mp-1} = 0 \tag{H.15}$$

$$C_{m|PM}^{III} r_{iv}^{mp} + D_{m|PM}^{III} r_{iv}^{-mp} - C_{m|PM}^{IV} r_{iv}^{mp} - D_{m|PM}^{IV} r_{iv}^{-mp} = G_{m|PM}^{IV} \tag{H.16}$$

$$\mu^{IV} C_{m|PM}^{III} r_{iv}^{mp-1} - \mu^{IV} D_{m|PM}^{III} r_{iv}^{-mp-1} - \mu^{III} C_{m|PM}^{IV} r_{iv}^{mp-1} + \mu^{III} D_{m|PM}^{IV} r_{iv}^{-mp-1} = 0 \tag{H.17}$$

$$C_{m|PM}^{IV} r_v^{mp-1} - D_{m|PM}^{IV} r_v^{-mp-1} = 0 \tag{H.18}$$

with

$$r_{ii} = r_n - \frac{h}{2} - \ell_g - h_m \tag{H.19}$$

$$r_{iii} = r_n - \frac{h}{2} - \ell_g \tag{H.20}$$

$$r_{iv} = r_n + \frac{h}{2} + \ell_g \tag{H.21}$$

$$r_v = r_n + \frac{h}{2} + \ell_g + h_m \tag{H.22}$$

and

$$G_{m|PM}^{II} = -\frac{4(r_n - \frac{h}{2} - \ell_g - \frac{h_m}{2}) B_{rem} \cos m\beta}{m^2 \pi} \tag{H.23}$$

$$G_{m|PM}^{IV} = -\frac{4(r_n + \frac{h}{2} + \ell_g + \frac{h_m}{2}) B_{rem} \cos m\beta}{m^2 \pi} \tag{H.24}$$

$$\begin{bmatrix} r_{ii}^{mp-1} & -r_{ii}^{-mp-1} & & & & \\ r_{iii}^{mp} & r_{iii}^{-mp} & -r_{iii}^{mp} & -r_{iii}^{-mp} & & \\ \mu^{III} r_{iii}^{mp-1} & -\mu^{III} r_{iii}^{-mp-1} & -\mu^{II} r_{iii}^{mp-1} & \mu^{II} r_{iii}^{-mp-1} & & \\ & & r_{iv}^{mp} & r_{iv}^{-mp} & -r_{iv}^{mp} & -r_{iv}^{-mp} \\ & & \mu^{IV} r_{iv}^{mp-1} & -\mu^{IV} r_{iv}^{-mp-1} & -\mu^{III} r_{iv}^{mp-1} & \mu^{III} r_{iv}^{-mp-1} \\ & & & & r_v^{mp-1} & -r_v^{-mp-1} \end{bmatrix}.$$

$$\begin{bmatrix} C_{m|PM}^{II} \\ D_{m|PM}^{II} \\ C_{m|PM}^{III} \\ D_{m|PM}^{III} \\ C_{m|PM}^{IV} \\ D_{m|PM}^{IV} \end{bmatrix} = \begin{bmatrix} 0 \\ -G_{m|PM}^{II} \\ 0 \\ G_{m|PM}^{IV} \\ 0 \\ 0 \end{bmatrix} \tag{H.25}$$

APPENDIX I

Analytical – FEM Comparison for Test Machine II

I.1 Introduction

In this section the validity of the analytical model derived in this dissertation is tested against against the Maxwell® 2D FEA model of Test Machine II, given in section E.2 of Appendix E. Good correlation between the analytical and FEA results were obtained as is shown in the following sections. One exception is however that of the torque output as shown in Figure I.9. The ripple torque of the FEA simulation is clearly not correct as can be seen from harmonic spectrum shown in Figure I.10. There is clearly some sort of "computational resonance" present at the twelfth harmonic in the Maxwell® 2D result.

I.2 Radial and Azimuthal Flux-density Comparison

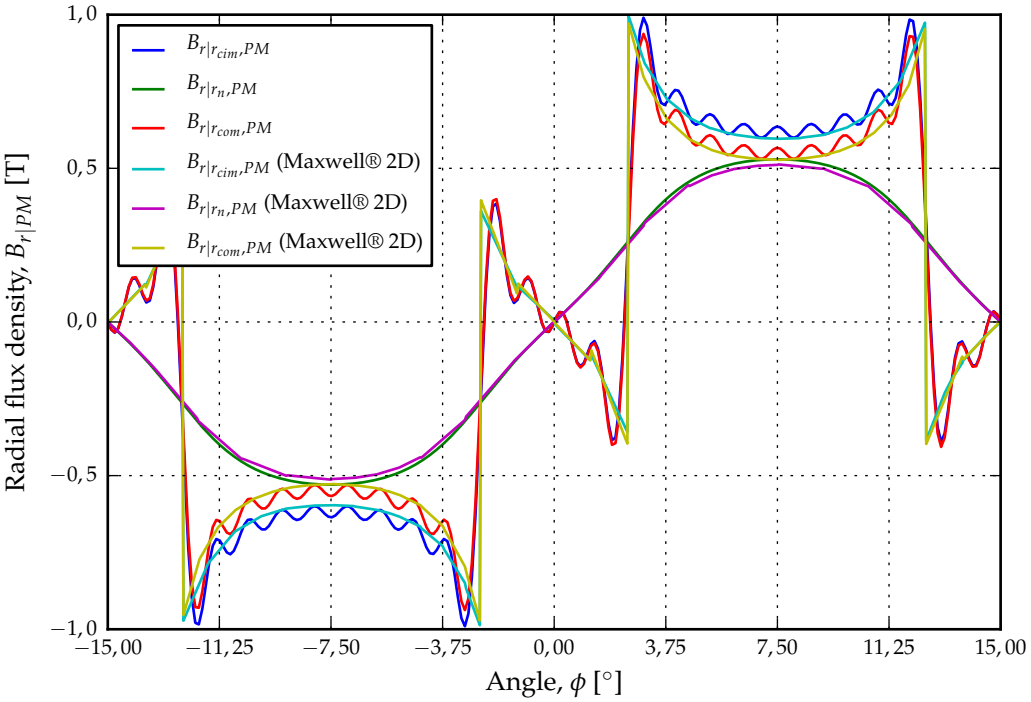

Figure I.1: The radial flux-density distribution.

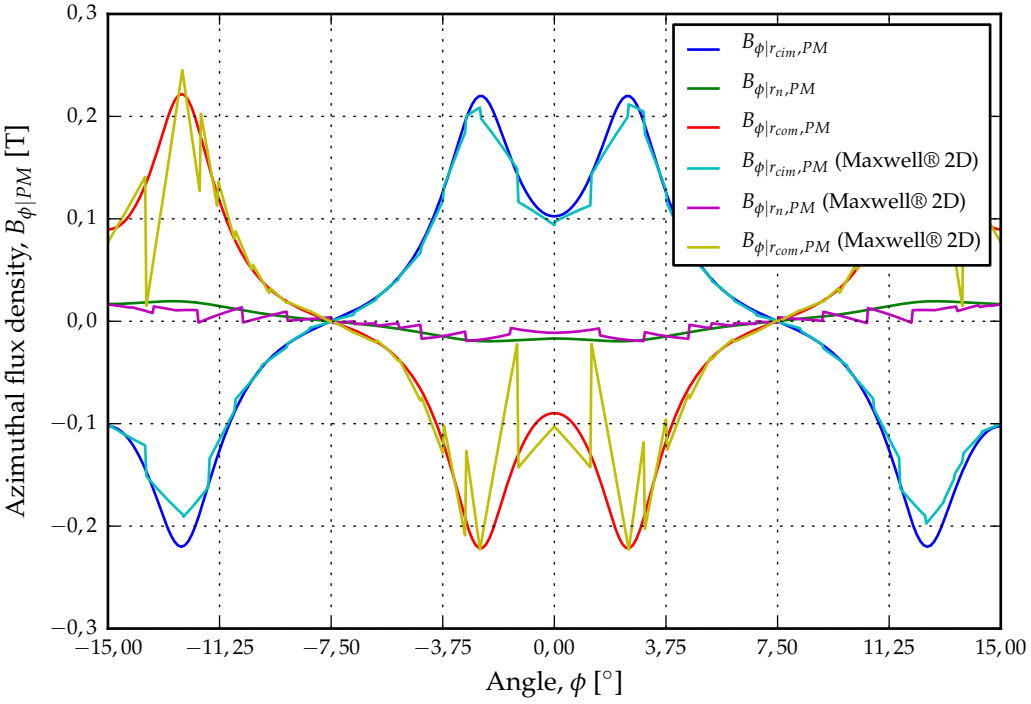

Figure I.2: The azimuthal flux-density distribution.

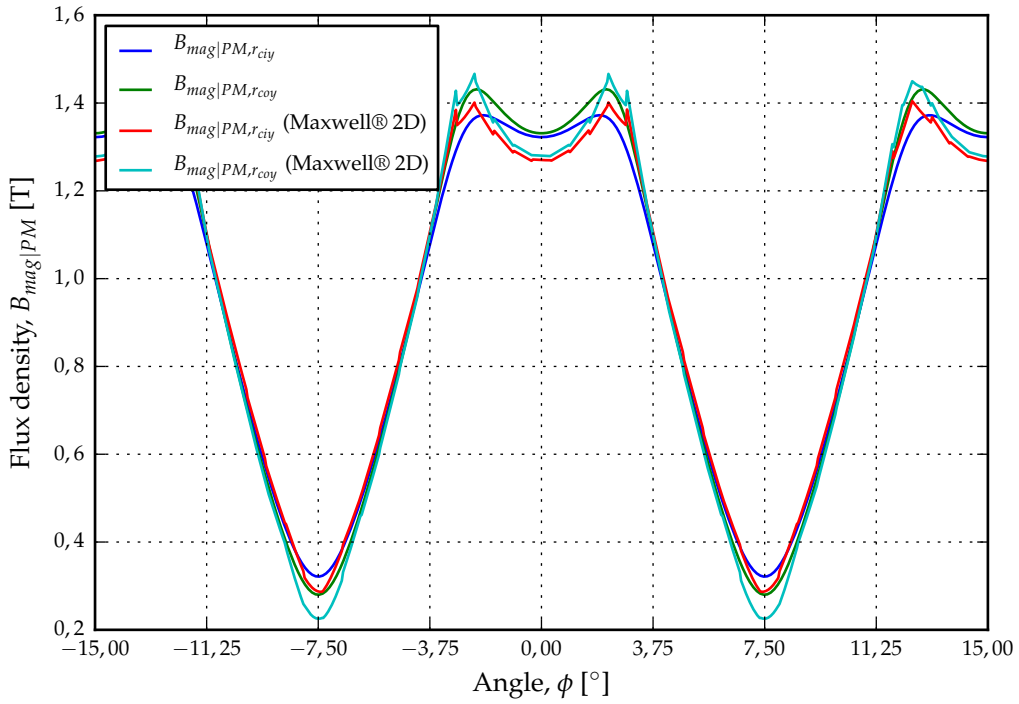

Figure I.3: The variation in the flux-density in the centre of the rotor yokes.

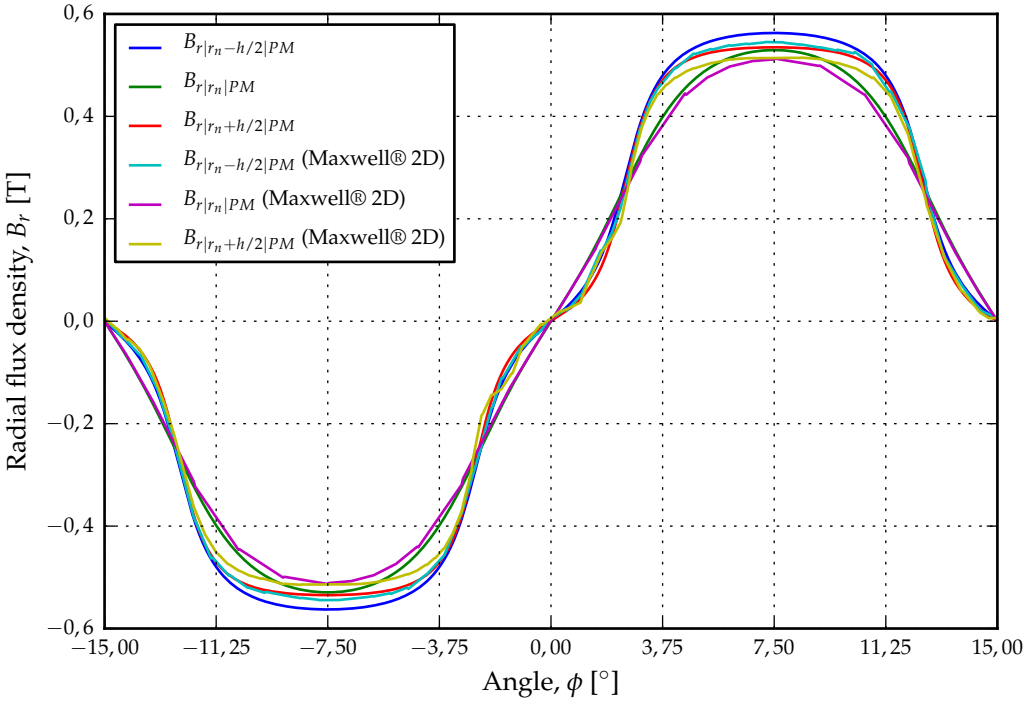

Figure I.4: The variation in the shape radial flux-density distribution in the stator windings shown on the outer –, centre – and inner radius of the stator for the analytical analysis method compared the the FEA analysis done using Maxwell® 2D.

I.3 Flux-linkage and Back-EMF Comparison

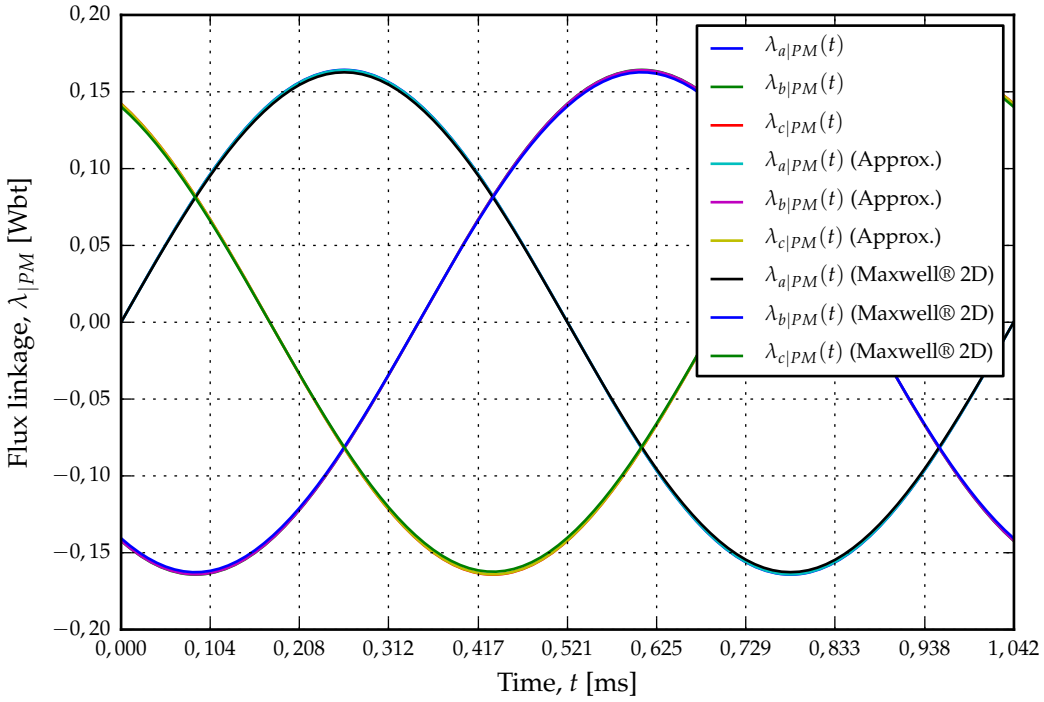

Figure I.5: Comparison of the flux-linkage calculations for the Type II winding configuration.

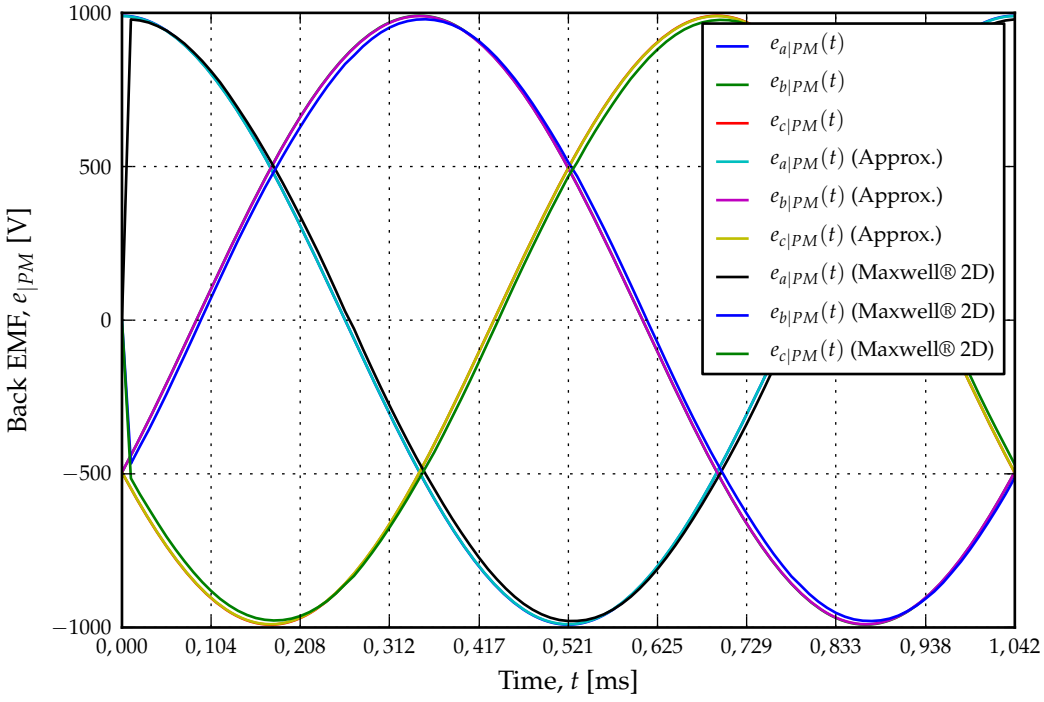

Figure I.6: Comparison of the back-EMF calculations for the Type II winding configuration.

I.4 Armature Reaction Flux-density Comparison

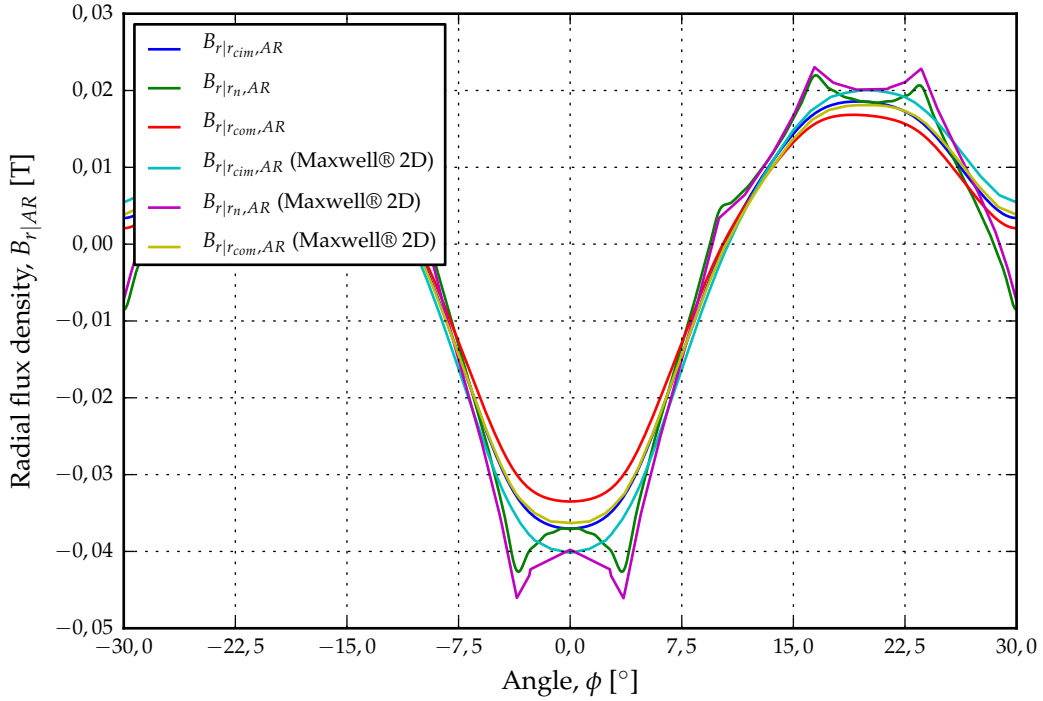

Figure I.7: The radial flux-density distribution due to armature reaction.

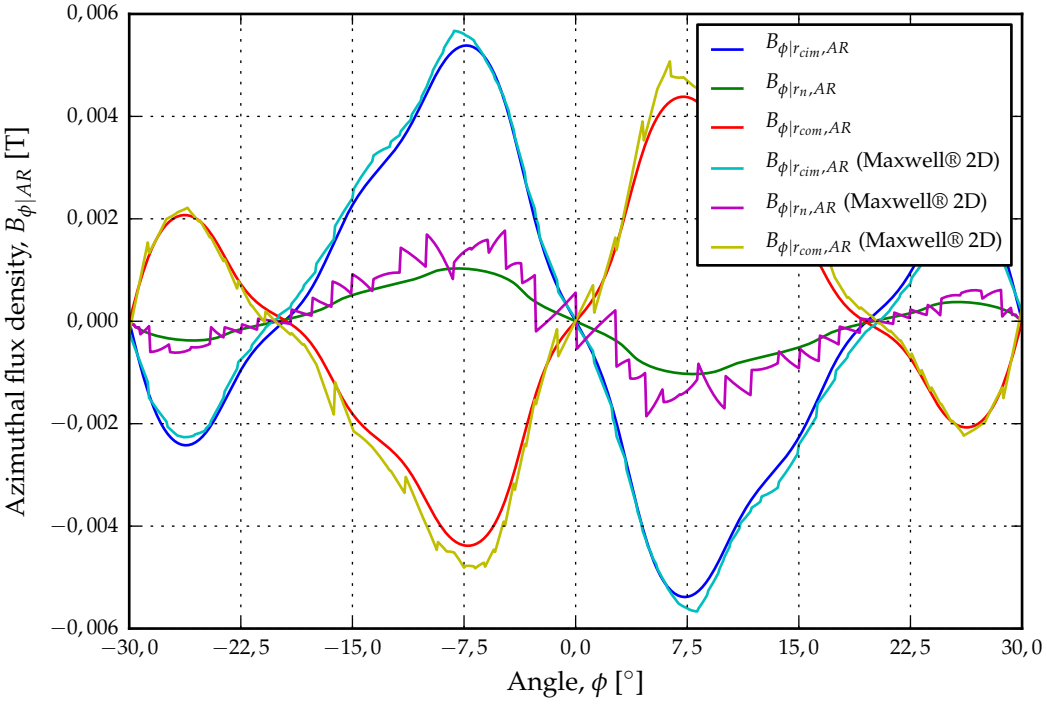

Figure I.8: The azimuthal flux-density distribution due to armature reaction.

I.5 Output Torque Comparison

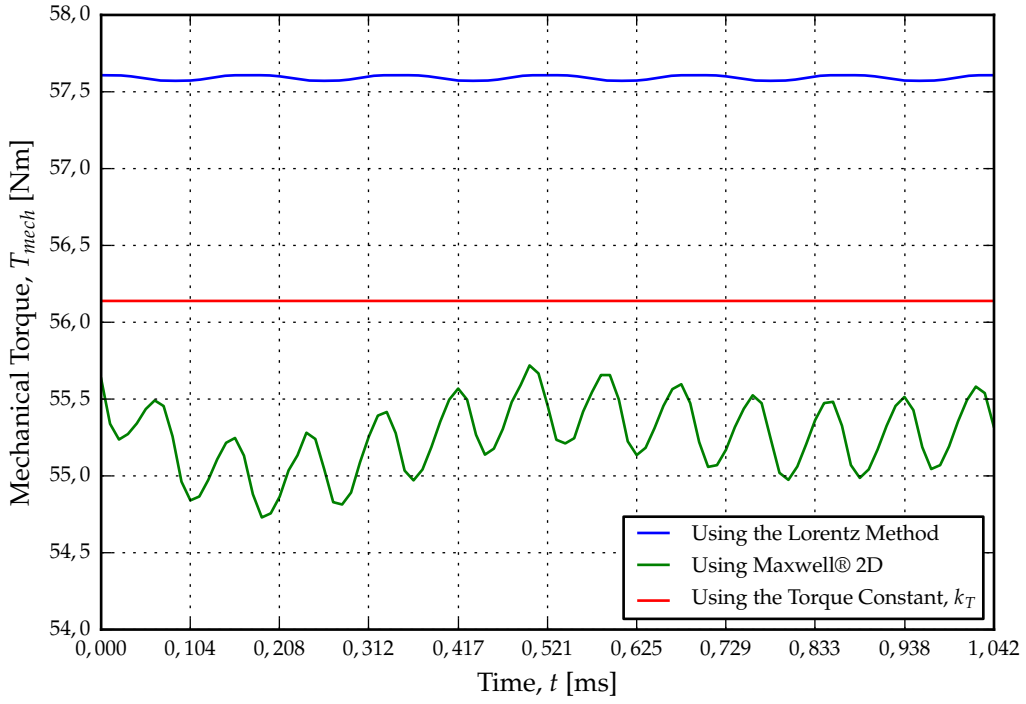

Figure I.9: The torque ripple waveforms for the Type II winding configuration.

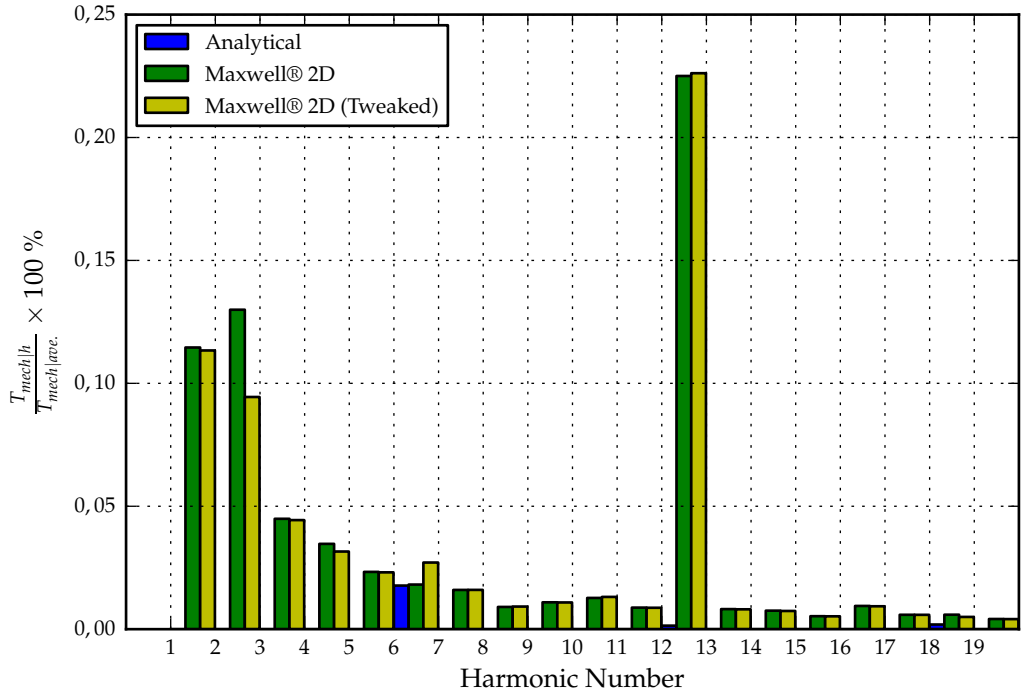

Figure I.10: A FFT of the torque ripple harmonics for the Type II winding configuration.

APPENDIX J

Brief Python™ Code Desciption

J.1 Introduction

In this Appendix, the Python™ code[1] that was developed for the analysis of the Double-sided Rotor Radial Flux Air-cored Permanent Magnet (RFAPM) machine will be briefly discussed. The Python™ code makes use of the *Numpy* module developed by Oliphant [55] specifically for "Scientific Computing". The *Numpy* module adds multi-dimensional array capabilities to Python™. This give Python™ similar features to Matlab®, just using multi-dimensional arrays instead of two-dimensional matrices.

For visualisation of the results, the excellent add-on package, *Matplotlib* by Hunter [42] is used. The `pylab` library inside the *Matplotlib* package could be described as a "Matlab®–like plotting library for Python™ " with near identical keyword used, e.g. `plot`, `xlabel`, `ylabel`, `axis`, `grid`, `linspace`, etc.

The interactive Python™ environment of *IPython* created by Perez and Granger [56], provides the ideal interactive scripting, testing and debugging environment for the implementation of the analytical solution into Python™ code.

J.2 Python™ Scripts to call Maxwell® 2D via the COM Interface

`test_machine_i.py` – The data for Test Machine I.

`test_machine_ii.py` – The data for Test Machine I.

`poly.py` – A collection of polygon functions.

`farey.py` – An implementation of the Farey function, implemented in Python™.

[1] This code is available for download at `http://staff.ee.sun.ac.za/pjrandewijk/downloads/phd/`.

pyMaxwell2D.py – Some Python™ wrapper classes for the ActiveX or COM functions of Maxwell® 2D.

rfapm.py – The main Python™ script that "draws" and simulates the RFAPM machine in Maxwell® 2D depending on whether `test_machine_i.py` or `test_machine_ii.py` were imported..

J.3 Python™ Scripts to do the Analytical Analysis

test_machine_i.py – The data for Test Machine I, same file as in section J.2.

test_machine_ii.py – The data for Test Machine I, , same file as in section J.2.

mxwltxt.py – Contains the `loadmxwltxt` function to to convert the Maxwell® 2D output `*.txt` file into a *Numpy* record array for easier plotting with *Matplotlib*.

analytical_solution_i.py – The main script that does the analytical calculations for Test Machine I

analytical_solution_ii.py – The main script that does the analytical calculations for Test Machine II, essentially the same script as the above, with the only difference in the scaling of the *Matplotlib* graphs

References

[1] Gieras, J.F. and Wing, M.: *Permanent Magnet Motor Technology – Design and Applications*. Second edi edn. Marcel Dekker, Inc., 2002. ISBN 0-8247-0739-7. 1.2.1, F.6

[2] Hesmondhalgh, D.E. and Tipping, D.: Slotless construction for small synchronous motors using samarium cobalt magnets. *Electric Power Applications, IEE Proceedings B*, vol. 129, no. 5, pp. 251–261, 1982. ISSN 0143-7038. 1.2.2

[3] England, T.R.: Unique surface-wound brushless servo with improved torque ripple characteristics. *Industry Applications, IEEE Transactions on*, vol. 24, no. 6, pp. 972–977, 1988. ISSN 0093-9994. 1.2.2

[4] Kaddouri, A. and Le-Huy, H.: Analysis and design of a slotless NdFeB permanent-magnet synchronous motor for direct drive. In: *Industry Applications Society Annual Meeting, 1992., Conference Record of the 1992 IEEE*, pp. 271—-278 vol.1. 1992. 1.2.2

[5] Arkadan, A.A., Vyas, R., Vaidya, J.G. and Shah, M.J.: Effect of toothless stator design and core and stator conductors eddy current losses in permanent magnet generators. *Energy Conversion, IEEE Transactions on*, vol. 7, no. 1, pp. 231–237, 1992. ISSN 0885-8969. 1.2.2, 6.4

[6] Atallah, K., Zhu, Z.Q. and Howe, D.: Armature reaction field and winding inductances of slotless permanent-magnet brushless machines. *Magnetics, IEEE Transactions on*, vol. 34, no. 5, pp. 3737–3744, 1998. ISSN 0018-9464. 1.2.2, 3.6.1, 4.1

[7] Zhu, Z.Q. and Howe, D.: Instantaneous magnetic field distribution in brushless permanent magnet {DC} motors, Part {II}: Armature-reaction field. *Magnetics, IEEE Transactions on*, vol. 29, no. 1, pp. 136–142, 1993. ISSN 0018-9464. 1.2.2, 2.3.3, 4.1

[8] Gieras, J.F., Wang, R.J. and Kamper, M.J.: *Axial flux permanent magnet brushless machines*. 2nd edn. Springer Verlag, 2008. 1.2.3

[9] Wang, R.-J.: *Design Aspects and Optimisation of an Axial Fielf Permanent Magnet Machine with an Ironless Stator*. Ph.D. thesis, Stellenbosch University, March 2003. 1.2.3

[10] Wang, R.-J., Kamper, M.J., der Westhuizen, K. and Gieras, J.F.: Optimal design of a coreless stator axial flux permanent-magnet generator. *Magnetics, IEEE Transactions on*, vol. 41, no. 1, pp. 55–64, 2005. ISSN 0018-9464. 1.2.3

[11] Cros, J. and Viarouge, P.: Synthesis of high performance PM motors with concentrated windings. *Energy conversion, ieee transactions on*, vol. 17, no. 2, pp. 248–253, 2002. ISSN 0885-8969. 1.2.4

[12] Wong, D.: Going beyond e-waste recycling: Inside a computer rebuilding operation. 2011. Available at: http://www.neowin.net/news/going-beyond-e-waste-recycling-inside-a-computer-rebuilding-operation 1.2.4, 1.1

[13] Kamper, M.J., Wang, R.-J. and Rossouw, F.G.: Analysis and Performance of Axial Flux Permanent-Magnet Machine With Air-Cored Non-overlapping Concentrated Stator Windings. *Industry Applications, IEEE Transactions on*, vol. 44, no. 5, pp. 1495–1504, 2008. ISSN 0093-9994. 1.2.4, 1.2.5, 2.3.1, 5.2, 6.1

[14] Randewijk, P.J., Kamper, M.J. and Wang, R.J.: Analysis and Performance Evaluation of Radial Flux Air-Cored Permanent Magnet Machines with Concentrated Coils. In: *Power Electronics and Drive Systems, 2007. PEDS '07. 7th International Conference on*, pp. 189–195. 2007. 1.2.5, 1.3, 2.6, 5.2, 6.1, 7.1

[15] Stegmann, J.A.: *Design and Analysis Aspects of Radial Flux Air-cored Permanent Magnet Wind Generator System for Direct Battery Charging Applications*. Master of Science in Engineering, Stellenbosch University, 2010. 1.2.5, 1.2, 1.3, 2.6, 7.3, E.1

[16] Stegmann, J.A. and Kamper, M.J.: Design aspects of medium power double rotor radial flux air-cored PM wind generators. In: *Energy Conversion Congress and Exposition, 2009. ECCE 2009. IEEE*, pp. 3634–3640. 2009. 1.2.5, 2.6, 7.1, E.1

[17] Groenewald, D.J.: *Evaluation of a radial flux air-cored permanent magnet machine drive with manual transmission drivetrain for electric vehicles*. Master of Science in Engineering, Stellenbosch University, Stellenbosch, 2011. 1.3, 2.6, 7.3, E.2

[18] Gerber, S., Strauss, J.M. and Randewijk, P.J.: Evaluation of a hybrid finite element analysis package featuring dual air-gap elements. In: *Electrical Machines (ICEM), 2010 XIX International Conference on*, pp. 1–6. 2010. 1.3, 5.3.2.3, 7.1

[19] Fitzgerald, A.E., Kingsley, C. and Umans, S.D.: *Electric Machinery*. Sixth edit edn. McGraw-Hill, 2003. ISBN 0-07-366009-0. 2.2, 2.4, F.2

[20] Slemon, G.R.: *Electric machines and drives*. Addison-Wesley, 1992. ISBN 0-201-57885-9. 2.3.2, 5.2

[21] Holm, S.R., Polinder, H. and Ferreira, J.A.: Analytical Modeling of a Permanent-Magnet Synchronous Machine in a Flywheel. *Magnetics, IEEE Transactions on*, vol. 43, no. 5, pp. 1955–1967, May 2007. ISSN 0018-9464. 2.3.2, 3.2, 3.6.1, 3.7.2

[22] Zhu, Z.Q., Howe, D. and Chan, C.C.: Improved analytical model for predicting the magnetic field distribution in brushless permanent-magnet machines. *Magnetics, IEEE Transactions on*, vol. 38, no. 1, pp. 229–238, 2002. 2.3.3, 3.2, 3.6.1, 3.7.1, 3.7.2, 4.1

[23] Zhu, Z.Q., Wu, L.J. and Xia, Z.P.: An Accurate Subdomain Model for Magnetic Field Computation in Slotted Surface-Mounted Permanent-Magnet Machines. *Magnetics, IEEE Transactions on*, vol. 46, no. 4, pp. 1100–1115, 2010. ISSN 0018-9464. 2.3.3, 3.2, 3.6.1, F.1

[24] Holm, S.R.: *Modelling and optimization of a permanent magnet machine in a flywheel.* Doctoral, Technische Universiteit Delft, 2003. 2.3.3, 3.2, 3.12.1, 4.1, 5.3, 6.4

[25] Rossouw, E. and Kamper, M.J.: Use of Air-Cored Axial Flux Permanent Magnet Generator in Direct Battery Charging Wind Energy Systems. In: *Power Electronics and Drive Systems, 2007. PEDS '07. 7th International Conference on*, pp. 1102–1107. 2007. 2.3.3, 6.1

[26] Stegmann, J.A. and Kamper, M.J.: Design Aspects of Double-Sided Rotor Radial Flux Air-Cored Permanent-Magnet Wind Generator. *IEEE Transactions on Industry Applications*, vol. 47, no. 2, pp. 767–778, March 2011. ISSN 0093-9994. 2.6, 3.11.3, 7.1, E.1

[27] Boules, N.: Two-Dimensional Field Analysis of Cylindrical Machines with Permanent Magnet Excitation. *Industry Applications, IEEE Transactions on*, vol. IA-20, no. 5, pp. 1267–1277, 1984. ISSN 0093-9994. 3.2

[28] Boules, N.: Prediction of No-Load Flux Density Distribution in Permanent Magnet Machines. *Industry Applications, IEEE Transactions on*, vol. IA-21, no. 3, pp. 633–643, 1985. ISSN 0093-9994. 3.2, 3.4, 3.6.3, B

[29] Zhu, Z.Q., Howe, D., Bolte, E. and Ackermann, B.: Instantaneous magnetic field distribution in brushless permanent magnet {DC} motors, Part: {I}: Open-circuit field. *Magnetics, IEEE Transactions on*, vol. 29, no. 1, pp. 124–135, 1993. ISSN 0018-9464. 3.2, 3.6.1, 3.7.1, 3.7.2

[30] Kumar, P. and Bauer, P.: Improved Analytical Model of a Permanent-Magnet Brushless DC Motor. *Magnetics, IEEE Transactions on*, vol. 44, no. 10, pp. 2299–2309, 2008. ISSN 0018-9464. 3.2

[31] Virtic, P., Pisek, P., Marcic, T., Hadziselimovic, M. and Stumberger, B.: Analytical Analysis of Magnetic Field and Back Electromotive Force Calculation of an Axial-Flux Permanent Magnet Synchronous Generator With Coreless Stator. *Magnetics, IEEE Transactions on*, vol. 44, no. 11, pp. 4333–4336, 2008. ISSN 0018-9464. 3.2

[32] Virtic, P., Pisek, P., Hadziselimovic, M., Marcic, T. and Stumberger, B.: Torque Analysis of an Axial Flux Permanent Magnet Synchronous Machine by Using Analytical Magnetic Field Calculation. *Magnetics, IEEE Transactions on*, vol. 45, no. 3, pp. 1036–1039, 2009. ISSN 0018-9464. 3.2

[33] Chan, T.F., Lai, L.L. and Xie, S.: Field Computation for an Axial Flux Permanent-Magnet Synchronous Generator. *Energy Conversion, IEEE Transactions on*, vol. 24, no. 1, pp. 1–11, 2009. ISSN 0885-8969. 3.2

[34] Abdel-Razek, A., Coulomb, J., Feliachi, M. and Sabonnadiere, J.: Conception of an air-gap element for the dynamic analysis of the electromagnetic field in electric machines. *Magnetics, IEEE Transactions on*, vol. 18, no. 2, pp. 655–659, March 1982. ISSN 0018-9464. 3.2

[35] Cheng, D.K.: *Field and wave electromagnetics*. Addison-Wesley Reading, Mass, 1989. 3.3, 3.4, 3.5, 3.5, B, C.1, F.2

[36] Guru, B.S. and Hiziroglu, H.R.: *Electromagnetic field theory fundamentals*. Cambridge university press, 2004. 3.3, 3.4, 3.5

[37] Binns, K.J., Lawrenson, P.J. and Trowbridge, C.W.: *The analytical and numerical solution of electric and magnetic fields*. Wiley Chichester, UK, 1992. 3.3, 3.5, 3.6.1, 3.6.2

[38] Stratton, J.A.: *Electromagnetic theory*. Wiley-IEEE Press, 2007. ISBN 0470131535. 3.4, 3.4

[39] Reece, A.B.J. and Preston, T.W.: *Finite element methods in electrical power engineering*. Oxford University Press, USA, 2000. 3.5, 3.5, 3.7.1

[40] Gockenbach, M.S.: *Partial differential equations: analytical and numerical methods*. Society for Industrial Mathematics, 2002. 3.6.2

[41] Bleecker, D. and Csordas, G.: *Basic partial differential equations*. CRC Press, 1995. 3.7.1

[42] Hunter, J.D.: Matplotlib: A {2D} Graphics Environment. *Computing in Science & Engineering*, vol. 9, no. 3, pp. 90–95, 2007. ISSN 1521-9615. 3.11.1, J.1

[43] Mohan, N.: *Electric drives: an integrative approach*. MNPERE, 2003. ISBN 0-9715292-1-3. 3.14, 5.2, 5.2

[44] Rossouw, F.G.: *Analysis and design of axial flux permanent magnet wind generator system for direct battery charging applications*. Ph.D. thesis. 4.1

[45] Shin-Etsu Chemical Co., L.: {N48} {NdFeB} Magnet Demagnetization Curves at Elevated Temperature. May 2007. 4.8.2, F.5

[46] Benhama, A., Williamson, A.C. and Reece, A.B.J.: Force and torque computation from 2-D and 3-D finite element field solutions. *Electric Power Applications, IEE Proceedings -*, vol. 146, no. 1, pp. 25–31, 1999. ISSN 1350-2352. 5.1

[47] Kabashima, T., Kawahara, A. and Goto, T.: Force calculation using magnetizing currents. *Magnetics, IEEE Transactions on*, vol. 24, no. 1, pp. 451–454, January 1988. ISSN 0018-9464. 5.1

[48] Muller, W.: Comparison of different methods of force calculation. *Magnetics, IEEE Transactions on*, vol. 26, no. 2, pp. 1058–1061, March 1990. ISSN 0018-9464. 5.1, 5.3

[49] Choi, H.S., Park, I.H. and Lee, S.H.: Generalized equivalent magnetizing current method for total force calculation of magnetized bodies in contact. *Magnetics, IEEE Transactions on*, vol. 42, no. 4, pp. 531–534, April 2006. ISSN 0018-9464. 5.1

[50] Coulomb, J.: A methodology for the determination of global electromechanical quantities from a finite element analysis and its application to the evaluation of magnetic forces, torques and stiffness. *Magnetics, IEEE Transactions on*, vol. 19, no. 6, pp. 2514–2519, November 1983. ISSN 0018-9464. 5.1

[51] Coulomb, J. and Meunier, G.: Finite element implementation of virtual work principle for magnetic or electric force and torque computation. *Magnetics, IEEE Transactions on*, vol. 20, no. 5, pp. 1894–1896, September 1984. ISSN 0018-9464. 5.1

[52] Lebedev, A.V., Lomonova, E.A., Van Leuven, P.G., Steinberg, J. and Laro, D.A.H.: Analysis and initial synthesis of a novel linear actuator with active magnetic suspension. In: *Industry Applications Conference, 2004. 39th IAS Annual Meeting. Conference Record of the 2004 IEEE*, vol. 3, pp. 2111 – 2118 vol.3. 2004. ISSN 0197-2618. 5.1

[53] Abdel-Razek, A., Coulomb, J., Feliachi, M. and Sabonnadiere, J.: The calculation of electromagnetic torque in saturated electric machines within combined numerical and analytical solutions of the field equations. *Magnetics, IEEE Transactions on*, vol. 17, no. 6, pp. 3250–3252, 1981. ISSN 0018-9464. 5.3.2.3

[54] Shin-Etsu Chemical Co., L.: {N48H} {NdFeB} Magnet Demagnetization Curves at Elevated Temperature. May 2007. F.5

[55] Oliphant, T.E.: Python for Scientific Computing. *Computing in Science & Engineering*, vol. 9, no. 3, pp. 10–20, 2007. ISSN 1521-9615. J.1

[56] Perez, F. and Granger, B.E.: IPython: A System for Interactive Scientific Computing. *Computing in Science & Engineering*, vol. 9, no. 3, pp. 21–29, 2007. ISSN 1521-9615. J.1